ANDERSON CATAPAN
HEAD ORGANIZER

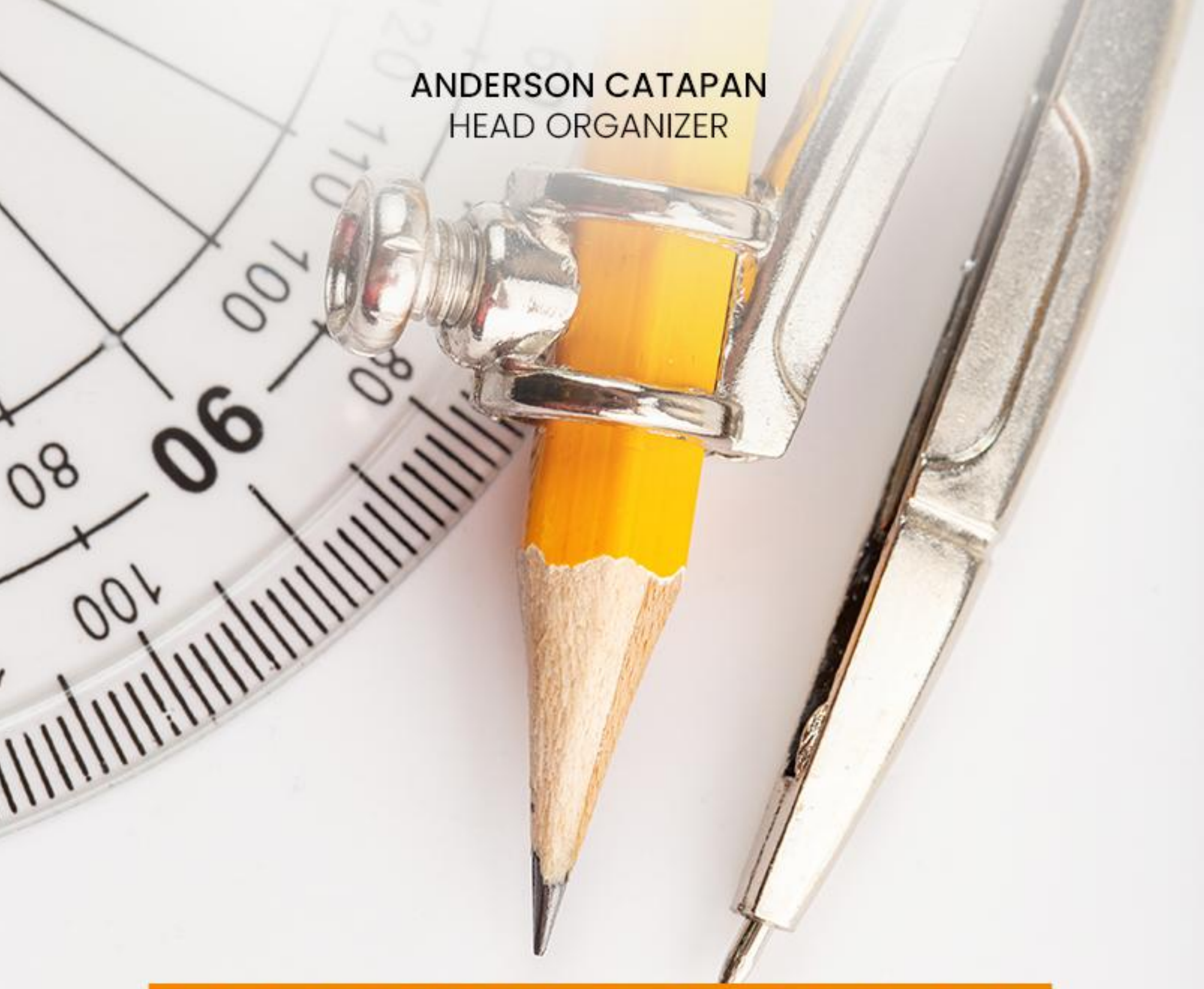

TECHNOLOGICAL DEVELOPMENT AND THE EXACT SCIENCES

CURITIBA
STUDIES PUBLICAÇÕES E EDITORA
2026

Anderson Catapan
Head Organizer

Technological Development and the Exact Sciences

Editora Studies Publicações
2026

Copyright © Editora Studies Publicações
Text Copyright © 2026 The Authors
Edition Copyright © 2026 Editora Studies Publicações
Layout: Publisher
Art Editing: Publisher
Proofreading: The Authors

The content of the articles and their data, in terms of form, accuracy, and reliability, are the sole responsibility of the author. Downloading and sharing of this work are permitted provided that credit is given to the author, but without any possibility of modification or commercial use.

Editorial Board:

Maria Lucia Teixeira Guerra de Mendonça – Pontifical Catholic University of Rio de Janeiro, Rio de Janeiro, Brazil.
Fernando Busato Ramires – University of Passo Fundo, Rio Grande do Sul, Brazil.
Halley Ferraro Oliveira
Federal University of Sergipe, Sergipe, Brazil.
Nelson Barrelo Junior – University of Sao Paulo, São Paulo, Brazil.
Adriane Aparecida de Souza Mahl Mangaroti – State University of Mato Grosso do Sul, Mato Grosso do Sul, Brazil.
Educélio Gaspar Lisbôa – State University of Pará, Pará, Brazil.
Aldalúcia Macêdo dos Santos Gomes – State University of Amazonas, Amazonas, Brazil.
Educélio Gaspar Lisbôa – State University of Pará, Pará, Brazil.
Aldalúcia Macêdo dos Santos Gomes – State University of Amazonas, Amazonas, Brazil.
Paula Wiethölter – Faculdade Especializada na Área de Saúde do Rio Grande do Sul, Rio Grande do Sul, Brazil.
Andréa Cristina Marques de Araújo – Fernando Pessoa University, Porto, Portugal.
Fernando Busato Ramires – University of Passo Fundo, Rio Grande Sul, Brazil.
Sérgio Eustáquio Lemos da Silva – Paulista State University, São Paulo, Brazil.
Lucas Araújo Ferreira – Universidade Federal do Pará, Pará, Brasil.
Shirleide Pereira da Silva Cruz – Universidade de Brasília, Brasília – DF, Brasil.
Ronaldo Salvador Vasques – Universidade Estadual de Maringá, Paraná, Brasil.
Francisca das Chagas Gaspar Rocha – Universidade Federal do Piauí, Piauí, Brasil.
Nayara Kelly Felix Ferreira – Centro Universitário Tabosa de Almeida – ASCES/UNITA, Pernambuco, Brasil.
Wenderson Gomes dos Santos – Universidade Federal do Amazonas – UFAM, Amazonas, Brasil.

STUDIES
PUBLICAÇÕES

Dados Internacionais de Catalogação na Publicação (CIP)

Technological Development and the Exact Sciences / Anderson Catapan. Curitiba. Editora Studies Publicações, 2026.

Format: PDF
System requirements: Adobe Acrobat Reader
Access mode: World Wide Web
Includes: Bibliography
ISBN: 978-65-83309-52-5
DOI: 10.54033/stebook.978-65-83309-52-5

1. Technological. 2. Sciences. 3. Mathematics.
I. Catapan, Anderson. II. Title.

Editora Studies Publicações
Curitiba – Paraná – Brasil
www.studiespublicacoes.com.br
editora@studiespublicacoes.com.br

PRESENTATION

Technological Development and the Exact Sciences is a work dedicated to understanding the scientific foundations that underpin contemporary technological progress. In a context defined by continuous innovation and increasing technical complexity, the interaction between technological development and the Exact Sciences becomes increasingly strategic.

The publication brings together reflections and studies that highlight the structural role of disciplines such as mathematics, physics, and engineering in the creation of solutions, methodologies, and processes that influence multiple sectors of society. By emphasizing scientific rigor, analytical reasoning, and solid theoretical grounding, the book underscores the importance of exact knowledge as a foundation for innovation.

It represents a meaningful academic contribution to research advancement and scientific education, encouraging critical analysis and continuous updating in response to technological transformation.

This book is recommended for professors, researchers, undergraduate and graduate students, as well as professionals working in scientific and technological fields who seek theoretical depth and technical development.

SUMÁRIO

CHAPTER 1

MODELING OF THE SECONDARY GRINDING SYSTEM AT SAMARCO MINERAÇÃO

Gabriel Gava de Castro
Metallurgical Engineer
Universidade Federal de Ouro Preto
E-mail: gabrielgavacastro2@gmail.com

Vladmir Kronemberger Alves
Doctorate in Metallurgical and Mining Engineering
Universidade Federal de Minas Gerais
E-mail: vladmir.alves@ufop.edu.br

Paulo Henrique Cirilo
Bachelor's degree in Metallurgical Engineering
Universidade Federal de Ouro Preto (UFOP)
E-mail: paulo.cirilo@aluno.ufop.edu.br

Alexandro Uliana
Master's Degree in Mineral Engineering
Universidade de São Paulo
E-mail: alexandro.uliana@samarco.com

ABSTRACT: Overflow ball mills are pivotal in iron ore processing worldwide, despite their significant operational costs and energy demands. Since industrial-scale testing is often time-consuming and expensive, this research employed laboratory-scale experiments using the Population Balance Model to optimize Samarco's regrinding circuit. By applying the MolyCop Tools software to data collected from the industrial site, the study characterized samples and conducted batch kinetic tests to define breakage and selection parameters. The final model demonstrated strong reliability, proving that laboratory data can accurately simulate and enhance industrial grinding performance.

KEYWORDS: iron ore, ball milling, process simulation, population balance.

RESUMO: Moinhos de bolas do tipo transbordo ("overflow") são componentes essenciais no processamento global de minério de ferro, embora demandem altos custos operacionais devido ao elevado consumo de energia. Dada a complexidade e o custo de realizar testes em escala industrial, este estudo buscou uma alternativa mais ágil e econômica para aprimorar o circuito de remoagem da Samarco por meio de ensaios laboratoriais baseados no Modelo de Balanço Populacional. A metodologia envolveu a utilização do software MolyCop Tools® para processar dados obtidos na amostragem integral do circuito da empresa. Foram realizados testes de cinética em regime de batelada para determinar os parâmetros das funções de quebra e seleção. Os resultados confirmaram a alta precisão do modelo, validando o uso de experimentos em pequena escala para projetar e otimizar diferentes cenários operacionais na planta industrial.

PALAVRAS-CHAVE: minério de ferro, moagem de bolas, simulação de processos, balanço populacional.

1. INTRODUCTION

In Samarco Mineração's regrinding sector, ball mills are used mainly for the production of pellet feed (material with 80% of particles below 45 microns). This strict particle size adjustment is vital to ensure the necessary mineral release and the viability of transporting the pulp through the slurry pipeline to the pelletizing unit in Ubu (ES).

Historically, the sizing of these circuits has been based on energy consumption models, such as the Bond method (1952). However, although widely accepted, these traditional models have limitations, as they cannot predict the complete particle size distribution of the product or accurately describe the behavior of ores with specific grindability characteristics (Alves, 2006; Alves *et al.*, 2023, Puperi, 2024; Alves *et al.,* 2024).

To overcome these restrictions, the Population Balance Model, introduced by Austin (1973), emerged as an interesting tool because it uses mathematical functions that correlate feed and final product in detail (NAPIER-MUNN *et al.*, 1996).

The main purpose of this study is to determine the kinetic parameters of breakage and selection through bench mill tests, aiming to project the behavior of industrial re-grinding. Through this methodology, we seek to demonstrate that the transposition of laboratory data to the industrial scale, as discussed by Mazzinghy (2009), allows us to identify opportunities for operational optimization with safety and precision.

2. THEORETICAL REFERENCE

The family of population balance models uses techniques that allow the monitoring of ore particle size distributions while it is being comminuted. For this reason, they enable comminution circuits to be simulated without assuming that particle size distributions follow a normal curve. This requires extensive computational modeling and configuration of various parameters (WILLS; FINCH, 2016). The equations are used for scaling and simulating industrial plants based on smaller-scale laboratory tests.

Alves (2006) proved the effectiveness of this model in his work when he optimized an industrial mill by suggesting a change in the grinding load through laboratory tests.

Mazzinghy (2009), for example, used this method to simulate and optimize a gold ore grinding circuit with hydrocyclone classification. In his work, he indicated considerable specific energy savings through a reduction in the degree of filling and adequate replacement of the grinding body. The same author participated in the preparation of studies in which he demonstrates the *scale-up* of a vertical mill using the model in question (MAZZINGHY, 2012; MAZZINGHY *et al.*, 2015).

In 2019, Faria *et al*. (2019) published a paper on the optimization of a ball mill in the production of pellet feed for iron ore pelletization. The authors were able to predict the particle size distribution of the product from a pilot-scale mill operating under different conditions based on laboratory tests. In addition, they optimized the percentage of solids in the industrial mill.

These are some practical examples of successful work using the Population Balance Model applied to ore grinding.

2.1 BREAKAGE AND SELECTION FUNCTION

According to Austin, Klimpel, and Luckie (1984), the population balance model for batch mills, i.e., non-continuous mills, follows an equation. This equation is based on the rate of emergence of particles of certain sizes from the breakage of larger sizes, minus the disappearance of particles due to their breakage into smaller sizes during the grinding process. Figure 1 visually demonstrates this process.

Figure 1. Visual representation of the population balance in batch grinding. Size 1 is comminuted into sizes 2, 3, 4, and 5. Size 2 has an addition of material from size 1 and is comminuted into sizes 3, 4, and 5. The process is repeated for smaller sizes up to size 5.

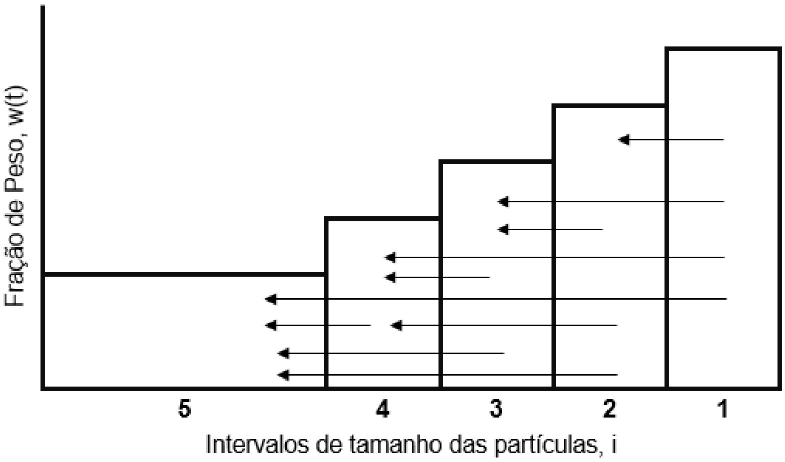

Source: Austin *et al.*, 1984.

The authors also present the formula that represents this process in equation 1.

$$\frac{dm_i(t)}{dt} = -S_i m_i(t) + \sum_{j=1}^{i-1} b_{ij} S_j m_j(t) \qquad (1)$$

where:

m_i (t) = fraction of particle mass contained in size i after a grinding time t;

b_{ij} = size distribution over size i from the breaking process of size j;

S_i = specific breakage rate of particles of size i.

According to the formula, there is a breakage function B_{ij} that describes the particle size distribution of the fragments produced as a result of the comminution event in the mill. There is also a selection function S_i , which describes the kinetics (speed) of fracture of each particle.

Equation 2 shows the function B_{ij}(Austin et al., 1984):

$$B_{ij} = \beta_0 \left(\frac{d_{i-1}}{d_j}\right)^{\beta_1} + (1-\beta_0)\left(\frac{d_{i-1}}{d_j}\right)^{\beta_2} \qquad (2)$$

The parameters β_0, $\beta_{(1)}$,and $\beta_2$depend on the material, not on the grinding conditions.

Similarly, in equation 3, the selection function S_i:

$$S_i = \frac{\alpha_0 (d_i)^{\alpha_1}}{1+\left(\frac{d_i}{d_{crít}}\right)^{\alpha_2}} \qquad (3)$$

The parameters α_0, α_1, $\alpha_{(2)}$,and $d_{crit}$are characteristic parameters of both the material and the grinding conditions. d_i(mm) is the average geometric size of the i-th fraction.

Herbst and Fuerstenau (1973) showed that the selection function maintains proportionality with the energy consumed during the grinding process. This relationship is shown in equation 4.

$$S_i = S_i^E \left(\frac{P}{H}\right) \qquad (4)$$

where:

Si (min-1) = selection function for each size class
SiE (t/kWh) = specific energy selection function
P (kW) = net grinding power
H(t) = amount of particulate material inside the mill.

This equation is used to determine the power required in a circuit based on the grinding of a certain product and its particle size distribution.

Simulators generally find values for the parameters α0, α1, α_2, d_{crit}, β_0, β_1, and $\beta_2$in order to minimize the objective function φ, which relates the differences between simulated and actual values in the particle size distributions. According to equation 5:

$$\varphi = \sum_{i=1}^{n} w_i \left[\frac{(F_i - f_i)}{fi}\right]^2 \qquad (5)$$

F_i represents the size distribution of the ground product in terms of the percentage passing through the sieve measured in the sample, and f_i represents the calculation by the model for F_i based on the particle size curve of the sample feed and a set of parameters found. w_i is the weight chosen for each parameter, which in this study was set at 1 with no variation.

3. METHODOLOGY

Sampling was carried out at all key points of the direct and reverse closure regrinding stage at the Germanão complex of the Samarco mining company in Mariana, MG. All process variables, as well as equipment characteristics, were monitored and recorded. Examples include critical speed, mill fill level, feed rate, power, cyclone pressure, number of cyclones in operation, and dimensions of mills and classifiers. The samples were characterized at Samarco's Process Development Laboratory in order to determine the particle size distribution curves, densities, percentage of solids, chemical composition, and specific surface area.

After this stage, a mass balance was performed and aliquots of the mill feed were composed for kinetic tests in the batch mill. High-chromium steel balls were used, graded according to Bond's equilibrium distribution (Bond, 1960), with a maximum size of 25 mm. All parameters used in the laboratory tests were defined as being the same as those in the industrial circuit ( ).

After the tests, the parameters of the breakage and selection functions were calculated to calibrate the mathematical models. These parameters were compared to the mass balance of the production process through simulations. *Molycop Tools* spreadsheets were used in the mass balance, model calibration, and simulation stages.

Figure 2 shows the flowchart for regrinding at Samarco's Concentrator 3. It shows the collection points for all flows in the circuit (circles) and the blended sample in the laboratory for use in batch tests (squares). This sample was blended, homogenized, and quartered to generate aliquots for testing.

Figure 2. Flowchart of the grinding unit operation at Samarco's Concentrator 3.

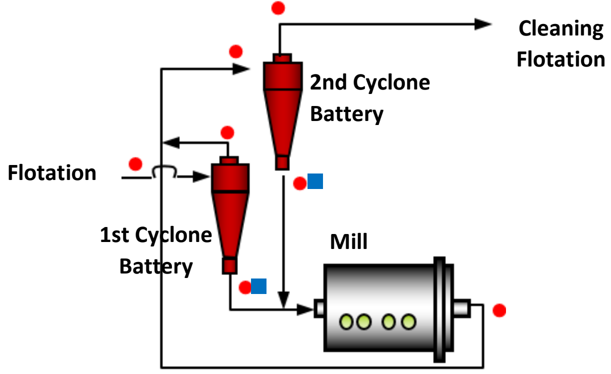

Source: Prepared by the authors.

For batch grinding, a 25.4 cm x 25.4 cm mill was used, where the aliquots were wet ground for 7 different times in order to obtain particle size curves of the products for calculating the breakage and selection functions. The times used were 1, 2, 4, 8, 20, 40, and 60 minutes, covering a wide range of particle sizes of the grinding product.

The percentage of critical speed used was 77%, ball filling was 28%, and interstitial space filling was 1.71, according to industrial parameters. The grinding load scaling was based on the studies by Bond (1960) and Austin *et al.* (1984), found in Table 1.

Table 1. Scaling used in the laboratory batch test with steel balls.

Average Ball Diameter (mm)	%	Weight (g)
25	36	5,932
20	41	6,749
15	23	3,796

Source: Prepared by the authors.

4. RESULTS AND DISCUSSIONS

Table 2 shows the parameters of the break and selection function after calibrating the model for laboratory tests. The result of the objective function to be minimized for model adherence is also shown.

Table 2. Breakdown and selection function parameters of the Population Balance model for batch tests, using MolyCop Tools spreadsheets.

	Selection Function				Break Function			Objective Function
	α_0	α_1	α_2	d_{crit}	β_0	β_1	β_2	
Result	0.001146	1.310	2.3	6471	0.01836	0.1706	2.066	0.40

The results of the laboratory tests can be seen in Figure 3. To analyze the adherence of the laboratory results to the industrial measurements, the circuit was simulated and the model results were compared with the mass balance. These results are shown in Figure 4.

Figure 3. Results of batch grinding tests with steel balls. Symbols represent measured distributions and lines represent calculated distributions.

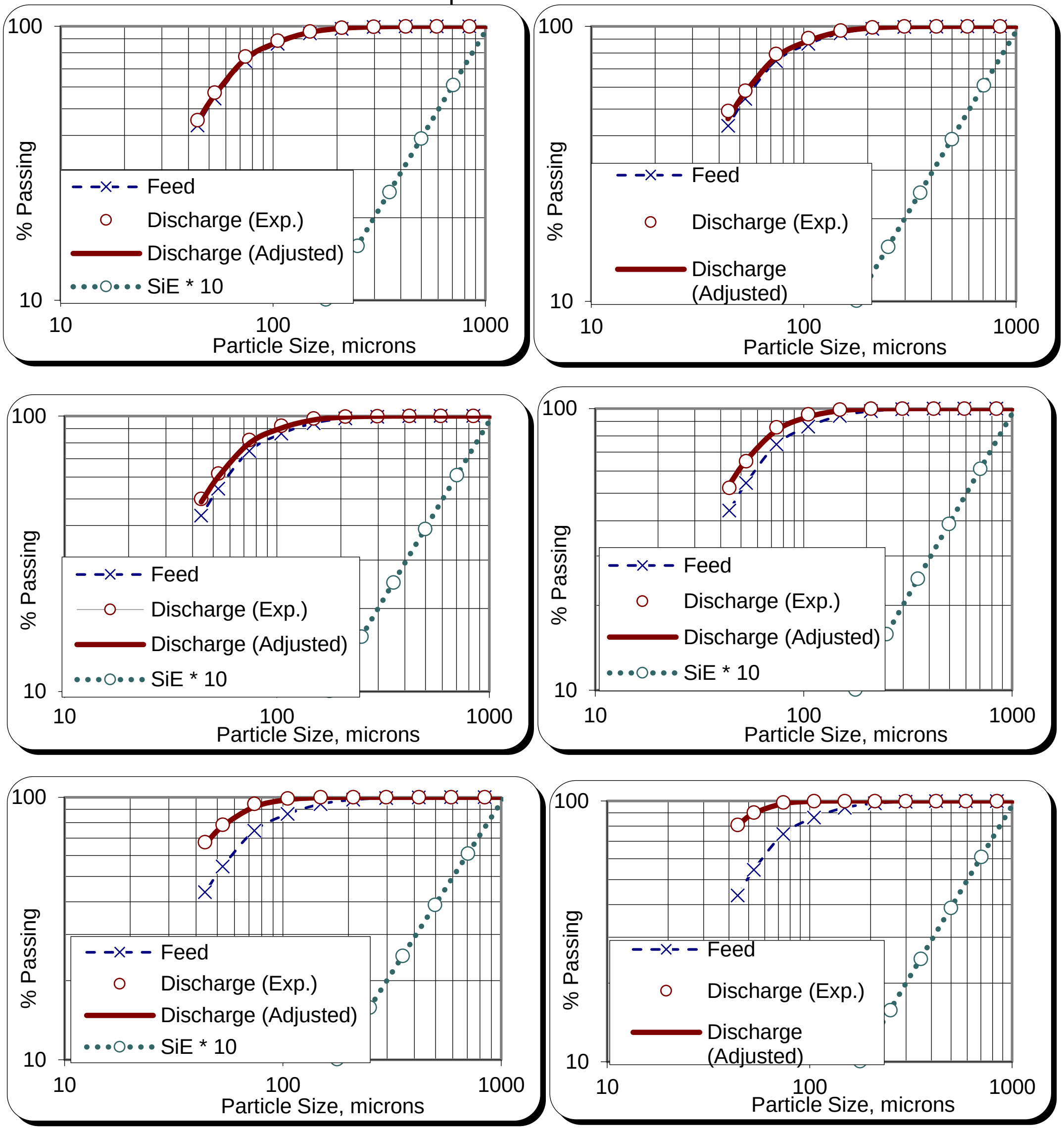

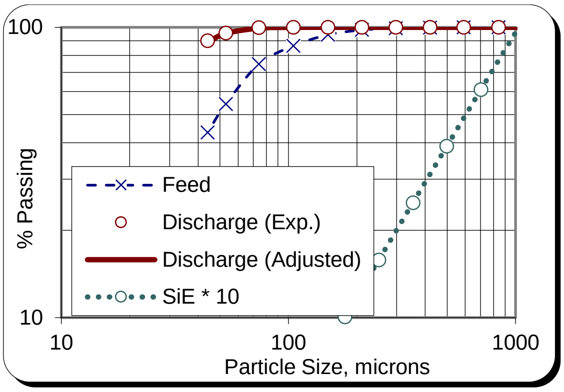

Source: Prepared by the authors using *Molycop Tools* spreadsheets.

Figure 4. Results of simulations using the calculated parameters of the breakage and selection functions on a laboratory scale compared with industrial data. Symbols represent measured data and lines represent simulated results.

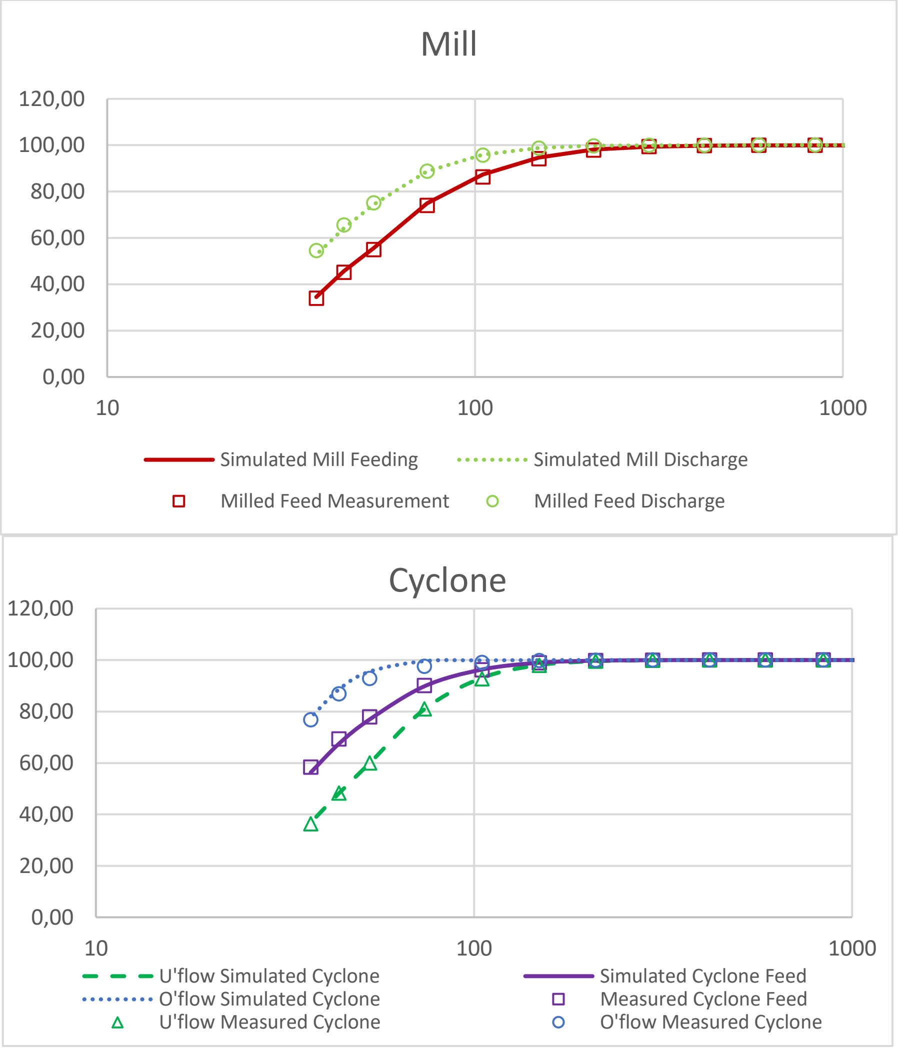

Source: Prepared by the authors.

5. CONCLUSION

The results of the laboratory-scale tests proved that it is possible to model and predict the crushing and selection behavior of the secondary grinding of Samarco's concentrator 3, using the population balance model and the mill of the Process Development Laboratory. It is therefore possible to use this resource to optimize the circuit depending on the input variables. This method contributes to decision-making in the face of new types of ore or grinding technologies, using a small sample size and saving time and money. In addition, it allows the evaluation of the grinding conditions studied in the laboratory with satisfactory prediction of particle size distribution, an important parameter for the subsequent stages of beneficiation. Similarly, these methods can be used in other processing plants to optimize circuits using laboratory-scale samples. It is recommended for future work that the technique be used in conjunction with modifications to the original circuits and gains in relation to them.

ACKNOWLEDGMENTS

We would like to thank Samarco's Process Development Laboratory in Mariana, Minas Gerais, for the tests and analyses, and the Federal University of Ouro Preto for its quality teaching.

REFERENCES

ALMEIDA H.J. *et al*. **Soil Type and Zinc Doses in Agronomic Biofortification of Lettuce Genotypes**. "Agronomy". 10, 124, 2020. doi:10.3390/agronomy10010124.

ALVARES, C. A.; STAPE, J. L.; SENTELHAS, P. C.; GONÇALVES, J. L. M.; SPAROVEK, G. **Koppen**. Meteorologische Zeitschrift, v.22, n. 6, p.711-728, 2013.

ARRIEL, N. H. C. *et al*. **The culture of sesame** - Brasília, DF: EMBRAPA Information Technology, 72p. 2007.

ARRIEL, N. H. C. *et al*. **Gergelim BRS Seda**, Campina Grande, PB: EMBRAPA, Brazilian Agricultural Research Corporation, 2009. Available at:https://ainfo.cnptia.embrapa.br/digital/bitstream/item/25691/1/FolderBRSSeda3edicao.pdf; Accessed: 23 Sep. 2024

BORTOLON, L.; GIANELLO, C. (2009). **Availability of copper and zinc in soils of southern Brazil**. Revista Brasileira de Ciência do Solo, v.33. ed.3, p.647–658. 2009

BOUIS, H. E.; SALTZMAN, A. **Improving nutrition through biofortification: A review of evidence from Harvest Plus**, 2003 through 2016. Global Food Security, v.12: p.49-58, 2017

BUTURI, C. V. *et al*. **Mineral Biofortification of Vegetables as a Tool to Improve Human Diet. Foods**, [s.l.], v. 10, n. 2, p. 223, 2021.

CALMAK, Ismail. **The role of potassium in alleviating detrimental effects of abiotic stresses in plants**. Journal of Plant Nutrition and Soil Science, v. 168, n. 4, p.521-530, 2005.

CHAVES, L. H. G. *et al*. **Zinc adsorption in Argisol from Paraíba State, Brazil: effect of Ph**. Revista CiênciaAgronômica, v. 39, n. 4, p.511-516, Oct-Dec, 2008

CHAVES, L. H. G. *et al*. **Effect of zinc and copper on the nutritional status of castor bean, BRS Paraguaçu**, Revista Caatinga, v.22, n4, p.129-135, 2009.

CONAB – Companhia Nacional de Abastecimento. **Sesame, 12th crop survey 2023/24**, September 2024. Available at https://www.conab.gov.br/info-agro/safras/graos/boletim-da-safra-de-graos .Accessed: 02/10/2024.

DE MUNER, L.H. et al. Zinc availability for maize in response to phosphorus location in soil. Revista Brasileira de Engenharia Agrícola e Ambiental, v.15, p.29-36, 2011.
DRISSI, S., *et al*. **Response of corn silage (Zea mays L.) to zinc fertilization on a sandy soil under field and outdoor container conditions**. Journal of the Saudi Society of Agricultural Sciences, v.16, ed. 2, pp. 145–153. 2017.

EMBRAPA, Brazilian Soil Classification System. Ed.5. Magazine and Enlarged. Brasília-DF. 355p. 2018.

FAGERIA, N.K. Adequate and toxic levels of zinc in the production of rice, beans, corn, soybeans and wheat in cerrado soil. Revista Brasileira de Engenharia Agrícola e Ambiental, v.4, p.390-395, 2000.

FAGERIA, N.K.; BALIGAR, V.C; Responde of common bean, upland rice, corn, wheat, and soybean to soil fertility of an Oxisol.Journal of plant Nutrition, v.20, n.10 p.1279-1289, 1997.

FERNANDES A.R. *et al*. **Growth and nutrient uptake by Freijó seedlings (*Cordia goeldiana*) as a function of phosphorus and zinc doses**. Revista Árvore, Viçosa-MG, v.31, n.4, p.599-608, 2006.

FERREIRA, A. C. B. *et al*. **Agronomic and nutritional characteristics of corn fertilized with nitrogen, molybdenum and zinc**. Scientia Agricola, Piracicaba, v.58, n. 1, p.131-138, Mar., 2001.

FRANCISCO, P. R. M.; SANTOS, D. **Climatologia do Estado da Paraíba**. 1. ed. Campina Grande, EDUFCG, 2017. 75p.

GUPTA, N., RAM, H., KUMAR, B. **Mechanism of Zinc absorption in plants: uptake, transport, translocation and accumulation**.Reviews in Environmental Science and Bio/Technology, v. 15, p. 89–109, 2016.

HAN, X. *et al*. **Zinc fractions and availability to soybeans in represent soils of Northeast China**. Journal of Soils and Sediments, v.11. ed.4. p.596-606, 2011.

HANSCH, R.; MENDEL, R. R. **Physiological functions of mineral micronutrients (Cu, Zn, Mn, Fe, Ni, Mo, B, Cl)**. "Plant Biology". Germania, v. 12, n. 3, p.259-266, July 2009.

HURRELL, R.; EGLI, I. **Iron bioavailability and dietary reference values**. The American Journal of Clinical Nutrition, v. 91, n. 5, p.1461S-1467S, 2010.

IBGE. **Sesame production in Brazil: census data - 2017**. Rio de Janeiro: IBGE, Available at: https://www.ibge.gov.br/explica/producao-agropecuaria/gergelim/br ; Accessed: 23 Sep. 2024

JOY, E. J., Ander *et al*. **Dietary mineral supplies in Africa**. Physiologia Plantarum, v.151, ed.3, p.208-229.2014.

KACHINSKI, W. D.; VIDIGAL, J. C. B.; ÁVILA, F. W.; **Zinc in soil, plant and human health: a review**. Research, Society and Development, v.9, n.7, 2020.

KÖPPEN, W.; GEIGER, R. (1928). **"Klimate der Erde"**. Gotha: Verlag Justus Perthes.
KUMSSA, D. B., *et al*. **Dietary calcium and zinc deficiency risks are decreasing but remain prevalent**. Scientific reports, v.5, ed.1, 10974p. 2015.

LIVINGSTONE C. **Zinc: Physiology, deficiency, and parenteral nutrition**. Nutrition in Clinical Practice v.30. p.371-382.2015.

LINHARES, L. A. *et al*. **Use of Langmuir and Freundlich models in the adsorption of copper and zinc in Brazilian soils**. Acta Agronômica, v.59 ed.3, p.303–315. 2010.

LOPES, G. W. **Germination and vigor of sesame seeds treated with growth stimulant**. 2024. 22p. Course Completion Work (Degree in Agronomy) - Federal Institute Goiano, Iporá - GO.

MA, X. *et al*. **A comprehensive review of bioactive compounds and processing technology of sesame seed** .OilCrop Science, v.7: p.88-94, 2022

MANOS, M. G. L., WILKINSON, J. **Mapping of Sociotechnical Controversies: the Case of Biofortification of Basic Foods in Brazil**. In: Proceedings of the 5th Ibero-American Congress on qualitative research, 2016

MOLOTO, R. M., *et al*.**Biofortification of common bean as a complementary approach to addressing zinc deficiency in South Africans**. Acta Agriculturae Scandinavica, Section B — Soil & Plant Science, v.68, ed.7, p.575–584. 2018

MONIKA. G. *et al*. **Biofortification: A long-term solution to improve global health-a review**. (Chemosphere. 314:137713). 2023

MUNER, L. H. D. *et al*.; **Availability of zinc for maize in response to the location of phosphorus in the soil**. Revista Brasileira de Engenharia Agrícola e Ambiental, v. 15, ed.1, p.29-38.2011.

OLIVEIRA, F. S.; **Agronomic biofortification of green corn with iron and zinc**. 2019. 49p. Dissertation (Master in Tropical Horticulture) - Federal University of Campina Grande, Pombal, PB.

OLIVEIRA, F. C. De. *et al*. **Different doses and times of application of zinc in soybean**. Journal of Neotropical Agriculture, pp. 28–35. 2017.

PEDRAZA, D. F., & SALES, M. C. **Zinc deficiency: diagnosis, Brazil estimates and prevention**. Nurture. See 40. ed.3, p.397-408.2015

PHATTARAKUL, N. *et al*. **Biofortification of rice grain with zinc through zinc fertilization in different countries**. Plant and Soil, v. 361, ed. 1-2, pp. 131–141. 2012.

QUEIROGA, V.P.*et al.***Manual harvesting and different forms of use of sesame grains**. RevistaAgro@mbiente Online, v. 4, n. 2, p.110-117, Jul-Dec, 2010

RAM, H., *et al*. **Biofortification of wheat, rice and common bean by applying foliar zinc fertilizer along with pesticides in seven countries**. Plant and soil, v.403, ed. 1-2, p.389-401.2016.

RENGEL, Z.Availability of Mn, Zn and Fe in the rhizosphere. *Journal of Soil Science and Plant Nutrition*, v. 15, n. 2, p. 397–409, 2015. DOI: 10.4067/S0718-95162015005000036.

SADEGHZADEH, B. **Review of zinc nutrition and plant breeding**. Journal of Soil Science and Plant Nutrition, v.13. ed. 4. p.905-927, 2013.

SILVA, Fábio Cesar *et al*. **Manual of chemical analysis of soils, plants and fertilizers**. Brasilia, DF: Embrapa Technological Information; Rio de Janeiro: Embrapa Solos, 2009.

SILVA, G. C. C; **Soy Biofortification with Zinc** – Dissertation (Master in Soil and Plant Nutrition), Federal University of Viçosa, Viçosa, MG, 2017. 22p.

SOCCOL, C. P. *et al*.**Biofortified foods in Brazil and their importance in combating hidden hunger**. IFSC: Campus Xanxerê. 2021.

SOUZA, G. A., *et al*. **Evaluation of germplasm effect on Fe, Zn and Se content in wheat seedlings**. Plant science, ed.210, p.206-213.2013b

TAIZ, Lincoln *et al*. **Physiology and plant development**. 6 ed. Porto Alegre: ArtmedEditora, 2017. 858p.

TENYANG, N. *et al*. **Effects of boiling and roasting on proximate composition, lipid oxidation, fatty acid profile and mineral content of two sesame varieties commercialized and consumed in Far-North Region of Cameroon**. Food Chemistry, v. 221: p.1308-1316, 2017.

WHITE, P. J.; BROADLEY, M. R. **Physiological limits to zinc biofortification of edible crops**. Frontiers in Plant Science, v.2, pp.1-11.2011.

ZAMAN, Q. U. *et al*. Zinc biofortification in rice: leveraging agriculture to moderate hidden hunger in developing countries. Archives of Agronomy and Soil Science, v.64. ed. 2, p.147-161.2017.

CHAPTER 2

ERGONOMICS IN FOCUS: TECHNOLOGY PROSPECTION OF PLANTAR SUPPORT DEVICES UNDER REGULATORY STANDARD NO. 17

Paulino Sousa Vanderley
Master's Degree in Intellectual Property and Technology Transfer for Innovation
Universidade Federal do Sul e Sudeste do Pará (UNIFESSPA)
E-mail: paulinomaria@unifesspa.edu.br

Elias Fagury Neto
Doctor of Materials Science and Engineering
Universidade Federal do Sul e Sudeste do Pará (UNIFESSPA)
E-mail: fagury@unifesspa.edu.br

Renata Lilian Ribeiro Portugal Fagury
Doctor of Chemistry
Universidade Federal do Sul e Sudeste do Pará (UNIFESSPA)
E-mail: renatafagury@unifesspa.edu.br

Fernanda Carla Lima Ferreira
Doctor of Physics
Universidade Federal do Sul e Sudeste do Pará (UNIFESSPA)
E-mail: fernandaferreira@unifesspa.edu.br

Márcio Paulo de Araújo Mafra
Doctor of Mechanical Sciences
Universidade Federal do Sul e Sudeste do Pará (UNIFESSPA)
E-mail: mafra@unifesspa.edu.br

José Elisandro de Andrade
Doctorate in Condensed Matter Physics
Universidade Federal do Sul e Sudeste do Pará (UNIFESSPA)
E-mail: elisandro@unifesspa.edu.br

Denilson da Silva Costa
Doctorate in Metallurgical and Mining Engineering
Universidade Federal do Sul e Sudeste do Pará (UNIFESSPA)
E-mail: denilson@unifesspa.edu.br

Paulo Augusto Pinheiro Bentes
Specialist in Computer Network Structure and Management
Centro Universitário Internacional (UNINTER)
E-mail: augustobentes59@yahoo.com

Suzana Oliveira da Silva Bentes
Master's Degree in Intellectual Property and Technology Transfer for Innovation
Universidade Federal do Sul e Sudeste do Pará (UNIFESSPA)
E-mail: suzanasilva@unifesspa.edu.br

Jeovane Gonçalves Ferreira
Specialist in Executive MBA in Strategic Management of Technological Innovation and Industrial Property
UniBF Centro Universitário
E-mail: jeovane50@unifesspa.edu.br

Adriana Vasconcelos da Costa
Graduate in Law
Universidade Federal do Sul e Sudeste do Pará (UNIFESSPA)
E-mail: adrianavasconcelos@unifesspa.edu.br

Ofélia Regina Batista Neves
Specialist in Public Management
Faculdade Educacional da Lapa (FAEL)
E-mail: ofelia.neves@unifesspa.edu.br

ABSTRACT: Ergonomics in the professional environment is an essential requirement to ensure that workers perform their activities with health, comfort, and safety, positively impacting productivity. Foot support equipment constitutes an essential ergonomic resource for workstations in which individuals remain seated for prolonged periods. The objective of this study was to conduct a technological prospection of plantar support devices in order to characterize the state of the art of the technologies implemented in these accessories, evaluating their advantages and disadvantages according to the requirements and guidelines of Regulatory Standard No. 17 (NR-17). Patent databases were consulted, including Questel Orbit, Espacenet, and the Brazilian National Institute of Industrial Property (INPI), using search filters to refine the results. After selecting and analyzing the retrieved documents, graphs were generated and active patent inventions were assessed. The results show that in 2021 there was a significant increase in the number of patent applications for foot support devices, driven by the creation of home-based workstations encouraged by preventive lockdown measures. Furthermore, Brazil demonstrates, within the field of Industrial Property, an increasing concern with ergonomic issues as reflected in normative documents. Finally, only two of the thirty-nine devices analyzed comply with the requirements of NR-17, revealing a niche in the field of Industrial Property, the lack of public policies to encourage the protection of intangible assets, and prompting further research into the development of ergonomic models with market potential and compliance with current national regulations.

KEYWORDS: ergonomics, plantar support device, NR-17, technology prospection, industrial property.

RESUMO: A Ergonomia no ambiente profissional é requisito indispensável para que os trabalhadores exerçam suas atividades com saúde, conforto e segurança, impactando positivamente na produtividade. Os equipamentos de apoio para os pés constituem um recurso ergonômico essencial para postos de trabalho em que o indivíduo permanece sentado por períodos prolongados. O objetivo deste estudo foi realizar prospecção tecnológica de equipamentos de apoio plantar, no intuito de caracterizar o estado da arte das tecnologias implementadas nesses acessórios, avaliando suas vantagens e desvantagens conforme requisitos e diretrizes da Norma Regulamentadora nº 17 (NR-17). Foram utilizadas as bases de dados de patentes: Questel Orbit, Espacenet e INPI, empregando-se filtros de busca para refinamento dos resultados. Após a seleção e análise dos documentos obtidos, foram gerados gráficos e avaliadas as invenções de patentes ativas. Os resultados mostram que, no ano de 2021, foi elevado o número de depósitos de patente de suporte para os pés, devido à criação de postos de trabalho no ambiente doméstico, incentivada pelas ações preventivas de lockdown. Além disso, o Brasil demonstra acompanhar, no campo da Propriedade Industrial, a preocupação com a questão ergonômica veiculada por meio dos documentos normativos. Por fim, somente dois dos 39 equipamentos descritos atendem aos requisitos da NR-17, revelando um nicho no campo da Propriedade Industrial, a falta de políticas públicas de incentivo à proteção de ativos intangíveis e suscitando novas pesquisas para o desenvolvimento de modelos ergonômicos com potencial mercadológico e adequação às normas nacionais vigentes.

PALAVRAS-CHAVE: ergonomia, dispositivo de apoio plantar, NR-17, prospecção tecnológica, propriedade industrial.

1. INTRODUCTION

Ergonomics seeks to reduce the harmful effects of the production system on workers: fatigue, stress, errors, and accidents, providing them with safety, satisfaction, and health during their relationship with this system (Iida, 2005). Its main objectives are the comfort and satisfaction of individuals and ensuring that work practices and the use of equipment/products do not cause damage to health (Corrêa; Boletti, 2015).

In Brazil, Regulatory Standard No. 17 – Ergonomics (NR-17), dated October 7, 2021, is the regulatory document that establishes the guidelines and requirements for adapting working conditions to the psychophysiological characteristics of workers, in order to promote comfort, safety, health, and efficient performance at work (Brazil, 2021). This standard highlights the need for footrests in workplaces where individuals remain seated for long periods.

Such equipment is an ergonomic resource that helps maintain proper posture (Grandjean, 1998); improves blood flow to the lower limbs by allowing the knees to be symmetrical with the hips (Lida, 2005); has the potential to reduce pressure on the spine during computer tasks, as well as being a tool for adapting to the anthropometric differences of workers in office jobs (Wang *et al.*, 2022).

The objective of this study was to conduct a technological survey of foot support equipment through patent databases in order to characterize the state of the art of the technologies implemented in these ergonomic accessories and to evaluate their advantages and disadvantages from the perspective of NR-17, thus contributing to the areas of Ergonomics, Health, and Occupational Safety.

2. THEORETICAL REFERENCE

2.1 REGULATIONS APPLICABLE TO WORKSTATION FURNITURE

Ergonomics investigates the interaction between humans and their techniques and workplaces, aiming to improve their well-being and safety (Vieira *et al*., 2014).

The Brazilian Federal Constitution guarantees workers the right to "reduction of risks inherent to work, through health [...] and safety standards"

(Brazil, 1988, chap. II, art. 7, inc. XXII). This standardization is carried out through the Regulatory Standards of the Ministry of Labor and Employment (MTE), which constitute obligations, rights, and duties that workers and employers must comply with in order to ensure health and safety in the professional environment. These are complementary provisions to Law No. 6,514, of December 22, 1977, which deals with occupational safety and medicine (Brazil, 2020).

Specifically, NR-17, when referring to workplace furniture, stipulates that furniture must allow for adjustments that adapt it to the anthropometric characteristics of workers, and footrests may be used whenever the worker is unable to keep their feet completely flat on the floor. For checkout operators, the availability of this ergonomic accessory is imperative, regardless of the chair; and for work in call centers/telemarketing, it must be provided in cases where the operator's feet do not reach the floor, even after adjusting the seat, and must be adaptable to the length of the user's legs, have adjustable inclination, and a surface coated with non-slip material (Brazil, 2021).

The requirement regarding the inclination of the footrest is reiterated in the Application Manual for Regulatory Standard No. 17 (Brazil, 2002).

In synergy with health and safety aspects, ergonomics is also concerned with user comfort. A study conducted by Wang *et al.* (2022), for example, with computer-using workers, concluded that the use of a footrest promoted the use of the chair backrest, with a consequent change in spine flexion, suggesting that this equipment should be recognized as a resource for treating back discomfort.

In turn, Fujimaki and Mitsuya (2002) showed that a reclined sitting posture combined with the use of a footrest proved effective for computer users, as it reduced seat pressure, making it more widely dispersed; decreased foot volume (swelling); and reduced fatigue and discomfort in the lower body.

Pereira and Santos (2021), when reporting the results of a survey with participants who evaluated, among other items, the comfort and ergonomic aspects of four models of footrests, also highlight that height adjustment, non-slip texture, and adjustable angle were determining characteristics for the positive evaluations of certain models.

2.2 TECHNOLOGY SCOUTING

Technology foresight involves a structured method for analyzing and identifying trends related to a specific technology (Teixeira, 2013). It allows the identification of characteristics of competing technologies and niches to be filled, enabling a specific technology or its variants to gain a competitive advantage (Quintella *et al*., 2011).

Prospective studies are of paramount importance for decision-making processes associated with innovation (Paranhos; Ribeiro, 2018), presenting information ranging from the state-of-the-art technologies in various fields, developed in laboratories, to their implementation in industries/companies and their products (Longa, 2018). Examining patent documents in a specific technological sector allows companies and R&D centers to identify the direction in which to invest and research, while avoiding reinventions (Jannuzzi; Amorim; Souza, 2007). Such documents are recognized as the main source of technological information due to their comprehensiveness, standardization, and ease of access and retrieval through electronic databases. It is estimated that approximately 70% of global technology is disclosed exclusively through this medium (Quintella *et al*., 2018).

The patent system is highly suitable for technological prospecting studies due to its constantly updated databases and its clear and objective systematization (Paranhos; Ribeiro, 2018). The disclosure of knowledge in patent documents is based on the premise that new technologies serve as the foundation for new inventions, thus promoting a virtuous cycle of technological development and innovation. In this context, patents play a role in disseminating information (Baltazar *et al.*, 2017).

Technological prospecting has guided the efforts employed in the development of technologies by both public and private institutions in different countries for several decades (Mayerhoff, 2008), guiding research, development, and innovation (Amparo; Ribeiro; Guarieiro, 2012).

3. METHODOLOGY

The prospective study was conducted by mapping patents on foot support equipment, located in the *Questel Orbit, Espacenet,* and National Institute of Industrial Property (INPI) databases. In the first two databases, the search considered patent documents filed over a period of twenty years (2004 to 2024); while in the INPI database, in order to provide an overview of patent filings in Brazil, the search did not establish a time limit.

Due to the specific characteristics of each database, in terms of advanced search field options and language, and the particularities of patent indexing by technological domain at the INPI, we describe below the search filter used in each database: a) *Questel Orbit*: *"foot rest* OR *footrest* OR *foot support* device", CIP code "A47C 16/02", "priority date" from June 17, 2004 (period of 20 years prior to the search date), status "active"; *Espacenet*: *"foot rest* OR footrest"; CIP code "A47C 16/02", "publication date" from June 26, 2004 (20-year period prior to the search date); INPI: "(support OR stand) AND feet", CIP code "A47C 16/00 OR A47C 16/02 OR A47C 07/50", search supplemented by basic search using the term "foot support", due to the inconsistency of this database in returning documents covered by the advanced search filter.

The selection criterion used for specific analysis of the documents was one that identified, through the title, images, and descriptive report, a footrest that could be used in the workplace.

In the *Questel Orbit* database, the search returned 195 patent families, of which 31 documents were selected for specific analysis. The *Espacenet* database returned 87 results, of which 4 were selected for analysis and 8 were discarded because they were identical to documents already selected in the Questel Orbit database. From the INPI database, the 19 documents returned in the advanced search were analyzed in general, plus 10 documents selected from the basic search (which returned 81 results); and specifically, the four active patent documents were analyzed.

4. RESULTS AND DISCUSSIONS

4.1 ANALYSIS OF PATENT DATA FROM THE *QUESTEL ORBIT* DATABASE

First, we observe the evolution of the number of patent filings for footrests between 2004 and 2024. The choice of this time frame is justified by its correspondence with the term of a patent for invention.

After a period with insignificant numbers from 2004 to 2012, an increase in the number of filings was observed from 2013 onwards, followed by a progressive evolution. In 2020, there was a slight reduction, followed by the highest number of applications in 2021. In 2022 and 2023, there was a slight decline.

It should be noted that in March 2020, the World Health Organization classified the spread of SARS-CoV-2 (*Severe acute respiratory syndrome coronavirus 2*) as a pandemic, causing many social and economic changes due to preventive *lockdown* measures, which may be associated with the higher number of filings in 2021, as it followed the trend of setting up work and/or study stations in the home environment, increasing the need for ergonomic accessories.

Figure 1 illustrates the evolution of patent filings over time.

Figure 1. Patent families by year of filing – 20 years.

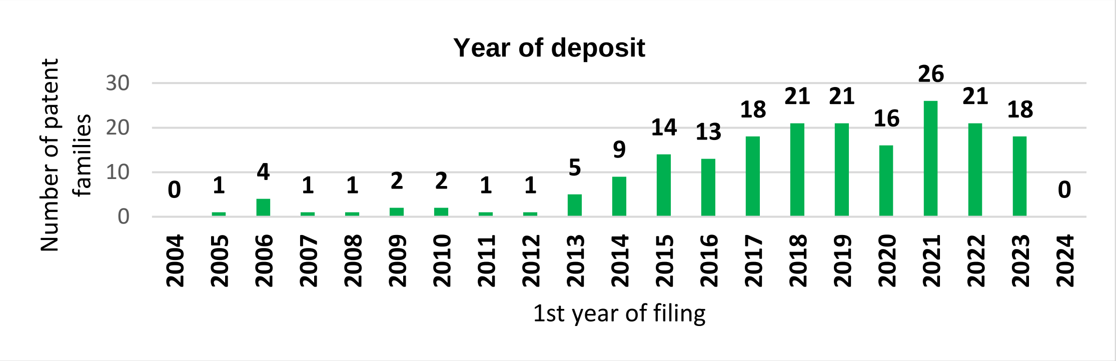

Source: Prepared by the authors based on data from the *Questel Orbit* database (2024).

Among the countries with the highest number of patent applications published, China ranks first, with a significantly higher number, followed by the United States and the Republic of Korea.

Regarding China's prominent position, as noted by Christodoulou, Lev, and Ma (2018), Chinese government policy has promoted a strategic change: the transformation from a labor-intensive economy to an innovation-oriented incentive system, resulting in China's unparalleled growth in patent applications and grants. The significant number of filings in China, therefore, reflects the importance of investing in public policies that encourage Research, Development, and Innovation (RD&I).

National filings serve as indicators of markets in need of protection. They reveal applicants' patenting strategy, helping to identify target markets. Some filers protect the geographic regions where their competitors' production units are located (Questel, 2024).

Figure 2 shows the number of documents published in the various national offices, considering the ten countries with the highest numbers.

Figure 2. Patent families by country of publication – Top 10.

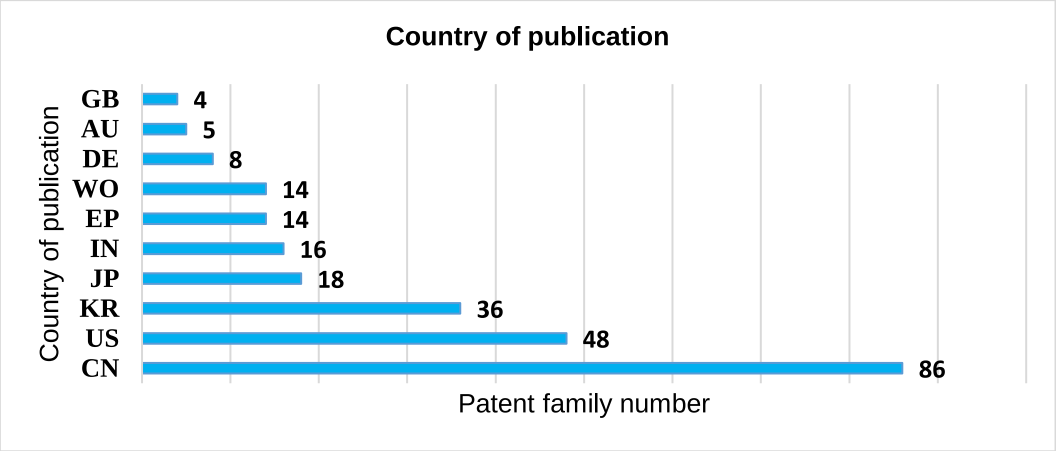

Source: Prepared by the authors based on data from the *Questel Orbit* database (2024).

Another variable observed is the patent portfolio of the applicants, an indicator of their level of inventiveness, as well as potential partnerships.

The three companies with the highest number of patents in their portfolios in the subject area studied are UE Furniture, with 20.83%, Shanghai Rotai Body Building Equipment, with 12.5%, and Squatty Potty, also with 12.5%. The first is one of China's largest seat manufacturers, focusing on research, development, production, and sales of healthy seats. It cooperates with Zhejiang and Hunan Universities through research on ergonomics and technology integration in seats (China International Furniture Fair - CIFF, 2024). The second-ranked company, also Chinese, is a sports equipment manufacturer. The third is a US company specializing in the manufacture of footrests for use in toilets, with the aim of improving user posture.

Figure 3 shows the companies with the highest number of patents in their portfolios in the subject area studied.

Figure 3. Patent families by owner – top 10.

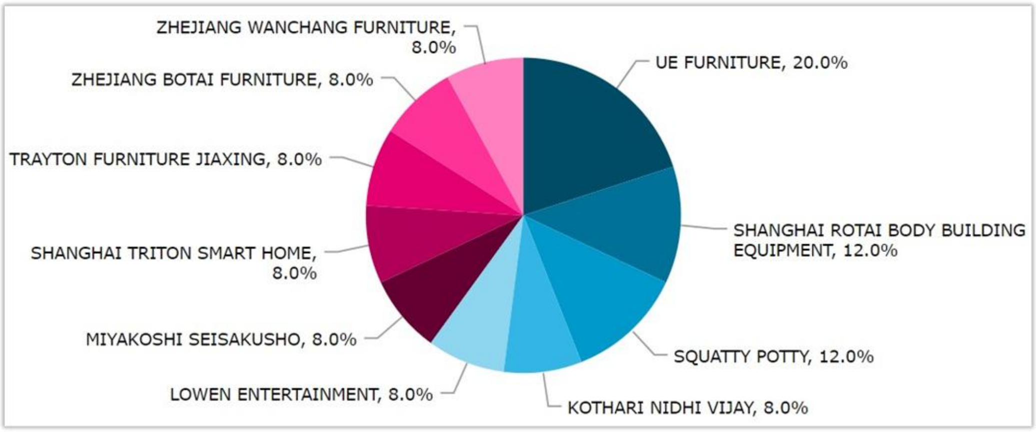

Source: *Questel Orbit* (2024).

Having made these considerations about the total number of patent families returned in the search, we then analyzed the patent documents specifically related to the object of investigation of this study: footrests that are independent (from other furniture) and can be used at a workstation.

The advantages and disadvantages of the inventions are described according to the criteria mentioned in NR No. 17: height adjustment, tilt, and non-slip texture; and, occasionally, according to the advantages described in the descriptive report of the patent document itself. Table 1 describes the patents selected from the *Questel Orbit* database.

Table 1. Technologies used in “footrests” – selection from the Questel Orbit database.

Patent	Title	Image	Advantages	Disadvantages
JP 6662607 B2	Footrest	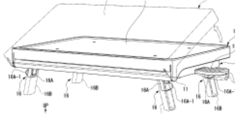	Features tilt adjustment.	No height adjustment, or non-slip texture.
KR 101226741 B1	A device to support the feet	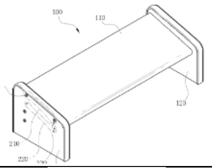	It has (limited) height and tilt adjustment; simple structure for production.	No non-slip texture; reduced inclination.
KR 102668291 B1	2 multifunctional foot supports with 2 steps	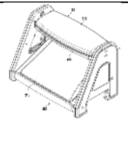	It has support for feet and legs; non-slip texture.	No height adjustment; upper tilt adjustment only.
KR 1020220169281 A	Footrest with adjustable angle	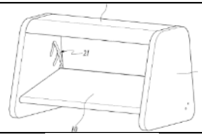	Tilt adjustment; two height options; simple structure for production.	No height adjustment; No non-slip texture.
KR 200478240 Y1	2 multifunctional 2-stage footrests	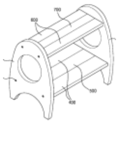	Simple structure for manufacturing; two support options support options.	Does not have tilt adjustment; height adjustment; or non-slip texture.
CN 211748264 U	Footrest for chair	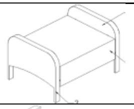	Height adjustable (pre-assembled); Non-slip texture.	Does not allow tilting.
CN 218390401 U	Wooden footrest with lifting mechanism	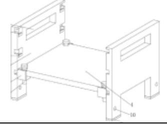	Height adjustable; Foldable structure.	Does not allow tilting; No non-slip texture.
JP 2016002171 A	Footrest	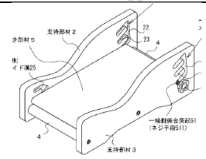	It has height adjustment (limited); Has tilt adjustment.	Tilt adjustment is interdependent with height adjustment; does not have a non-slip texture.
KR 1020170009174 A	Mounted footrest	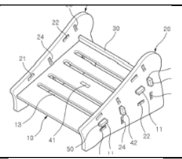	Has tilt adjustment.	No non-slip texture or height adjustment.
KR 101775962 B1	The structure of a footrest	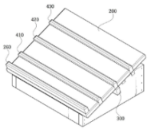	Simple structure for manufacturing.	Fixed height and tilt; no non-slip texture.
KR 20220070796 A	Footrest	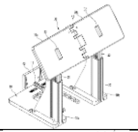	Height adjustable; foldable structure.	No tilt adjustment or non-slip texture.
JP 2021146039 A	Footrest	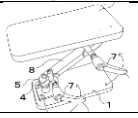	Height and tilt adjustment.	It does not have a non-slip texture.

US 958548 9 B1	Portable foot and leg support set	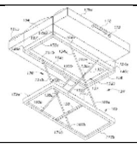	Features a portable structure; height adjustment.	Does not allow tilt; does not have a non-slip texture.
GR 1009271 B	Foldable pedestal	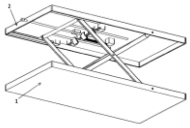	Height adjustable; foldable structure; Lightweight construction for transport.	Does not allow tilting; no non-slip texture.
WO 202235 310 A1	Footrest with height-adjustable scissor structure	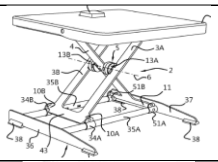	Height adjustable.	No tilt adjustment or non-slip texture.
CN 208447 024 U	Foot placement plate	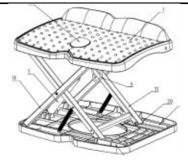	Height adjustable; non-slip texture; Retractable structure; height adjustment is activated with the foot.	Does not allow for tilt adjustment.
CN 215015 445 U	Footrest with massage device	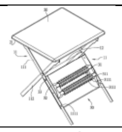	Features a foot massage function.	No tilt or height adjustment, nor non-slip texture.
WO 201911 008 A1	Footrest	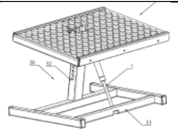	It has height adjustment; Non-slip texture.	No tilt adjustment.
CN 217885 520 U	Footplate	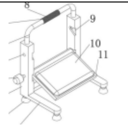	Height and tilt adjustment; non-slip feet; massage feature.	No non-slip texture.
WO202 220342 4A1	Two-stage foot support device	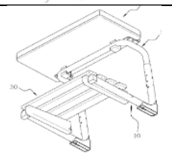	Height adjustable.	Does not have tilt adjustment or non-slip texture.
GR 100938 3 B	Footrest with grounding for the human body	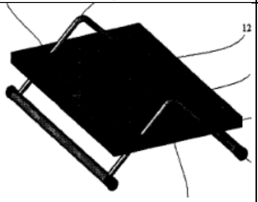	Features tilt adjustment; antifungal, antimicrobial, analgesic, and biomagnetic properties.	No height adjustment or non-slip texture.
CN 217309 650 U	Sports footrest with adjustable height and angle	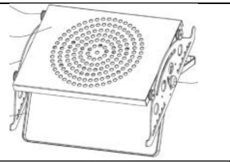	Features height and tilt adjustment.	It has a non-slip texture only in the central part of the platform.
CN 206507 631 U	Pedal plate	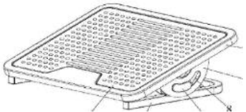	Features non-slip texture; tilt adjustment.	No height adjustment or angle lock.
CN 211961 505 U	Office footrest	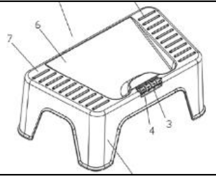	Features a foot massage function.	No tilt or height adjustment; non-slip texture only at the ends.

CN1150 88977A	Multifunctional footrest	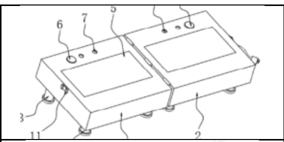	Features distance sensor and heating function.	No tilt or height adjustment, no non-slip texture.
KR 1016514 59 B1	Multifunctional footrest	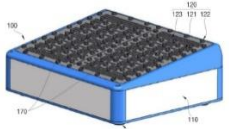	Features non-slip texture, massage function, heating/cooling, and temperature sensor.	It does not have tilt or height adjustment.
KR 102020 011778 5 A	Separate footrest	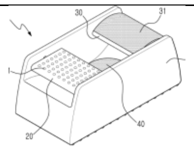	Features non-slip texture; tilt adjustment; acupressure and thermal massage functions.	No height adjustment.
KR 102022 003823 7 A	Footrest for exercises	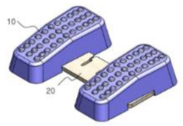	Features non-slip texture; foot and leg movement feature.	No tilt or height adjustment.
KR 101702 644 B1	Footrest	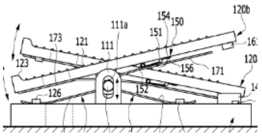	Features tilt adjustment; rotation counting feature; allows leg and foot movement.	No height adjustment.
CN 2147601 74 U	Pedal plate	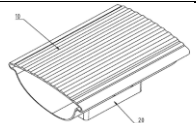	Features tilt adjustment; non-slip texture; allows movement.	No height adjustment.
JP 2016101 193 A	Footrest with rocker for chair	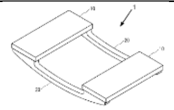	Allows movement of legs and feet.	Does not have non-slip texture; tilt, or height adjustment.

Source: Authors

According to Table 1, there is a variety of models, characteristics, and technological features used in footrest equipment.

Regarding the requirements and guidelines recommended by NR-17 for these accessories, it was found that only one of the inventions (CN 217309650 U) meets the characteristics of height adjustment, inclination, and non-slip texture, although the latter only partially, as this texture is applied exclusively in the central area of the platform. This data reveals a gap in the market for the importation of related devices by Brazilian companies, since, in the set of active patents analyzed, there is no equipment available whose characteristics fully comply with national ergonomic standards for workplace furniture.

4.2 ANALYSIS OF PATENT DATA FROM THE *ESPACENET* DATABASE

Table 2 presents a description of the selected results from the *Espacenet* database.

Table 2. Technologies used in "footrests" – selection from the Espacenet database.

Patent	Title	Image	Advantages	Disadvantages
KR 101653390B1	Footrest	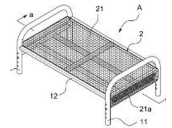	Height adjustable (pre-assembled); non-slip, flexible surface that keeps feet cool.	Does not allow tilting.
KR 200464934Y1	Portable footrest	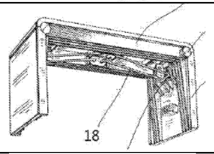	Features width adjustment; height adjustment (pre-assembly).	Does not allow tilting; No non-slip texture.
CN 206699850 U	Foldable foot steps	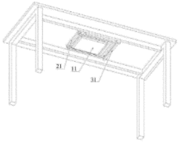	Foldable; simple manufacturing structure.	No height adjustment, no non-slip texture; does not tilt.
KR 102041583B1	Foot bar with heater		Features foot heating and cooling options; non-slip texture; shoe support.	No height or tilt adjustment.

Source: Authors

It should be noted that the documents are all of Asian origin, with three from the Republic of Korea and one from China. The equipment described has in common the characteristic of not allowing the footrest platform to tilt or having angle adjustment, therefore not complying with the provisions of NR-17 regarding workplace furniture.

4.3 ANALYSIS OF PATENT DATA FROM THE INPI DATABASE

The fundamental patent directly related to a footrest that can be used at a workstation was filed with the INPI on May 8, 1989, by Hanka Maldonado Indústria e Comércio Ltda (BR/SP), under identification PI 8902128 A and with the title “Footrest.” The patent application was filed on June 28, 1994, due to lack of proof and payment of the annual fee.

In addition to this, six other patent applications were filed due to non-payment of annual fees(s) (BR 2020170094699 U2, MU 88015300 U2, MU

86006207 U2, MU 86000250 U2, MU 85019453 U2, MU 72011823 U2); two were filed due to failure to prove payment of the patent letter issuance fee (PI 09033335 A2, MU 77009711 U2); three were filed due to failure to request examination within the period provided for in Article 33 of the LPI (MU 84005297 U2, MU 80011055 U2, PI 96055464 A2); four applications were rejected for failure to meet legal requirements (BR 2020120099344 U2, BR 202012 0282254 U2, MU 87023024 U2, PI 97005592 A2); three were shelved due to non- n compliance with the requirements (BR 2020190172385 U2, MU 87023202 U2, MU 77025326 U2).

Of the eight patents granted, three were terminated due to non-payment of annual fees (MU 87017555 Y1, MU 75020815 Y1, MU 75010860 Y1); three were fully valid and were revoked due to the expiration of the term of legal protection (MU 82022038 Y1, MU 81010699 Y1, PI 99052962 B1); and two are currently in force (BR 2020190034187 Y1 and BR 20 2014 0211131 Y1). Two patent applications are also active (BR 2020220174488 U2, BR 10 20190234261 A2), totaling four active patents at present.

Table 3 shows the legal status of selected patent filings from the INPI database.

Table 3. Legal status of patent applications – selection from the INPI database.

Patents granted or awaiting examination		**Archived applications**	
Current status	**Total**	**Reason**	**Total**
Expired due to the expiration of the legal protection period	3	Non-payment of annual fees	7
Extinguished due to non-payment of annual fees	3	Failure to provide proof of payment for the issuance of the charter	2
In force	2	No examination requested within the stipulated period	3
Published requests – awaiting technical review	2	Failure to meet legal requirements	4
		Non-compliance with requirements	3

Source: Authors

It can therefore be observed that, despite the considerable number of patent applications, few have proven to be long-lasting, although there is no evidence in the database itself to explain the reasons for this. However, the information listed here is considered relevant both for understanding the current scenario, through the history of filings, and for verifying what is already available in the public domain and constitutes the state of the art.

All patent applications in Brazil related to footrests are restricted to the Southeast (mainly) and South regions, which may be related to the high percentage of participation of these regions in the national industry, as shown by data from the Brazilian Institute of Geography and Statistics (IBGE) referring to the Annual Industrial Survey for the year 2022 (IBGE, 2024). The state of São Paulo stands out considerably as the federative unit with the highest number of applicants, with 19 applications (corresponding to 66% of the total results). Five applications come from Rio de Janeiro, four from Santa Catarina, and one from Rio Grande do Sul.

Figure 4 illustrates the percentage distribution of patent applications according to the origin of the applicant.

Figure 4. Percentage of applicants by state

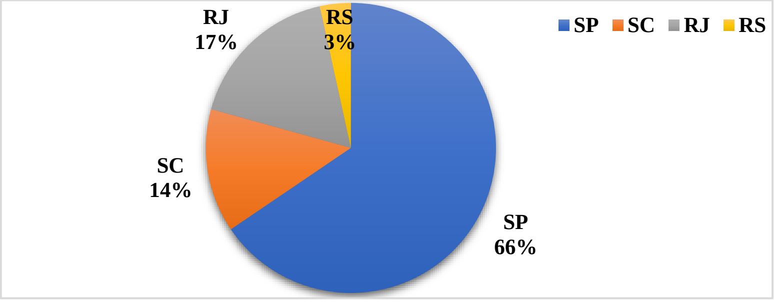

Source: Authors

In relation to the number of filings per year, a certain stability can be observed: in general, there is one filing per year (14 occurrences). There were three years in which there were two filings and another three years in which there were three filings. In terms of frequency, there are periods with one or more filings in consecutive years (11 cases) and periods with an interval of two (4 cases) or three years (5 cases) between filings, with this consistency maintained from 1989 to 2022.

Figure 5 illustrates the number of patent applications for foot support devices per year.

Figure 5. Number of patent applications filed with the INPI per year.

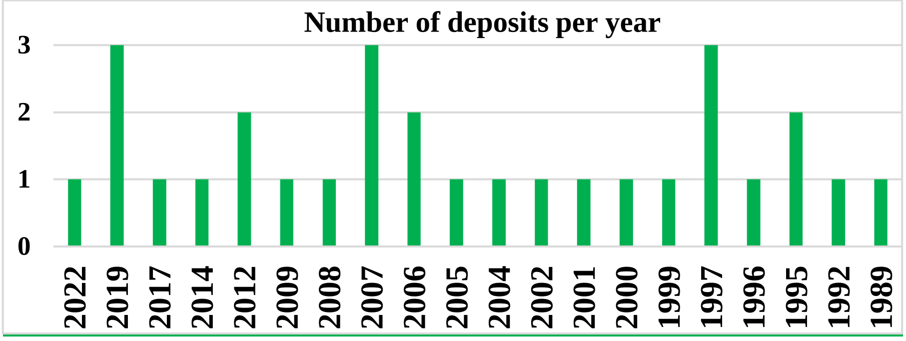

Source: Authors

The period when applications for intellectual property protection for plant support equipment began in Brazil was the late 1980s, corresponding to the period when computers began to become popular, marked by reduced costs and increased processing power. Until the previous decade, computers had been restricted to universities and government levels (Pereira, 2014). This fact may be an indicator that the increase in the number of computer-based jobs, which began with the popularization of computers, also increased the demand for seated postures among workers. This situation can be seen as a market opportunity for companies manufacturing footrests, which, in the field of industrial property, followed the concern with the ergonomic issue of professional furniture, as verified in the regulatory documents of that period.

The first version of NR No. 17 was published on July 6, 1978, and in 1989, the year in which the fundamental patent for a footrest that could be used at a workstation was filed, the Ministry of Labor Ordinance - MTb No. 3,223, dated June 29, 1989, established a working group to review the normative text. The new wording was published through Ministry of Labor and Social Security Ordinance - MTPS No. 3,751, dated November 23, 1990, including regulations related to equipment used in electronic data processing with video terminals, i.e., equipment that should already be part of work environments in the country. Since its first version, however, NR No. 17 already regulated, in item 17.3.1, the obligation to provide footrests for employees (Brazil, 1978), an obligation that became conditional, in the 1990 version (item 17.3.4), on ergonomic analysis of the work (Brazil, 1990).

Next, the content of active patents was analyzed.

Table 4. Technologies used in "footrests" - selection from the INPI database.

Patent	Title	Image	Advantages	Disadvantages
BR 2020220174 48 U2	Footrest layout introduced	FIG. 2 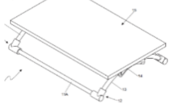	Features tilt adjustment; simple structure for manufacturing.	It does not have height adjustment or non-slip texture.
BR 1020190234 21 A2	Mechanical footrest with active movement	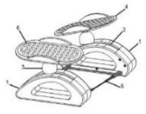	It has tilt adjustment, non-slip texture, and a feature for moving the legs and feet.	No height adjustment or angle locking.
BR 2020190034 17 Y1	Construction layout applied to footrest	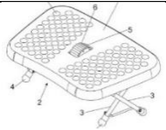	Features height adjustment, tilt adjustment (forward and backward), and non-slip texture.	It does not have angle locking.
BR 20201 4 02111 3 Y1	Ergonomic structure for foot and leg support	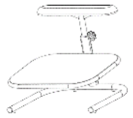	Features tilt and height adjustment; foot and leg support.	It does not have a non-slip texture.

Source: Authors

As shown in Table 4, only one of the patents currently active in Brazil (BR 202019003417 Y1) meets all the requirements of NR-17, which may indicate a niche in the field of Industrial Property, as well as a lack of public policies to encourage the protection of intangible assets.

5. CONCLUSIONS

The characterization of the state of the art of foot support equipment, the central objective of this study, makes a significant contribution to the field of Ergonomics, Health, and Safety at Work, in addition to revealing the importance of patent documentation as a source of technological information.

The prospecting activity allowed us to verify everything from very simple technologies, apparently obvious to a technician in the field, to more elaborate features employed in these devices. The thorough analysis of patent documents was a distinguishing feature of this study, as it reported the advantages and disadvantages of the inventions described, in accordance with the guidelines and requirements of NR-17, in addition to systematizing more general aspects of the universe of patent data through figures and discussions.

The investigation of the INPI database considered all foot support patent filings in the national territory, providing a historical, geographical, and legal overview *of* these documents. This analysis allowed us to conclude that Brazil, with a total of 29 patent applications for foot support equipment over a period of 33 years (1989 to 2022), demonstrates, in the field of Industrial Property, a tendency to follow concerns with ergonomics, as verified through national regulatory documents. This can be seen as a positive aspect both for manufacturing companies, through the benefits resulting from the commercial monopoly of protected inventions, and for workers, who are potentially the target audience for these devices.

The data showed that only two foot support devices (CN 217309650 U and BR 202019003417 Y1), of the total of 39 patent documents described, met the requirements of NR-17, prompting research activities for the development of new ergonomic models with the potential for intellectual property protection and market competition.

It should be noted that the growing trend toward remote work, both in the public and private sectors, increases the demand for these accessories, since this type of work is characterized, above all, by computer workstations, which require adaptation to ergonomic standards, as is the case in the face-to-face work environment.

The technologies of patent documents in the public domain have not been described in this article. It is hoped that this study will provide a basis for new technological prospecting activities focused on ergonomic foot support design projects for people with disabilities, for example, depending on the consumer market to be targeted. Also, the investigation of sustainable materials for the production of this equipment can be a great opportunity to incorporate commercial value and to stimulate Research, Development, and Innovation (RD&I) and sustainable public procurement.

REFERENCES

AL-QURAINI, J. A. M. T. **Portable foot and leg rest assembly**. Depositante: Jeehan A. M. T. Al-Quraini. Procurador: Litman Richard C. US 9585489 B1. Depósito: 31 ago. 2016. Concessão: 07 mar. 2017.

AMPARO, K. K. dos S.; RIBEIRO, M. do C. O.; GUARIEIRO, L. L. N. Estudo de caso utilizando mapeamento de prospecção tecnológica como principal ferramenta de busca científica. **Perspectivas em Ciência da Informação**, *[S. l.]*, v. 17, n. 4, p. 195–209, 2012. Disponível em: https://periodicos.ufmg.br/index.php/pci/article/view/22815. Acesso em: 15 out. 2024.

ANDRADE FILHO, F. S. M de. **Disposição construtiva introduzida em suporte para apoio de pés provido de faces com aplicação publicitária**. Depositante: Floriano Soares Moreira de Andrade Filho. MU 8801530-0 U2. Depósito: 20 jun. 2008.

BALTAZAR, L. F.; VILHA, A. M.; FERREIRA, F. D.; CHINELLATO, A. C.; VIDOTTI, S. E.; RODRIGUES, R. C. PATENTES COMO FONTE DE INFORMAÇÃO TECNOLÓGICA PARA SUBSÍDIO À PESQUISA: UMA ANÁLISE AMOSTRAL DA UNIVERSIDADE FEDERAL DO ABC. **Cadernos de Prospecção**, *[S. l.]*, v. 10, n. 4, p. 681, 2017. DOI: 10.9771/cp.v10i4.23208. Disponível em: https://periodicos.ufba.br/index.php/nit/article/view/23208. Acesso em: 29 jan. 2026.

BRASIL. [Constituição (1988)]. **Constituição da República Federativa do Brasil**. Brasília, DF: Senado Federal, 2016. Disponível em: https://www2.senado.leg.br/bdsf/bitstream/handle/id/518231/CF88_Livro_EC91_2016.pdf. Acesso em: 23 out. 2024.

BRASIL. Ministério do Trabalho e da Previdência Social. Portaria MTPS n.º 3.751, de 23 de novembro de 1990. **Diário Oficial da União**: seção 1, Brasília, DF, p. 22576-22577, 26 nov. 1990. Disponível em: https://www.gov.br/trabalho-e-emprego/pt-br/acesso-a-informacao/participacao-social/conselhos-e-orgaos-colegiados/comissao-tripartite-partitaria-permanente/normas-regulamentadora/normas-regulamentadoras-vigentes/norma-regulamentadora-no-17-nr-17. Acesso em: 15 out. 2024.

BRASIL. Ministério do Trabalho e Emprego. **Normas Regulamentadoras – NR**. Brasília, DF: Ministério do Trabalho e Emprego, 2020. Disponível em: https://www.gov.br/trabalho-e-emprego/pt-br/assuntos/inspecao-do-trabalho/seguranca-e-saude-no-trabalho/ctpp-nrs/normas-regulamentadoras-nrs. Acesso em: 16 set. 2024.

BRASIL. Ministério do Trabalho e Previdência. Portaria MTP n.º 423, de 07 de outubro de 2021. Aprova a nova redação da Norma Regulamentadora n.º 17 – Ergonomia. **Diário Oficial da União**: seção 1, Brasília, DF, nº 192, p. 122, 08 out. 2021. Disponível em: https://www.in.gov.br/en/web/dou/-/portaria/mtp-n-423-de-7-de-outubro-de-2021-351614985. Acesso em: 15 out. 2024.

BRASIL. Ministério do Trabalho. **Manual de Aplicação da Norma Regulamentadora Nº 17**. 2. ed. Brasília: MTE, SIT, 2002. Disponível em: https://www.gov.br/trabalho-e-emprego/pt-br/assuntos/inspecao-do-trabalho/escola/e-biblioteca/manual-de-aplicacao-da-nr-17-ano-2002.pdf. Acesso em: 15 out. 2024.

BRASIL. Ministério do Trabalho. Portaria MTb n.º 3.214, de 08 de junho de 1978. **Diário Oficial da União**: seção 1, Parte 1, Suplemento. Brasília, DF, p. 63, 08 jun. 1978. Disponível em: https://www.ergocompany.com.br/wpcontent/uploads/2021/02/DOU-NR-17-Ergonomia-06.07.1978.pdf. Acesso em: 15 out. 2024.

BRASIL. Ministério do Trabalho. Portaria MTb n.º 3.223, de 29 de junho de 1989. **Diário Oficial da União**: seção 1, Brasília, DF, p. 10.974, 03 jul. 1989. Disponível em: https://www.gov.br/trabalho-e-emprego/pt-br/acesso-a-informacao/participacao-social/conselhos-e-orgaos-colegiados/comissao-tripartite-partitaria-permanente/normas-regulamentadora/normas-regulamentadoras-vigentes/norma-regulamentadora-no-17-nr-17. Acesso em: 15 out. 2024.

BYEON, Y. M. **Foot rest**. Depositante: Dazon. Procurador: Sang Moo You. KR 101653390 B1. Depósito: 19 abr. 2016. Concessão: 09 set. 2016.

CAVIGLIA, N. **Apoio ergonômico para os pés para usuários de computadores**. Depositante: Caviglia & Cia Ltda. Procurador: Escritório Fernando Marchetti S/C Ltda. MU 8001105-5 U2. Depósito: 13 jun. 2000.
CÉLIA, R. **Suporte para os pés e membros inferiores**. Depositante: Regina Célia. BR nº PI 0903333-5 A2. Depósito: 28 set. 2009.

CHIARADIA, D. M. F. **Apoio para os pés**. Depositante: B & S Equipamentos de Segurança Ltda. Procurador: José Henrique de Lima Rodrigues. BR 2020120099344 U2. Depósito: 27 abr. 2012.

CHRISTODOULOU, D.; LEV, B.; MA, L. The productivity of Chinese patents: The role of business area and ownership type. **International Journal of Production Economics**, v. 199, p. 107-124, 2018. DOI: 10.1016/j.ijpe.2017.12.024. Disponível em: https://doi.org/10.1016/j.ijpe.2017.12.024. Acesso em: 15 out. 2024.

CIFF - China International Furniture Fair. **UE Furniture CO., LTD**. Guangzhou: CIFF, 2024. Disponível em: https://www.ciff-gz.com/en/exhibitor/34. Acesso em: 15 out. 2024.

CORRÊA, V. M.; BOLETTI, R.R. **Ergonomia**: Fundamentos e Aplicações. Porto Alegre: Bookman, 2015.

DA SILVA, M. A. N. R. **Apoio para os pés**. Depositante: Maria Aparecida Novak Rocha da Silva. BR nº PI 9700559-2 A2. Depósito: 17 abr. 1997.

DA SILVA, M. F. **Apoio para tratar e enxugar as pernas e os pés.** Depositante: Marco Francisco da Silva. BR nº PI 9605546-4 A2. Depósito: 12 nov. 1996.

ESPACENET. **Patent Search**. [S. l.]: European Patent Office, 2024. Disponível em: https://worldwide.espacenet.com/. Acesso em: 15 out. 2024. Base de dados.

EUNG, K. J. **Portable foot rest**. Depositante: Kim Jung Eung. Procurador: Keon Soo Paek. KR 200464934 Y1. Depósito: 28 jan. 2010. Concessão: 28 jan. 2013.

FEIYAN, M.; YISHU, YU. **Pedal plate,** Depositante: Meng Feiyan. Procurador: Du Qigang; Shenzhen Shikefeng Patent Agency Office. CN 214760174 U. Depósito: 28 abr. 2021.

FERRO, M. O. **Disposição introduzida em elemento de apoio para os pés**. Depositante: Maxoel Oliveira Ferro. Procurador: Rose Anny Rodrigues Ferreira de Souza. MU 7201182-3 U2. Depósito: 03 ago. 1992.

FUJII, M. **Footrest**. Depositante: Masahiro Fuji. JP 2021146039 A. Depósito: 23 mar. 2020.

FUJIMAKI, G; MITSUYA, R. Study of the seated posture for VDT work. **Displays**, Shanghai, vol. 23, p. 17-24, 2002. DOI: 10.1016/S0141-9382(02)00005-7. Disponível em: https://doi.org/10.1016/S0141-9382(02)00005-7. Acesso em 15 out. 2024.

FURONG, Z. **Footstool with foot massage device.** Depositante: Zhuang Furong. Pocurador: Ceng Yaoxian; Wei Yuan Patent Law LLC**.** CN 215015445 U. Depósito: 02 mar. 2021.

GRANDJEAN, E. **Manual de Ergonomia**: adaptando o trabalho ao homem. Tradução: João Pedro Stein. 4. ed. Porto Alegre: Artes Médicas, 1998.

HARTE, S. **Estrutura ergonômica para apoio dos pés e pernas**. Depositante: Sebastian Harte. Procurador: Célia Novaes & Associados Sociedade Simples Ltda. BR 2020140211131 Y1. Depósito: 18 ago. 2014. Concessão: 16 nov. 2021.

HARTE, S. **Suporte regulável para apoio de pés e pernas**. Depositante: Sebastian Harte. Procurador: Célia Novaes & Associados Sociedade Simples Ltda. MU 8701755-5 Y1. Depósito: 29 nov. 2007. Concessão: 24 nov. 2015.

HONG, S. K. **Separate type foot support.** Depositante: Sam Ha. Procurador: Ui Seop Yoon; Sujin Kim. KR 1020200117785 A. Depósito 05 abr. 2019.

HYE, k. b.; HUN, R. J. **Angle-adjustable footrest.** Depositante: Kyungil University, Mobilefurs. Procurador: Kwang And Jang Patent Law Firm; Cheon Jee International Patent & Law Firm. KR 1020220169281 A. Depósito:18 jun. 2021.

IBGE – Instituto Brasileiro de Geografia e Estatística. Pesquisa Industrial Anual: Em 2022, minério de ferro perde posição e petróleo bruto se torna o principal produto industrial do país. *[S. l.]:* ***Agência IBGE notícias****, 27 jun. 2024. Disponível em:* https://agenciadenoticias.ibge.gov.br/agencia-noticias/2012-agencia-de-noticias/noticias/40486-em-2022-minerio-de-ferro-perde-posicao-e-petroleo-bruto-se-torna-o-principal-produto-industrial-do-pais. Acesso em: 15 out. 2024.

IDE, S. M. **Disposição construtiva aplicada em suporte apoio para os pés**. Depositante: Air Micro Ltda. Procurador: ABM Assessoria Brasileira de Marcas Ltda. BR 2020190034187 Y1. Depósito: 20 fev. 2019. Concessão: 26 set. 2023.

IIDA, I. **Ergonomia:** projeto e produção. 2. ed. São Paulo: Edgard Blücher, 2005.

IMAI, T. **Apoio para pés com balanço e altura ajustável com o próprio pé**. Depositante: Takeshi Imai. Procurador: ABM Assessoria Brasileira de Marcas Ltda. BR nº PI 9905296-2 B1. Depósito: 08 set. 1999. Concessão: 21 out. 2008.

INPI – Instituto Nacional da Propriedade Industrial. **Base de dados de patentes**. Rio de Janeiro: INPI, 2024. Disponível em: https://www.gov.br/inpi/pt-br/servicos/patentes. Acesso em: 15 out. 2024. Base de dados.

JANNUZZI. A. H. L.; AMORIM, R. C. R.; SOUZA, C. N. Implicações da categorização e indexação na recuperação da informação tecnológica contida em documentos de patentes. **Ciência da Informação**, Brasília, DF, v. 36, n. 2, p. 27–34, maio/ago. 2007. DOI: 10.1590/S0100-19652007000200003. Disponível em: https://revista.ibict.br/ciinf/article/view/1173. Acesso em: 15 out. 2024.

KIM, J. **Footrest**. Depositante: Jae-Woo Kim. Procurador: Yon-Jae Yeo; Kyo Jun Seo. KR20220070796A. Depósito: 23 nov. 2020.

KIM, KWANG KI. **2 multo-function 2 stage feet support**. Depositante: Kwang Ki Kim. KR 200478240 Y1. Depósito: 20 ago. 2014.

KIM, P. J. **An apparatus for supporting feet.** Depositante: Pyoung Jin Kim. Procurador: Ki Hyun Yoo. KR 101226741 B1. Depósito: 24 nov. 2010. Concessão: 25 jan. 2013.

KIM, Y. J. **2 Multi-function 2 stage feet support**. Depositante: Yeon Jae Kim. Procurador: Aju Kim Chang & Lee. KR 102668291 B1. Depósito: fev. 2023. Concessão: 22 mai. 2024.

KONGHE, Z. **Office footrest**. Depositante: KONGHE ZHU. Procurador: Xu Lingai; Taizhou Zhongwei Patent Agency (General Partnership). CN 211961505 U. Depósito: 16 dez. 2019.

KOUTSAVLIS, T. K. **Squatty potty.** Depositante: Theodoros Konstantinou Koutsavlis. GR 1009271 B. Depósito: 18 mai. 2018. Concessão: 31 mai. 2018.

LAZZAROTTO, F. **Suporte de apoio para os pés.** Depositante: Flávio Lazzarotto. Procurador: Regina Magro Poletto. MU 8600025-0 U2. Depósito: 10 jan. 2006.

LEE, Y. P.; KIM, DO-Y. **Exercise Footrest**. Depositante: Yong Pyo Lee; Do-Young Kim. KR 1020220038237 A. Depósito: 19 set. 2020.

LIM, S. H.; K. Y.; SHIN, M.; YANG, H. H.; KIM, S. Y. **Multifunctional feet supporter**. Depositante: Koreatech. Procurador: Kim, Min-Tae. KR 101651459 B1. Depósito: 30 dez. 2014. Concessão: 26 ago. 2016.

LINGHUA, X.; XIAOPING, F. **Footstool for chair**. Depositante: Linhai Chenli Handicraft. Procurador: Zhu Shuanghai; Beijing Industry & Information Intellectual Property Co. Ltd. CN 211748264 U. Depósito: 19 jan. 2020.

LONGA, L. C. D. Prospecção Tecnológica: conceito e aplicação. In: ANDRADE, H. S.; SILVA, M. B.; CHAGAS JUNIOR, M. F.; OLIVEIRA, W. S. (org.). **A Ciência e a Tecnologia do Futuro**: aplicação dos métodos de previsão e prospecção no âmbito científico-tecnológico e social. vol 1. Jundiaí: Edições Brasil, 2018. p. 17-26. Disponível em: http://plutao.sid.inpe.br/col/sid.inpe.br/plutao/2018/12.14.21.05.15/doc/ciencia%20e%20tecnologia%20do%20futuro.pdf. Acesso em: 15 out. 2024.

MALDONADO. G. L. **Apoio para os pés**. Depositante: Hanka Maldonado Indústria e Comércio Ltda. Procurador: João Britavaldo Marcondes. BR nº PI 8902128 A. Depósito: 08 mai. 1989.

MAMARELIS, N. K. **Human body-earthing foot rest**. Depositante: Nikolaos Konstantinou Mamarelis. GR 1009383 B. Depósito: 12 abr. 2017.

MASAHIKO, N., YASUHIRO, Y. **Foot placement base and foot placement base use method**. Depositante: Nishiura. Procurador: Takaaki Funabiki. JP2016002171A. Depósito: 16 jun. 2014.

MAYERHOFF, Z. D. V. L. Uma Análise sobre os Estudos de Prospecção Tecnológica. **Cadernos de Prospecção**, *[S. l.]*, v. 1, n. 1, p. 7–9, 2008. DOI: 10.9771/cp.v1i1.3538. Disponível em: https://periodicos.ufba.br/index.php/nit/article/view/3538. Acesso em: 15 out. 2024.

MIN, S. **Pedal plate**. Depositante: Qingdao Xinao Xuzhao Packaging Products. CN 217885520 U. Depósito: 03 ago. 2022.

MOREIRA, J. P. **Apoio para os pés com regulagem de altura**. Depositante: B & S Equipamentos de Segurança Ltda.MU 8702302-4 U2. Depósito: 19 nov. 2007.

NAOKI, N.; MASAHITO, K. **Footrest**. Depositante: Okamura. Procurador: Matsunuma Yasushi et al.; Suzuki Yoshiyuki; Shiga Masatake. JP 6662607 B2. Depósito: 05 nov. 2015. Concessão: 11 mar. 2020.

OH, S. J. **Assembly type foot rest.** Depositante: Seung Jae Oh. Procurador: Dae Sun Lee. KR 1020170009174 A. Depósito: 16 jul. 2015.

PARANHOS, R. C. S.; RIBEIRO, N. M. Importância da Prospecção Tecnológica em Base de Patentes e seus Objetivos da Busca. **Cadernos de Prospecção**, *[S. l.]*, v. 11, n. 5, p. 1274, 2018. DOI: 10.9771/cp.v11i5.28190. Disponível em: https://periodicos.ufba.br/index.php/nit/article/view/28190. Acesso em: 15 out. 2024.

PARK, S. S. **Two-stage foot support device**. Depositante: Sang Soo Park. Procurador: (WO2022/203424) Shinsegi Patent Law Firm [KR]. WO 2022203424 A1. Depósito: 24 mar. 2022.

PEREIRA, J. F.; SANTOS, J. E. G. **Apoio de pés mecânico com movimentação ativa**. Depositante: Universidade Estadual Paulista Julio De Mesquita Filho. Procurador: Renan Padron Almeida. BR 1020190234261 A2. Depósito: 07 nov. 2019.

PEREIRA, J. F.; SANTOS, J. E. G. PROTOTIPAGEM RÁPIDA: UM APOIO DE PÉS ERGONÔMICO PARA AUXILIAR O RETORNO VENOSO. **Revista Conhecimento Online**, *[S. l.]*, v. 2, p. 114–129, 2021. DOI: 10.25112/rco.v2i0.2543. Disponível em: https://periodicos.feevale.br/seer/index.php/revistaconhecimentoonline/article/view/2543. Acesso em: 15 out. 2024.

PEREIRA, L. D. A. Os primórdios da informatização no Brasil: o “período paulista" visto pela ótica da imprensa. **História**. *[S. l.]*, v. 33, n. 2, p. 408-422, 2014. DOI: 10.1590/1980-436920140002000019. Disponível em: https://doi.org/10.1590/1980-436920140002000019. Acesso em: 15 out. 2024.

PFEIFFER, L. G. **Disposição em apoio para pés**. Depositante: Luís Grassmann Pfeiffer. Procurador: SPI Marcas e Patentes S/C Ltda. MU 7700971-1 U2. Depósito: 24 abr. 1997.

PONTICELLI, V. **Apoio para pés multiposicionável**. Depositante: Associação de Pais e Amigos dos Excepcionais de Blumenau (APAE). Procurador: King's Marcas E Patentes Ltda Me. MU 8400529-7 U2. Depósito: 12 abr. 2004.

PRADO, J. M. A. A. **Suporte dos pés com regulagem de altura**. Depositante: APF - Informática Ltda. Procurador: City Patentes e Marcas ltda. MU 7501086-0 Y1. Depósito: 05 jun. 1995. Concessão: 14 dez. 2000.

QIONGQIONG, Z. **Solid wood footrest with lifting structure**. Depositante: Zhao Qiongqiong. Procurador: Sun Li; Haodong Law Firm. CN 218390401 U. Depósito: 24 out. 2022.

QUESTEL. **Orbit Intelligence**. [S. l.]: Questel, 2024. Disponível em: https://www.orbit.com. Acesso em: 15 out. 2024. Base de dados.

QUINTELLA, C. M.; MEIRA, M.; GUIMARÃES, A. K.; TANAJURA, A. S.; SILVA, H. R. G. Prospecção Tecnológica como uma ferramenta Aplicada em Ciência e Tecnologia para se Chegar à Inovação. **Revista Virtual de Química**, [s.l.], v. 3, n. 5, p. 406-415, dez., 2011. Disponível em: https://rvq-sub.sbq.org.br/index.php/rvq/article/download/193/203/1821. Acesso em 15 out. 2024.

QUINTELLA, C. M.; ALMEIDA, B. A.; SANTOS, W. P.; RODRIGUES, L. M. T. S. Busca de Anterioridade. In: RIBEIRO, N. M. (org.). **Prospecção Tecnológica**. Vol. 1. Salvador: IFBA, 2018. p. 109-140. Disponível em: https://www.profnit.org.br/livros-profnit/. Acesso em 15 out. 2024.

RAVARA, L. A. C. **Disposição construtiva aplicada em suporte para apoio de pés**. Depositante: Espectro Industria e Comercio de Produtos Ergonomicos Ltda. EPP. Procurador: Princesa Marcas e Patentes Ltda. MU 8702320-2 U2. Depósito: 22 nov. 2007.

RAVARA, L. A. C. **Sistema de transmissão para elevação do apoio de pés giro central**. Depositante: Espectro Industria e Comercio de Produtos Ergonômicos Ltda. EPP. BR 202019017238-5 U2. Depósito: 19 ago. 2019.

REICHERT, J. **Disposição introduzida em apoio para pés**. Depositante: Jonas Reichert. Procurador: Melissa Pontes Quevedo. BR 202022017448-8 U2. Depósito: 31 ago. 2022.

REICHERT, J. **Dispositivo de apoio dos pés para pessoas sentadas**. Depositante: Jonas Reichert. Procurador: Alice Fausto de Oliveira Ramos. MU 8501945-3 U2. Depósito: 14 set. 2005.

SAITO, M. **Disposição aplicada em apoio móvel para os pés**. Depositante: Mauro Saito. Procurador: Vilage Marcas & Patentes S/S LTDA. MU 8600620-7 U2. Depósito: 03 abr. 2006.

SANTOS, V. M. C. **Apoio regulável para pés**. Depositante: Venétia Maria Corrêa Santos. Procurador: Sandoval Cláudio de Oliveira. MU 7502081-5 Y1. Depósito: 29 set. 1995. Concessão: 13 mai. 2003.

SONG, M. K.; KWON, C. M. **Foot bar having heater.** Depositante: Joyn Company. Procurador: Seong Je Jo. KR 102041583 B1. Depósito: 02 fev. 2018.

TADAO, K. **Rocking footrest for chair.** Depositante: AOI Seiko. Procurador: Tatsuhiko Kato. JP 2016101193 A. Depósito: 27 nov. 2014.

TEIXEIRA, Luciene Pires. **Prospecção tecnológica: importância, métodos e experiências da Embrapa Cerrados**. Planaltina, DF: Embrapa Cerrados, 2013. Disponível em: https://ainfo.cnptia.embrapa.br/digital/bitstream/item/100348/1/doc-317.pdf. Acesso em 15 out. 2024.

VAN HOOFT, J. T. L.; FRENCKEN, T. M. R. P. **Footrest with height adjustable scissor structure**. Depositante: OAHWIP. Procurador: Witmans, H. A. [NL]. WO 202235310 A1. Depósito: 14 ago. 2020.

VELLOSO, C. F. **Banqueta para apoio das pernas e pés**. Depositante: Caio Ferraz Velloso. Procurador: GOBERNATE - Marcas e Patentes S/C Ltda. MU 7702532-6 U2. Depósito: 11 dez. 1997.

VIEIRA, A. J. O.; JULIÃO FILHO, C. A. B.; FIRMINO, R. T.; GRANVILLE-GARCIA, A. F.; MENEZES, V. A. de. Conhecimento de ergonomia e desordens osteomusculares entre estudantes de Odontologia. **Revista da Faculdade de Odontologia - UPF**, *[S. l.]*, v. 19, n. 3, 2015. DOI: 10.5335/rfo.v19i3.3996. Disponível em: https://seer.upf.br/index.php/rfo/article/view/3996. Acesso em: 23 out. 2024.

WANG, R. **Multifunctional footstool.** Depositante: Rui Wang. CN 115088977 A. Depósito: 22 jun. 2022.

WANG, X; LAVENDER, S. A.; SOMMERICH, C. M.; RAYO, M. F. The effects of using a footrest during computer tasks varying in complexity and temporal demands: a postural and electromyographic analysis. **Applied Ergonomics**, Pittsburgh, vol. 98, jan. 2022. DOI: 10.1016/j.apergo.2021.103550. Disponível em: https://doi.org/10.1016/j.apergo.2021.103550. Acesso em 15 out. 2024.

WEISHAUPT JÚNIOR, L. **Aperfeiçoamento em dispositivo de apoio, descanso e exercício para os pés**. Depositante: Cotrim Indústria e Comércio Ltda. Procurador: Sul América Marcas e Patentes S/C Ltda. MU 8202203-8 Y1. Depósito: 20 set. 2002. Concessão: 27 jul. 2010.

WEISHAUPT JÚNIOR, L. **Dispositivo de apoio, descanso e exercício para os pés**. Depositante: Cotrim Indústria e Comércio Ltda. Procurador: Sul América Marcas e Patentes S/C Ltda. MU 8101069-9 Y1. Depósito: 02 jul. 2001. Concessão: 10 fev. 2009.

YAJUN, H. **Pedal Plate**. Depositante: Foshan Designa Technology. Procurador: Liang Ying; Guangzhou Huaxue Intellectual Property Agency Co., Ltd; Gu Siyan; Guangzhou Huaxue Intellectual Property Agency Co., Ltd. CN 206507631 U. Depósito: 29 ago. 2016.

YONGZHEN, Y. **Foldable foot steps on**. Depositante: ONLEAD. Procurador: Liu Yisheng; Shenzhen Talent Patent Service. CN 206699850 U. Depósito: 16 ago. 2016.

YOU, G. Y. **The structure of a foot support**. Depositante You Yeul. Procurador: Hyen-Seok Jo. KR 101775962 B1. Depósito: 20 mar. 2017. Concessão: 07 set. 2017.

YU, Y. **Foot placing plate**. Depositante: Yishu Yu. CN208447024U. Depósito: 03 abr. 2018.

YU, Y. **Footrest**. Depositante: Shenzhen Omax Technology; Yishu Yu. WO201911008A1. Depósito: 27 mar. 2018.

ZELA, H.; GEORG, I. **Suporte basculante para os pés**. Depositante: Hermes Zela; Itamar Georg. BR 202017009469-9 U2. Depósito: 04 mai. 2017.

ZHANG, J. **Sports footrest with adjustable height and angle**. Depositante: Jianfeng Zhang. Procurador: Mao Mao; Nanchang Hedaxin Intellectual Property Agency Office (General Partnership). CN 217309650 U. Depósito: 25 mai. 2022.

CHAPTER 3

SHEAR THICKENING-SHEAR THINNING AND SHEAR THINNING-SHEAR THICKENING TRANSITIONS IN POLYMERIC SYSTEMS

José Edilson Neves
Master's Degree in Chemical Engineering
Universidade Federal de Campina Grande (UFCG)
E-mail: edilson@uaepetro.ufcg.edu.br

Taynah Pereira Galdino
Doctor of Science and Materials Engineering
Universidade Federal de Campina Grande (UFCG)
E-mail: taynah.galdino@certbio.ufcg.edu.br

Antonio Gilson Barbosa de Lima
Doctor of Mechanical Engineering
Universidade Federal de Campina Grande (UFCG)
E-mail: antonio.gilson@ufcg.edu.br

Marcus Vinicius Lia Fook
Doctor of Chemistry
Universidade Federal de Campina Grande (UFCG)
E-mail: marcus.liafook@certbio.ufcg.edu.br

Rômulo Feitosa Navarro
Doctor of Process Engineering
Universidade Federal de Campina Grande (UFCG)
E-mail: romulonavarro13@gmail.com

ABSTRACT: This review explores the complex rheological behaviors of hydrogels, specifically focusing on shear thinning-shear thickening (PD) and the less common shear thickening-shear thinning (DP) transitions. While shear thinning (viscosity decrease with increasing shear rate) is widely utilized in applications like 3D printing and injectables, and shear thickening (viscosity increase) is observed in concentrated suspensions, the transitions between these states are critical for advanced material design. The PD transition, often occurring at higher shear rates, is attributed to mechanisms such as hydrodynamic clustering, frictional contacts, and network rearrangement. In contrast, the DP transition, particularly noted in chitosan hydrogels, manifests at very low shear rates. This low-shear DP behavior, characterized by an initial viscosity increase followed by a decrease, is proposed to stem from a competition between temporary shear- induced associations and subsequent structure breakdown or chain alignment. The precise molecular mechanisms for DP transitions remain largely unelucidated and require further experimental validation. Understanding and controlling these distinct rheological transitions are crucial for rationally designing tunable hydrogels with tailored flow properties for diverse applications in biomedical engineering, drug delivery, tissue regeneration, food products, and cosmetics.

KEYWORDS: hydrogels, shear thickening, shear thinning, low-shear viscosity.

RESUMO: Esta revisão explora os complexos comportamentos reológicos de hidrogéis, com foco específico nas transições de afinamento-espessamento por cisalhamento (PD) e nas menos comuns transições de espessamento- afinamento por cisalhamento (DP). Enquanto o afinamento por cisalhamento (diminuição da viscosidade com aumento da taxa de cisalhamento) é amplamente utilizado em aplicações como impressão 3D e formulações injetáveis, e o espessamento por cisalhamento (aumento da viscosidade) é observado em suspensões concentradas, as transições entre esses estados são críticas para o projeto avançado de materiais. A transição PD, frequentemente ocorrendo em taxas de cisalhamento mais elevadas, é atribuída a mecanismos como aglomeração hidrodinâmica, contatos por fricção e rearranjo da rede. Em contraste, a transição DP, particularmente observada em hidrogéis de quitosana, manifesta-se em taxas de cisalhamento muito baixas. Esse comportamento DP em baixas taxas de cisalhamento, caracterizado por um aumento inicial da viscosidade seguido de uma diminuição, é proposto como resultado de uma competição entre associações temporárias induzidas pelo cisalhamento e a subsequente ruptura da estrutura ou alinhamento das cadeias. Os mecanismos moleculares precisos para as transições DP permanecem amplamente desconhecidos e requerem validação experimental adicional. Compreender e controlar essas transições reológicas distintas é crucial para o desenvolvimento racional de hidrogéis ajustáveis, com propriedades de fluxo sob medida, para diversas aplicações em engenharia biomédica, liberação de fármacos, regeneração tecidual, produtos alimentícios e cosméticos.

PALAVRAS-CHAVE: hidrogéis, espessamento por cisalhamento, afinamento por cisalhamento, viscosidade de baixo cisalhamento.

1. INTRODUCTION

1.1 RHEOLOGY OF POLYMERIC MATERIALS AND HYDROGELS

The study of rheology, which examines the flow and deformation of matter, as defined by Bingham and accepted when the American Society of Rheology was founded in 1929 (Schowalter, 1978), is fundamental to understanding and manipulating polymeric materials, including hydrogels (Alves *et al*., 2025). Unlike simple Newtonian fluids where viscosity is constant regardless of the applied shear rate, polymers in solution, melt, or gel states typically exhibit complex, non-Newtonian flow behaviors (Squires; Mason, 2010; Barnes, 1989).

These behaviors include shear thinning (pseudoplasticity), where viscosity decreases with increasing shear rate; shear thickening (dilatancy), where viscosity increases with increasing shear rate (see Figure 1); and the presence of a yield stress, below which the material behaves like a solid (Barnes, 1989; Mari *et al*., 2014; Hu; Boltenhagen; Pine, 1998; Enoch; Somasundaram, 2023; Herrada-Manchón; Fernández; Aguilar, 2023; Malkin; Isayev, 2022; Chhabra; Richardson, 2011; Kulichikhin; Malkin, 2022; Barrulas; Corvo, 2023; Craciun; Morariu; Marin, 2022). Furthermore, many polymeric systems display viscoelasticity, exhibiting both liquid-like (viscous) and solid-like (elastic) characteristics depending on the timescale and frequency of the applied deformation (Schowalter, 1978; Alves *et al*., 2025; Barnes, 1989; Wagner; Brady, 2009; Morris, 2020; Seto *et al*., 2013; Pednekar; Chun; Morris, 2017).

Figure 1. Newtonian, pseudoplastic and dilatant rheolgical behaviours

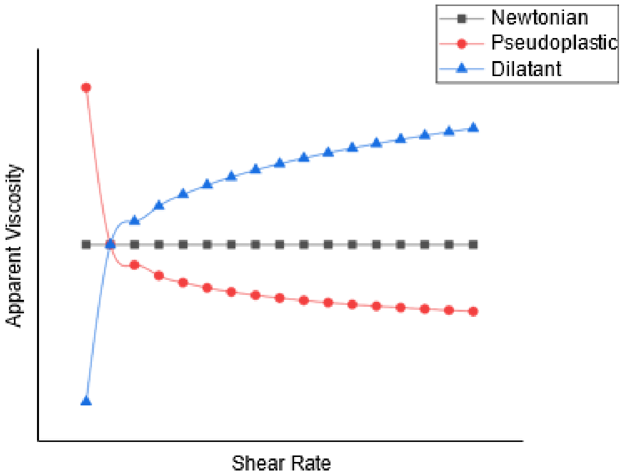

Source: Prepared by the authors

Hydrogels, three-dimensional networks of hydrophilic polymers capable of absorbing large quantities of water, represent a particularly interesting class of complex fluids (Mari *et al*., 2014; Barrulas; Corvo, 2023). Their rheological properties are intricately linked to their network structure, the type and density of crosslinks (which can be physical, such as hydrogen bonds or chain entanglements, or chemical covalent bonds), polymer composition, and interactions with the solvent (Mari *et al*., 2014; Hu; Boltenhagen; Pine, 1998; Barrulas; Corvo, 2023; Wagner; Brady, 2009Understanding hydrogel rheology is crucial for their successful application in diverse fields such as biomedical engineering, drug delivery, tissue regeneration, 3D printing (bioinks), food products, and personal care formulations (Barnes, 1989; Mari *et al*., 2014).

For instance, shear-thinning behavior is often desirable for injectable hydrogels or extrusion-based 3D printing, facilitating the flow of material through a needle or nozzle under high shear but regain viscosity and structure upon cessation of shear (a property related to thixotropy). The extensive study of shear thinning in hydrogels highlights its established importance, often aiming for materials that exhibit significant viscosity reduction under shear coupled with rapid recovery and sufficient yield stress to maintain shape post-extrusion or injection (Barnes, 1989).

1.2 SHEAR-RATE DEPENDENT VISCOSITY TRANSITIONS

Beyond simple shear thinning or shear thickening, some polymeric systems exhibit more complex rheological behavior involving transitions between these states as the shear rate is varied.

Shear thinning, or pseudoplasticity, is the most commonly encountered non-Newtonian behavior in polymer solutions and hydrogels (Schowalter, 1978; Alves *et al*., 2025; Barnes, 1989; Mari *et al*., 2014; Hu; Boltenhagen; Pine, 1998; Enoch; Somasundaram, 2023; Herrada-Manchón; Fernández; Aguilar, 2023; Malkin; Isayev, 2022; Chhabra; Richardson, 2011; Barrulas; Corvo, 2023; Craciun; Morariu; Marin, 2022; Seto *et al*., 2013;). It is generally attributed to the disruption of the material's internal structure under shear, such as the alignment of polymer chains in the direction of flow, disentanglement of polymer coils, or the breakdown of weakly interacting aggregates or temporary networks (Barnes, 1989; Mari *et al*., 2014; Herrada-Manchón; Fernández; Aguilar, 2023; Malkin; Isayev, 2022; Chhabra; Richardson, 2011

Shear thickening, or dilatancy, is characterized by an increase in apparent viscosity with increasing shear rate (Alves *et al*., 2025; Barnes, 1989; Malkin; Isayev, 2022; Chhabra; Richardson, 2011; Wagner; Brady, 2009; Seto *et al*., 2013; Pednekar; Chun; Morris, 2017). This behavior is often observed in concentrated suspensions and is typically explained by the formation of transient, shear-induced structures that increase resistance to flow. Proposed mechanisms include the formation of hydrodynamic clusters (hydroclusters), jamming phenomena where particles become locked into non-flowing configurations, a transition from lubricated to frictional contacts between particles at high shear stress, or shear-induced bridging of particles by polymer chains (Alves *et al*., 2025).

Of particular interest are the transitions between these pseudoplastic and dilatant behaviors:

Shear Thinning → Shear Thickening (PD): This transition involves an initial decrease in viscosity followed by an increase at higher shear rates or stresses. It is relatively well-documented, particularly in concentrated colloidal suspensions (Alves *et al*., 2025) and some polymer systems like certain micellar solutions (Seto *et al*., 2013) or specific hydrogels under large deformation or high shear (see Figure 2) (Wagner; Brady, 2009; Pednekar; Chun; Morris, 2017). For example, thermoreversible hydrogels based on poly(alkylene oxide)-grafted hyaluronic acid or carboxymethyl- cellulose exhibit shear thickening alongside strain hardening (Wagner; Brady, 2009), and silk solutions can transit from shear thinning to shear thickening (Berret, 2006). Even suspensions of flexible fibers, which typically shear thin, have shown unusual shear thickening behavior under certain conditions (Sorbie; Clifford; Jones, 1989). This type of transition represents a nonlinear rheological response often triggered at high defor- mation rates or stresses (Schowalter, 1978; Alves *et al*., 2025; Wagner; Brady, 2009; Pednekar; Chun; Morris, 2017; Manukonda *et al*., 2020).

Shear Thickening → Shear Thinning (DP): This sequence, where an initial dilatant behavior (viscosity increase) is followed by pseudoplastic behavior (viscosity decrease) as shear rate increases (see Figure 3), is explicitly noted in the literature as being less common (Thambi; Li; Lee, 2017). It is often characterized by the dilatant phase occurring within a narrow range at very low shear rates, typically below 1-2 s^{-1} as reported in the literature (Thambi; Li; Lee, 2017).

This low shear rate regime and the potential subtlety of the viscosity increase make the DP transition challenging to observe experimentally. It can be easily confused with instrumental artifacts, mechanical oscillations, or simply overlooked if rheological measurements do not probe sufficiently low shear rates or use inappropriate protocols (Thambi; Li; Lee, 2017). Consequently, this behavior might be significantly underreported in the literature, especially in studies employing standard rheological sweeps that commence at moderate shear rates.

Figure 2. Schematic representation of PD transition

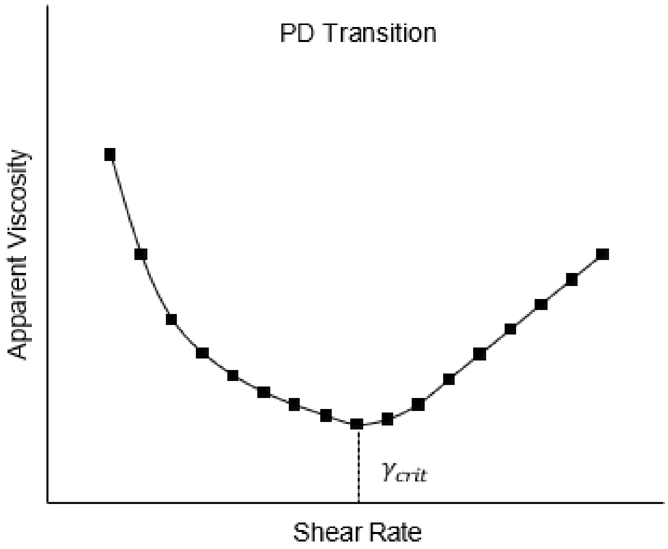

Source: Prepared by the authors

Figure 3. Schematic representation of DP Transition

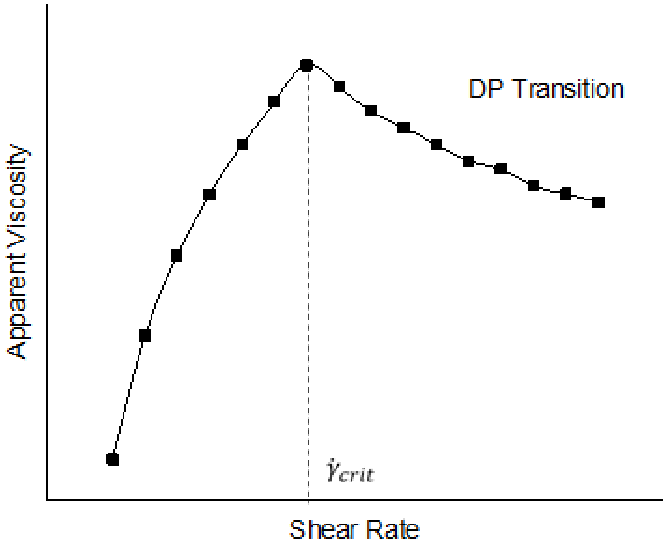

Source: Prepared by the authors

The need for analysis within a restricted, low shear rate range is critical for its clear identification. The distinction between the high-shear DP transition and the low-shear DP transition is therefore crucial, as the order of phenomena and the shear rate regime imply fundamentally different underlying mechanisms (Thambi; Li; Lee, 2017).

1.3 PD TRANSITIONS IN POLYMERIC SYSTEMS

1.3.1 General observations of PD transitions

The transition from shear-thinning behavior at lower shear rates to shear-thickening behavior at higher shear rates (PD) is a well-recognized, albeit complex, rheological phenomenon observed in various concentrated systems cited below (Alves *et al*., 2025). Initially, as shear rate increases, the viscosity decreases due to mechanisms like particle alignment, chain disentanglement, or disruption of weak structures. However, beyond a critical shear rate or stress, the viscosity begins to increase, sometimes dramatically (Alves *et al*., 2025; Sorbie *et al*., 1989). This transition is commonly reported in dense suspensions of hard or soft particles (Alves *et al*., 2025), concentrated polymer solutions, associative polymers, and wormlike micellar solutions (Seto *et al*., 2013). Even suspensions of flexible fibers, which typically exhibit strong shear thinning, have been shown to undergo shear thickening under specific conditions, representing a departure from their usual behavior (Sorbie *et al*., 1989). The onset and magnitude of shear thickening in these systems are sensitive to several factors, all of them crucial, like particle/polymer concentration, particle shape and interactions, solvent properties and temperature (Seto *et al*., 2013; Sorbie *et al*., 1989).

1.3.2 Hydrogel systems exhibiting PD

While many hydrogels primarily exhibit shear thinning or simple viscoelastic solid behavior, some specific hydrogel systems have been reported to display PD transitions, particularly under conditions of large deformation or high shear stress.

PAO-Grafted HA/CMC Hydrogels: Thermoreversible physical hydrogels formed from poly(alkylene oxide) (PAO) grafted onto hyaluronic acid (HA) or carboxymethylcellulose (CMC) have been shown to exhibit shear thick- ening in conjunction with elastic strain-hardening. These systems go from a fluid to a viscoelastic solid upon heating. The rheological behavior is linked to the formation of a transient network where the number of physical crosslinking microdomains remains relatively constant, but the aggrega- tion number of the thermosensitive PAO grafts within these domains in- creases with temperature. This temperature-induced strengthening likely contributes to the observed thickening/hardening under deformation (Wag- ner & Brady, 2009).

Silk Solutions and Gels: Solutions of silk fibroin (natural protein that forms the core structural component of silk fibers) can exhibit complex rhe- ology, including non-linear shear thinning at lower strain amplitudes fol- lowed by shear thickening at higher shear amplitudes. Electrically induced silk gels (e-gels) and pH-induced gels also showed similar non-linear be- havior, including strain-stiffening at high shear, although they displayed a larger linear viscoelastic regime compared to the precursor solution (Ber- ret, 2006).

Dual-Network Hydrogels: Hydrogels composed of interpenetrating networks, such as acrylamide/sodium alginate dual-network (DN) hydrogels, can show significant shear thickening and strain hardening, especially un- der large amplitude oscillatory shear (LAOS) or large deformations. The nonlinear behavior in these systems is strongly influenced by the concen- tration of the crosslinker for the secondary network (e.g., Ca^{2+} ions for al- ginate) (Pednekar, Chun, & Morris, 2017).

1.3.3 Mechanisms for PD Transitions

The mechanisms driving the transition from shear thinning to shear thickening are diverse and depend heavily on the specific nature of the material system. A comparative analysis reveals that different physical principles govern this transition in suspensions versus polymeric or networked systems.

Hydrodynamic Clustering and Jamming: In concentrated suspensions, particularly of hard spheres, shear thickening is often attributed to the for- mation of transient, shear-induced clusters of particles known as hydro- clusters (Alves *et al*., 2025). As shear rate increases, the stabilizing lubri- cation layers between particles can break down, leading to increased hy- drodynamic interactions and the formation of these flow-resisting clusters. At sufficiently high concentrations and shear rates, this can lead to a jam- ming transition where particles lock into a disordered solid-like state, caus- ing a dramatic viscosity increase (Alves *et al*., 2025).

Frictional Contacts: An alternative or complementary mechanism, particularly relevant for non-Brownian suspensions, involves a transition from lubricated, near-contact interactions to direct frictional contacts between particles as the applied shear stress overcomes repulsive forces or squeezes out lubricating fluid (Sorbie *et al*., 1989). The onset of wide- spread frictional contacts significantly increases the energy dissipation and thus the apparent viscosity.

Network Rearrangement/Formation: In systems involving polymers or other associating components, shear flow can induce changes in the net- work structure. In polymer-particle suspensions, shear thickening has been linked to the formation of temporary bridges between particles by polymer chains. In entangled fiber suspensions, shear thickening was as- sociated with shear-induced bending of fibers leading to increased topo- logical entanglements (Sorbie *et al*., 1989). In wormlike micellar solutions, complex transitions involving shear-induced structure formation or changes in micelle breakage/reformation kinetics can lead to thickening (Seto *et al*., 2013).

Chain Stretching Effects: In some polymer solutions or melts, high shear rates can cause significant chain stretching and alignment. While often leading to thinning, under certain conditions (e.g., strong intermolecular interactions, specific architectures), chain stretching might increase the ef- fective hydrodynamic volume or enhance intermolecular friction, contrib- uting to thickening.

Mechanism in PAO-grafted HA/CMC: As mentioned, the thickening/hardening in these thermogels is linked to the temperature-dependent aggregation of grafts within a transient network, leading to a stiffer struc- ture that resists deformation more strongly (Wagner & Brady, 2009).

Mechanism in Acrylamide/Alginate DN Hydrogels: The nonlinear rheology, including shear thickening and strain hardening, is explained by the sequential failure of the two networks. The more brittle ionic network (algi- nate crosslinked by Ca^{2+}) fractures first under increasing strain, dissipating energy (contributing to toughness and hardening). At larger strains, the more extensible covalent network (polyacrylamide) takes over the load- bearing, and its resistance to further deformation and eventual breakdown contributes to the observed thickening. The Ca^{2+} ions are critical in forming the initial alginate network structure whose failure initiates the nonlinear response (Pednekar, Chun, & Morris, 2017).

It is evident that PD transitions arise from fundamentally nonlinear phenomena occurring at sufficiently high shear rates, stresses, or strains, where the system's microstructure is significantly perturbed by the flow field (Schowalter, 1978; Alves *et al*., 2025; Wagner & Brady, 2009; Pednekar, Chun, & Morris, 2017; Manukonda *et al*., 2020). This contrast markedly with the DP transition reported in chitosan hydrogels, which occurs in the low shear rate regime.

1.4 DP TRANSITIONS IN POLYMERIC SYSTEMS

1.4.1 General observations of PD transitions

The rheological behavior characterized by an initial increase in viscosity (shear thickening or dilatancy) followed by a decrease in viscosity (shear thinning or pseudoplasticity) with increasing shear rate is referred to as the DP transition. As previously noted, this sequence is considered less common than the opposite PD transition (Thambi, Li, & Lee, 2017). A key characteristic distinguishing this phenomenon is its typical occurrence within a limited range of low shear rates, often below 2 s^{-1} and sometimes initiated at rates as low as 0.01-0.03 s^{-1} (Thambi, Li, & Lee, 2017).

The subtlety of the initial viscosity increases and its confinement to low shear rates contribute to the experimental challenges in reliably observing and characterizing this transition, leading to potential misinterpretation as instrumental noise or oscillation, or simply being missed in standard rheological tests (Thambi, Li, & Lee, 2017). Careful experimental design, focusing measurements on the very low shear rate regime, is essential for its detection (Thambi, Li, & Lee, 2017).

1.4.2 Mechanisms for DP Transition in Polymeric Systems

Despite detailed descriptions and analyses of influencing factors, the precise molecular mechanisms underlying the observed low-shear dilatant pseudoplasticity (DP) transition in polymeric systems, particularly chitosan hydrogels, are not explicitly proposed or experimentally verified in the primary source. The discussion largely correlates macroscopic behavior with compositional and environmental parameters. However, based on observed dependencies and known polymer chemistry, several plausible mechanistic hypotheses can be inferred.

The transition likely stems from a competition between shear-induced structure formation or network resistance (dominating at very low shear rates and causing thickening) and structure breakdown or chain alignment (dominating at slightly higher shear rates and causing thinning).

Initial Thickening (Low Shear Dilatancy)

The initial viscosity increase at minimal shear rates could arise from several contributing factors related to the polymeric system's inherent structure. In the context of chitosan hydrogels, this structure is "peculiar" (Thambi, Li, & Lee, 2017), formed under acidic conditions followed by partial neutralization:

Transient Shear-Induced Associations: Gentle shear might promote temporary, weak associations between polymer chains or chain segments. These could involve hydrogen bonding, hydrophobic interactions (espe- cially if the degree of acetylation, DA, is higher), or transient ionic cross- links mediated by counter-ions. Such associations could increase the ef- fective size of flow units or create temporary networks that resist defor- mation, leading to increased viscosity.

Interplay of Electrostatic and Attractive Forces: In a partially neutralized state, there's a complex balance between residual electrostatic repul- sion among protonated amino groups and various attractive forces (H- bonding, van der Waals). At very low shear, the polymeric system might explore configurations where attractive interactions or temporary physical entanglements dominate, leading to a structure that resists easy flow.

Constrained Network Dynamics: The polymeric network, formed by entanglements and physical crosslinks (potentially ionic bridges formed dur- ing neutralization), possesses a certain elasticity. At very low shear rates, deformation might be primarily elastic or involve slow relaxation pro- cesses. If the network resists rearrangement on the timescale of the ap- plied shear, this resistance could manifest as an apparent increase in vis- cosity (thickening). The observation that chemical crosslinking with genipin lowers $\dot{\gamma}_{\mathrm{crit}}$, supports this view, as a stiffer network would be expected to exhibit such resistance at lower deformation rates.

Subsequent Thinning (Low Shear Pseudoplasticity)

As the shear rate increases beyond $\dot{\gamma}_{\mathrm{crit}}$, the mechanisms causing the initial thickening are overcome:

Breakdown of Temporary Structures: The shear stress becomes sufficient to disrupt the weak, transient associations or networks formed during the thickening phase.

Chain Alignment: Polymer chains begin to disentangle and align in the direction of flow, reducing intermolecular friction and hydrodynamic re- sistance. This is the classical mechanism for shear thinning in polymer solutions and gels (Barnes, 1989; Mari *et al*., 2014; Hu, Boltenhagen, & Pine, 1998; Malkin & Isayev, 2022; Chhabra & Richardson, 2011; Barrulas & Corvo, 2023; Craciun, Morariu, & Marin, 2022).

Disruption of Physical Crosslinks: Hydrogen bonds or ionic interactions that contributed to the initial resistance are broken by increasing shear en- ergy, allowing polymer chains to move more freely past each other. Crucially, the available literature lacks direct experimental evidence (e.g.,

from in-situ structural probes) or detailed theoretical modeling to confirm these hypothesized mechanisms for the DP transition in polymeric systems, particularly chitosan hydrogels. This remains a significant knowledge gap.

1.5 SYNTHESIS AND COMPARATIVE ANALYSIS

1.5.1 Comparison of PD and DP transitions

The two types of transitions involving both shear thickening and shear thinning present distinct rheological signatures and are generally associated with different underlying physics. The more commonly studied PD transition typically occurs at higher shear rates or stresses, often in concentrated particulate or specific polymeric systems, and is driven by mechanisms like hydrocluster formation, frictional contacts, or shear-induced network formation/stretching (Alves *et al*., 2025; Wagner & Brady, 2009; Seto *et al*., 2013; Pednekar, Chun, & Morris, 2017).

In contrast, the DP transition manifests at very low shear rates. Its mechanism, while not fully elucidated, appears linked to subtle, low-energy structural rearrangements, temporary associations, or network resistance within the hydrogel, followed by breakdown and alignment under slightly increased shear (Alves *et al*., 2025). The relative rarity of reports on DP compared to PD might stem from both its less frequent occurrence and the experimental challenges associated with probing the very low shear rate regime accurately.

1.5.2 Implications for applications

The distinct DP rheological profile, characterized by initial resistance to flow at very low shear followed by easier flow at slightly higher shear, could offer advantages in specific applications where conventional shear-thinning or yield-stress behavior is not ideal (Thambi, Li, & Lee, 2017).

Drug Delivery and Injectables: For injectable formulations, the initial thickening at near-zero shear might enhance stability and retention imme- diately upon injection, preventing rapid dispersion before the material sets or adheres. The subsequent shear thinning would still allow for extrusion through a needle or catheter once a critical shear stress/rate is exceeded. This biphasic response could be particularly relevant for ophthalmic drug delivery, where low shear forces are exerted by blinking; the initial thickening could prolong residence time on the ocular surface, while thin- ning allows spreading (Thambi, Li, & Lee, 2017). The specific advantage over a simple yield-stress fluid lies in the potential for a more gradual tran- sition and controlled flow once initiated.

Tissue Engineering and Bioprinting: While strong and immediate shear thinning is often preferred for high-resolution extrusion bioprinting (Zhang *et al*., 2023), the initial thickening phase of an DP material might offer some benefit in terms of immediate shape retention of the printed filament under low gravitational stress, potentially reducing slumping before post-printing crosslinking occurs. However, this must be balanced against the increased extrusion force required to overcome the initial thickening. The DP behav- ior might be more relevant for scaffold stability in the low-stress environ- ment post-implantation.

Food Products and Cosmetics: In food science, the DP profile could translate to unique textural properties, such as an initial firmness or re- sistance followed by a smooth breakdown in the mouth. Similarly, in per- sonal care products like lotions or creams, it could provide an initial feeling of substance or structure that yields to easy spreading upon application (Thambi, Li, & Lee, 2017).

However, realizing these potential benefits requires a deeper understanding and precise control over the DP transition, which is currently hampered by the lack of detailed mechanistic knowledge.

1.6 KNOWLEDGE GAPS AND CHALLENGES

Despite progress in identifying and characterizing the DP phenomenon in polymeric systems, for exemple, chitosan hydrogels, several significant knowledge gaps and challenges remain:

Mechanism Elucidation: The most critical gap is the lack of a detailed, experimentally validated molecular-level mechanism explaining the origin of the low-shear DP transition in these specific chitosan hydrogels (Thambi, Li, & Lee, 2017). Current explanations are largely inferred from macroscopic observations.

Systematic Parameter Exploration: While pH, molarity, and concentration are identified as key factors (Thambi, Li, & Lee, 2017), further system- atic investigation is needed to map the DP behavior across broader ranges of chitosan molecular weight, degree of acetylation, different types and densities of crosslinkers (chemical and physical), and the influence of dif- ferent counter-ions or solvent compositions.

Experimental Standardization and Reproducibility: Given the reported difficulty in observing the low-shear DP transition and potential confusion with artifacts (Thambi, Li, & Lee, 2017), developing standardized, highly sensitive rheological protocols is crucial for ensuring reproducibility and enabling reliable comparison between different studies. Advanced tech- niques like microrheology or coupling rheometry with structural probes (e.g., scattering methods (Schowalter, 1978; Alves *et al*., 2025)) could pro- vide valuable insights into the microstructural changes occurring during the transition.

Preprint Validation: The detailed characterization of the DP transition in chitosan hydrogels currently relies heavily on findings presented in a pre- print (Thambi, Li, & Lee, 2017). Validation of these specific results through peer-reviewed publication is essential for strengthening the conclusions.

Correlation with Application Performance: There is a need for studies that directly link the observed DP rheological profile to functional outcomes in specific applications. For example, demonstrating improved retention or efficacy of drug delivery systems formulated with DP hydrogels compared to conventional formulations.

1.7 FUTURE RESEARCH DIRECTIONS

Addressing the identified gaps requires focused research efforts:

Mechanistic Investigations: Employing advanced characterization techniques concurrently with rheological measurements is paramount. Rheo-SANS/SAXS could probe nanoscale structural evolution, while techniques like NMR spectroscopy might provide insights into molecular mobility and interactions during the transition. Molecular dynamics simulations could also offer theoretical insights into the chain dynamics and intermolecular forces at play under low shear conditions. An interdisciplinary approach combining polymer chemistry, physics, and computational modeling will likely be necessary to fully unravel the mechanism (Thambi, Li, & Lee, 2017).

Controlled Synthesis and Formulation: Developing synthetic strategies that allow for precise control over the chitosan hydrogel network architec- ture (e.g., controlled crosslinking density, defined physical interactions) would enable more systematic investigation of structure-property relation- ships governing the DP transition.

Comparative Studies: Exploring whether similar low-shear DP transitions can be induced in hydrogels based on chemically modified chitosan (e.g., varying hydrophobicity or charge density) or other polysaccharides with tunable properties could help determine the generality of the phenomenon and the key molecular requirements.

Application-Driven Design and Testing: Research should move towards rationally designing chitosan hydrogel formulations that exhibit specific, tailored DP profiles optimized for targeted applications (e.g., oph- thalmic delivery, minimally invasive therapies). This requires not only con- trolling the transition but also rigorously testing the functional performance of these materials in relevant in vitro or in vivo models. Understanding and harnessing the unique low-shear DP transition, if controllable, offers the potential to engineer novel "smart" hydrogels with finely tuned flow prop- erties for specialized applications where conventional rheological behav-iors fall short.

2. CONCLUSION

This review has comprehensively explored the intricate rheological behaviors of hydrogels, particularly focusing on the dynamic transitions between shear thinning (pseudoplasticity) and shear thickening (dilatancy). We have highlighted two distinct types of transitions: the more commonly observed shear thinning-shear thickening (PD) transition, typically occurring at higher shear rates and driven by mechanisms such as hydrodynamic clustering and network formation, and the less understood shear thickening-shear thinning (DP) transition, which uniquely manifests at very low shear rates.

The DP transition, as exemplified by chitosan hydrogels, presents a fascinating challenge and opportunity. Its initial resistance to flow at minimal shear, followed by easier flow at slightly higher shear, suggests a complex interplay of temporary associations and structural rearrangements. However, the precise molecular mechanisms governing this low-shear DP behavior remain largely speculative and require rigorous experimental validation.

The ability to understand, predict, and ultimately control these rheological transitions holds immense promise for the rational design of "smart" hydrogels. Such materials, with their finely tuned flow properties, could revolutionize diverse applications ranging from advanced biomedical engineering (e.g., injectable drug delivery systems, bioinks for 3D printing, tissue regeneration scaffolds) to consumer products like food and cosmetics, where specific textural and application-dependent flow characteristics are paramount.

Addressing the existing knowledge gaps, particularly concerning the DP transition, necessitates a concerted future research effort. This includes in-depth mechanistic investigations utilizing advanced characterization techniques (e.g., rheo-SANS/SAXS, NMR spectroscopy, molecular dynamics simulations), systematic exploration of material parameters (e.g., polymer molecular weight, crosslinking density, solvent effects), standardization of experimental protocols for accurate low-shear rheometry, and direct correlation of rheological profiles with real-world application performance. By bridging these gaps, we can unlock the full potential of hydrogels as highly versatile and responsive materials for a new generation of innovative technologies.

ACKNOWLEDGEMENTS

The authors would like to express gratitude to the funding agencies (CNPq, CAPES and FINEP) for the financial support, to the CERTBIO/UFCG for the physical infrastructure and to the cited authors which contributed significantly to the inprovement of the work.

REFERENCES

ALVES, S. J. d. M.; SANTOS, M. A.; NETO, J. E. d. S., *et al*. Combined Effect of pH and Neutralizing Solution Molarity on the Rheological Properties of Chi- tosan Hydrogels for Biomedical Applications. **Gels**, 2025, 11, 212.

BARNES, H. Shear-thickening (“Dilatancy”) in suspensions of nonaggregating solid particles dispersed in Newtonian liquids. **Journal of Rheology**, 1989, 33, 329-366.

BARRULAS, R. V.; CORVO, M. C. Rheology in product development: an insight into 3D printing of hydrogels and aerogels. **Gels**, 2023, 9, 986.

BERRET, J.-F. Rheology of wormlike micelles: Equilibrium properties and shear banding transitions. In **Molecular gels: materials with self-assembled fibrillar networks**; SPRINGER, 2006, 667-720.

CHHABRA, R. P.; RICHARDSON, J. F. **Non-Newtonian flow and applied rheology: engineering applications**. Butterworth-Heinemann, 2011.

CRACIUN, A. M.; MORARIU, S.; MARIN, L. Self-healing chitosan hydrogels: Preparation and rheological characterization. **Polymers**, 2022, 14, 2570.

ENOCH, K.; SOMASUNDARAM, A. A. Rheological insights on Carboxymethyl cellulose hydrogels. **International Journal of Biological Macromolecules**, 2023, 253, 127481.

HERRADA-MANCHÓN, H.; FERNÁNDEZ, M. A.; AGUILAR, E. Essential guide to hydrogel rheology in extrusion 3D printing: how to measure it and why it mat- ters? **Gels**, 2023, 9, 517.

HU, Y.; BOLTENHAGEN, P.; PINE, D. Shear thickening in low-concentration solutions of wormlike micelles. I. Direct visualization of transient behavior and phase transitions. **Journal of Rheology**, 1998, 42, 1185-1208.

KULICHIKHIN, V. G.; MALKIN, A. Y. The role of structure in polymer rheology. **Polymers**, 2022, 14, 1262.

MALKIN, A. Y.; ISAYEV, A. I. **Rheology: concepts, methods, and applications**. Elsevier, 2022.

MANUKONDA, B. H.; CHATTERJEE, V. A.; VERMA, S. K.; BHATTACHARJEE, D.; BISWAS, I.; NEOGI, S. Rheology based design of shear thickening fluid for soft body armor applications. **Periodica Polytechnica Chemical Engineering**, 2020, 64, 75-84.

MARI, R.; SETO, R.; MORRIS, J. F.; DENN, M. M. Shear thickening, frictionless and frictional rheologies in non-Brownian suspensions. **Journal of Rheology**, 2014, 58, 1693-1724.

MORRIS, J. F. Shear thickening of concentrated suspensions: Recent develop- ments and relation to other phenomena, **Annual Review of Fluid Mechanics**. 2020, 52, 121-144.

NAVARRO, R. F. Application of Non-Linear Rheological Model to Shear-Ticken- ing Polymeric Systems. **Polímeros**, 2002, 12, 41-47.

PEDNEKAR, S.; CHUN, J.; MORRIS, J. F. Simulation of shear thickening in at- tractive colloidal suspensions. **Soft Matter**, 2017, 13, 1773-1779.

SCHOWALTER, W. R. **Mechanics of Non-Newtonian Fluids**. Oxford: Pergamon Press, 1978.

SETO, R.; MARI, R.; MORRIS, J. F.; DENN, M. M. Discontinuous shear thick- ening of frictional hard-sphere suspensions. **Physical Review Letters**, 2013, 111, 218301.

SORBIE, K.; CLIFFORD, P.; JONES, E. The rheology of pseudoplastic fluids in porous media using network modeling. **Journal of Colloid and Interface Science**, 1989, 130, 508-534.

SQUIRES, T. M.; MASON, T. G. Fluid mechanics of microrheology. **Annual Review of Fluid Mechanics**, 2010, 42, 413-438.

THAMBI, T.; LI, Y.; LEE, D. S. Injectable hydrogels for sustained release of therapeutic agents. **Journal of Controlled Release**, 2017, 267, 57-66.

WAGNER, N. J.; BRADY, J. F. Shear thickening in colloidal dispersions. **Phys- ics Today**, 2009, 62, 27-32.

ZHANG, H.; SU, S.; LIU, S., *et al*. Effects of chitosan and cellulose derivatives on sodium carboxymethyl cellulose-based films: A study of rheological proper- ties of film-forming solutions. **Molecules**, 2023, 28, 5211.

CHAPTER 4

DEVELOPMENT OF A PID CONTROLLER FOR THERMAL REGULATION OF THE EXTRUDER OF A PET BOTTLE FILAMENT MACHINE FOR 3D PRINTING

Caio César Silva de Carvalho
Bachelor’s Degree in Control and Automation Engineering
Instituto Federal do Pará (IFPA)
E-mail: caiocscarvalhoo@gmail.com

Juan Victor dos Santos Tavares
Undergraduate student in Control and Automation Engineering
Instituto Federal do Pará (IFPA)
E-mail: juanvictor.ifpa@gmail.com

Rejane de Barros Araújo
PhD in Automation and Systems Engineering
Universidade Federal de Santa Catarina (UFSC)
E-mail: Rejane.barros@ifpa.edu.br

Benedito Coutinho Neto
PhD in Civil Engineering
Escola de Engenharia de São Carlosda, Universidade de São Paulo (EESC - USP)
E-mail: benedito.coutinho@ifpa.edu.br

ABSTRACT: This study proposes the development of a Proportional, Integral and Derivative (PID) controller, tuned through the Generalized Minimum Variance (GMV) technique, with the objective of regulating the temperature of the extruder of a PET Bottle Filament Machine, a sustainable filament option for 3D printing. The research presents a detailed theoretical review, addressing the history of 3D printing, rapid prototyping, control engineering concepts, identification of linear systems, classical PID control theory, and advanced control techniques such as Recursive Signal Tracking (RST) and GMV. The methodology includes building the machine, conducting control tests, producing PET filament and applying it in printing. The results demonstrate that the developed thermal control system is efficient, ensuring the stability of the temperature necessaryfor the production of the PET filament, contributing to the quality and viability of the process.

KEYWORDS: 3D printing, filament machine, gmv control, pid control, pet bottle, amazônia.

RESUMO: Este estudo propõe o desenvolvimento de um controlador Proporcional, Integral e Derivativo (PID), sintonizado por meio da técnica de Variância Mínima Generalizada (GMV), com o objetivo de regular a temperatura da extrusora de uma Máquina de Filamento de Garrafa PET, uma opção de filamento sustentável para impressão 3D. A pesquisa apresenta uma revisão teórica detalhada, abordando o histórico da impressão 3D, prototipagem rápida, conceitos de engenharia de controle, identificação de sistemas lineares, teoria clássica do controle PID e técnicas avançadasde controle, como Rastreamento de Sinal Recursivo (RST) e GMV. A metodologia inclui a construção da máquina, a realização de testes de controle, a produção de filamento de PET e sua aplicação na impressão. Os resultados demonstram que o sistema de controle térmico desenvolvido é eficiente, garantindo a estabilidade da temperatura necessária para a produção do filamento de PET, contribuindo para a qualidade e a viabilidade do processo.

PALAVRAS-CHAVE: impressão 3d, máquina de filamento, controle gmv, controle pid, garrafa pet, amazônia.

1. INTRODUCTION

The 3D Printing, Additive Manufacturing (AM), or Rapid Prototyping industry is becoming increasingly prevalent in everyday life. It is a technology that uses the Fused Deposition Modeling (FDM) process as one of the methods for constructing parts and prototypes using a 3D printer. Three-dimensional objects are manufactured by adding material layer by layer, based on a digital model created using Computer-*Aided Design (*CAD) *software* (Yokota, 2021; Pedrosa, 2015).

In this context, the primary raw material for 3D printing using the FDM process is thermoplastic, a type of plastic that can be molded and recycled without losing its properties. The main thermoplastics used are Acrylonitrile Butadiene Styrene (ABS) and Polylactic Acid (PLA) biopolymer, but other materials also stand out, such as Polyethylene Terephthalate (PET), Polypropylene (PP), Polystyrene (PS), Polycarbonate (PC), and High-Density Polyethylene (HDPE) (Pedrosa, 2015). The use of PET, derived from recycled bottles, emerges as a viable and sustainable alternative. The accumulation of PET bottles in the environment, combined with the possibility of their recycling, presents an innovative solution both for environmental problems and for the development of low-cost, efficient filaments for 3D printing.

However, the efficient production of PET filaments for 3D printing faces technical challenges, such as the need for thermal control during the extrusion process. Temperature fluctuations in the extruder can result in irregular, low-quality filaments. Thus, this work proposes the design and implementation of a machine capable of integrating physical and electronic structures, using PID control tuned with the GMV technique to ensure a stable temperature and optimize the filament production process. This study is justified by the urgency of addressing the environmental problem of PET bottles and offers an economical solution for the production of high-quality filaments.

2. THEORETICAL FRAMEWORK

2.1 CONTROL

According to Coelho, Jeronymo, and Araújo (2019), the control system is essential for the efficient and safe operation of processes in engineering. It acts as the link that ensures critical system variables, such as temperature or pressure, are monitored and adjusted in real time, allowing the process to operate within established parameters. This adaptability is crucial in closed-loop systems, which use continuous measurements to correct errors and compensate for uncertainties, ensuring the system’s stability, robustness, and reliability in the face of changes or external disturbances.

Furthermore, control is a key component in technological advancement, with applications ranging from industrial automation—optimizing production lines and reducing waste—to modern transportation systems, such as autonomous vehicles and high-speed rail networks. It is also indispensable in critical areas such as power generation and distribution, healthcare (control of medical equipment), and even in the aerospace sector, standing out as a tool to meet the growing demands for efficiency, precision, and sustainability in today’s systems.

2.1.1 PID Control

The PID (Proportional, Integral, and Derivative) controller is widely recognized in industrial applications for its efficiency in process control and the simplicity it offers in operation (Dorf; Bishop, 2012). According to Ogata (2010), it is a closed-loop control system that combines the proportional, integral, and derivative actions to regulate the process output, as described in Equation 01. Figure 1 presents the block diagram, which demonstrates the calculation and sum of the gains that generate the control signal.

$$u(t) = K_c e(t) + \frac{K_c}{T_i} \int_{t0}^{t} e(\tau)d\tau + K_c T_d \frac{de(t)}{dt} \qquad (1)$$

Figure 1. Block diagram of the Ideal PID structure

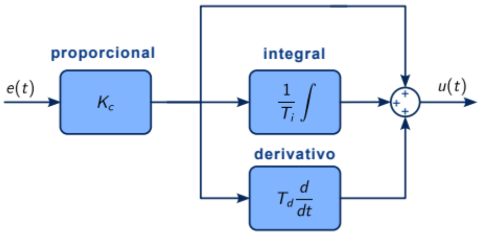

Source: Santos Júnior (2024)

The I+PD controller, shown in Figure 2 and described by Equation 02, reduces the proportional and derivative gains, resulting in a more conservative response. During the implementation of PID controllers, it is essential to validate the gain values, as each component plays a specific role: the proportional gain adjusts the system based on the current error, the integral gain corrects for the accumulated error, and the derivative gain accounts for the rate of change of the error.

$$u(t) = K_c\left(\frac{1}{T_i}\int_{t_0}^{t} e(\tau)d\tau - T_d\frac{de(t)}{dt} - y(t)\right) \quad (2)$$

Figure 2. Block diagram of the I+PD structure

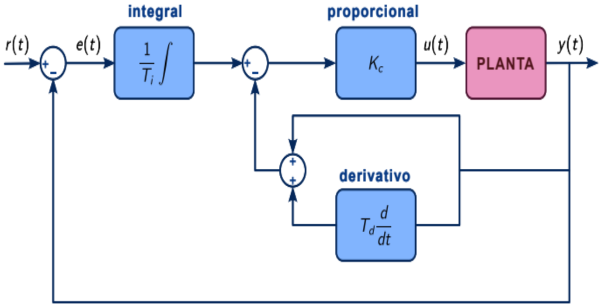

Source: Santos Júnior (2024)

2.1.2 Digital control

Digital control employs computers as central elements to process reference signals and calculate the output required for the desired system performance, as illustrated in the diagram in Figure 3 (Dorf; Bishop, 2012).

Figure 3. Block diagram of a digital control system

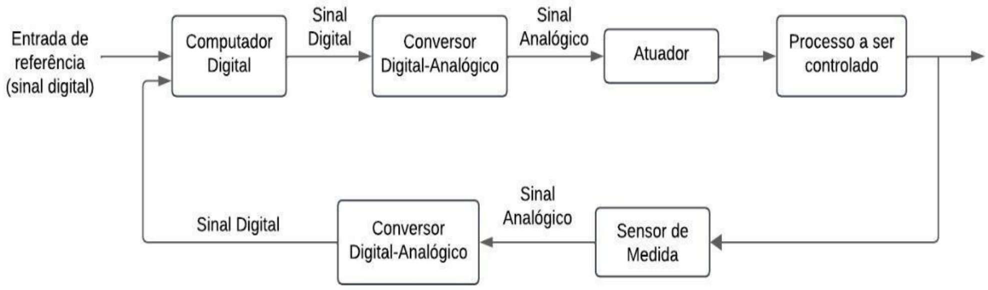

Source: Adapted from Dorf and Bishop (2012)

The key difference between digital and analog controllers lies in signal processing: analog controllers operate in continuous time, while digital controllers use sampling at fixed intervals (Ts). Among the advantages of digital control are greater precision, the use of encoded signals, integration with sensors and microprocessors, lower sensitivity to noise, and flexibility in reconfiguration via *software* (Dorf; Bishop, 2012).

2.1.3 Digital PID and I+PD Control

Digital PID adapts the PID controller for discrete systems, calculating the proportional, integral, and derivative terms based on error samples at regular intervals. It is widely used in systems with digital control, such as microcontrollers and PLCs. Digital I+PD, a variation of PID, combines the integral and derivative terms, favoring the elimination of accumulated error and a more stable dynamic response, with lower sensitivity to noise.

Using the *Backward Rectangular Method* (*BRM*) and the control signal samples at the instants$t = k$ and$t = k - 1$, as shown in equations 1 and 2, it is possible to derive the discrete control equations for the ideal PID and I+PD structures, which are expressed in Equations 03 and 04.

$$\Delta u(k) = K_c\left(1 + \frac{T_s}{T_i} + \frac{T_d}{T_s}\right)e(k) - K_c\left(1 + \frac{2T_d}{T_s}\right)e(k-1) + \left(\frac{T_d}{T_s}\right)e(k-2) \qquad (3)$$

$$\Delta u(k) = \frac{K_c T_s}{T_i}r(k) - K_c\left(1 + \frac{T_s}{T_i} + \frac{T_d}{T_s}\right)y(k) + K_c\left(1 + \frac{2T_d}{T_s}\right)y(k-1) - \frac{K_c T_d}{T_s}y(k-2)$$
(4)

2.1.4 RST Control

The structure of the Recursive Signal *Tracking* (RST) controller is shown in the block diagram in

Figure 4. This controller consists of the filters R(Z^{-1}) and S(Z^{-1}), which are designed to achieve the desired response and reject disturbances, while the filter T(Z^{-1}) is designed for reference tracking (Landau, 1998). Thus, the RST control signal is described by Equation 05, whose structure allows for separating reference tracking from the handling of disturbance rejection and parameter variation, since the polynomial S(Z^{-1}) is distinct from the polynomial T(Z^{-1}) (Åström; Wittenmark, 2008).

Figure 4. Block diagram of the RST control

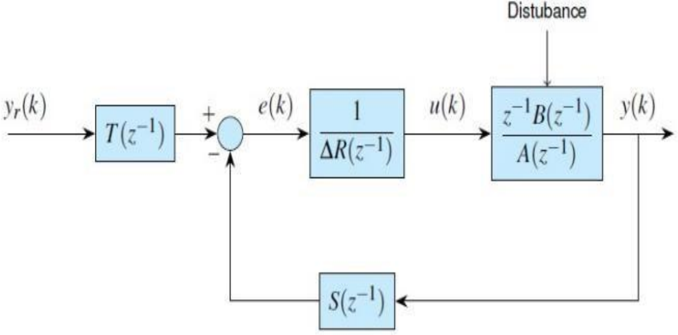

Source: Santos Júnior (2024)

$$R(Z^{-1})\Delta u(k) = T(Z^{-1})y_r(k) - S(Z^{-1})y(k) \qquad (5)$$

2.1.5 GMV Control

The Minimum Variance (MV) controller, introduced by Aström and Wittenmar (1970), is primarily designed to mitigate the impact of noise on a process's output (Araújo, 2017). Subsequently, Clarke and Gawthrop (1975) expanded this approach, proposing the Generalized Minimum Variance (GMV) controller, which emerged as an evolution of the MV controller. According to Araújo (2017), the GMV derives its control law from the minimization of a cost function associated with the concept of generalized systems. This controller is widely used in various applications, such as offset correction, noise variance reduction, increasing the robustness of control system performance, and reducing energy consumption in the face of disturbances. The GMV controller has two distinct versions, one for the positional case and another for the incremental case; depending on the approach, the linear input-output model of the process, the control law, the generalized auxiliary output, and the cost function to be optimized take on different forms in the discrete-time domain (Araújo, 2017; Silveira, 2012). Due to its flexibility, GMV is used in a variety of fields, such as medicine, aeronautical systems, telecommunications, power engineering, and robotics (Araújo, 2017).

According to Coelho, Jeronymo, and Araújo (2019), the generalized auxiliary output for GMV control can be illustrated in the block diagram shown in Figure 5. In this context, the equation describing the process is modeled by the *Deterministic Controlled Auto-Regressive* (*DCAR*) model, which is expressed by equation (06). In this model, $y(k)$ represents the output signal, $u(k)$ is the control signal, and d corresponds to the transport delay. Furthermore, the roots of the polynomials $A(z^{-1})$ and $B(z^{-1})$ indicate, respectively, the poles and zeros of the open-loop plant.

Figure 5. Overview of the PET Bottle Filament Machine

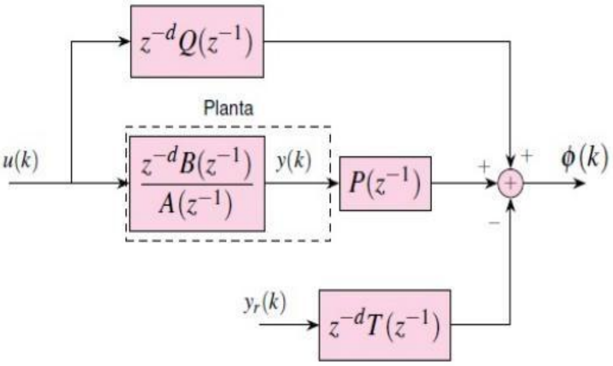

Source: Santos Júnior (2024)

$$A(Z^{-1})\Delta y(k) = Z^{-d}B(Z^{-1})\Delta u(k) \qquad (6)$$

A lei de controle do GMV incremental é representada pela equação (07).

$$[B(z^{-1}) + Q(z^{-1})]\Delta u(k) = T(z^{-1})y_r(k) - S(z^{-1})\, y(k) \qquad (7)$$

2.1.6 PID Control Tuned Using the GMV Technique

To tune the PID controller using GMV, it is essential to consider the DCAR model from Equation 06, along with the GMV incremental control law equation (Equation 07), the digital PID control law equation (Equation 03), and Equations 08, 09, and 10. With these elements, it is possible to rewrite the GMV control equation, as illustrated by Equations 9 and 10, as shown in Equation 11.

$$Q(z^{-1}) = \frac{q_1(z^{-1})}{b_0} \qquad (8)$$

$$B(z^{-1})E(z^{-1}) + Q(z^{-1}) = B(1)E(1) + Q(1) = \frac{1}{q_0} \qquad (9)$$

$$T(z^{-1}) = S(z^{-1}) = s_0 + s_1 z^{-1} + s_2 z^{-2} \qquad (10)$$

$$\Delta u(k) = q_0[s_0 e(k) + s_1 e(k-1) + s_2 e(k-2)] \qquad (11)$$

Thus, by comparing equations (03) and (11), it is possible to determine the PID controller tuning parameters using the GMV method, as shown in equations 12 (K_c), 13 (T_i), and 14 (T_d). The impact of the energy parameter of the control signal (q_0) on the system's dynamic behavior directly reflects in the way the proportional gain of the PID controller varies.

$$K_c = -q_0(s_1 + 2s_2) \qquad (12)$$

$$T_i = -\frac{(s_1+2s_s)T_s}{s_0+s_1+s_2} \qquad (13)$$

$$T_d = -\frac{2s_sT_s}{s_1+2s_2} \qquad (14)$$

3. MATERIALS AND METHODS

3.1 PET BOTTLE FILAMENT MACHINE

The designed PET Bottle Filament Machine essentially consists of three main components: the filer, the extruder, and the draw-off unit (Figure 6a). Its purpose is to convert PET bottles into PET filaments, following the process described in the flowchart shown in Figure 7.

Following the flowchart, the process begins with the collection and cleaning of the PET bottles, which involves removing the logo and cleaning internal and external residues. Afterward, during bottle processing, the bottom is removed and a cut is made to fit the filleting machine (Figure 6b), as shown in the second step of the flowchart (Figure 7).

Figure 6. Overview of the Filament Machine and the PET Bottle Cleaning and Treatment Process

Source: Author (2024)

From there, in the third stage, the PET bottle undergoes the filleting process (Figure 8a), which consists of transforming the previously cleaned and treated PET bottles into a rectangular fillet approximately 10 mm thick, as illustrated in Figure 8b.

Finally, in the fourth stage, the PET bottle filament manufacturing process involves the extruder shaping the strip into a cylindrical filament with a thickness of 1.8 mm, and in the fifth stage, the take-up unit is responsible for winding the PET filament. Thus, in the 6th step, the PET filament is obtained, ready for use in the 3D printer (Figure 8b).

Figure 7. Flowchart of PET bottle filament manufacturing

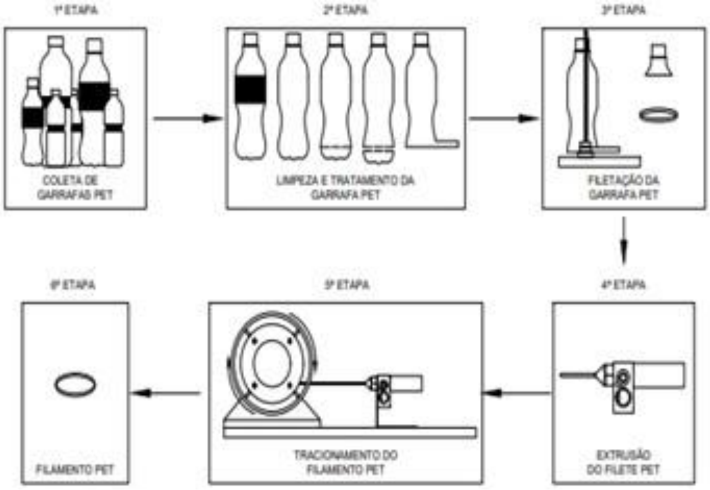

Source: Author (2024)

Figure 8. Bottle filation process and PET filament

Source: Author (2024)

4. RESULTS AND DISCUSSION

The tests conducted to analyze the performance of the GMV controller with a first-order filter and PID tuning covered aspects such as reference tracking, disturbance rejection, and control effort. The tested conditions included: maintaining the temperature at 250 °C, both with and without PET filament production, as well as changes in the temperature reference from 200 °C to 250 °C and from 250 °C to 200 °C. All experiments were conducted in a climate-controlled environment maintained at 20 °C. To complement the analysis, the *Integrated Absolute Error* (IAE) and *Total Variation of Control* (TVC) performance indices were calculated, allowing for a numerical comparison between the controllers.

4.1 TEMPERATURE CONTROL

The first temperature test was performed at 250 °C without PET filament production, during which 2,000 samples were collected over approximately 33 minutes. In Figure 9a, it is possible to analyze the behavior of the GMV controller with a first-order filter, while Figure 9b illustrates how the PI controller, tuned via GMV, behaves.

Figure 9. Temperature control at 250 °C of the GMV and PI controllers (tuned via GMV) with a first-order filter without filament formation

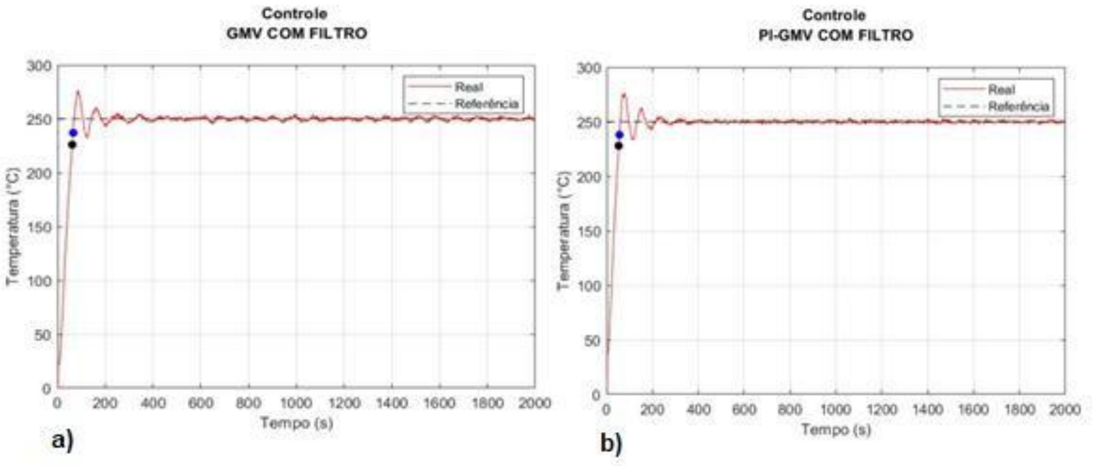

Source: Author (2024)

Figures 10a and 10b show the control signals applied during the process by the GMV and PI controllers, respectively, both configured via GMV. Based on these results, it can be concluded that both controllers were able to maintain the desired setpoint and mitigate external disturbances, taking into account that the thermal process is continuously exchanging heat with the environment. Furthermore, it is observed that the PWM control signal of the GMV controller experienced an initial saturation and subsequently varied between 40% and 50% of the duty cycle. From another perspective, the PWM control signal of the PI controller, via GMV, also underwent an initial saturation and subsequently varied between 30% and 40% of the duty cycle. Thus, Table 1 shows the results for rise time, settling time, and *overshoot*, while Table 2 shows the performance indices of the controllers. Consequently, it can be seen that both controllers have similar characteristics, and the variations in values are due to environmental disturbances themselves.

Figure 10. Control signal from the GMV controller and signal from the PI controller tuned via GMV with a first-order filter without filament formation

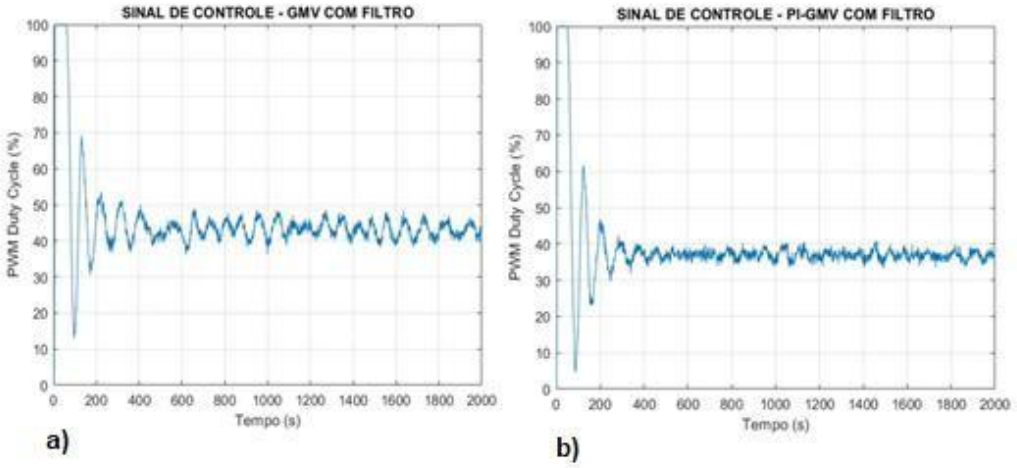

Source: Author (2024)

Table 1. Characteristics of the thermal process control without PE filament formation

Controller	Rise time	Time settling settling	Overshoot
GMV	1 min and 2 s	1 min and 6 s	26 °C
PI via GMV	55 s	59 s	24 °C

Source: Authors

Table 2. Performance indices of controllers without PET filament production

Controller	IAE	TVC
GMV	12182	5.2906×10^3
IP via GMV	9.9059×10^3	5.3039×10^3

Source: Authors

The second temperature test was conducted at 250 °C, involving the production of PET filament and the collection of 2,000 samples over approximately 33 minutes. Figure 11a shows the behavior of the GMV controller with a first-order filter, while Figure 11b presents the PI controller via GMV. Figures 12a and 12b, meanwhile, illustrate the control signal applied by both controllers, respectively. The results indicate that both maintained the setpoint and rejected disturbances from the manufacturing process and the environment, as the thermal process exchanges heat with the filament and the surrounding medium. It is also observed that the PWM signal of the GMV controller exhibited initial saturation and oscillations at the beginning and end of manufacturing, with a variation between 50% and 60% in the duty cycle. From another perspective, the PWM control signal of the PI controller via GMV also underwent an initial saturation, oscillation in the control signal when PET filament production begins and ends, in which a variation of between 40 and 50% of the duty cycle is observed during this process

Figure 11. Temperature control at 250 °C of the GMV controller and the PI controller tuned via GMV with a first-order filter during filament production

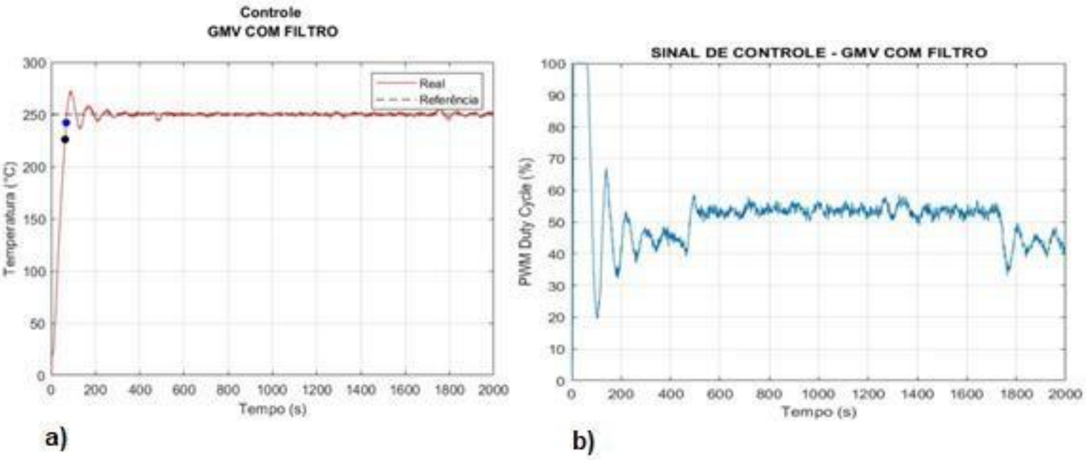

Source: Author (2024)

Thus, Table 3 shows the performance indices of the controllers, while Table 4 presents the results for rise time, settling time, and *overshoot*. It can be seen that both controllers took approximately 20 minutes to manufacture the filament, in addition to having similar characteristics, and the variations in values are due to environmental disturbances.

Figure 12. Control signal from the GMV controller and signal from the PI controller tuned via GMV with a first-order filter using filament fabrication,

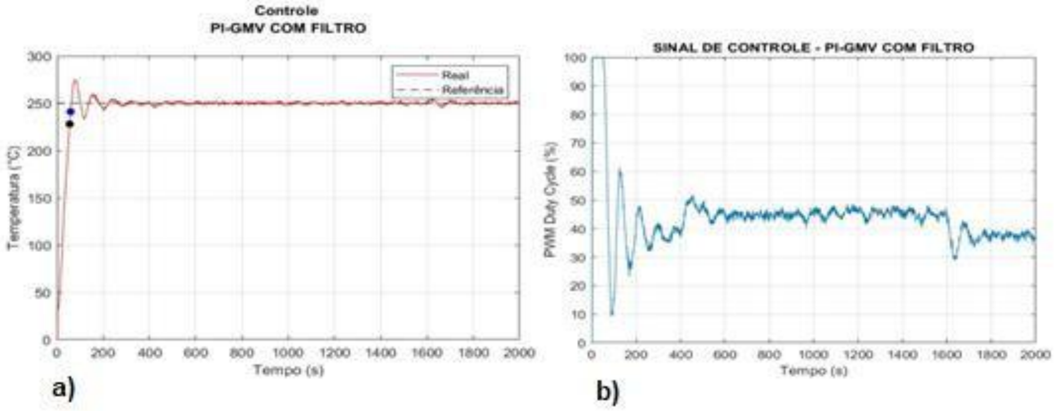

Source: Author (2024)

Table 3. Performance indices of controllers with PET filament manufacturing

Controller	IAE	TVC
GMV	12014	5.2682×10^3
PI via GMV	1.0452×10^4	4.9827×10^3

Source: Authors

Table 4. Characteristics of thermal process control in PET filament manufacturing

Controller	Rise time	Settling time	*Overshoot*
GMV	1 min and 3 s	1 min and 8 s	25 °C
PI via GMV	57 s	1 min and 1 s	23 °C

Source: Authors

4.2 PET FILAMENT

After several PET filament production tests, it was noted that the optimal settings for the PET Bottle Filament Machine to produce filament are: extruder temperature 250 °C and 20% of the maximum speed of the take-up motor, which is approximately 2100 RPM; thus, under these parameters, a strong filament with uniform fill was obtained (Figure 13a).

For the filament tests, the 3D models recommended by 3D Fila were used. The models tested were the Temperature Calibration Tower and *Benchy*. In the PET filament production process, 2-liter PET bottles were used, with an average yield of 5.8 m of filament strand and 6 m of filament. In addition, the *Creality* CR 10 *Smart* PRO 3D printer, shown in Figure 13b, was used, along with the *Creality Slicer* to adjust the parameters of the 3D print model.

Figure 13. PET filament and *Creality* CR 10 *Smart PRO* 3D printer

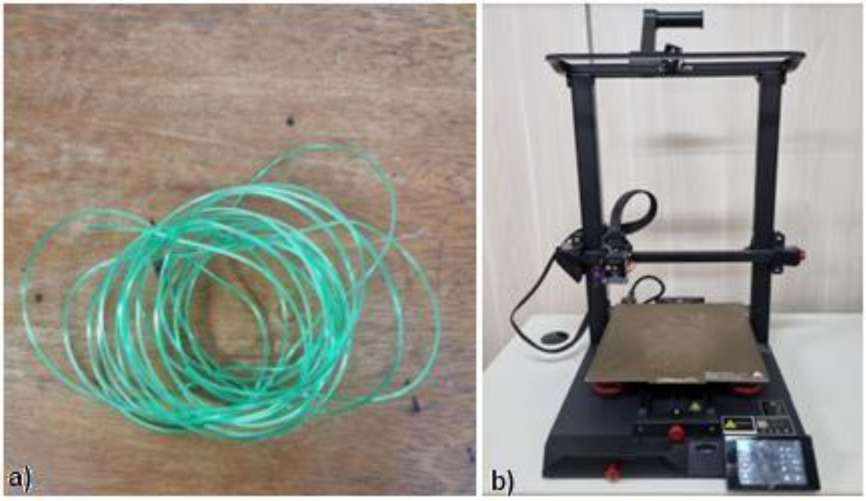

Source: Author (2024)

4.3 TEMPERATURE CALIBRATION TOWER

The following parameters were used for printing: a bed temperature of 70 °C and a print speed of 100%. The tests were conducted using filaments derived from transparent and green PET bottles. When analyzing the prints of the Temperature Calibration Tower using filaments from the transparent and green bottles, as shown in Figures 14a and 14b, respectively, it was observed that the minimum printing temperature required to achieve good results was 250 °C. Additionally, the prints exhibited a low level of *stringing.*

Benchy is a 3D model created by *Creative Tools*, widely used to test 3D printer configurations and filaments. This model poses a challenge for many printers, as it was designed to be printed without the need for support materials. Furthermore, it allows for the evaluation of aspects such as surface quality, print accuracy, and warping.

Figure 14. Printout of the Temperature Calibration Tower for transparent and green PET filament

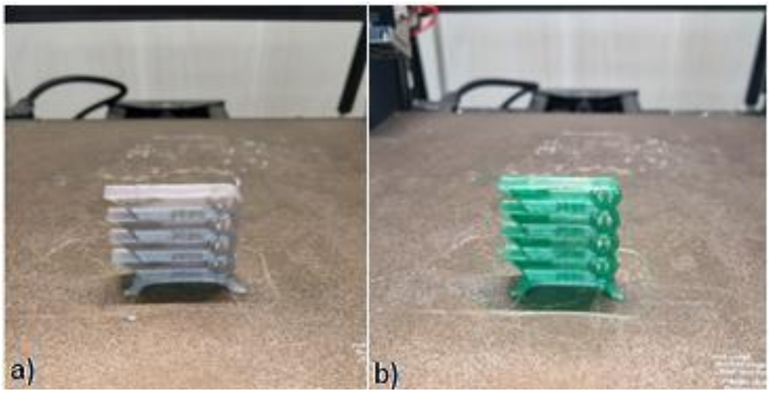

Source: Author (2024)

The following parameters were used for printing: bed temperature at 70 °C, print temperature at 255 °C, and print speed at 100%. Upon analyzing the print of the *Benchy* model, shown in Figure 15. Here, it can be observed that the model’s hull has a curved, wide, and smooth surface, while the print remained well-symmetrical. The smooth, circular surfaces, as well as the reliefs and the fishing rod holder, were printed with high precision. Furthermore, the letters at the bottom of the print showed no defects in the first layer, remaining legible.

Figure 15. Print of the *Benchy* model using PET filament

Source: Author (2024)

5. CONCLUSION

The design of the PET Bottle Filament Machine for 3D printing has led to significant advancements in areas such as engineering control, identification of linear systems, classical PID control, advanced GMV control, as well as controller tuning and electronic circuits. It also facilitated the development of skills in 3D modeling and 3D printing.

The GMV controller demonstrated effectiveness in achieving the established objectives, such as precise reference tracking, disturbance rejection, and the maintenance of a reduced control effort. However, to ensure optimal controller performance, it was necessary to implement a first-order filter, since temperature control is susceptible to environmental interference. On the other hand, the PID controller, tuned using the GMV technique, successfully incorporated the qualities of advanced control in a satisfactory manner.

In addition, the machine developed proved to be efficient in the production of high-quality PET filament, demonstrating the effectiveness of the system as a whole.

ACKNOWLEDGMENTS

The authors thank CNPq and PROPPG at IFPA for providing support for this research.

REFERENCES

ARAÚJO, R. d. B. Filtered predictive controllers using multi-objective optimization to ensure offset-free performance and robustness. 2017.

ÅSTRÖM, K.; WITTENMARK, B. **Adaptive Control**. Dover Publications, 2008. (Dover Books on Electrical Engineering). ISBN 9780486462783.

COELHO, A.; JERONYMO, D.; ARAUJO, R. **Classical and Discrete Predictive Control of Dynamic Systems**. UFSC Press, 2019.

COELHO, A. A. R.; COELHO, L. dos S. **Identification of Linear Dynamic Systems**. [No place]: UFSC, 2016.

DORF, R. C.; BISHOP, R. H. **Modern Control Systems**. 12th ed. Rio de Janeiro: LTC, 2012.

JÚNIOR, N. D. S. **Development of a teaching setup for a horizontal angular positioning control system for a model aircraft using Arduino and a graphical interface in Python, applying advanced control techniques**. 2024. Undergraduate Thesis - Institute of Technology, Federal University of Pará, Belém, PA, 2024.

SILVEIRA, A. da S. **Contributions to generalized minimum variance control: A state-space design approach**. 2012. Thesis (Ph.D. in Electrical Engineering) – Federal University of Santa Catarina, Florianópolis, SC, 2012.

CHAPTER 5

STRUCTURAL ANALYSIS OF A METAL SILO USING PLATE THEORY WITH THE ANSYS COMPUTATIONAL METHOD

Abel Costa Alves
Bachelor of Science in Civil Engineering
Universidade Federal do Oeste da Bahia (UFOB)
E-mail: abel.a3468@ufob.edu.br

Kuelson Randello Dantas Maciel
PhD in Energy and the Environment
Universidade Federal da Bahia (UFBA)
E-mail: kuelson.maciel@ufob.edu.br

Pedro Cláudio dos Santos Vieira
PhD in Structural Engineering and Civil Engineering
Universidade de Brasília (UNB)
E-mail: pedro.vieira@ufob.edu.br

Pedro Paulo Martins de Carvalho
PhD in Structural Engineering and Civil Engineering
Universidade de Brasília (UNB)
E-mail: pedro.carvalho@ufob.edu.br

Georgeano Dantas Maciel
Master's Degree in Production Engineering
Universidade Federal do Amazonas (UFAM)
E-mail: georgeano.maciel@gmail.com

ABSTRACT: Os silos metálicos são estruturas essenciais para o armazenamento de grãos no agronegócio, especialmente em regiões de alta produtividade como o Oeste da Bahia. A segurança e a eficiência dessas estruturas dependem de um dimensionamento preciso, que considere as complexas tensões geradas pelos grãos armazenados e pelas ações externas. O objetivo principal dessa pesquisa foi analisar as tensões resultantes no corpo do silo utilizando a teoria das placas por meio do Método de Elementos Finitos (MEF) no software ANSYS. Para isso, foi desenvolvido um modelo computacional do silo, aplicando-se as cargas de acordo com a teoria de Janssen e as normas técnicas vigentes. Os resultados da simulação numérica demonstraram que a tensão máxima equivalente de von Mises (366,91 MPa) concentrou-se na base dos montantes, permanecendo abaixo da resistência de cálculo do aço (436,36 MPa), o que válida a segurança da estrutura no Estado Limite Último (ELU). A deformação máxima de 11,32 mm mostrou-se compatível com os limites de serviço normativos. A análise confirmou o papel crucial dos montantes na absorção e distribuição das tensões, reduzindo a solicitação nas chapas de vedação. Conclui-se que o método computacional é uma ferramenta eficaz para a verificação estrutural de silos por meio das tensões e deslocamento, fornecendo subsídios para um dimensionamento mais otimizado e seguro, o que resulta em estruturas mais eficientes e econômicas.

KEYWORDS: silos, ANSYS, chapas metálicas, teoria das placas.

RESUMO: Metal silos are essential structures for grain storage in agribusiness, especially in high-productivity regions like Western Bahia. The safety and efficiency of these structures depend on accurate sizing that considers the complex stresses gener- ated by the stored grain and external factors. The main objective of this research was to analyze the resulting stresses in the silo body using plate theory and the Finite Element Method (FEM) in ANSYS software. To this end, a computational model of the silo was developed, applying loads in accordance with Janssen's theory and current technical standards. The numerical simulation results demon- strated that the maximum equivalent von Mises stress (366.91 MPa) was con- centrated at the base of the uprights, remaining below the steel design strength (436.36 MPa), validating the structure's safety in the Ultimate Limit State (ULS). The maximum deformation of 11.32 mm was compatible with the normative ser- vice limits. The analysis confirmed the crucial role of the uprights in absorbing and distributing stresses, reducing the load on the sealing plates. It is concluded that the computational method is an effective tool for structural verification of silos through stress and displacement, providing support for more optimized and safer design, resulting in more efficient and economical structures.

PALAVRAS-CHAVE: silos, ANSYS, metal sheets, plate theory.

1. INTRODUCTION

Brazilian agribusiness accounts for a significant portion of the national economy. According to the Center for Advanced Studies in Applied Economics (CEPEA, 2025), the sector accounts for 29.4% of the Gross Domestic Product (GDP), totaling R$ 3.78 trillion. This continuous growth has driven demand for grain storage and processing facilities, making storage a strategic element in the production chain by acting as a link between production and distribution.

Despite the growth in agricultural production, storage capacity in Brazil has not kept pace with this progress, leading to recurring deficits with each harvest (CNA, 2023). In western Bahia, a large portion of the harvest is sent to mills in other regions. The installation of Moinho Centro Norte in Luís Eduardo Magalhães, with four silos totaling 2,000 tons, should allow about one-third of the production to remain locally (AIBA, 2023).

Grain storage can be carried out in different types of structures, such as metal silos, concrete silos, and grain warehouses.

Among these options, metal silos stand out as an efficient and widely adopted alternative in the sector (Nascimento *et al*., 2009; Gandia *et al*., 2021).

Brazil, due to its continental size and favorable climate, stands out for its high agricultural potential. For the year 2025, grain production is estimated at 350.2 million tons, representing a 16.3% increase (equivalent to 49.1 million tons) compared to the 2024 harvest (CONAB, 2025).

According to the Brazilian Institute of Geography and Statistics (IBGE, 2024), in the first half of 2024, the available capacity for agricultural storage in the country reached 222.3 million tons, marking a 5.4% increase compared to the previous half of 2023. With regard to usable storage capacity, silos continue to predominate, totaling 117.5 million tons—equivalent to 52.9% of the national usable capacity. Compared to the second half of 2023, silos showed a 6.8% increase in capacity.

In western Bahia, metal silos are widely used, constituting standardized structures that are essential for the logistics and preservation of agricultural production. Given the importance of these structures, this research aims to contribute to the improvement of structural calculations for silos, focusing on the analysis of stresses acting on their cylindrical body (Fank, 2017).

The design of silos involves two complementary approaches: structural analysis and material flow analysis. The first aims to ensure that the structure withstands the applied forces, while adhering to ultimate and service limit states. The second seeks to optimize the geometry and discharge conditions, ensuring the fluidity of the material and preventing obstructions (Madrona, 2008).

The design of metal silos must comply with the guidelines of standard NBR 17066 – Corrugated sheet metal silos — Methods for predicting pressures exerted by free-flowing plant grains and basic requirements for design (ABNT, 2022), based on established international standards such as ANSI/ASAE S433.1 (ANSI, 2019), ISO 11697 (ISO, 1995),

EN 1991-4 (EN, 2006), and NBR 14762 (ABNT, 2010), particularly regarding the calculation of structural connections.

In recent decades, the Finite Element Method (FEM) has established itself as an effective approach for analyzing the structural behavior of silos and the stored material. Its versatility and ability to adapt to different operating conditions make it an economically viable and technically accurate tool for evaluating stresses in steel structures (Kobyłka and Molenda, 2014; Gallego, Ruiz, and Aguado, 2015; ZHU *et al*., 2023).

MEF allows for the modeling of complex geometries and the consideration of multiple physical parameters, making it capable of representing phenomena that cannot be adequately addressed by conventional theories (Jayachandran; Nitin; Rao, 2019). Several studies have investigated the internal pressures exerted by grains on silo walls, using finite element-based numerical simulations with different plasticity models, boundary conditions, and contact parameters (Amorós *et al*., 2002; Vidal, Guaita, and Ayuga, 2005; GOODEY, BROWN, and ROTTER, 2017; Matchett, 2020; Patel and Kute, 2021).

Compared to laboratory tests, numerical simulations offer greater flexibility and the ability to explore complex scenarios. Advances in engineering software and high- -performance computing methods have made it possible to process large volumes of data and analyze particle interactions using the Discrete Element Method (Kobyłka; Molenda, 2014; Gallego; Ruiz; Aguado, 2015; ZHU *et al*., 2023), expanding the possibilities for investigating granular behavior. Scalabrin (2008) performed an additional structural verification using the plate method to validate the adopted sizing. Gallego, Ruiz, and Aguado (2015), in turn, used FEM-based ANSYS software to compare simulated internal pressures with experimental data, demonstrating the reliability of the approach.

Patel and Kute (2021) conducted a detailed investigation of normal and vertical pressures, arch stresses, and longitudinal stresses in ferrocement silos, using the Drucker-Prager model and taking into account the elastoplastic behavior of the stored materials. The modeling was conducted using finite element (FE) simulations in ANSYS 15 software, whose results showed good agreement with classical analytical solutions. With vertical pressures ranging from 2.618 kPa to 105.94 kPa at the base of the silo, the arch stresses obtained fell within the limits predicted by the Janssen equation, being directly influenced by the friction coefficient. Furthermore, the analysis of silos with a capacity of 600 m^3 and an H/D ratio between 1 and 7 revealed consistency between the numerical results and the analytical models, reinforcing the reliability of the computational approach adopted.

This study aims to correlate different stress calculation methodologies, with an emphasis on the application of the Finite Element Method as an effective tool for evaluating variations resulting from different load combinations. FEM stands out not only for its precision in identifying internal stresses but also for enabling an in-depth analysis of structural behavior, combining technical robustness with an excellent cost-benefit ratio—a fundamental aspect for the safe and efficient design of metal silos. The results obtained aim to provide insights for the development of more reliable and durable designs, directly contributing to the safety of metal structures used in grain storage.

2. MATERIALS AND METHODS

The research began with the development of a silo model representative of the structures used in western Bahia, in partnership with Kepler Weber, which provided the silo and the necessary technical data. The practical application took place at Fazenda Boiadeiro, in Luís Eduardo Magalhães (BA), where internal stresses in the metal plates were analyzed using Plate Theory, with computational modeling performed in ANSYS software. The model’s properties are detailed in Table 1, and its schematic representation is shown in Figure 1.

Table 1. Characteristics of the 6024 model (Kepler Weber)

Model	Ring	Volume (m³)	Tons of Soybeans (t)	Height (m)	Nominal Diameter (m)	Uprights
60	24	6,139	4,881	27.27	18,189	40

Source: Kepler Weber (2024)

Figure 1. Side view and top view of the Kepler Weber metal silos at Fazenda Boiadeiro.

Source: Prepared by the authors (2025)

2.1 SILO DESIGN

The uprights and plates of the metal silo were manufactured from ARC 600 steel, which offers high structural strength and durability. With a yield strength of 480 MPa and a Z350 zinc coating (350 g/m², 99% pure), the material ensures excellent corrosion protection and is suitable for harsh environments.

Table 2. Physical properties of ARC 600 steel

Property	Value	Unit
Yield Strength (fy)	480	MPa
Tensile Strength (ft)	600	MPa
Elongation	≥ 10	%
Density	7.85	g/cm³
Modulus of Elasticity	~200	GPa
Thermal Conductivity	~50	W/m·K

Source: Kepler Weber (2025)

A computational model was developed to represent the metal silo, taking into account its dimensions and structural characteristics. The modeling will be performed using SpaceClaim software, which is compatible with ANSYS, including elements such as corrugated sheets, uprights, reinforcement rings, and thickness variations along the height, as shown in Table 3.

Table 3. Structural characteristics of metal silo 6024

No. of Uprights (UND)	40	
No. of Sheets per Ring (UND)	20	
Number of Rings and their respective side thicknesses (UND)	3	0.95 mm
	3	1.25 mm
	2	1.55 mm
	3	1.95 mm
	4	2.3 mm
	5	2.7 mm
	4	3 mm
Sheet thickness (mm)	914.4	
Reinforcement Ring No. (UND)	3	

Source: Kepler Weber (2025)

The support and loading conditions for the silo were defined by simulating the actual operating scenario. The base of the silo will be considered fixed, representing its attachment to the ground (concrete foundation), while the top will be considered free, allowing for deformation under load.

2.2 CHARACTERIZATION OF THE GRAIN AND ACTING LOADS

The static pressures were determined based on Janssen's theory, considering the silo's geometry and the physical properties of the stored grain. Figure 2 shows the distribution of pressures along the height of the silo, highlighting the effects of lateral friction on the walls.

Figure 2. Conceptualization of pressure application in the model silo.

Source: Prepared by the authors (2025)

In the structural analysis of the silo, soybeans were used as the reference material, considering their physical properties that affect internal pressures. The applied loads, such as self-weight and wind, are detailed in Table 4.

Table 4. Coefficients, combinations, and load parameters

Parameter	Value	Symbol	Unit
Specific weight of grain	8.0	γ	kN/m³
Silo height	22.0	h	m
Lateral pressure coefficient	0.5	K	-
Coefficient of friction	0.4	μ	-
Wind speed	40.0	Vk	m/s
Silo diameter	18.0	r	m
Sheet thickness	3.0	t	mm
Weighting factor (G)	1.35	FG	-
Weighting factor (Q)	1.35	FQ	-
Weighting factor (Wind)	1.50	FV	-
Self-weight	99.5		kN

Source: Prepared by the authors (2025)

2.3 PLATE THEORY METHOD

The stresses in the silo walls were calculated based on the static pressures from Janssen's theory, using the equations of cylindrical shell theory. Circumferential and longitudinal stresses, which are essential for structural stability, were considered in accordance with the parameters provided by Ugural (2010) in Equation 02.

$$N_\theta = -\frac{Etw}{a} = \gamma a h \left[1 - \frac{x}{h} - f_4(\beta x) - \left(1 - \frac{1}{\beta h}\right) f_2(\beta x)\right] \quad (1)$$

$$M_x = -D\frac{d^2 w}{dx^2} = \frac{2\beta^2 \gamma a^2 D h}{Et}\left[-f_2(\beta x) + \left(1 - \frac{1}{\beta h}\right) f_4(\beta x)\right] \quad (2)$$

$$M_\theta = vM_x \quad (3)$$

2.3.1 Computational method—finite element method (ANSYS)

The stress analysis was performed using ANSYS Workbench software, a multiphysics simulation platform that integrates various analysis tools into a unified environment (Figure 3).

Figure 3. Initial Ansys Workbench interface

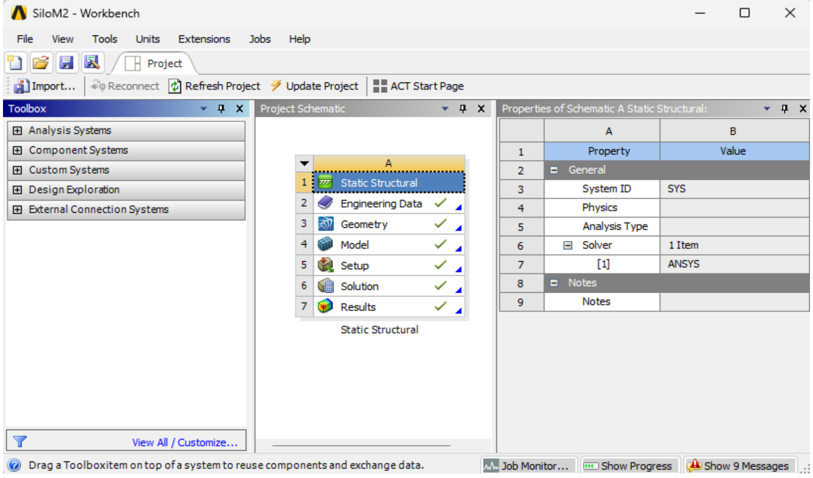

	A	B
1	Property	Value
2	General	
3	System ID	SYS
4	Physics	
5	Analysis Type	
6	Solver	1 Item
7	[1]	ANSYS
8	Notes	
9	Notes	

Drag a Toolbox item on top of a system to reuse components and exchange data.

Source: Prepared by the authors (2025)

The initial parameters for characterizing the materials used in the analysis systems were defined, with particular emphasis on the models and properties relevant to the metal silo (Figure 4). Based on their structural characteristics, the silo components were computationally represented using the SHELL209 finite element (Figure 5).

Figure 4. Engineering Data stage in Ansys and characteristics of SHELL209 in Ansys.

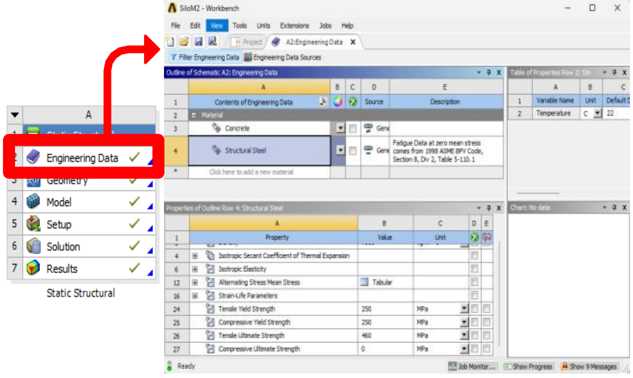

	A	B	C	D	E
1	Contents of Engineering Data			Source	Description
2	Material				
3	Concrete		☐	Gene	
4	Structural Steel		☐	Gene	Fatigue Data at zero mean stress comes from 1998 ASME BPV Code, Section 8, Div 2, Table 5-110.1
*	Click here to add a new material				

	A	B	C
1	Variable Name	Unit	Default C
2	Temperature	C	22

	A	B	C	D	E
1	Property	Value	Unit		
4	Isotropic Secant Coefficient of Thermal Expansion			☐	
6	Isotropic Elasticity			☐	
12	Alternating Stress Mean Stress	Tabular		☐	
16	Strain-Life Parameters			☐	
24	Tensile Yield Strength	250	MPa	☐	☐
25	Compressive Yield Strength	250	MPa	☐	☐
26	Tensile Ultimate Strength	460	MPa	☐	☐
27	Compressive Ultimate Strength	0	MPa	☐	☐

Source: Prepared by the authors (2025)

Figure 5. Characteristics of SHELL209 in Ansys

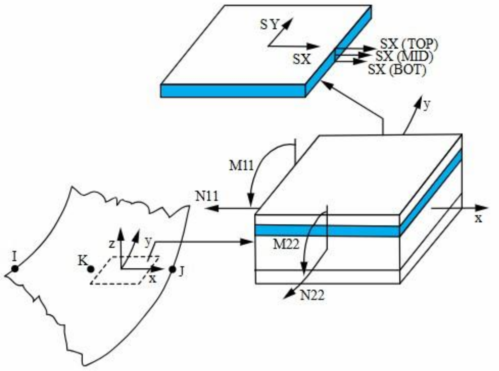

Source: AnsysHelp (2025)

Figures 6 and 7 show the silo model imported from Ansys.

Figure 6. Silo geometry in Ansys

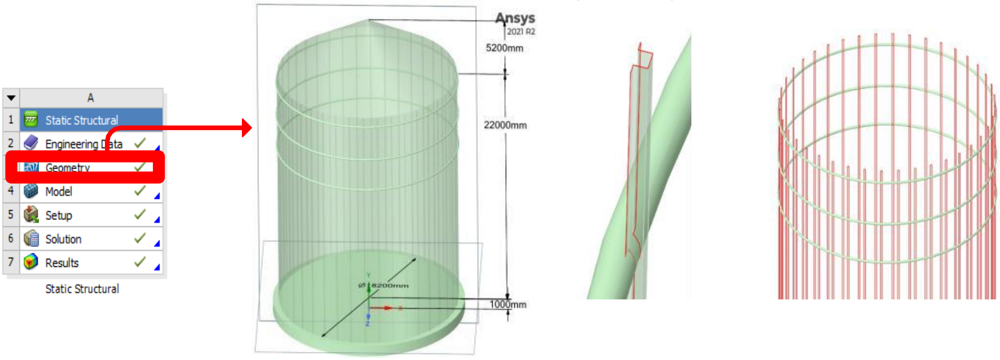

Source: Prepared by the authors (2025)

The silo geometry was discretized into finite elements to enable a detailed structural analysis. The mesh density was adjusted to strike a balance between accuracy and computational efficiency (Figure 7).

Figure 7. Mesh for the silo model in Ansys

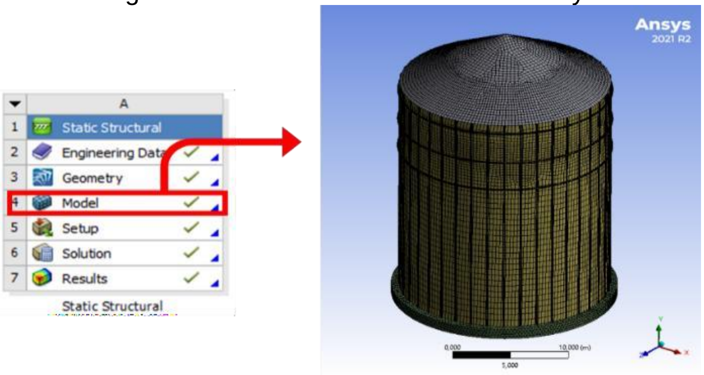

Source: Prepared by the authors (2025)

The applied loads, such as self-weight, grain pressure, and wind, were applied to the model, along with the boundary conditions: fixed base and free top (Figure 8).

Figure 8. Boundary conditions of the silo in Ansys

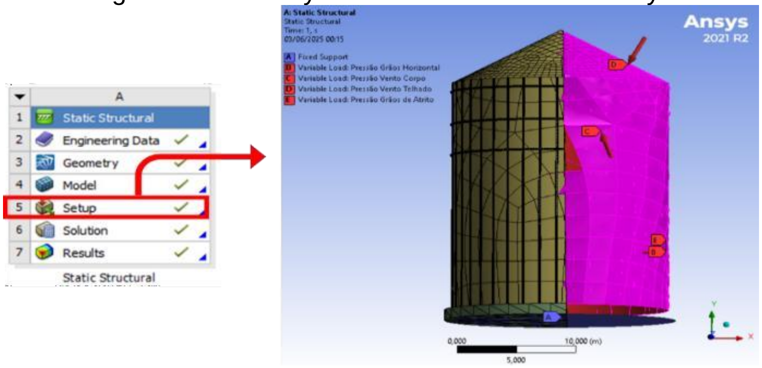

Source: Prepared by the authors (2025)

The loads will be applied as shown in Figures 9a—horizontal pressures—and Figure 9b—wind pressure.

Figure 9. Horizontal pressure applied to the silo walls (a) and wind pressure (b)

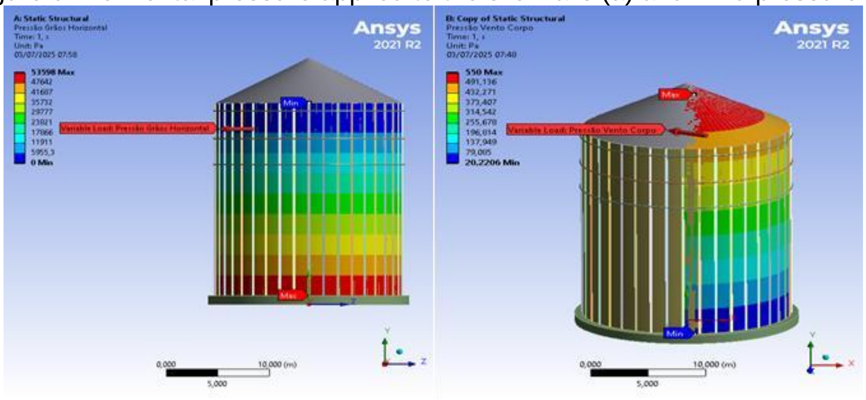

(a) (b)

Source: Prepared by the authors (2025)

The stress results obtained in ANSYS will be compared to the strength of the steel to verify structural compliance. The analysis will consider different combinations of load, accuracy, complexity, and processing time, aiming at practical implications for the design of metal silos with a focus on safety and efficiency.

3. ANALYSIS AND INTERPRETATION OF RESULTS

3.1 SILO MODELING AND APPLIED LOADS

The simplified model (6024), with homogeneous metal plates of constant thickness, was used to evaluate the structural behavior of the silo under wind and grain loads, as illustrated in Figure 10.

Figure 10. Dimensions of silo 6024 modeled in Ansys

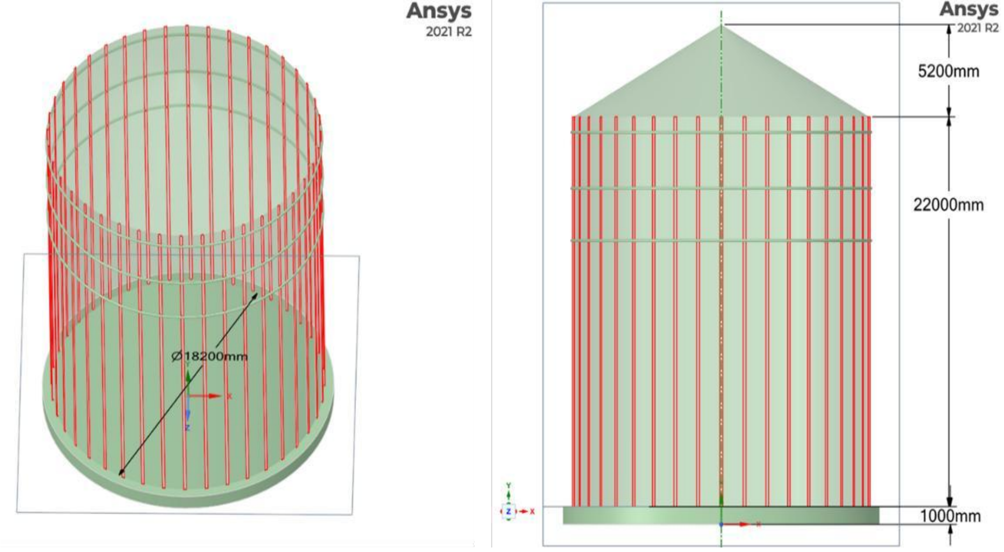

Source: Prepared by the authors (2025)

The grain pressure was calculated and validated according to technical standards and Janssen's theory, representing the main structural load on the silo. Its distribution across the walls, generated by the stored soybeans, was obtained through an analytical solution, as illustrated in Figure 11.

Figure 11. Curve of silo height versus grain pressures.

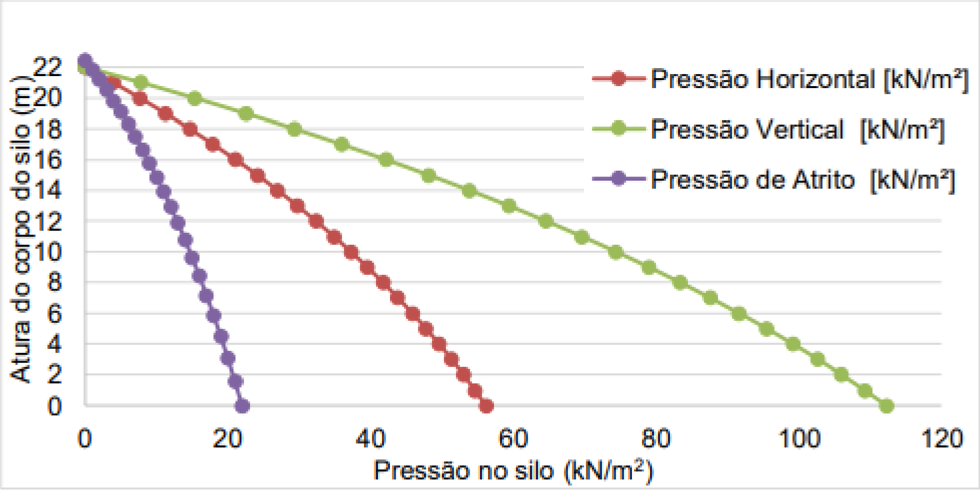

Source: Prepared by the authors (2025)

The nonlinear behavior of internal pressures in the silo is described by Janssen's Theory (1895), which accounts for the arching effect of the grains, which transfer part of their weight to the walls through friction. As a result, the vertical pressure at the base is reduced (≈114 kN/m²), while the horizontal pressure—essential for sizing—reaches 55 kN/m², and the friction pressure, responsible for axial stresses, reaches 25 kN/m². These profiles are applied to the geometric model to ensure realism in the structural analysis. Figure 12 shows the static wind pressure, which increases with height, reaching up to 0.48 kN/m² at the top.

Figure 12. Silo height based on wind pressure applied to the silo

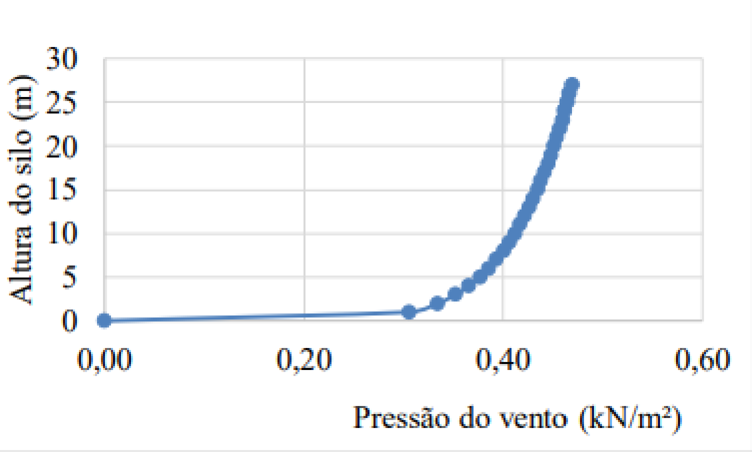

Source: Prepared by the authors (2025)

Despite the low wind pressure at the base, its action along the height of the silo generates maximum bending and shear stresses in the foundation, determining the design of the anchorage at the concrete base. To evaluate the most critical conditions, static simulations were performed at the Ultimate Limit State (ULS). The load from the stored material and the wind pressure were applied simultaneously, with permanent action weighting coefficients for the grains of γ_g = 1.35 and a variable action weighting coefficient of γ_q = 1.50 for the wind, in accordance with structural safety standards. This approach allows for the identification of maximum stresses and displacements, the results of which will be presented in the following sections.

3.2 RESULT OF THE RESULTANT DISPLACEMENT

The analysis of metal silos, classified as shell structures, presents challenges due to their high slenderness ratio. Simulations in ANSYS (Figure 13) reveal a higher concentration of stresses at the base, where the uprights are crucial for structural strength. At the top, the reinforcement rings help prevent buckling, contributing to the overall stability of the silo.

Figure 13. Resultant deformation diagram of the complete silo

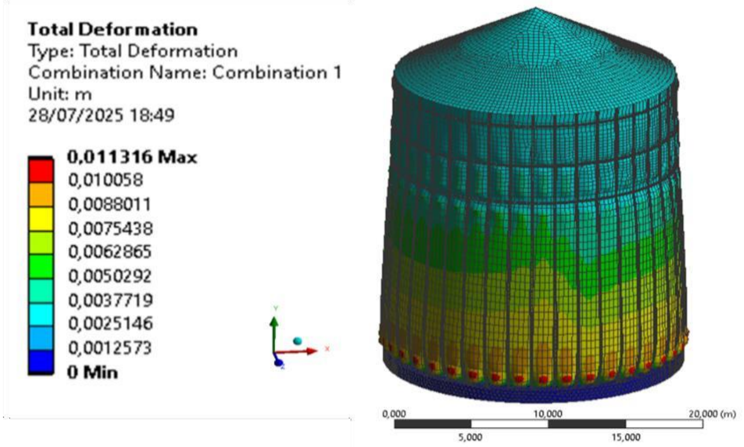

Source: Prepared by the authors (2025)

The numerical simulation indicated a maximum deformation of 11.32 mm, equivalent to 1/1590 of the silo’s diameter (18,000 mm), which is within the acceptable limits according to EN 1993-1-6:2007. Figure 14 highlights the role of stiffeners (rings and uprights) in containing critical deformations, such as ovalization and wrinkling, promoting elastic and controlled structural behavior.

Figure 14. Diagram of the resulting deformation in the rings and roof

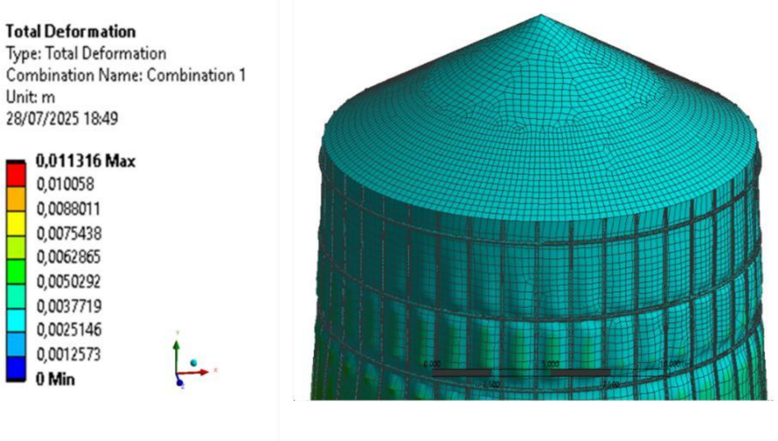

Source: Prepared by the authors (2025)

3.3 RESULTS OF RESULTANT VON MISES STRESSES

Figure 15 shows the distribution of equivalent von Mises stresses (σ_v), used to evaluate the onset of yielding in ductile materials such as steel. This scalar parameter results from the combination of normal and shear stresses, allowing for direct comparison with the material's strength. In the silo, the stresses were generated by the combination of self-weight, grain pressure, and wind action.

Figure 15. Resultant stress diagram for the complete silo

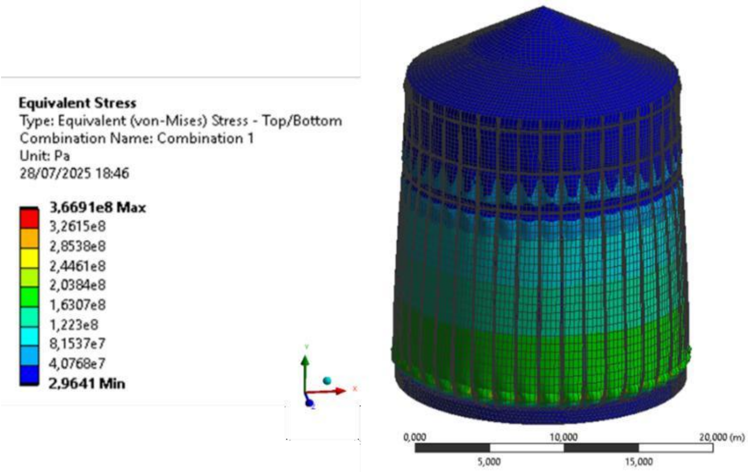

Source: Prepared by the authors (2025)

The stress diagram reveals complex structural behavior, with moderate stresses predominating at the base of the silo, except in the regions where the plates meet the uprights, where there is a critical concentration of stresses. As shown in Figure 15, this area reaches a maximum stress of $\sigma_{v\_max} = 366.91$ MPa, associated with wrinkling patterns typical of local buckling under axial compression.

Figures 16 and 17 show that the studs absorb most of the stresses in the plate-stud system. The plate acts as a diaphragm, distributing the loads to the studs, which function as structural stiffeners, stabilizing the plate against buckling and directing the stresses to the supports.

Figure 16. Enlarged view of the base of the stress diagram for the silo

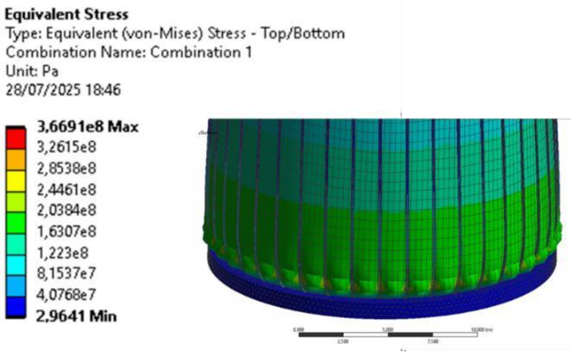

Source: Prepared by the authors (2025)

Figure 17. Close-up of the roof showing the resulting stress diagram for the silo

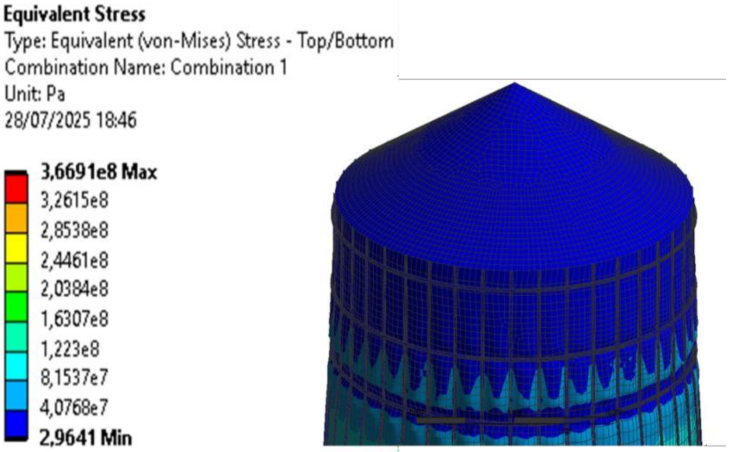

Source: Prepared by the authors (2025)

This behavior generates a non-uniform stress field with localized peaks. Therefore, the design of the uprights must ensure that their design strength $\sigma_{Rd,montante}$ is significantly greater than that of the plate $\sigma_{Rd,chapa}$, thereby preventing yielding or premature instability in the reinforcing elements.

For the ultimate limit state (ULS) safety check, ARC 600 steel was used, with a characteristic yield strength of f_{yk} = 400 MPa. According to NBR 8800 (ABNT 2024), the design yield strength is f_{yd} =436.36 MPa, considering the weighting coefficient γa1=1.10. The maximum stress obtained in the analysis, σ_{v_max} (366.91 MPa) < f_{yd} (436.36 MPa), is within the limit established by NBR 8800 (ABNT 2024), indicating compliance with the ULS and structural behavior in the elastic regime with localized plastic yielding.

Figure 18 shows the stress profile along the silo wall, highlighting lower stresses in the sealing plate compared to the uprights, which concentrate the structural forces.

Figure 18. Resultant stress along a path in the silo wall through the plates

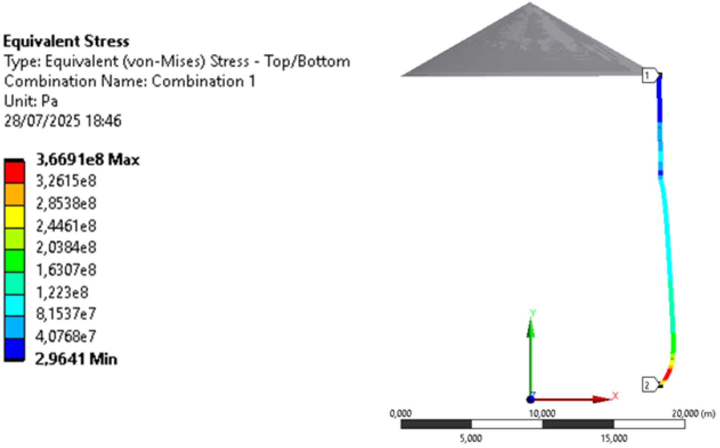

Source: Prepared by the authors (2025)

The results confirm the typical behavior of plate-stud systems, in which the studs, due to their greater stiffness and inertia, absorb and redirect stresses, thereby reducing the load on the plate. Throughout the height of the silo, the stresses in the sheet remained low, with a maximum value of 111 MPa, highlighting its function as a load-distributing diaphragm, while the studs bear the most intense stresses.

4. CONCLUSION

The study conducted a detailed structural analysis of the Kepler Weber metal silo, model 6024, evaluating stresses and displacements under grain and wind loads, based on Plate Theory and the Finite Element Method (FEM) using ANSYS.

The results demonstrated compliance with Ultimate Limit State (ULS) criteria, evidencing structural safety and elastic behavior of the structure. The maximum deformation of 11.316 mm (≈1/1590 of the diameter) is within the limits of standard EN 1993-1-6:2007.

The von Mises stress, with a peak of 366.91 MPa, remained below the design strength of ARC 600 steel. The columns acted as the primary stiffening elements, absorbing the critical stresses, while the plates functioned as diaphragms and load distributors . It is concluded that the design of the silo is safe for the analyzed static conditions, and that the use of FEM is an effective tool for the design and optimization of steel structures in the industrial sector.

It can therefore be concluded that the silo’s design is adequate for the static loading conditions analyzed. The simplified approach, based on membrane theory and combined with the application of the FEM, proved to be fundamental for an accurate, safe, and efficient evaluation of structural behavior, contributing to the improvement of metal silo designs in an industrial context.

ACKNOWLEDGMENTS

The Federal University of Western Bahia (UFOB) and the PROPGP/UFOB program for supporting the publication of scientific articles.

REFERENCES

AMERICAN SOCIETY OF AGRICULTURAL AND BIOLOGICAL ENGINEERS.

ANSI/ASAE S433.1: **Loads exerted by free-flowing grain on bins.** St. Joseph, MI: ASABE, 2019.

AMORÓS, J. L. *et al*. Projeto de Silos para o Armazenamento de Materiais na Forma de Pó. Problemas Associados à Etapa de Descarga. **Cerâmica Indus- trial**, v. 7, n. 1, p. 12–23, 2002.

ASSOCIAÇÃO BRASILEIRA DE NORMAS TÉCNICAS. **NBR 8800: Projeto de** estruturas de aço e de estruturas mistas de aço e concreto de edifícios. Rio de Janeiro – RJ, Brasil, 2008.

. **NBR 14762: Dimensionamento de estruturas de aço constituídas por perfis formados a frio**. Rio de Janeiro: ABNT, 2010.

. NBR 17066: Silos metálicos de chapas corrugadas — Métodos de previsão de pressões exercidas por grãos vegetais de fluxo livre e requi- sitos básicos para dimensionamento**. Rio de Janeiro: ABNT, 2022.**

ASSOCIAÇÃO DE AGRICULTORES E IRRIGADORES DA BAHIA – AIBA. O agro que sustenta. **Revista AIBA Rural.** Ed. 25, Ano IX, Luís Eduardo Maga- lhães, BA, 2023.

CENTRO DE ESTUDOS EM ECONOMIA APLICADA, CEPEA. **PIB do agronegócio registra crescimento de 6,49% no primeiro trimestre de 2025**. [s.l: s.n.]. https://www.cnabrasil.org.br/publicacoes/pib-do-agronegocio-registra-crescimento-de-6-49-no-primeiro-trimestre-de-2025. Acessado em 14 jul. 2025.

CONFEDERAÇÃO DA AGRICULTURA E PECUÁRIA DO BRASIL – CNA; CENTRO DE ESTUDOS EM ECONOMIA APLICADA – CEPEA. **PIB agronegócio CEPEA/CNA: PIB do agronegócio sofre queda no primeiro trimestre devido à pressão dos preços mais baixos.** Piracicaba – SP, 2023. Disponível em: https://www.cnabrasil.org.br/storage/arquivos/dtec.pib_agronegocio_mar_2024.9jul2024vf.pdf. Acesso em: 04 jul. 2024.

COMPANHIA NACIONAL DE ABASTECIMENTO-CONAB. **Acompanhamento Da Safra Brasileira,** Brasília, DF, v.12 – Safra 2024/25, n.12 - Décimo segundo levantamento, p. 1-237, 2025.

EUROPEAN COMMITTEE FOR STANDARDIZATION. **EN 1991-4: Eurocode 1 — Actions on structures — Part 4: Silos and tanks.** Brussels: CEN, 2006.

. EN 1993-1: Eurocode 3: Design of steel structures – Part 1-6: Strength and stability of shell structures**. Brussels: CEN, 2007.**

FANK, M. Z. **Pressões em silos verticais cilíndricos metálicos: determinação experimental e cálculos teóricos por normas estrangeira.** Tese (Doutorado em Engenharia Agrícola) – Universidade Federal de Campina Grande, Campina Grande – PB, 2017.

GALLEGO, E.; RUIZ, A.; AGUADO, P. J. Simulation of silo filling and discharge using ANSYS and comparison with experimental data. **Computers and Elec- tronics in Agriculture**, v. 118, p. 281–289, 2015.

GANDIA, R. M. *et al*. Static and dynamic pressure measurements of maize grain in silos under different conditions. **Biosystems Engineering**, v. 209, p. 180–199, 2021.

GOODEY, RJ; BROWN, CJ; ROTTER, JM Silos retangulares de aço: previsões de elementos finitos para pressões de preenchimento de paredes. **Engineering Structures** , v. 132, p. 61-69, 2017.

INTERNATIONAL ORGANIZATION FOR STANDARDIZATION. **ISO 11697: Bases for design of structures — Loads due to bulk materials**. Geneva: ISO, 1995.

INSTITUTO BRASILEIRO DE GEOGRAFIA E ESTATÍSTICA - IBGE. **Capacidade de armazenagem agrícola cresce 5,4% e chega a 222,3 milhões de toneladas no 1º semestre de 2024**. Agência de Notícias IBGE, 14 nov. 2024. Disponível em: Agência IBGE. Acessado em : 15 mar.2024.

JAYACHANDRAN, L. E.; NITIN, B.; RAO, P. S. Simulation of the stress regime during grain filling in bamboo reinforced concrete silo. **Journal of Stored Prod- ucts Research**, v. 83, p. 123–129, 2019.

KOBYŁKA, R.; MOLENDA, M. DEM simulations of loads on obstruction at- tached to the wall of a model grain silo and of flow disturbance around the ob- struction. **Powder Technology**, v. 256, p. 210–216, 2014.

MADRONA, F. S. **Pressões em silos esbeltos com descarga excêntrica.** Dissertação (Mestrado em Engenharia de Estruturas) – Universidade de São Paulo, São Carlos – SP, 2008.

MATCHETT, A. J. Exponential stress in silos — An example from literature. **Chemical Engineering Research and Design**, v. 161, n. 3, p. 125–129, 2020.

NASCIMENTO, J. W. B. DO *et al*. Blocos de concreto para construção modular de silos cilíndricos. **Revista Brasileira de Engenharia Agrícola e Ambiental**, v. 13, n. suppl, p. 991–998, 2009.

PATEL, C. P.; KUTE, S. Prediction of wall pressures and stresses developed by grainy materials in cylindrical ferrocement silo in static condition. **Asian Journal of Civil Engineering**, v. 22, n. 7, p. 1235–1248, 2021.

SCALABRIN, L. A. **Dimensionamento de silos metálicos para armazenamento de grãos**. Dissertação (Mestrado em Engenharia Civil) – Universidade Federal do Rio Grande do Sul, Porto Alegre – RS, 2008

UGURAL, A.C. **Stresses in beams, plates, and shells.** New York – USA: CRC Press, 2010

VIDAL, P.; GUAITA, M.; AYUGA, F. Analysis of dynamic discharge pressures in cylindrical slender silos with a flat bottom or with a hopper: Comparison with eu- rocode 1. **Biosystems Engineering**, v. 91, n. 3, p. 335–348, 2005.

ZHU, D. *et al*. Investigação numérica do padrão de fluxo de partículas e distribuição de pressão em bunker de carvão. **Journal of Geophysics and Engineering** , v. 20, n. 4, p. 841-853, 2023.

CHAPTER 6

MARANHAO 2045: FROM ORE EXPORTER TO GLOBAL PLAYER – THE VERTICAL INTEGRATION OF RARE EARTH MINERALS

Felipe de Oliveira Carvalho
Master in Environmental Sciences
Universidade Federal do Maranhão (UFMA)
E-mail: fc.engenharia.ma@gmail.com

Rakel Dourado de Oliveira Murad
Master in Law and Institutions of the Justice System
Universidade Federal do Maranhão (UFMA)
E-mail: rakeldourado@hotmail.com

ABSTRACT: The growing global demand for Rare Earth Elements (REEs), essential inputs for the energy transition, is marked by a high geopolitical concentration in the supply chain. In this context, Brazil seeks to position itself as an alternative supplier, facing the historical challenge of vertically integrating its mineral production. This article analyzes the prospective potential of the state of Maranhão to consolidate itself as an integrated industrial hub for rare earth elements (REEs), with a horizon up to 2045. The methodology was based on qualitative document analysis, triangulating data from geological reports, infrastructure and business plans, and national strategic studies. The results identify four main geological axes with potential for REE (Lower Itapecuru, Northwest, East/Southeast, and Southwest/South-Central), rich in minerals such as monazite and xenotime. More crucially, the existence of a mature logistical-industrial advantage is noted, composed of the triad of Itaqui Port, Carajás Railway, and the Bacabeira Export Processing Zone(EPZ), which enables local processing. It is concluded that the unique synergy between geological resources and existing logistical infrastructure offers Maranhão the conditions for the vertical integration of the production chain. The success of this vision, however, is contingent upon overcoming critical challenges, notably the technological mastery of oxide separation metallurgy and the rigorous management of radioactive waste (NORM/TENORM).

KEYWORDS: Rare Earths, strategic minerals, maranhão, regional development, industrial verticalization.

RESUMO: A crescente demanda global por Elementos de Terras Raras (ETR), insumos essenciais para a transição energética, é marcada por uma alta concentração geopolítica na cadeia de suprimentos. Nesse contexto, o Brasil busca se posicionar como um fornecedor alternativo, enfrentando o desafio histórico da integração vertical de sua produção mineral. Este artigo analisa o potencial prospectivo do estado do Maranhão para se consolidar como um polo industrial integrado de elementos de terras raras (ETR), com um horizonte até 2045. A metodologia baseou-se em análise documental qualitativa, triangulando dados de relatórios geológicos, planos de infraestrutura e negócios, e estudos estratégicos nacionais. Os resultados identificam quatro principais eixos geológicos com potencial para ETR (Baixo Itapecuru, Noroeste, Leste/Sudeste e Sudoeste/Centro-Sul), ricos em minerais como monazita e xenotima. Mais importante ainda, destaca-se a existência de uma vantagem logístico-industrial consolidada, composta pela tríade Porto de Itaqui, Ferrovia Carajás e Zona de Processamento de Exportação (ZPE) da Bacabeira, que viabiliza o processamento local. Conclui-se que a sinergia singular entre os recursos geológicos e a infraestrutura logística existente oferece ao Maranhão as condições para a integração vertical da cadeia produtiva. O sucesso dessa visão, contudo, está condicionado à superação de desafios críticos, notadamente o domínio tecnológico da metalurgia de separação de óxidos e a gestão rigorosa de resíduos radioativos (NORM/TENORM).

PALAVRAS-CHAVE: Terras Raras, minerais estratégicos, maranhão, desenvolvimento regional, verticalização industrial.

1. THE GLOBAL IMPERATIVE AND BRAZIL'S STRATEGIC POSITIONING

Rare Earth Elements occupy a central position in the contemporary economy due to their application in critical technologies, such as wind turbines, electric vehicles, catalysts, and advanced electronic systems. The high global dependence on Chinese production drives supply diversification strategies, opening up space for new production hubs. In this context, Brazil stands out as a relevant alternative, with the state of Maranhão standing out for its unique combination of geological potential and consolidated logistics infrastructure.

The objective of this study is to analyze the potential of Maranhão to structure an integrated REE hub by 2045, evaluating the feasibility of productive verticalization and its strategic insertion in the global critical minerals economy.

2. THE GEOPOLITICS OF VERTICALIZATION: THE DEFINITION AND CRITICALITY OF REES IN THE NEW ECONOMY

The concept of "strategic mineral" is dynamic and intrinsically linked to national objectives. The National Mining Plan 2030 (PNM-2030) adopts a three-pillar definition, perfectly framing Rare Earth Elements (REEs), a group of 17 chemical elements, as "bearers of the future." These elements are divided into "light" (LREE – Light Rare Earth Elements) and "heavy" (HREE – Heavy Rare Earth Elements). Their criticality stems from their irreplaceable physicochemical properties in cutting-edge applications. The main demand vector is Neodymium-Iron-Boron (NdFeB) permanent magnets, essential for the efficiency and miniaturization of wind turbine generators (especially offshore, using direct drive technology) and electric and hybrid vehicle motors. Other REEs, such as Lanthanum (La) and Cerium (Ce), are vital in catalysts, and Europium (Eu) and Yttrium (Y) in efficient lighting.

2.1 GEOPOLITICS AND VERTICAL INTEGRATION OF RARE EARTH ELEMENTS

The Rare Earth Elements (REE) market is characterized by a high level of geopolitical concentration, with China dominating more than 90% of global REE oxide production and approximately 75% of permanent magnet manufacturing. This dominance has prompted industrialized economies to seek diversification of supply chains through cooperative initiatives such as the Minerals Security Partnership (MSP). In this scenario, Brazil presents significant geological potential but remains historically constrained to the export of low-value mineral concentrates, a structural limitation associated with the lack of technological capacity in the stages of oxide separation and advanced metallurgy, where value addition is highest.

The overcoming of this bottleneck depends on the vertical integration of the production chain, and the state of Maranhão offers a differentiated institutional and logistical framework for this transition. The Bacabeira Export Processing Zone (EPZ) constitutes the central platform for upstream value addition, enabling the installation of facilities for the separation of rare earth oxides and subsequent industrial processing. Supported by a stable legal and regulatory regime—defined by federal legislation, customs control and fiscal incentives at both federal and regional levels—the EPZ provides predictability and cost efficiency for capital-intensive and technology-driven investments. This configuration positions Maranhão as a strategic hub capable of internalizing value and integrating Brazil into the global REE supply chain.

2.2 ATTRACTIVENESS AND LEGAL SECURITY OF THE ZPE REGIME

The Export Processing Zone (EPZ) regime provides a stable and predictable institutional environment, aligned with global competitiveness standards and particularly suited to industries of high technological complexity and capital intensity, such as Rare Earth Elements (REE) processing. The Bacabeira EPZ offers a set of tax, exchange rate and customs incentives that significantly reduce installation and operating costs, enhancing the economic feasibility of upstream value-added activities.

Key advantages include the suspension and exemption of federal taxes on machinery, equipment and inputs (Import Tax, IPI and PIS/COFINS), as well as the possibility of up to a 75% reduction in Corporate Income Tax through SUDENE incentives. Exchange rate freedom allows the retention of export revenues in foreign currency, mitigating volatility risks and increasing financial liquidity. In addition, the EPZ operates as a primary customs area, ensuring streamlined clearance procedures and objective governance, thereby providing the legal security required for long-term investments in strategic mineral sectors.

2.3 TECHNICAL LOCATION, SIZE AND INFRASTRUCTURE

The Bacabeira Export Processing Zone (EPZ) is a structured and strategically positioned solution for large-scale industries, combining logistical, territorial, and technical conditions that reduce costs and accelerate operations. Located in the municipality of Bacabeira, in a logistically coordinated area close to the capital São Luís, the EPZ is situated within a regional axis that facilitates integration with urban centers and industrial hubs. This location is crucial for optimizing the transport of raw materials and finished products, as well as enhancing connectivity with the Itaqui Port Complex and intermodal terminals, ensuring efficient distribution to the global market.

Figure 1. Location and road and rail networks

Source: Authors (2025).

Road access represents another significant advantage. The ZPE has a direct connection to the federal highways BR-135 and BR-402, as well as the state highway MA-110, ensuring efficient mobility for cargo and operational teams.

2.4 THE INTEGRATED MULTIMODAL LOGISTICS MATRIX

Investors in the ETR (Extractable Mineral Resources) sector demand a robust and continuous logistics chain. Maranhão offers an integrated multimodal solution that reduces operational risks and increases competitiveness. Inbound logistics are resolved through the direct integration of the Bacabeira Export Processing Zone (ZPE) with the Carajás Railway, essential infrastructure for receiving mineral concentrates from producing regions. Outbound logistics are guaranteed by the connection to the Port of Itaqui, a deep-water hub crucial for exporting ETR oxides to international markets. The strategic combination of the ZPE (tax/exchange incentives), the Railway (inputs), and the Port (global distribution) establishes Maranhão as a superior logistics hub for vertical integration of the supply chain.

Figure 2. Direct and indirect area of influence of the ZPE (EPZ)

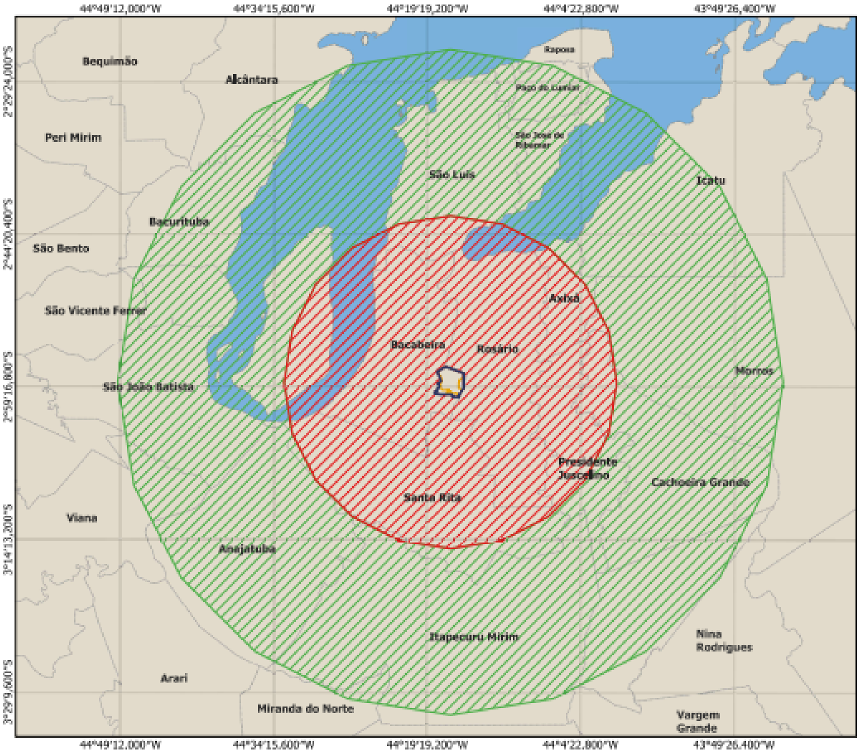

Source: Authors (2025).

Beyond logistical connectivity, there is a full guarantee of energy sustainability, an indispensable element for highly complex chemical and metallurgical operations. The project has access to the national interconnected system through existing transmission lines in the region, ensuring a stable high-voltage supply. This condition meets the technical requirements of the separation plant and is expressly aligned with the project's framework within the National Energy Policy, reinforcing security and long-term operational viability.

2.5 RISK MANAGEMENT, ENVIRONMENTAL COMPLIANCE AND INSTITUTIONAL STABILITY

The long-term viability of Rare Earth Elements (REE) processing projects depends on rigorous environmental risk management, particularly regarding waste generated during monazite beneficiation, which involves materials with radiological characteristics. Effective control and safe handling of residues classified as NORM and TENORM constitute one of the most critical operational challenges, requiring robust engineering solutions, continuous monitoring and strict compliance with national and international regulatory standards to ensure environmental and operational safety.

In this context, the Bacabeira Export Processing Zone (EPZ) provides a stable and predictable institutional framework for capital-intensive and long-maturity investments. Anchored in a permanent federal legal regime, the EPZ ensures regulatory continuity, standardized governance and administrative coordination, reducing institutional risk. The alignment with ESG principles further strengthens project viability by integrating environmental control, energy efficiency and low-carbon energy sources, including renewable generation and natural gas as a transition fuel. This combination of environmental rigor and institutional stability enhances investor confidence and supports the sustainable development of a vertically integrated REE production chain.

3. POTENTIAL FOR RARE EARTH RESERVES AND COMPETITIVE ADVANTAGES IN MARANHÃO

Maranhão stands out as a strategic rare earth element (REE) province within Brazil, a country that holds the world’s second largest estimated REE reserves. The state is characterized by Proterozoic geological formations enriched in monazite and xenotime, hosting critical elements such as neodymium, cerium, lanthanum, yttrium and dysprosium, which are essential for renewable energy systems, advanced ceramics and high-temperature technologies. The integration of these mineral occurrences within established mineral provinces and modern infrastructure supports reliable resource assessment and sustainable exploration through geotechnical studies, detailed surveys and geological modeling.

The development of the REE sector in Maranhão is reinforced by a favorable institutional and policy environment. At the federal level, the National Mining Plan 2030 recognizes the strategic nature of REEs and promotes industrial verticalization through regulatory facilitation and support for research and development. At the state level, fiscal and exchange incentives, legal stability and continuous investments in logistics infrastructure particularly the Porto do Itaqui and the Carajás Railway reduce regulatory risk and enhance predictability, positioning Maranhão as an attractive REE cluster aligned with global markets.

In addition to geological and institutional strengths, Maranhão offers significant cost advantages in exploration and processing. The proximity between deposits and the Export Processing Zone (EPZ) reduces CAPEX and OPEX associated with internal logistics, shortens lead times and improves economies of scale from the early stages of implementation. Exchange rate freedom, combined with tax incentives and a mature multimodal logistics system, enhances financial predictability and competitiveness, placing Maranhão in a favorable cost position relative to established REE centers in Asia, North America and Africa.

4. METHODOLOGY

This qualitative research adopts an exploratory and prospective approach, based on documentary and content analysis (BARDIN, 2011), synthesizing and triangulating relevant secondary data from technical reports, government plans (PNM-2030) and sectoral analyses to construct a prospective scenario for Maranhão 2045 on the vertical integration of the ETRs chain.

The procedure followed three sequential steps: (1) protection and systematization of geological (Proterozoic formations, monazite/xenotime), logistical (Porto Itaqui, Carajás Railway, Bacabeira ZPE) and economic (tax incentives, governance models) data; (2) cross-triangulation comparing Maranhão's competitive advantages with global geopolitical challenges (Chinese dominance) and national R&D bottlenecks; (3) construction of prospective scenarios via adapted SWOT matrix, evaluating technical, economic and regulatory solutions up to 2045.

The validation occurred through convergence of independent sources (ALVES, 2025; ZEE MARANHÃO, 2021), ensuring analytical robustness without generating primary geological data.

5. RESULTS AND DISCUSSIONS

5.1 VALIDATION OF STRATEGIC GEOLOGICAL POTENTIAL AND INDUSTRIAL SYNERGY

This section consolidates the geological basis of the project, demonstrating the clear link between the potential for REEs and the capacity for industrial verticalization in Maranhão, a critical factor for cost optimization and the attractiveness of capital-intensive investments.

The prospecting for REEs focuses on middle and upper Proterozoic igneous and volcano-sedimentary units, environments developed by magmatic and hydrothermal concentration (ZEE MARANHÃO, 2021) of monazite (main source of REEs levels: Ce, La, Nd) and xenotime (heavy REEs: Y, Dy, Tb) (MARTINS *et al*., 2014).

The area of greatest strategic relevance, due to logistical synergy, is the Lower Itapecuru Axis (Rosário, Bacabeira, Axixá, Icatu), associated with the São Luís Cratonic Fragment and, mainly, with the Rosário Intrusive Suite — alkaline granites with magnetic differentiation favorable to level and medium REEs (Ce, La, Nd, Pr, Y, Dy) (ZEE MARANHÃO, 2021; BUSINESS PLANO, 2024).

Figure 3. Detail of the Lower Itapecuru Region Axis (Municipalities of Rosário, Bacabeira, Icatu and Axixá), highlighting the Rosário Intrusive Suite.

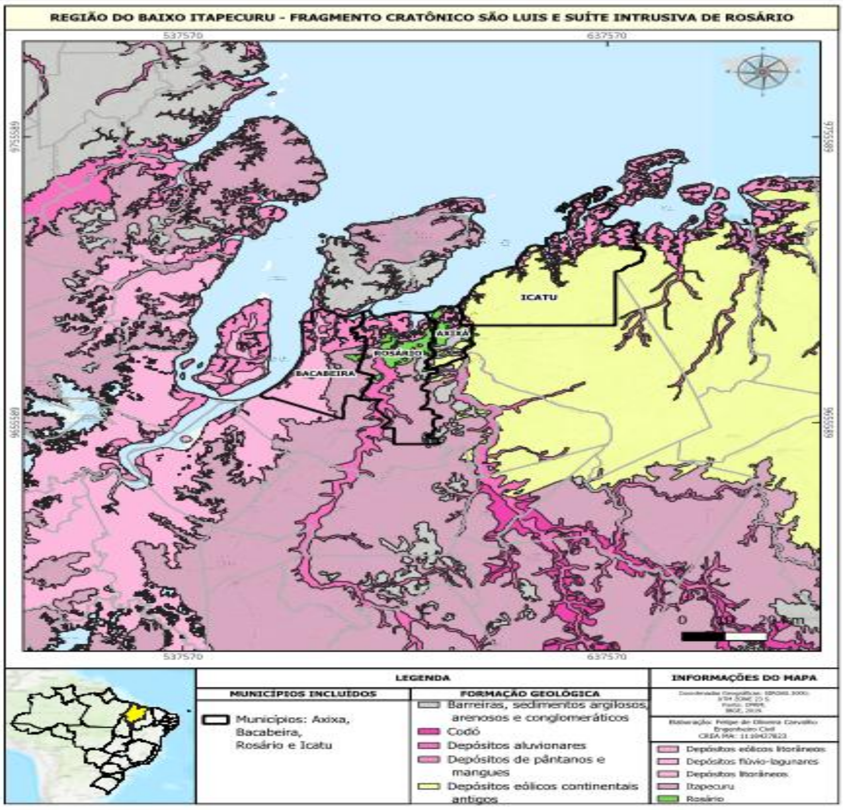

Source: Authors (2025)

A second axis of interest is located in the Northwest of the state (municipalities of Centro Novo do Maranhão, Carutapera, Luís Domingues and Cândido Mendes). This region presents a complex geology with multiple units of interest, highlighting the Chega-Tudo and Igarapé de Areia Volcanic and Volcano-Sedimentary Formations, which record the presence of the accessory minerals monazite and xenotime. Additionally, plutonic formations such as the Itapeva Complex are cited as potential hosts of REE (ZEE MARANHÃO, 2021; LOPES; TEIXEIRA, 2013).

Figure 4. Detail of the East/Southeast Region Axis (Municipalities of São João dos Patos, Pastos Bons, Paraibano), highlighting the Sardinha and Pastos Bons Formations

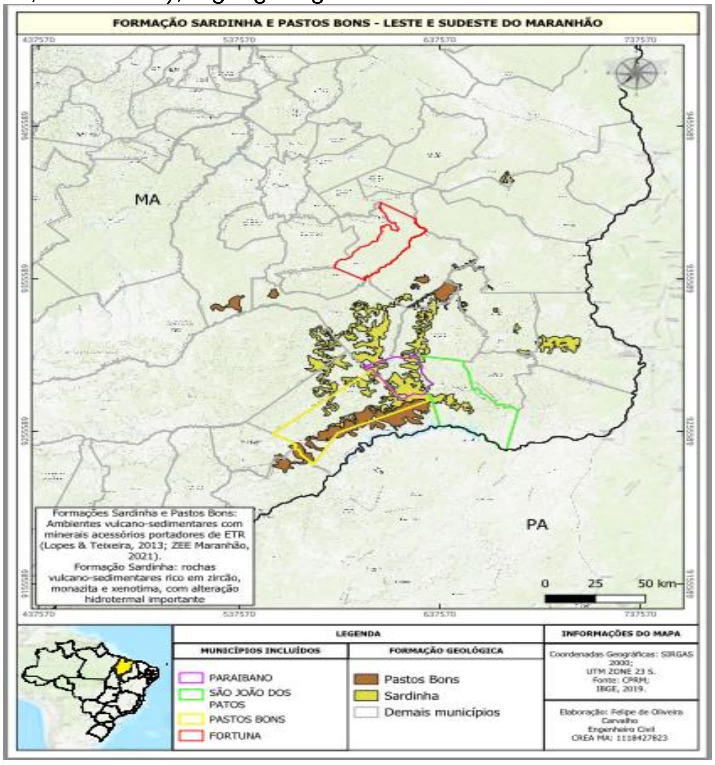

Source: Authors (2025)

Further inland, the East/Southeast Axis (São João dos Patos, Pastos Bons, Paraibano, Fortuna), located on the border of the Tocantins Province, presents the Sardinha and Pastos Bons Formations. These are described as volcano-sedimentary environments with significant hydrothermal alteration, rich in accessory minerals bearing REEs (ZEE MARANHÃO, 2021; UEMA, 2005).

Figure 5. Detail of the Southwest/South-Central Region Axis, highlighting the Mosquito and Corda Formations.

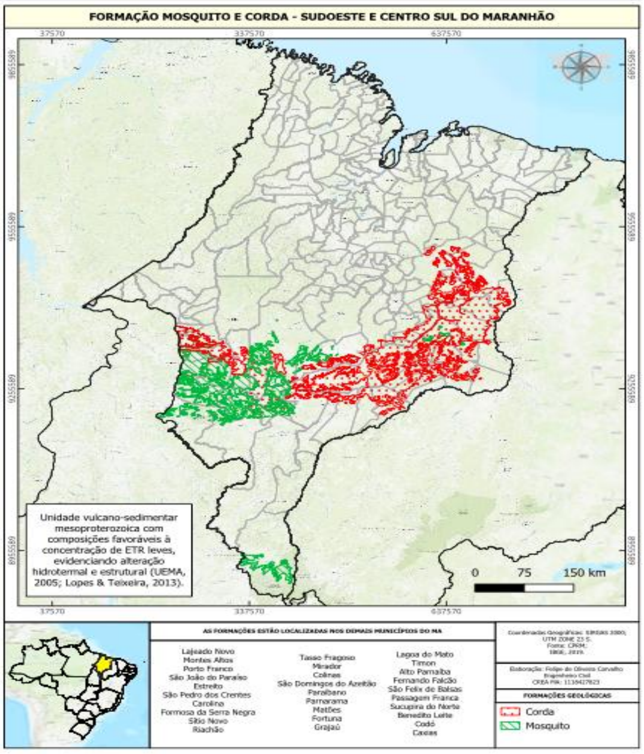

Source: Authors (2025)

The Southwest/South-Central Axis (Grajaú, Codó, Barra do Corda region) includes the Mosquito Formation, a Mesoproterozoic volcano-sedimentary unit favorable to the concentration of light REEs (LOPES; TEIXEIRA, 2013), and the Corda Formation, which indicates potential for prospecting (BUSINESS PLAN, 2024; UFPA, 2024).

The map below shows the distribution of volcanic, volcano-sedimentary, and plutonic formations in northwestern Maranhão and part of Pará, highlighting geological units such as Chega Tudo, Tromaí, Igarapé de Areia, and associated granitic formations with distinct colors. The cartographic representation shows areas where ancient magmatic, intrusive, and extrusive events occurred, allowing visualization of the spatial relationship between these units and the municipalities of Carutapera, Centro Novo do Maranhão, Cândido Mendes, and Luís Domingues.

Figure 6. Sedimentary formations in the State of Maranhão

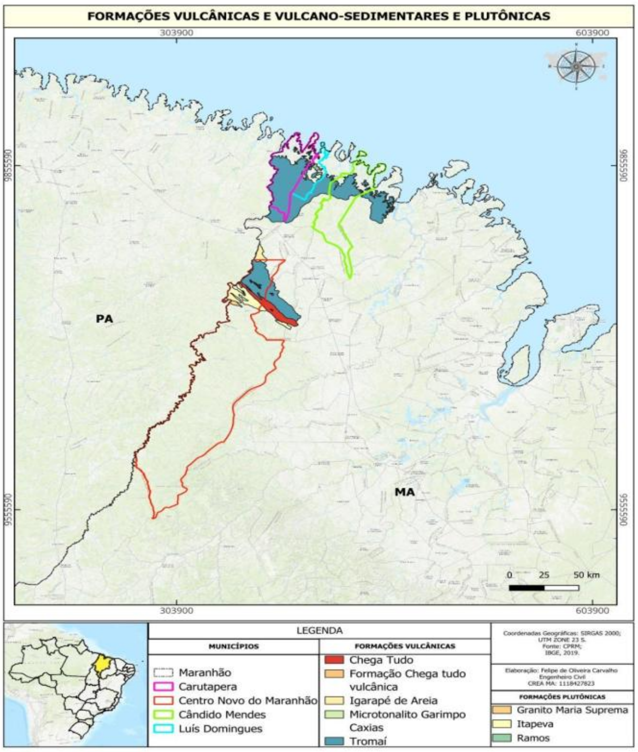

Source: Authors (2025).

Operating in Special Economic Zones (SEZs) offers specific tax and exchange incentives for companies, making the business environment more attractive for long-term investments in beneficiation and industrialization, stages with high capital costs and technological expertise. The presence of these zones strengthens Maranhão's capacity to transcend the "resource trap" (OLIVEIRA, 2014), promoting the creation of a true REE industrial cluster, which could even foster research and local development through partnerships with universities (BUSINESS PLAN, 2024).

5.2 LOGISTICS AND INDUSTRIAL INFRASTRUCTURE AS A COMPETITIVE ADVANTAGE

Project forecasts for ETRs (Extractive Mineral Resources) depend not only on geological resources, but crucially on local transportation and processing capacity for value aggregation. Maranhão has a mature logistics-industrial platform (BUSINESS PLAN, 2024), significantly reducing initial CAPEX and enabling a cluster of mineral strategies.

The first pillar is the São Luís Port Complex, especially the Port of Itaqui a world-class deep-water port that facilitates the export of refined concentrates/oxides and the import of chemical inputs for processing.

The second pillar is land connectivity via the Carajás Railway (EFC) and the BR-135 highway, linking production zones to the port. The third is the incentivized ZPE (Special Economic Zone) with ready-made energy infrastructure (including renewables) and logistics, eliminating downstream plant construction costs and positioning the Lower Itapecuru Axis (Bacabeira) as an initial strategic focus.

5.3 OPPORTUNITY FOR VERTICAL INTEGRATION: THE SYNERGY BETWEEN GEOLOGY AND LOGISTICS

The results revealed a rare confluence between geological potential (Rosário Intrusive Suite, northwest formations) and mature logistical-industrial infrastructure (Port of Itaqui, Carajás Railway, ZPE). Although geology is a necessary condition, the existing infrastructure creates sufficient conditions for the development of an industrial hub.

This synergy differentiates Maranhão, overcoming the Brazilian bottleneck in REEs not due to a lack of reserves, but a historical deficit in R&D and the absence of beneficiation/refining plants (MARTINS *et al*., 2014; CGEE, 2013). The Bacabeira ZPE offers a ready-made industrial platform, reducing CAPEX for a pilot plant for separating REE oxides (REO) and proposing an integrated value chain instead of exporting raw ore.

The cluster model mining + processing in the ZPE + transportation through Itaqui represents the Brazilian paradigm for internalizing the most profitable stages of the chain (MARTINS *et al*., 2014, p. 50), reinforced by the proximity of the Lower Itapecuru Axis to the reserves of rare earth elements.

5.4 STRATEGIC CRITICALITY ANALYSIS OF MARANHÃO'S RETAINING MINERALS

To validate vertical integration, the Strategic Value Matrix of Martins *et al*. (2014, pp. 141-143) is applied, which evaluates minerals based on five criteria (geological criticality, supply concentration, demand growth, revenues/profits, importance for sustainable development), classifying the target REEs of Maranhão as a priority focus.

Identified elements — neodymium (Nd), praseodymium (Pr), dysprosium (Dy), and yttrium (Y) — receive a "High" rating in almost all criteria (MARTINS *et al*., 2014, Table 39). Nd and Dy score "High" in all five, with Nd being the main component of permanent magnets (NdFeB) and Dy being essential for high-temperature operation (electric vehicle motors) (MARTINS *et al*., 2014, pp. 88-89).

The geological targets of Maranhão are not generic rare earth minerals (REMs), but the most critical and highest value-added minerals for a new economy, with a "High Concentration of Supply" that reinforces the geopolitical urgency of diversification. Vertical integration in the state is justified by the high criticality of these strategic minerals.

5.5 CRITICAL CHALLENGES: TECHNOLOGY, RADIOACTIVITY AND GOVERNANCE

Despite the favorable convergence of geological potential and infrastructure, the consolidation of a Rare Earth Elements (REE) hub in Maranhão is conditioned by three critical challenges that have historically constrained similar projects in Brazil: technological capacity, environmental management and regulatory governance. The primary bottleneck is technological, as the highest value of REEs is concentrated in the separation of pure oxides and subsequent metallurgical processing—stages dominated globally by China. Brazil’s structural deficit in mineral R&D necessitates substantial and coordinated investments to internalize these technologies and avoid the continued export of low-value concentrates.

A second challenge relates to environmental licensing, particularly the management of residues classified as NORM and TENORM. Minerals such as monazite and xenotime contain thorium and uranium, which become concentrated in tailings after chemical processing, requiring stringent monitoring, engineered containment and compliance with nuclear regulatory standards.

Although these risks are recognized in project planning, their technical and financial execution has historically undermined project feasibility.

The third constraint involves governance and regulatory efficiency. Procedural bottlenecks and institutional delays in mining and environmental agencies increase uncertainty and inhibit long-term capital allocation. The viability of a Strategic Minerals Cluster in Maranhão therefore depends on a coordinated public–private governance model, combining legal certainty, regulatory agility and effective environmental and nuclear licensing frameworks.

6. PROJECTION "MARANHÃO 2045": AN INTEGRATED INDUSTRIAL HUB

The geological and logistical results, weighed against critical challenges, project a scenario conditioned by "Maranhão 2045": outdated technology, radioactivity, and governance, the protected state transcends to become an integrated REE industrial hub. The ZPE will house oxide separation (REO), alloy metallurgy, and permanent magnets, using Porto Itaqui and Ferrovia Carajás to export to the USA/EU/Japan (ALVES, 2025) and supply Brazilian neo-industrialization with Nd, Pr, and Dy for wind turbines and electric vehicles (MARTINS *et al*., 2014).

The prospecting focuses on Proterozoic igneous/volco-sedimentary units, rich in monazite (light REEs) and xenotime (heavy: Y, Dy, Tb). The Lower Itapecuru Axis (Rosário, Bacabeira, Axixá, Icatu), linked to the São Luís Cratonic Fragment and the Rosário Intrusive Suite (alkaline granites), is a geological hotspot for medium/level REEs.

The ZPE in Bacabeira (2,059 ha) creates direct synergy: proximity to the deposit-processing area optimizes costs, converts concentrate into pure oxides on-site, and integrates logistics (Carajás Railway, BRs 135/402/MA-110, Itaqui) for export, positioning Maranhão as a globally competitive hub for high-value/high-technology REEs.

7. STRATEGIC OUTLOOK: MARANHÃO AS A GLOBAL REE HUB (HORIZON 2045)

This analysis is valid for the prospective potential of Maranhão to consolidate an industrial cluster of REEs by 2045, with a unique confluence of geological assets (Rosário Intrusive Suite, Lower Itapecuru Axis; ZEE MARANHÃO, 2021; CPRM, 2023) and logistical assets (Bacabeira EPZ, Carajás Railway, Itaqui Port), attracting FDI and mitigating risks in the global critical REE chain (Nd, Dy, Y; MARTINS *et al*., 2014).

Operational synergy minimizes logistical frictions, verticalizing the chain via the production of pure oxides (REO) in the EPZ, overcoming the export of crude concentrates (CGEE, 2013). However, success depends on overcoming three challenges: (1) massive investment in R&D for hydrometallurgy; (2) rigorous management of NORM/TENORM (monazite/xenotime); (3) Agile and secure regulatory governance.

It is concluded that Maranhão possesses fundamental assets for a REE hub, conditioned on holistic investments in human capital (UFMA/UEMA/IFMA) and technology (BNDES/FINEP). Studies of technical-economic forecasts for beneficiation routes of the Rosário Suite and mass balance of radionuclides in tailings are recommended.

REFERENCES

ALVES, Francisco. (Ed.). **The Race for Strategic Minerals**. Brasil Mineral International Issue, São Paulo, Special Issue 2025, ISSN 0102-4728, p. 3, 2025.

ARRAES, Tássia de Melo; SILVA, Cristina Ferreira Correia; PRATA, Alvaro Toubes. **Production chains for rare earths in Brazil**. In: MARTINS, Colbert (Rapporteur) *et al*. Strategic minerals and rare earths. Brasília: Chamber of Deputies, Edições Câmara, 2014. p. 163-173.

AZEVEDO, Luís Maurício. **ABPM hopeful that regulatory bottlenecks will not block capital inflow**. Brasil Mineral International Issue, São Paulo, Special Issue 2025, ISSN 0102-4728, p. 48-52, 2025.

BARDIN, Laurence. **Content analysis**. São Paulo: Edições 70, 2011.

BUSINESS PLAN - **Rare Earth Prospecting in Maranhão**. [S.l.: s.n.], 2024.

CGEE - CENTER FOR MANAGEMENT AND STRATEGIC STUDIES. **Uses and applications of Rare Earths in Brazil: 2012-2030**. Brasília, DF: CGEE, 2013.

CPRM - GEOLOGICAL SURVEY OF BRAZIL. **Geological and mineral resources map of the state of Maranhão**. Brasília: CPRM, 2023.

LOPES, R. S.; TEIXEIRA, M. A. **Geological diagnostic report of the Parnaíba basin in Maranhão**. Embrapa, 2013.

MARTINS, Colbert (Rapporteur) *et al*. **Strategic minerals and rare earths. Brasília: Chamber of Deputies**, Edições Câmara, 2014. 241 p.

MARTINS, José Eduardo Alves; ANDRADE, Romualdo Homobono Paes de. **Strategic minerals and rare earth elements**. In: MARTINS, Colbert (Rapporteur) *et al*. **Strategic minerals and rare earths**. Brasília: Chamber of Deputies, Edições Câmara, 2014. p. 174-189.

OLIVEIRA, Inocêncio (Deputy). Preface. In: MARTINS, Colbert (Rapporteur) *et al*. **Strategic Minerals and Rare Earths.** Brasília: Chamber of Deputies, Edições Câmara, 2014. p. 11-12.

RODRIGUES, D.; DE CASTRO, J.A.; DE CAMPOS, M.F. P**erspectives for Rare-Earth Magnets in Brazil.** In: REPM2014 (23rd International Workshop on Rare Earth and Future Permanent Magnets and their Applications), 2014, Annapolis. Proceedings... [Place of publication unknown: publisher unknown], 2014.

SCLIAR, Claudio. **Mining: what is strategic for Brazil**. In: MARTINS, Colbert (Rapporteur) *et al*. Strategic minerals and rare earths. Brasília: Chamber of Deputies, Edições Câmara, 2014. p. 232-241.

TUNES, Marcelo Ribeiro. **An annotated view on strategic minerals and rare earths**. In: MARTINS, Colbert (Rapporteur) *et al*. Strategic minerals and rare earths. Brasília: Chamber of Deputies, Edições Câmara, 2014. p. 190-201.

UEMA - STATE UNIVERSITY OF MARANHÃO. **Geology of northwestern Maranhão: Chega-Tudo Formation and associated mineralizations**. São Luís: UEMA, 2005.

UFPA - FEDERAL UNIVERSITY OF PARÁ. **The zeolitic zone of the Corda Formation**, Parnaíba Basin. Belém: UFPA, 2024.

XAVIER, Roberto Perez. **Brazil has the potential to become a major global player**. Brasil Mineral International Issue, São Paulo, Special Issue 2025, ISSN 0102-4728, p. 40-43, 2025.

ZEE MARANHÃO. **Technical report on Geology, Geomorphology and Hydrogeology of Maranhão**. São Luís: ZEE Maranhão, 2021.

CHAPTER 7

COMPARATIVE ANALYSIS OF NUMERICAL METHODS FOR SOLVING INVERSE HEAT TRANSFER PROBLEMS IN MACHINING

Daniel Schwan Monteiro de Sousa
Bachelor of Science in Mechanical Engineering
Universidade Federal de Itajubá (UNIFEI)
E-mail: ss.daniel096@gmail.com

Rogério Fernandes Brito
Doctor in Mechanical Engineering
Universidade Federal de Itajubá (UNIFEI)
E-mail: rogbrito@unifei.edu.br

Ricardo Luiz Perez Teixeira
Doctor in Materials Engineering
Universidade Federal do Rio de Janeiro
E-mail: ricardo.luiz@unifei.edu.br

Paulo Mohallem Guimarães
Doctor in Mechanical Engineering
Universidade Federal de Itajubá (UNIFEI)
E-mail: pauloguimaraes@unifei.edu.br

José Carlos de Lacerda
Doctor in Mechanical Engineering
Universidade Federal de Itajubá (UNIFEI)
E-mail: jlacerda.cem@gmail.com

ABSTRACT: This work evaluates the impact of different numerical configurations on solving an inverse heat transfer problem during machining processes, using the Finite Element Method (FEM) coupled with the Levenberg-Marquardt algorithm. Initially, a controlled case with constant thermal properties was modeled, testing various mesh element types (tetrahedral and hexahedral), refinements, interpolation functions, and linear system solvers (direct and iterative). Simulations were performed in COMSOL Multiphysics 5.6 with MATLAB integration, quantifying processing time, memory usage, and deviations between simulated and experimental data. Results indicated that iterative solvers (especially FGMRES) with lower-order interpolation functions on optimized meshes significantly reduce computational time and file sizes while maintaining accuracy comparable to conventional methods. This configuration was then applied to a real machining case with temperature-dependent thermal properties, demonstrating relevant computational performance gains. The study highlights the importance of selecting appropriate numerical parameters in thermal engineering simulations, particularly in contexts where heat flux estimation is critical, such as in cutting tool wear.

KEYWORDS: COMSOL, finite element method, inverse heat transfer problem, machining, Levenberg-Marquardt.

RESUMO: Este trabalho avalia o impacto de diferentes configurações numéricas na solução de um problema inverso de transferência de calor durante o processo de usinagem, utilizando o Método dos Elementos Finitos (MEF) acoplado ao algoritmo de Levenberg-Marquardt. Inicialmente, foi modelado um caso controlado com propriedades térmicas constantes, no qual se testaram diferentes tipos de elementos de malha (tetraédricos e cúbicos), refinamentos, funções de interpolação e solucionadores de sistemas lineares (diretos e iterativos). As simulações foram realizadas no COMSOL Multiphysics 5.6 com integração via MATLAB, permitindo quantificar o tempo de processamento, o uso de memória e os desvios entre os valores simulados e os dados experimentais. Os resultados indicaram que o uso de solucionadores iterativos (especialmente o FGMRES) com funções de interpolação de ordem inferior em malhas otimizadas proporciona significativas reduções no tempo computacional e no tamanho dos arquivos, com precisão comparável aos métodos convencionais. Essa configuração foi então aplicada a um caso real de usinagem com propriedades térmicas dependentes da temperatura, demonstrando ganhos relevantes de desempenho computacional. O estudo destaca a importância da escolha adequada de parâmetros numéricos em simulações térmicas de engenharia, principalmente em contextos em que a estimativa de fluxos de calor é essencial, como no desgaste de ferramentas de corte.

PALAVRAS-CHAVE: COMSOL, Levenberg-Marquardt, método dos elementos finitos, problema inverso de transferência de calor, usinagem.

1. INTRODUCTION

In mathematics, problems can be solved in two main ways: analytical solutions and numerical solutions. While analytical solutions seek a comprehensive and continuous answer, numerical solutions are obtained by discretizing the domain and calculating the function only at specific points, resulting in approximations. The use of numerical methods offers advantages such as automated calculations and models that are closer to reality, and they are widely used in engineering to solve practical problems (Kendall, 2019).

Advances in computational processing power have driven the use of numerical simulation software, such as ANSYS CFX and COMSOL Multiphysics, which enable detailed analyses across various fields. Furthermore, these programs can be applied to inverse problems, which seek to determine the initial conditions of the problem based on observations of the phenomenon, benefiting industry both in product development and in process improvement, highlighting the importance of numerical simulation methodologies today (Kendall, 2019).

Machining is an essential technology in industry for achieving complex geometries and adjusting the finish of parts, being a process that is easily automated (Machado; Silva, 2004). During machining, the energy consumed is mainly converted into heat, generating high temperatures that affect the service life of cutting tools, requiring studies to reduce the heat absorbed (Carvalho, 2005).

The choice of cutting tool materials, such as cemented carbide, is crucial for addressing machining conditions and the class of material being machined (Machado; Silva, 2004). However, cemented carbide tools are subject to thermal oxidation at high temperatures, affecting their properties and performance—important factors to consider in the industry (Gu *et al*., 2012). Furthermore, studies reveal that the properties and wear of cemented carbide tools depend on the distribution and proportion of particles in the material (Lee *et al*., 2018).

2. THEORETICAL BACKGROUND

Machining is an essential manufacturing process in the metalworking industry, in which the controlled removal of material (excess metal) is carried out in the form of chips to obtain the desired dimensions and surface finish (Machado; Silva, 2004). The chip formation mechanism occurs in four stages: (1) application of shear stress due to contact between the tool and the workpiece, (2) deformation of the material against the tool's exit surface, (3) progressive plastic deformation until fracture, and (4) slippage of the chip over the tool, restarting the cycle (Machado; Silva, 2004).

Regarding the energy balance, most of the power consumed is converted into heat due to the shearing of the material. The chip dissipates the largest portion of this heat, while the tool absorbs a significant fraction, reaching temperatures exceeding 1100°C under severe cutting conditions (Carvalho, 2005). These high temperatures accelerate tool wear, reducing its service life and increasing operating costs.

The thermal energy stored ($\dot{E}_a$) in a given body over time can be described as the thermal energy resulting from the heat exchange that the body undergoes with its surroundings ($\dot{E}_q$) plus the energy generated within it ($\dot{E}_g$) .

$$\dot{E}_a = \dot{E}_q + \dot{E}_g \tag{1}$$

Let A be the area of the boundaries of the control volume subject to the heat flux$\vec{q}$, and let$\hat{n}$ be the unit vector pointing outward from the surface at a right angle; thus, the heat flux$\dot{E}_q$ is described by Equation (2). The generation term, on the other hand, is described as a function of the vector $\vec{r}$, which represents each point inside the tool, and is given by Equation (3); finally, the stored thermal energy is described by Equation (4).

$$\dot{E}_q = -\int_A \vec{q} * \hat{n} * dA = -\int_V \nabla \vec{q}(\vec{r}, t) * dV \tag{2}$$

$$\dot{E}_g = \int_V g(\vec{r}, t) * dV \tag{3}$$

$$\dot{E}_a = \int_V \rho\, c_p \frac{\partial T\ (\vec{r}, t)}{\partial t} * dV \tag{4}$$

Substituting the terms from Equations (2), (3), and (4) into Equation (1) and letting the control volume approach 0, i.e., V → 0, we arrive at Equation (5).

$$\rho c_p \frac{\partial T\,(\vec{r},t)}{\partial t} = -\,\nabla\vec{q}(\vec{r},t) + \, g(\vec{r},t) \tag{5}$$

According to Fourier’s law, a temperature gradient in a system naturally generates a heat flux. If this temperature gradient is considered in a solid, homogeneous, and isotropic medium with thermal conductivity k, the function describing heat diffusion within the material is given by Equation (7). By substituting the heat transfer function from Equation (7) into Equation (6), the term `$\overrightarrow{q}\,(\overrightarrow{r}\,,t)$ ` is eliminated, yielding Equation (8). Since the vector `$\overrightarrow{r}$ ` represents the spatial position in three directions (x, y, z), Equation (8) can be expressed in Cartesian coordinates as Equation (9).

$$\overrightarrow{q}\,(\overrightarrow{r}\,,t) = -k\nabla T\,(\overrightarrow{r}\,,t) \tag{6}$$

$$\rho c_p \frac{\partial T\,(\vec{r},t)}{\partial t} = \, -\nabla.\,[-\mathrm{k}\nabla \mathrm{T}\,(\overrightarrow{r}\,,t)] + g(\overrightarrow{r}\,,t) \tag{7}$$

$$\frac{\partial}{\partial x}\left(k\frac{\partial T}{\partial x}\right) + \frac{\partial}{\partial y}\left(k\frac{\partial T}{\partial y}\right) + \frac{\partial}{\partial z}\left(k\frac{\partial T}{\partial z}\right) + g = \rho c_p \frac{\partial T}{\partial t} \tag{8}$$

However, Equation (9) is used for continuous cases and is difficult to solve analytically for complex geometries, such as that of a cutting tool. To solve this problem, this study employed the Finite Element Method (FEM), which discretizes the domain into elements of simple geometry, allowing for the numerical solution of the differential equation.

In the FEM, the domain is divided into a mesh composed of nodes (discrete points) and elements (regions bounded by these nodes). Each element is defined by an interpolation function that approximates the temperature distribution within it. For example, in a linear triangular element, the temperature ϕ=f(x,y) varies linearly between the nodes, allowing the calculation of the partial derivatives present in Equation (9).

The Finite Element Method has been widely applied in various fields of engineering and science, demonstrating its versatility in the solution of complex problems. For example, Sampaio (2006) used the FEM to model incompressible viscous flows, while Brito (1999) applied it to heat transfer problems with laminar convection, including cases of forced, natural, and mixed convection.

Furthermore, the method has been employed in thermal analyses of industrial systems, such as in the study by Appadurai *et al.* (2020), which evaluated the cooling of induction motors through the optimization of fin design. Its application also extends to the medical field, as in Wu *et al.* (2021), who used FEM based on computed tomography images for the diagnosis of osteoporosis. In materials engineering, Chen and Hao (2021) applied the method to evaluate mechanical properties of titanium composites, such as flexural strength and elastic limit.

However, in certain practical cases, it is not possible to directly measure the cause of a phenomenon (such as a heat source), but only its effects (temperatures at specific points). To estimate these unknown parameters, inverse problems are used, solved by methods such as the Levenberg-Marquardt (LM) algorithm. Initially developed by Levenberg (1944) and refined by Marquardt (1963), this method remains widely applied due to its efficiency in nonlinear problems.

The LM algorithm combines gradient and quadratic approximation techniques, using a damping factor to balance accuracy and stability during iterations. Cui *et al.* (2016) improved the algorithm by incorporating complex differentiation for sensitivity analysis, optimizing the estimation of heat fluxes in transient problems. Studies such as that by Cui *et al.* (2017) have also related this factor to the objective function (a measure of the error between calculated and observed values), which is essential for convergence. Practical applications include the determination of heat fluxes in industrial processes, such as in the work by Torres *et al.* (2021) with oxyacetylene plates, and the estimation of thermophysical properties, exemplified by Vega-Suarez *et al.* (2018) in the characterization of orthotropic materials.

3. METHODOLOGY

In this study, Equation (9) will be solved using the finite element method to evaluate temperatures in two distinct situations: (1) in the simplified controlled case and (2) in a practical machining case. In the controlled case—due to its lower computational complexity—different combinations of numerical parameters (finite element type, mesh refinement level, interpolation function, and classes of linear system solvers) will be systematically tested to identify the optimal configuration that minimizes computational time. This optimized configuration will then be applied to the real machining case and compared with the standard COMSOL configuration. Regarding material parameters, in the controlled case thermal conductivity (k) will be considered constant, while in the real case thermal conductivity will be modeled as a function of temperature. In both cases, the specific mass (ρ) and specific heat (c_p) will be treated as constants independent of temperature.

Second-order partial differential equations, such as Equation (9), may have more than one solution. To ensure they have a unique solution, it is necessary to specify the initial conditions and boundary conditions of the system. The initial condition defines the temperature distribution of the system at time zero (t = 0) at any position in the domain, which will be considered the ambient temperature.

Boundary conditions, on the other hand, may vary depending on the problem under study and are generally the prescribed temperatures on the system's surface, the heat flux, and heat exchange by convection or radiation with the external medium (SODRÉ, 2003). In this study, temperatures were measured at specific points using thermocouples, which will be used as boundary conditions. The thermocouples used in this study collected temperature readings every 0.2 seconds.

The controlled case was based on the experiment by Carvalho (2005), illustrated in Figure 1, which used a carbide cutting tool (12.7 × 12.7 × 4.7 mm) with an electric heater coupled to a direct current (DC) power supply (MCE) for heat generation. A flux transducer positioned between the heater and the tool measured the heat flux, while two thermocouples recorded the temperature rise in the tool. The data were collected by an HP 75000 Series B data acquisition system with a computer-controlled E1326B voltmeter.

Figure 1. Setup of the controlled experiment

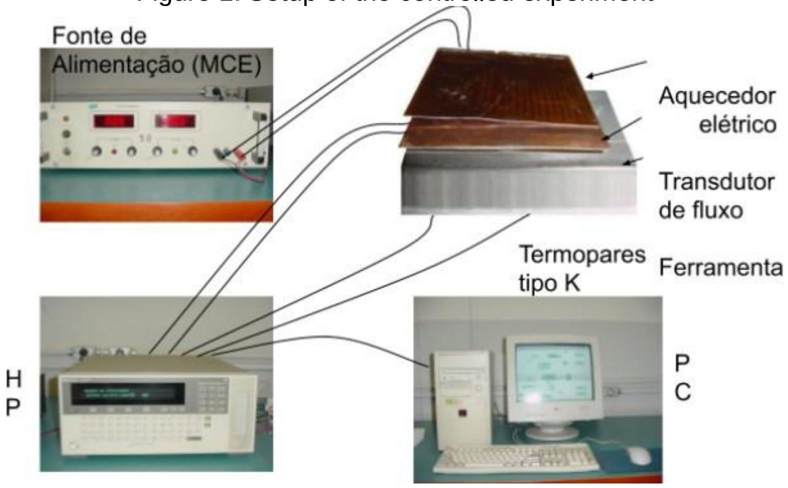

Source: Carvalho (2005)

COMSOL Multiphysics 5.6 offers two distinct approaches for solving linear systems in the FEM: direct solvers (MUMPS, PARDISO, SPOOLES, and Dense Matrix) and iterative solvers (GMRES, FGMRES, BiCGStab, TFQMR, and Conjugate Gradients). In addition to the choice of solver, the method allows for the selection of different interpolation functions—linear, Lagrangian, and Serendipity—which directly influence the approximation of the problem variables. To evaluate the impact of spatial discretization, six mesh configurations were tested, varying both the element type (tetrahedral or hexahedral) and the degree of refinement (coarse, normal, and fine), allowing for a comprehensive analysis of the influence of these parameters on the results. Table 1 shows the relationship between element type, refinement, and the resulting number of elements for the controlled case.

Table 1. Relationship between element type, refinement, and number of elements

Element Type	Refinement	Number of Elements
Tetrahedral	Coarse	905
Tetrahedral	Normal	5,868
Tetrahedral	Fine	36,078
Cubic	Coarse	72
Cubic	Normal	400
Cubic	Thin	2,499

Source: Authors’ data (2025)

All simulations in this study were performed on a computer with the following specifications: Processor: Intel(R) Core(TM) i5-7400 CPU @ 3.00 GHz; RAM: 8.156 GB; Graphics card: NVIDIA GeForce GTX 1050; Operating system: Windows 10 Pro.

4. RESULTS AND DISCUSSION

The simulations were performed in COMSOL Multiphysics software, using the Levenberg-Marquardt method via the commercial LiveLink™ for MATLAB package, which enables integration between COMSOL and MATLAB. Initially, the tests were conducted using different direct solvers, with a coarse mesh of tetrahedral elements and a quadratic Lagrange interpolation function, as these are part of the standard COMSOL configuration. The thermophysical properties of the cutting tool material were kept constant, adopting the reference values established by Carvalho (2005): thermal conductivity (k) of 43.1 W/(m·K) and thermal diffusivity (α) of 14.8 × 10^{-6} m²/s. The results obtained in these simulations are presented in Table 2, highlighting the processing time, the measured and calculated deviations in thermocouples 1 and 2, and the average deviation of the calculated heat flux. Figure 2 shows the difference between the calculated and measured heat flux.

Table 2. Analysis of the effect of different direct solvers for a controlled case

Direct Solution Method	Time(s)	Deviation Thermocouple 1	Deviation Thermocouple 2	Average Deviation Heat Flow
MUMPS	257	1.94%	1.85%	507.46%
PARADISE	151	1.94%	1.85%	507.46%
SPOOLES	690	1.94%	1.85%	507.46%
Dense Matrix	768	1.94%	1.85%	507.46%

Source: Authors' data (2025)

Figure 2. Measured heat flux and calculated heat flux

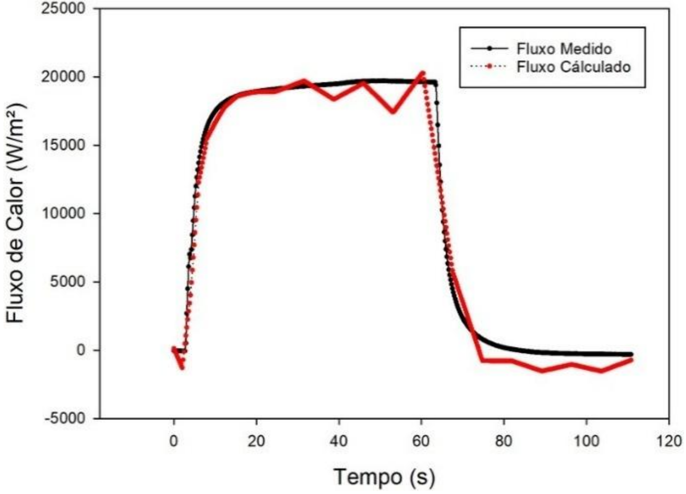

Source: Author

Table 3 shows the average deviation of the heat flux separated by time intervals. Thus, to evaluate the average deviations of the calculated heat flux in the simplified case, the interval from 5.2 to 70 seconds will be taken into account.

Table 3. Average heat flux deviation evaluated at different time intervals

Time Interval	Average Deviation Heat Flux
0 to 5 seconds	471.78%
5.2 to 70 seconds	6.35%
70.2 to 110.8 seconds	1307.34%

Source: Authors' data (2025)

Using the same coarse tetrahedral mesh, the effects of the interpolation function on the simulation results were evaluated using the PARDISO direct solver as the baseline.

Table 4. Results of different interpolation functions evaluated in the PARDISO direct solver on a coarse tetrahedral mesh.

Family	Order	Time(s)	Thermocouple 1 Deviation	Thermocouple 2 Deviation	Heat Flow Deviation
-	Linear	63	1.94%	1.85%	12.34%
Lagrange	2nd Order	142	1.94%	1.85%	6.35%
Lagrange	3rd Order	574	1.94%	1.85%	6.35%
Lagrange	4th Order	1668	1.94%	1.85%	7.33%
Lagrange	5th Order	4174	1.94%	1.85%	7.33%
Serendipity	2nd Order	134	1.94%	1.85%	6.35%
Serendipity	3rd Order	580	1.94%	1.85%	6.35%
Serendipity	4th Order	1540	1.94%	1.85%	7.13%

Source: Authors' data (2025)

The simulations were also evaluated using iterative methods to solve the system of equations. However, in this case, the solvers will be evaluated only on the linear and cubic functions of the Lagrangian and Serendipity families, still using the same mesh as in the previous case. The results are presented in Tables 5, 6, and 7.

Table 5. Iterative methods evaluated on the linear interpolation function

Iterative Method	Time (s)	Thermocouple 1 Deviation	Deviation Thermocouple 2	Heat Flow Deviation
GMRES	77	1.94%	1.85%	12.34%
FGMRES	66	1.94%	1.85%	12.34%
BiCGStab	81	1.94%	1.85%	12.34%
Gradient Conjugate	69	1.94%	1.85%	12.34%
TFQMR	76	1.94%	1.85%	12.34%

Source: Authors' data (2025)

Table 6. Iterative methods evaluated on the Lagrange cubic function

Iterative Method	Time (s)	Thermocouple 1 Deviation	Thermocouple 2 Deviation	Heat Flux Deviation
GMRES	1047	1.94%	1.85%	6.35%
FGMRES	816	1.94%	1.85%	6.35%
BiCGStab	1291	1.94%	1.85%	6.35%
Gradient Conjugate	942	1.94%	1.85%	6.35%
TFQMR	1154	1.94%	1.85%	6.35%

Source: Authors' data (2025)

Table 7. Iterative methods evaluated on the cubic serendipity function

Iterative Method	Time (s)	Thermocouple 1 Deviation	Thermocouple 2 Deviation	Heat Flux Deviation
GMRES	1003	1.94%	1.85%	7.33%
FGMRES	715	1.94%	1.85%	7.33%
BiCGStab	1235	1.94%	1.85%	7.33%
Gradient Conjugate	1157	1.94%	1.85%	7.33%
TFQMR	1129	1.94%	1.85%	7.33%

Source: Authors' data (2025)

To evaluate the effects of mesh element types and their refinement on numerically estimated temperatures and calculated flow, the iterative FGMRES method was used in the linear interpolation equation, as this configuration proved to be the fastest among all evaluated methods. The results are presented in the table below.

Table 8. Comparative results between different computational meshes

Mesh	Time(s)	Thermocouple 1 Deviation	Thermocouple 2 Deviation	Heat Flux Deviation
Coarse Tetrahedral	65	1.94%	1.85%	12.34%
Normal Tetrahedron	123	1.94%	1.85%	8.28%
Fine Tetrahedral	36078	1.94%	1.85%	7.33%
Coarse Cubic	47	1.95%	1.86%	12.34%
Standard Cubic	128	1.94%	1.86%	10.89%
Fine Cubic	404	1.94%	1.85%	7.33%

Source: Authors' data (2025)

Since the temperatures reached during the machining process are much higher than those in the control case, for this case, the thermal properties will be considered as a function of temperature. The temperature-dependent thermophysical properties of cemented carbide and 1045 steel were taken from the works of Grzesik *et al.* (2004), Grzesik *et al.* (2009), and Jiang *et al.* (2016). The values used are presented in the table below.

Table 9. Temperature-dependent thermophysical properties of cemented carbide and 1045 steel

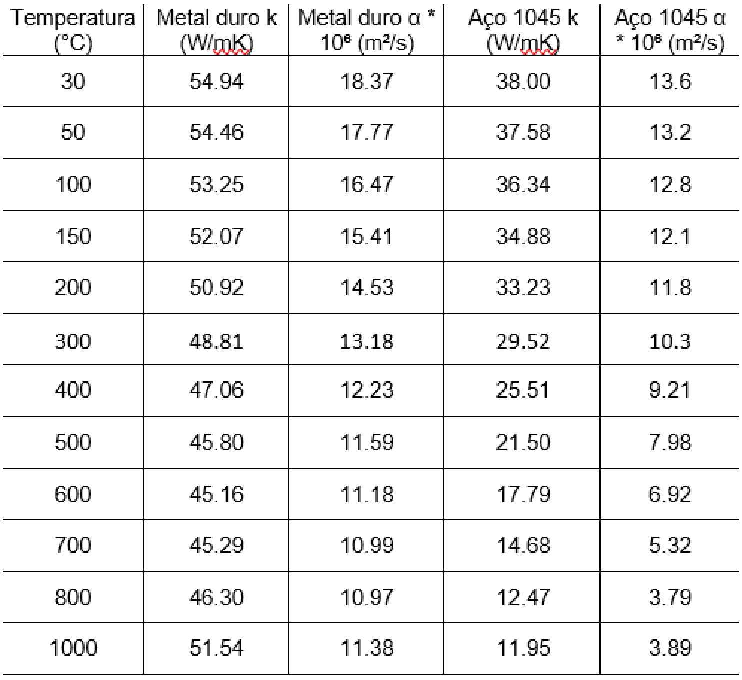

Temperatura (°C)	Metal duro k (W/mK)	Metal duro α * 10^6 (m²/s)	Aço 1045 k (W/mK)	Aço 1045 α * 10^6 (m²/s)
30	54.94	18.37	38.00	13.6
50	54.46	17.77	37.58	13.2
100	53.25	16.47	36.34	12.8
150	52.07	15.41	34.88	12.1
200	50.92	14.53	33.23	11.8
300	48.81	13.18	29.52	10.3
400	47.06	12.23	25.51	9.21
500	45.80	11.59	21.50	7.98
600	45.16	11.18	17.79	6.92
700	45.29	10.99	14.68	5.32
800	46.30	10.97	12.47	3.79
1000	51.54	11.38	11.95	3.89

Source: Grzesik *et al.* (2004), Grzesik *et al.* (2009), Jiang *et al.* (2016).

Figure 3 shows the cutting tool assembly, including the insert and tool holder, used in the experimental process conducted by Carvalho (2005). The positions of the thermocouples in the assembly, the contact area between the tool and the workpiece, and the mesh used to perform the experiment in the actual case are also illustrated.

Figure 3. Cutting tool assembly with thermocouple positions and computational mesh used in the simulation

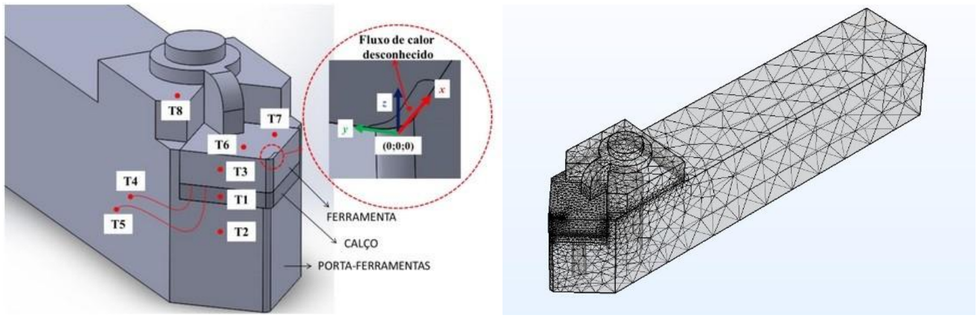

Source: Adapted from Carvalho (2005)

The thermal problem presented in this work is solved in two stages. In the first stage, the inverse problem is solved, which consists of estimating the heat flux at the chip-tool interface using experimental temperature data . The second stage consists of solving the direct problem to obtain the numerical temperature values throughout the domain, since all boundary conditions are already known.

Table 10 compares the results of the two inverse problem simulations performed on the cutting tool assembly consisting of a carbide insert, a carbide shank, and a 1045 steel tool holder used in the turning process. One uses COMSOL's standard solver (PARDISO + Lagrange quadratic function), and the other is configured based on studies conducted in the controlled case (FGMRES + linear function).

Table 10. Comparison of the effects of different configurations in the computational simulation of a real machining case

	FGMRES + Linear Function	PARDISO + Lagrange Quadratic Function
Time	9367 s (2h36min7s)	87,427 s (1d0h17min7s)
File size (GB)	0.73	4.54
Average thermocouple deviation 1	46.86%	46.93%
Average deviation of thermocouple 2	26.95%	69.31%
Average deviation of thermocouple 3	45.36%	33.45%
Average deviation of thermocouple 4	22.35%	2.33%
Average deviation of thermocouple 5	5.30%	4.36%
Average deviation of thermocouple 6	19.07%	22.10%
Average deviation of thermocouple 7	16.03%	15.07%
Average deviation of thermocouple 8	75.40%	77.90%

Source: Authors' data (2025)

5. CONCLUSION

The results demonstrate that the estimation of heat flux via the inverse problem is sensitive to the numerical configuration adopted. It was observed that coarse meshes and low-order interpolation functions tend to exhibit greater deviations in the heat flux estimate, especially in situations of abrupt thermal transition, such as the activation or deactivation of the heat source. This occurs due to the low density of control points, which hinders the accurate capture of the physical phenomenon.

However, the tests revealed that improving just one of these parameters (mesh refinement or interpolation function) is sufficient to significantly increase the accuracy of the simulations, since both have similar effects on the quality of the solution.

Furthermore, tetrahedral elements showed a smaller deviation in the estimated parameters, although they require a significantly larger number of elements to discretize the domain, which implies longer computation time. Iterative solvers, such as FGMRES, when combined with linear interpolation functions, exhibited superior computational performance without significant loss of accuracy, making them a viable alternative for complex simulations with time and computational resource constraints.

Compared to the standard COMSOL configuration (PARDISO + quadratic interpolation), the optimized approach proposed in this work (FGMRES + linear interpolation) reduced simulation time and memory usage by more than 90%, with similar accuracy results, reinforcing the feasibility of its application in industrial and academic environments.

ACKNOWLEDGMENTS

First and foremost, I thank God for the wisdom, strength, and opportunities that allowed me to complete this work.

To my family, for their unconditional support, constant encouragement, and patience throughout my academic journey.

To my friends and colleagues who, directly or indirectly, contributed with suggestions, discussions, and motivation throughout this process.

To the professors and advisors, for their valuable guidance, shared knowledge, and dedication in assisting with the development of this research.

Finally, to everyone who, in any way, contributed to the completion of this research, my sincere gratitude.

REFERENCES

APPADURAI, M*.* *et al.* Finite element design and thermal analysis of an induction motor used for a hydraulic pumping system. **Materials Today: Proceedings**, v. 45, p. 7100 – 7106, 2020. ISSN 22147853.

BRITO, R. F. Simulação Numérica da Transferência de Calor e do Escoamento de Fluidos. 1999. 366 p. Dissertação (Engenharia Mecânica) — UNIFEI.

CARVALHO, S. R. Determinação do Campos de Temperatura em Ferramentas de Corte Durante um Processo de Usinagem por Torneamento. 2005. Tese (Engenharia Mecânica) — Universidade Federal de Uberlândia.

CHEN, X.; HAO, Z. Biomimetic layered fiber-reinforced Ti–Al composites: Effects of vari-ous- parameters on their strength and ductility through finite elementanalysis. **Materials & Design**, v. 209, 2021.

CUI, M. *et al.* A modified Levenberg–Marquardt algorithm for simultaneousestimation of multi- parameters of boundary heat flux by solvingtransient nonlinear inverse heat conduction problems. International **Journal of Heat and Mass Transfer**, v. 87, p. 908 – 916, 2016. ISSN 00179310.

CUI, M. *et al.* A new approach for determining damping factors in Levenberg-Marquardt al-gorithm for solving an inverse heat conduction problem. **International Journal of Heat and Mass Transfer**, v. 107, p. 747 – 754, 2017. ISSN 00179310.

GRZESIK, W. *et al.* Finite Difference Analysis of the Thermal Behavior of Coated toll in Orthogonal Cutting of Steels**. International Journal of Machining Tools and Manufacture**, v. 44, p. 1451 – 1462, 2004.

GRZESIK, W. *et al*. Modeling of the Cutting Processs Analytical and Simulation Methods. **Advances ins Manufacturing Science and Technology**, v. 33, p. 5 – 29, 2009.

GU, W*. et al.* Thermal oxidation behavior of WC-Co hard metal machining tool tip scraps. **Journal of Materials Processing Technology**, v. 212, n. 6, 2012. ISSN 09240136.

JIANG, F*. et al*. Estimation of Temperature-Dependent Heat Transfer Coefficients in Near-Dry Cutting. **International Journal of Advanced Manufacturing Tehcnology**, v. 86, p. 1207 – 1218, 2016.

KENDALL, G. Would your mobile phone be powerful enough to get you to the moon? 2019. Disponível em: https://www.spacedaily.com/reports/Would_your_mobile_phone_be_powerful_enough_to_get_you_to_the_moon_999.html. Acesso em: 31/09/2021.

LEE, S. *et al.* Investigation on failure analysis and optimization of WC–Co hard metals after long-term use in a bottle cap forming machine**. International Journal of Refractory Metals and Hard Materials**, v. 74, p. 99 – 106, 2018. ISSN 22133917.

LEVENBERG, K. A method for the solution of certain nonlinear problems in least. Quart. Appl. Math., p. 164 – 168, 1944.
MACHADO, A. R.; SILVA, M. B. da. Usinagem dos Metais. 8. ed. Uberlândia: [s.n.], 2004.

MARQUARDT, D. An algorithm for least-squares estimation of nonlinear parameters**. SIAM Journal on Applied Mathematics**, 11(2), 431–441, 1963.

SAMPAIO, P. A stabilized finite element method for incompressible flow and heat transfer: A natural derivation based on the use of local time-steps. **Computer Methods in Applied Mechanics and Engineering**, v. 195, p. 6177 – 6190, 2006. ISSN 00457825.

SODRÉ, U. Equações Diferenciais Parciais. 2003. Disponível em: http://www.uel.br/projetos/ matessencial/superior/pdfs/edp.pdf. Acesso em: 31/09/2021.

TORRES, V. *et al.* Estimation of distributed heat flux parameters in localized heating processes. **International Journal of Thermal Science**, v. 116, 2021. ISSN 12900729.

VEGA-SUAREZ, J. *et al.* Thermal conductivities estimation in orthotropic materials making use of global optimization algorithms. **DYNA (Colombia**), v. 85, n. 205, p. 140 – 147, 2018. ISSN
00127353.

WU, S*. et al.* Risk assessment of vertebral compressive fracture using bone mass index and strength predicted by computed tomography image based finite element analysis. **Clinical Bio-mechanics**, v. 85, 2021. ISSN 18791271.

CHAPTER 8

HYPHANET ALGORITHM FOR EFICIENTE ROUTING IN AD HOC MOBILE NETWORKS

Clovis Ronaldo da Costa Bento
Doctor of Science, Specialization: Telecommunications and Networks
Universidade Tecnológica Federal do Paraná (UTFPR)
E-mail: clovisbento@utfpr.edu.br

Emilio Carlos Gomes Wille
PhD in Electronics and Telecommunications Engineering
Politecnico di Torino (POLITO)
E-mail: ewille@utfpr.edu.br

ABSTRACT: This work presents new perspectives on the bio-inspired routing algorithm based on fungal networks, called HyphaNet, designed for mobile ad hoc net-works (MANETs). Usually, communication network algorithms are based on the behavior of social insects such as bees, ants, fireflies, beetles, among others. However, HyphaNet breaks this paradigm and proposes a model based on fungal colonies, as these beings survive by developing adaptive, resilient, and efficient networks of hyphae for communication and nutrient transport. Hy-phaNet is inspired by the survival dynamics of fungi, in a multidisciplinary way associating the areas of engineering and biology. As a routing protocol for MANETs, HyphaNet is reactive and multipath. New simulations using NS-2.35, with more exact parameters, show improved performance, with lower delay in low mobility scenarios, superior delivery rate, and reduced packet loss, when compared to both classic protocols and those bio-inspired by ants.

KEYWORDS: Bio-Inspired Routing, Fungal Colony, *HyphaNet*, MANETs.

RESUMO: Este trabalho apresenta novas perspectivas sobre o algoritmo de roteamento bioinspirado em redes de fungos, denominado HyphaNet, projetado para redes móveis ad hoc (MANETs). Usualmente, algoritmos de redes de comunicação são baseados no comportamento de insetos sociais como abelhas, formigas, vaga-lumes, besouros, entre outros. Entretanto, o HyphaNet quebra este para-digma e propõe um modelo baseado nas colônias de fungos, pois estes seres sobrevivem desenvolvendo redes de hifas adaptativas, resilientes e eficientes na comunicação e transporte de nutrientes. O HyphaNet se inspira na dinâmi-ca de sobrevivência dos fungos, de forma multidisciplinar associando as áreas da engenharia e da biologia. Como um protocolo de roteamento para MANETs, o HyphaNet é do tipo reativo e multipath. Novas simulações com o NS-2.35, com parâmetros mais exatos, mostram melhoria no desempenho, com menor atraso em cenários de baixa mobilidade, taxa de entrega superior e perda de pacotes reduzida, quando comparado tanto com protocolos clássicos ou bioinspirados em formigas.

PALAVRAS-CHAVE: Roteamento Bioinspirado, Colônia de Fungos, *HyphaNet*, MANETs.

1. INTRODUCTION

Ad hoc mobile networks, known by the acronym MANETs, are a highly significant technology today. In the current landscape, mobile networks enable new applications in specific areas, such as:

a) Vehicular Networks, VANETs (Vehicular Ad Hoc Networks). These are vehicular networks characterized by a high degree of mobility (Bitam; Mellouk, 2014);

b) Wireless Sensor Networks (WSN). Networks for detecting events of interest, where energy is a scarce resource and mobility is low (Jin, et al., 2017);

c) Flying Ad Hoc Networks (FANETs). These are networks composed of unmanned aerial vehicles, featuring high mobility and remote connectivity (Guillen-Perez, et al., 2016);

d) Robot Networks, RWSN (Robotic Wireless Sensor Networks). A set of robots with communication and cooperation capabilities (Ghosh, et al., 2017).

e) Delay-Tolerant Networks, DTNs. These are known as opportunistic networks that tolerate disconnections (Yuxin, et al., 2019).

f) Wireless Mesh Networks (WMNs). More generic networks with little or no mobility (Ducatelle, 2007).

The greatest challenges facing MANETs are related to performance issues, due to the mobility and limited resources of the nodes (processing power, buffer storage space, and power consumption). Consequently, new protocols are frequently proposed by academia to advance MANETs. Similarly, industry develops and optimizes hardware for wireless communication, such as Wi-Fi, ZigBee, Bluetooth, LoRa, among others.

This work aims to demonstrate that fungal colonies can serve as objects for bio-inspiration and be compared to communication networks, based on how they communicate internally, demonstrating intelligence in distributing food and developing.

In particular, there is a notable example that relates fungal interconnection to railway line routes. This is Tero’s experiment (Tero, et al., 2010), which demonstrates fungi’s ability to solve routing problems.

In the experiment, the slime mold Physarum polycephalum was cultivated to simulate the interconnection of railway stations in Tokyo and its metropolitan area. To represent the scenario, oat flakes were placed on a layout depicting the major cities in positions corresponding to the map of the Tokyo region.

The initial slime mold was placed in a central position, representing Tokyo. To complete the setup, obstacles were simulated, such as mountains, rivers, lakes, and others. Initially, the slime mold densely covered the area; later, it thinned out, leaving only the most robust branches connecting the food sources.

The resulting network was strikingly similar to Tokyo's current railway system.

Figure 1 shows the similarity between the two topologies: the one built by the fungus and the actual Tokyo railway network.

Figure 1. Experiment with *Physarum polycephalum* for the interconnection of Tokyo's subway stations.

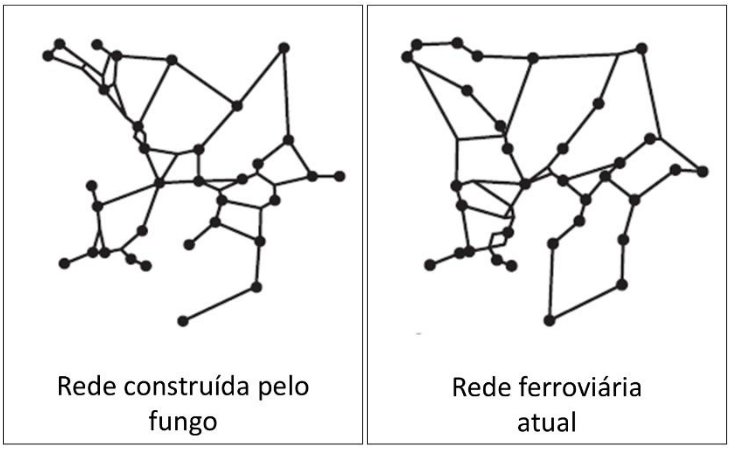

Source: (TERO, et al., 2010)

The authors conclude that the fungus *Physarum polycephalum* is capable of constructing networks with optimized topology.

Although the idea of copying nature is an old one, bioinspiration as a formal discipline and defined term emerged in the mid-20th century. The popularization of the term and the modern concept of biomimicry, as a systematic approach to solving sustainable problems, is often attributed to scientist and writer Janine Benyus, with her book "Biomimicry: Innovation Inspired by Nature," published in 1997 (Benyus, 1997). Since then, bio-inspired algorithms have been developed for application in computer science, logistics, and communication networks based on the behavior of social insects, swarms, and, in this work, fungi. Accordingly, this paper analyzes HyphaNet, a routing protocol for MANETs developed based on the observation of fungal colonies, whose performance has shown promise for future research and applications in MANETs (Bento; Wille, 2020).

The main contributions of this paper are:

a) HyphaNet as a proposed routing algorithm for MANETs;
b) An update to HyphaNet's parameters to improve performance;
c) New simulations using NS-2.35, with new scenarios and different types of traffic.

This article is organized as follows: Section 2 lists some of the main routing algorithms for MANETs. Section 3 presents a description of the HyphaNet algorithm, covering message types, route selection, and the concept of attractiveness. Section 4 presents the results of HyphaNet simulations in comparison with two well-known routing algorithms: AODV (Perkins, et al., 2003) and SARA (Correia; Vazão, 2010).

Finally, Section 6 presents the conclusions reached and suggestions for future work.

2. THEORETICAL FRAMEWORK

This section provides a theoretical framework on MANETs and concepts that enable a comparison between traditional networks and bio-inspired networks.

2.1 *AD HOC* MOBILE NETWORKS (MANETS)

MANETs consist of networks of mobile wireless communication devices that operate in a decentralized manner, using multi-hop routing, where nodes function as both endpoints and relay routers without any fixed infrastructure (Verma, 2025). Because it is a mobile network, its topology is dynamic and it possesses self-organizing capabilities to maintain communication processes (Srivastra; Raghav, 2017) (Abolhasan, *et al*., 2004) (Mueller, *et al*., 2004).

MANET Routing MANET protocols can be classified according to the type of routing they use:

Roteamento reativo: roteamento sob demanda (*on-demand*), precisam realizar a descoberta de rotas sempre que iniciarem uma nova transmissão de dados, exceto se ja houver rota disponivel para o destino. Exemplos: AODV (Marina; Das, 2006) e DSR (Johnson, *et al*., 2007);

a) Proactive routing: In this proactive (or table-driven) type, protocols periodically exchange topology information, systematically generating and maintaining routes even in the absence of traffic. Examples: DSDV (Lee, et al., 2005) and OLSR (Clausen; Jacquet, 2003);

b) Hybrid routing: In hybrid routing, protocols operate both proactively and reactively. Examples: HWMP and ZPR.

c) Bio-inspired routing: These are based on nature, social insects, swarm intelligence, or fungi. For example: ant colonies (Ant Colony Optimization—ACO) (Srivastra; Raghav, 2017), examples of which include SARA (Correia, Vazão, 2010) and AntHocNet (Di Caro, et al., 2005), those inspired by bee swarms (Artificial Bee Colony—ABC), such as the Bee-MANET protocol (Albayrak; Zengin, 2014), and fireflies (Firefly Algorithm—FA) (Yang, 2010). There are also proposals inspired by krill swarms (a species of crustacean) (Krill Herd Optimization - KHO) (Abualigah, et al., 2024), wolf packs (Gray Wolf Optimizer Algorithm - GWO) (Mirjalili, et al., 2014), cuckoo birds, bats, elephants, among others.

2.2 HYPHANET ALGORITHM

HyphaNet is a routing algorithm for MANETs inspired by the behavior of fungal colonies. The routing is reactive, multipath, and operates within the TCP/IP architecture. The route selection process is probabilistic, and the routing metric is based on the concept of "node attractiveness," inspired by the nutrient transport process in fungal networks (Bento; Wille, 2020).

According to microbiology, fungi are eukaryotic organisms, either unicellular or multicellular, with microscopic or macroscopic structures, and are aerobic or anaerobic, heterotrophic or facultative (Lindahl; Olsson, 2004). Fungi grow from the germination of spores and develop a structure called fungal mycelium. This growth is based on the distribution of nutrients that the fungus absorbs from the soil. These nutrients, called mobile biomass, are transported from the source toward their destinations; in this case, the destinations are the hyphae at the ends of the mycelium. The hyphae, in turn, are physical, tubular structures of fungal growth that originate from the spores. With the expansion and branching of the hyphae, networks are formed for the absorption, recycling, and transport of nutrients (mobile biomass) to the mycelium (Olsson, 2001). Flows follow routes within the hyphal network, managed by the nutrient transport process to ensure efficient distribution of mobile biomass to the fungal mycelium. As a route is used, the hyphae's structure is reinforced, resulting in the thickening of their walls, while idle hyphae are recycled and disappear. This process of reinforcing active routes through hyphal thickening is achieved by converting a fraction of mobile biomass into immobile biomass. The higher the concentration of immobile biomass in a hypha, the greater its attractiveness to new nutrient flows. Thus, more structured regions of the mycelium have greater capacity to attract and transport flows between distant points within the colony. Therefore, the flow of nutrients within the mycelium is a combination of two types of biomass: mobile biomass and immobile biomass (Olsson, 1995). This concept of attractiveness provides inspiration for route optimization in communication networks.

In the literature, there is an analogy between fungal networks and communication networks originally proposed in the FUNNet protocol (Xu, et al., 2009). Table 1 illustrates this analogy between the two networks.

Table 1. Fungal network vs. Communication network.

Fungal network Communication network	**Fungal network Communication network**
Hyphae Connections between nodes	Hyphae Connections between nodes
Hyphae tips Network nodes	Hyphae tips Network nodes
Mycelium Total network or routing table	Mycelium Total network or routing table
Mobile biomass Data traffic	Mobile biomass Data traffic
Mobile biomass transport mechanism Routing rules	Mobile biomass transport mechanism Routing rules
Stationary biomass Capacity or attractiveness	Stationary biomass Capacity or attractiveness
Biomass recycling Interaction between data traffic and flow attraction	Biomass recycling Interaction between data traffic and flow attraction
Biomass consumption Reduction in data traffic attraction over time	Biomass consumption Reduction in data traffic attraction over time
Nutrient absorption	Nutrient absorption Generation of data

Generation of data packets for transmission	packets for transmission
Hyphae death Disconnection of the link	Hyphae death Disconnection of the link

Source: Xu, *et al*., 2009

2.2.1 Types of HyphaNet messages

HyphaNet uses a set of messages to keep the system running, performing functions such as route discovery and maintenance, connection failure recovery, and data delivery acknowledgments. The HyphaNet messages are described in Table 2.

2.2.2 Route discovery

The route discovery process uses RREQUEST messages sent over the network from the source until the destination is found, and occurs when no route information is available in the routing table. In this process, the discovered routes are recorded in a database containing routing information for all nodes along the discovered path. To reduce the overhead in this process, HyphaNet adopts the CNB (Controlled Neighbor Broadcast) method to reduce broadcast messages (Mirza; Zhang, 2006).

Table 2. Types of messages.

Type Message Description	**Type Message Description**	**Type Message Description**
0 HELLO *Hello*. Periodic exchange of information between neighboring nodes.	0 HELLO *Hello*. Periodic exchange of information between neighboring nodes.	0 HELLO *Hello*. Periodic exchange of information between neighboring nodes.
1 RREQUEST *Route Request*. Route discovery initiated by the source node.	1 RREQUEST *Route Request*. Route discovery initiated by the source node.	1 RREQUEST *Route Request*. Route discovery initiated by the source node.
2 RREPLAY *Route Reply*. Confirmation of route discovery, generated by the destination node.	2 RREPLAY *Route Reply*. Confirmation of route discovery, generated by the destination node.	2 RREPLAY *Route Reply*. Confirmation of route discovery, generated by the destination node.
3 RERROR	3 RERROR *Route*	3 RERROR *Route Repair.* Error message

Route Repair. Error message generated by the node identifying a link failure after a failed repair attempt.	*Repair.* Error message generated by the node identifying a link failure after a failed repair attempt.	generated by the node identifying a link failure after a failed repair attempt.
4 RREPAIR-REQ *Route Repair Request*. Route repair request initiated by the node identifying a link failure.	4 RREPAIR-REQ *Route Repair Request*. Route repair request initiated by the node identifying a link failure.	4 RREPAIR-REQ *Route Repair Request*. Route repair request initiated by the node identifying a link failure.
5 RREPAIR-REP *Route Repair Reply*. Confirmation of repair of a failed link.	5 RREPAIR-REP *Route Repair Reply*. Confirmation of repair of a failed link.	5 RREPAIR-REP *Route Repair Reply*. Confirmation of repair of a failed link.
6 HYPHA-ACK *Hypha acknowledgment*. Confirmation of data delivery and distribution of mobile biomass.	6 HYPHA-ACK *Hypha acknowledgment*. Confirmation of data delivery and distribution of mobile biomass.	6 HYPHA-ACK *Hypha acknowledgment*. Confirmation of data delivery and distribution of mobile biomass.

Source: Bento, 2020

2.2.3 Route selection

In HyphaNet, the routes with the highest concentration of immobile biomass attract data flow because they have greater transport capacity. In fungi, this forms the basis of the concept of attractiveness to indicate the most suitable path for nutrient transport; by analogy, in HyphaNet it is used to select the best path. Attractiveness, therefore, is information recorded in the routing tables of the network nodes and indicates the best route for the data flow. Equation 1 shows the calculation of the attractiveness G of a node j, as a function of immobile biomass and the available space in the buffer. In this case, the available space in the buffer (ABS) corresponds to Quality of Service (QoS) information.

$$G_j = I_j^{\mu} . ABS_j^{\Omega} \qquad (1)$$

where:

$\mathrm{G_j}$ = node attractiveness j;

$\mathrm{I_j}$ = biomass associated with the node j;

ABS = available space in the node's buffer j;

μ = HyphaNet parameter for adjusting the sensitivity of I;

Ω = HyphaNet parameter for adjusting the sensitivity of ABS;

Thus, equation 2 calculates the route selection probability for each node i in the network to select a route toward a destination.

$$P_{i_n}^{d} = G_n . \left(\sum_{j \in N_i^d} G_j\right)^{-1}, \qquad \forall\ n \in\ N_i^d \qquad (2)$$

where:

$P_{i_n}^{d}$ = probability that node i selects n as the route to the destination d;

G = node attractiveness;

N_i^d = the neighborhood of i that contains a path to the destinationd.

2.2.4 Attractiveness Update

The attractiveness update model essentially consists of updating HyphaNet routes and comprises two distinct stages: pre-update and post-update. These stages are responsible for updating the stationary biomass value of each node within the active routes. In this model, the most frequently used routes will experience an increase in stationary biomass and a higher probability of being selected. The pre-update stage occurs during the data packet's journey to its destination, during which the data packet, in addition to transporting data, performs pre-update functions and collects information from buffers along the path. In this process, the source, when transmitting a data packet, generates a quantity E of fictitious mobile biomass that will be distributed to all nodes along the path, and the fraction of biomass for each node depends on the distance R, indicating the number of hops between source and destination. Thus, shorter routes tend to have a higher concentration of immobile biomass over time.

Equation 3 through 8 show the pre-updating model.

$$M_k = M_k + \frac{E}{R^2} \qquad (3)$$

$$\lambda_k = \alpha . M_k \qquad (4)$$

$$M_k = M_k - \lambda_k, \quad se \;\; M_k > \lambda_k \qquad (5)$$

$$I_k = I_k + \lambda_k \qquad (6)$$

$$I_k = \beta . I_k \qquad (7)$$

$$I_k = I_M \quad se \quad I_k > \epsilon \qquad (8)$$

where:

$M_k =$ the cumulative mobile biomass at each node k along the route;
$E =$ amount of fictitious mobile mass generated at the source;
$R =$ distance in jumps between the origin and destination;
$\lambda =$ indicates mobile biomass converted into immobile biomass;
$\alpha =$ conversion factor;
$I_k =$ accumulated biomass at each node k along the rotationa;
$\beta =$ degradation factor;
$I_M =$ maximum biomass at each node;
$\epsilon =$ upper limit of biomass;

Equation 3 shows the amount of mobile biomass M accumulated at each node k after distribution along the route. In equation 4, l denotes the mobile biomass converted to immobile biomass, and a is the conversion factor. Equation 5 corresponds to the reduction in the concentration of mobile biomass due to conversion. Equation 6 shows the increase in immobile biomass at node k, and equation 7 shows the recycling, or degradation, of a fraction of the biomass I, where b is the degradation factor. Equation 8 represents the control of immobile biomass to avoid the maximum limit IM, and the quantity ϵ is a control parameter. Convergence of the algorithm is ensured if the values a and b are less than one. Thus, in this first stage and according to data traffic, the system converts mobile biomass into immobile biomass, similar to fungi, resulting in the optimization of shorter routes over time.

The second stage, called post-update, is executed whenever the data packet is successfully delivered to the destination. Thus, the destination generates a confirmation message called HYPHA-ACK, which returns via the same path as the data. During the return, the fictitious mobile mass E will be redistributed to all nodes along the path, but using different criteria. Thus, the criteria used will be distance (in hops) and the occupancy of the buffers along the path between source and destination. Equations 9–16 show the post-update model.

$$ABS_k = \left(1 - \frac{L_k}{B_k}\right) \qquad (9)$$

$$\Lambda_k = R^{-2} \sum_j ABS_k \qquad (10)$$

$$M_k = M_k + E\Lambda_k, \qquad (11)$$

$$\lambda_k = \alpha . M_k \qquad (12)$$

$$M_k = M_k - \lambda_k, \quad se \;\; M_k > \lambda_k \qquad (13)$$

$$I_k = I_k + \lambda_k \qquad (14)$$

$$I_k = \beta . I_k \qquad (15)$$

$$I_k = I_M \quad se \quad I_k > \epsilon \qquad (16)$$

where:

ABS_k = buffer utilization for each node k along the route;
L_k = amount of buffer space used by the node k;
B_k = node buffer size k;
R = distance in jumps between the origin and destination;
Λ = indicates the route quality factor;
α = conversion factor;
I_k = the accumulated biomass at each node k along the route;
β = degradation factor;
I_M = maximum biomass at each node;

$\epsilon = \text{upper limit of biomass;}$

Equation 9 shows the occupancy of the buffer at node k, which belongs to the route, where Bk is the buffer size and Lk is the amount occupied. Therefore, the objective is to promote the highest-quality route according to the variable Λ, as shown in equation 10. Thus, each node receives a fraction E.Λ to accumulate in its mobile biomass, according to equation 11. Equation 11 through 16 show the remainder of the post-update model, with an objective identical to the previous case. Thus, in this stage, the shortest and highest-quality routes that successfully deliver packets tend to accumulate more immobile biomass over time. Therefore, this model results in the optimization of the shortest and least congested routes, according to data flow, in a system that converts mobile biomass into immobile biomass, similar to fungi.

2.2.5 Convergence test

To verify that HyphaNet is functioning correctly, a convergence test was conducted using the fixed topology with 18 nodes shown in Figure 2, in which there are two data sources, S1 and S2, and a single destination, D. The objective is to test the algorithm in two scenarios and observe the behavior of the data traffic.

Figure 2. Fixed topology with 18 nodes for convergence testing.

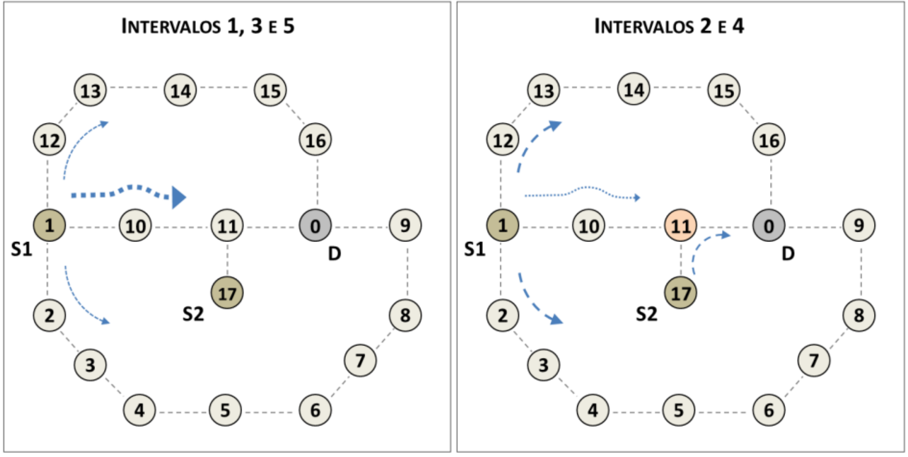

Source: Bento, 2020

Source S1 sends data to destination D continuously for five time slots. In the first scenario, only S1 sends data; in the second scenario, S2 transmits during time intervals two and four. At the start, there will be traffic only between S1 and D, and the protocol, being multipath, will construct the three possible routes between source and destination, which are: Route 1 (1-12-13-14-15-16-0), Route 2 (1-10-11-0), and Route 3 (1-2-3-4-5-6-7-8-9-0); after a few iterations, the algorithm will converge to the most suitable route. In this experiment, the NS-2.35 simulator and HyphaNet were used, configured with the same parameters as in Section 3. Figure 3 shows the graph of route usage. This value represents the number of times the route was selected by source S1, relative to the total number of data packets transmitted. The result shows that Route 2 was the most used in intervals 1, 3, and 5 (following probability logic) and there was a distribution of usage in intervals 2 and 4 due to the bottleneck generated by the buffer of node 11. It can be observed, in this case, that the sum of the usages totals 100%. Therefore, the average probability and utilization values for Route 2 show that there was convergence to the best route in cases where there are no signs of buffer occupancy.

Figure 3. Fixed topology with 18 nodes for convergence testing.

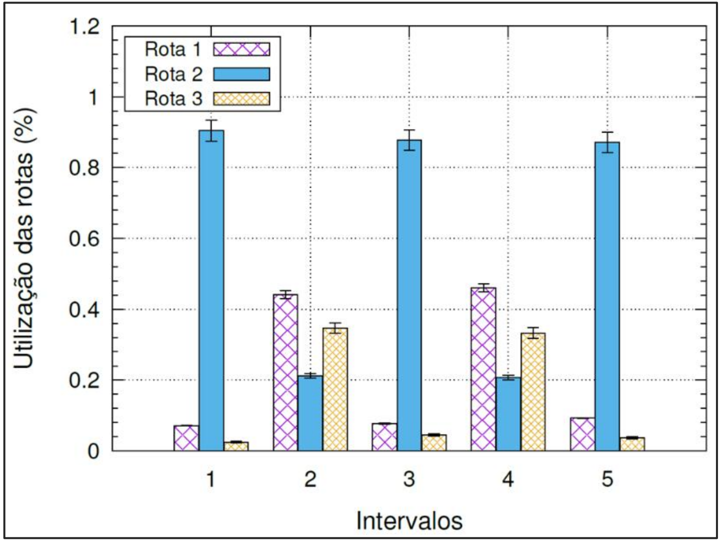

Source: Bento, 2020

3. SIMULATION AND ANALYSIS

To verify HyphaNet’s performance, new simulations were conducted using NS-2.35 software. HyphaNet’s operating parameters were updated and optimized. The results are presented as mean values and 95% confidence intervals. The network configurations, traffic type, and mobility model are listed below:

a) Link and physical layer: IEEE 802.11b (DCF) configured for a data rate of 11 Mbps and a basic frame control rate of 2 Mbps;

b) Propagation: Propagation/TwoRayGround with a range of 250 meters, Antenna/OmniAntenna, capture threshold in Watts CPThresh 10.0, carrier detection threshold CSThresh 3.59476e-10, reception threshold RXThresh 3.65262e-10;

c) Channel: Channel/WirelessChannel, bandwidth 11 MHz, Queue/DropTail/PriQueue;

d) Mobility model: RWP (Random WayPoint), speeds in the range [Vmin = 1, Vmax = 20] m/s, pause times: 0, 15, 30, 60, 120, and 240 s;

e) Traffic type: CBR/UDP, packet size and transmission rate vary according to the specific scenario; 6) Network topology: scenarios with 100 mobile devices over an area of 1000x1000 m²; Simulation duration: 180 s for all simulations.

The HyphaNet parameters used in all scenarios are shown in Table 3.

Figures 4 through 8 show a comparison of performance between the AODV, SARA, and HyphaNet protocols for the following metrics: delay, data transfer rate, and overhead, for a network scenario with 10 CBR/UDP traffic sources transmitting 512-byte packets at a rate of four packets per second. The mobility and traffic models were generated separately for each simulation.

Table 3. HyphaNet simulation parameters.

Parameter	**Descrição**
Interval between Hello messages	I_{HELLO} = 2 s
Conversion rate of mobile biomass to immobile biomass	α = 0,1
Fixed biomass recycling rate	β = 0,03
Sensitivity to fixed biomass	μ = 2,0
Sensitivity to buffer occupancy	Ω = 0,1
Maximum limit of fixed biomass	ϵ = 50
Initial mobile biomass	MMI = 0, 5
Initial fixed biomass	MII = 0, 5
Maximum mobile biomass	MM = 50
Global degradation rate	T_D = 0,95
Global degradation interval	I_D = 1, 0 s

Source: Prepared by the authors themselves.

Figure 4. Average packet delay.

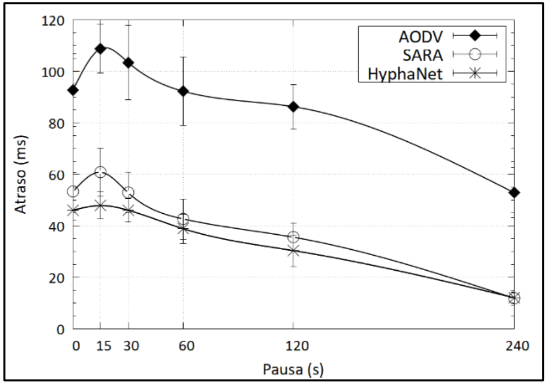

Source: Prepared by the authors themselves.

Figure 5. Delivery of packages.

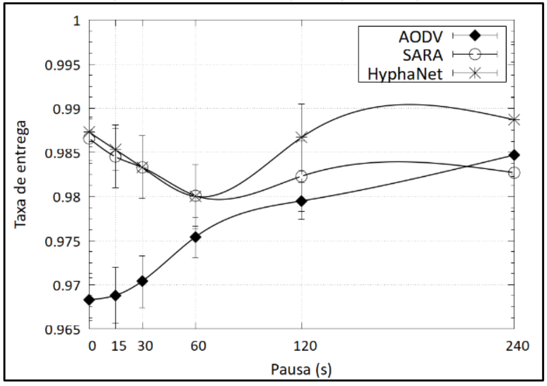

Fonte: Elaborardo pelos próprios autores.

In a first scenario involving variations in pause time, HyphaNet outperforms AODV and performs very similarly to SARA. Only in terms of overhead is HyphaNet less promising than AODV. HyphaNet exhibits significantly better values for delay, packet loss, and overhead than SARA. Regarding data transfer rate performance, no significant differences are observed between HyphaNet and SARA.

Figure 6. Transfer Rate.

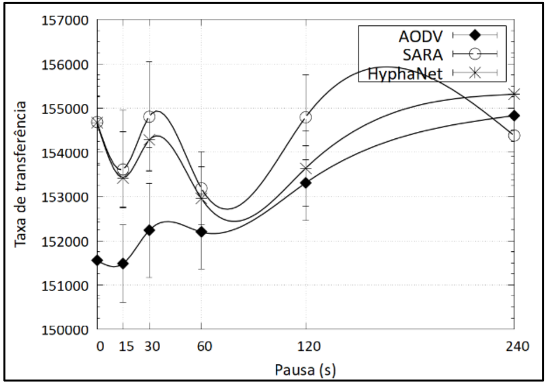

Source: Prepared by the authors themselves.

Figure 7. Overhead.

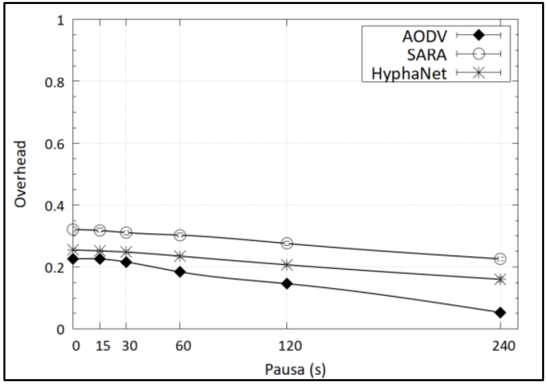

Source: Prepared by the authors themselves.

Figure 8. Packet loss.

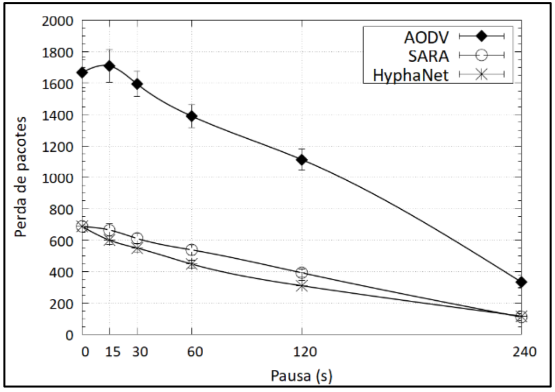

Source: Prepared by the authors themselves.

Figure 9. Delay for N sources.

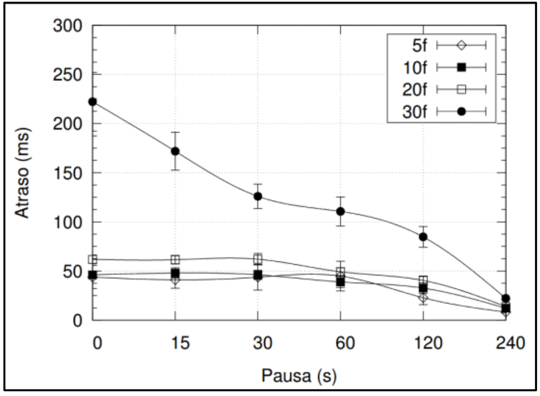

Source: Prepared by the authors themselves.

Figure 9 shows a comparison of AODV, SARA, and HyphaNet in terms of delay for a network scenario with varying numbers of transmitting sources and CBR/UDP traffic. In this scenario with varying numbers of sources, it can be observed that HyphaNet exhibits lower delay values than AODV and similar values to SARA, except in the case of 30 transmitting sources, where HyphaNet exhibited the highest delay among all. The throughput was similar across all protocols. Figure 10 shows the simulation results with varying transmission rates (2, 4, 6, and 8 pps) by the sources.

With varying transmission rates, HyphaNet exhibits lower delay values than AODV and similar to SARA, within the confidence interval. The throughput was similar across all protocols. Figure 11 shows the simulation results with varying packet sizes (64, 256, 512, and 1024 bytes). In this scenario of varying packet sizes, HyphaNet exhibits delay values lower than AODV and similar to SARA, within the confidence interval.

Figure 10. Delay for different shipping rates.

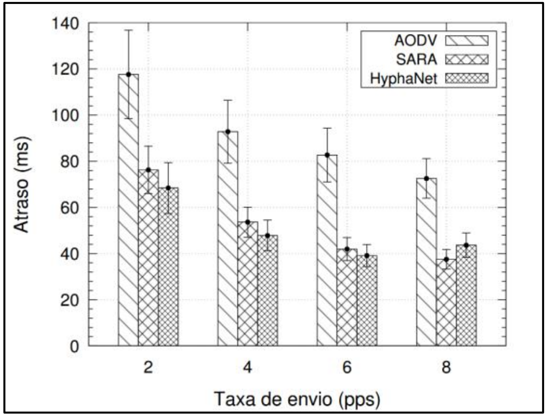

Source: Prepared by the authors themselves.

Figure 11. Delay for different package sizes.

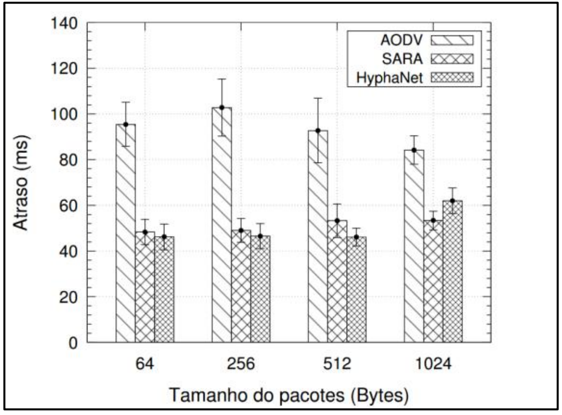

Source: Prepared by the authors themselves.

4. CONCLUSION

Based on the results obtained in the simulations using new parameters, HyphaNet demonstrated improved performance and showed promise as an alternative to bio-inspired protocols, both for future research and for applications in the field of mobile networks.

Validation tests confirmed that HyphaNet converges to more advantageous routes while exploring the search space. In simulations, HyphaNet demonstrated good performance in the metrics of packet delivery rate, average end-to-end delay, packet loss, and overhead.

Specifically, compared to AODV, the protocol showed better results, except for overhead, which was higher.

In direct comparisons with SARA, HyphaNet achieved similar performance in most scenarios. The reason for the inferior performance in some cases is related to the excess of acknowledgment messages (HYPHA-ACK) and the route repair mechanism, which are proportional to the volume of data traffic. However, the excess of messages appears to be beneficial when considering performance in terms of packet loss, which is the best among the simulated protocols, making HyphaNet the most robust of all. For future work, the challenge will be to reduce packet delay and overhead in traffic scenarios with more than 30 sources and rates higher than 8 pps, and to test the protocol in scenarios with more than 100 nodes.

REFERENCES

ABOLHASAN, Mehran; WYSOCKI, Tadeusz; DUTKIEWICZ, Eryk**. A review of routing protocols for mobile ad hoc networks**. *Ad Hoc Networks*, v. 2, p. 1-22, 2004.

ABUALIGAH, Laith; *et al*. **A review of krill herd algorithm: optimization and its applications**. In: *Metaheuristic Optimization Algorithms*. 2024. p. 231-239. ISBN 9780443139253.

ALBAYRAK, Z.; ZENGIN, A. **Bee-MANET: A new swarm-based routing protocol for wireless ad hoc networks.** *Electronics and Electrical Engineering*, v. 20, mar. 2014.

BENTO, Clovis; WILE, Emilio**. Hyphanet – um algoritmo para MANETs**. *IEEE*, mar. 2020, p. 367-375.

BENTO, Clovis R. C.; WILLE, Emilio C. G**. Bio-inspired routing algorithm for MANETs based on fungi networks.** *IEEE Transactions*, v. 107, 2020.

BENTO, Clovis Ronaldo da Costa. **Protocolo de roteamento bioinspirado para MANETs baseado em redes de fungos – HyphaNet**. 2020. Tese (Doutorado em ciências) - Área de concentração: Telecomunicações e Redes – Universidade Tecnológica Federal do Paraná (UTFPR), Curitiba, 2020.

BENYUS, Janine M**. Biomimicry: innovation inspired by nature**. New York: William Morrow & Company, 1997.

CLAUSEN, T.; JACQUET, P. **Optimized Link State Routing Protocol (OLSR).** *RFC 3626*. The Internet Society, 2003.

CORREIA, Fernando; VAZÃO, Teresa. **Simple Ant Routing Algorithm.** Ad Hoc Networks, v. 8, p. 810-823, nov. 2010.

DI CARO, Giani; DUCATELLE, Frederick; GAMBARDELLA, Luca Maria. **AntHocNet: an adaptive nature-inspired algorithm for routing in mobile ad hoc networks.** European Transactions on Telecommunications, v. 16, p. 443-455, 2005.

DUCATELLE, Frederick. **Adaptive routing in ad hoc wireless multi-hop networks**. 2007. Ph.D. Thesis (Doctoral Dissertation). IDSIA (Istituto Dalle Molle di Studi sull'Intelligenza Artificiale) - Faculty of Informatics, University of Lugano, Lugano, 2007.

GHOSH, Pradipta; KRISHNAMACHARI, Bhaskar; GASPARRI, Andrea; JIN, Jiong**. Robotic wireless sensor networks**. nov. 2017. DOI: 10.1007/978-3-319-92384-0_16.

GUILLEN-PEREZ, Antonio; *et al*. **WiFi networks on drones.** *IEEE*, nov. 2016. DOI: 10.1109/itu-wt.2016.7805730.

JIN, Wang; JU, Chunwei; KIM, Hye-jin; SHERRATT, R. Simon**. A mobile assisted coverage hole patching scheme based on particle swarm optimization for WSNs**. Cluster Computing, v. 22, dez. 2017. DOI: 10.1007/s10586-017-1586-9.

JOHNSON, David B.; MALTZ, David A.; HU, Yih-Chun. **The Dynamic Source Routing Protocol (DSR) for Mobile Ad Hoc Networks for IPv4.** RFC 4728. IETF Internet Draft, 2007.

LEE, U.; PARK, S.; MIDKIFF, S. F.; J. S. **Proactive routing protocol for multi-channel wireless ad-hoc networks (DSDV-MC).** In: International Conference on Information Technology: Coding and Computing (ITCC). IEEE, 2005.

LINDAHL, Björn D.; OLSSON, Stefan. **Fungal translocation – creating and responding to environmental heterogeneity.** Mycologist, v. 18, maio 2004.

LORAWAN ALLIANCE. **LoRaWAN: what is it? A technical overview of LoRa and LoRaWAN.** Technical Marketing Workgroup, 2015.

MARINA, Mahesh K.; DAS, Samir R**. Ad hoc on-demand multipath distance vector routing**. Wireless Communications and Mobile Computing, v. 6, 2006.

MELLOUK, Salim; BITAN, Abdelhamid**. Bio-inspired routing protocols for vehicular ad-hoc networks.** Wiley-ISTE, 2014.

MIRJALILI, Seyedali; MIRJALILI, Seyed Mohammad; LEWIS, Andrew. **Grey Wolf Optimizer.** Advances in Engineering Software, p. 46-61, 2014.

MIRZA, Muhammad; ZHANG, Yan. **Controlled neighbor broadcast in mobile ad hoc networks.** IEEE, 2006, p. 1-4.

MUELLER, S.; TSANG, R. P.; GHOSAL, D. (2004). **Multipath Routing in Mobile Ad Hoc Networks: Issues and Challenges.** In: Calzarossa, M.C., Gelenbe, E. (eds) Performance Tools and Applications to Networked Systems. MASCOTS 2003. Lecture Notes in Computer Science, vol 2965. Springer, Berlin, Heidelberg. https://doi.org/10.1007/978-3-540-24663-3_10

OLSSON, Stefan**. Colonial growth of fungi.** In: *Biology of the Fungal Cell*. Berlin: Springer, 2001.

OLSSON, Stefan. **Mycelial density profiles of fungi on heterogeneous media and their interpretation in terms of nutrient reallocation patterns**. Mycological Research, v. 99, fev. 1995.

PERKINS, C.; BELDING-ROYER, E.; DAS, S. **Ad hoc On-Demand Distance Vector (AODV).** *RFC 3561*. IETF, jul. 2003.

SRIVASTAVA, Niharika; RAGHAV, Piyush**. A review on swarm intelligence based routing algorithms in mobile ad hoc network.** In: 8th International Conference on Computing, Communication and Networking Technologies (ICCCNT). IEEE, jul. 2017;

TERO, A.; NAKAGAKI, S.; TAKAGI, T.; SAIGUSA, T.; ITO, K.; BEBBER, D. P.; FRICKER, M. D.; YUMIKI, K.; KOBAYASHI, R.; Y. T**. Rules for biologically inspired adaptive network design.** Science, v. 327, jan. 2010;

VERMA, Ridhi. **MANET – a wireless network: paradigm for multi-hop communication**. International Journal For Multidisciplinary Research – IJMR, Índia. V. 7, Issue 6, November-December. 2025. https://doi.org/10.36948/ijfmr.2025.v07i06.59629;

XU, Hao; FALCONER, Ruth; BRADLEY, David. **FUNNet – a novel biologically-inspired routing algorithm based on fungi.** IEEE, jul. 2009.

YANG, Xin She. **Firefly algorithm, Levy flights and global optimization**. Cambridge: University of Cambridge, 2010. arXiv:1003.1464v1.

YUXIN, Mao; LLORET, Jaime; ZHOU, Chenqian; LING, Yun. **An optimized probabilistic delay tolerant network (DTN) routing protocol based on scheduling mechanism for Internet of Things (IoT)**. Sensors, v. 19, p. 243, jan. 2019. DOI: 10.3390/s19020243.

CHAPTER 9

EVALUATION OF THE EFFICIENCY OF SILCAB-TYPE FILTERS FOR THE REMOVAL OF ANTIBIOTICS FROM WASTEWATER

Joana Elisa Willricha
Programa de Pós-graduação em Biotecnologia (UNIVATES)

Bruno Eduardo da Silvaa
Programa de Pós-graduação em Biotecnologia (UNIVATES)

Guilherme Schwingel Henna
Programa de Pós-graduação em Biotecnologia (UNIVATES)

Milena Libardonia
Programa de Pós-graduação em Biotecnologia (UNIVATES)

Gabriela Schabaccha
Programa de Pós-graduação em Biotecnologia (UNIVATES)

Ani Caroline Webera
Programa de Pós-graduação em Biotecnologia (UNIVATES)

Manoel Corrêa de Mello Netob
Dynamis world servisse

José Antonio Teixeira Alvesb
Dynamis world servisse

Elvio Leandro Burlania
Centro Universitário (UNIFTEC)

Lucélia Hoehnea
Programa de Pós-graduação em Ambiente e Desenvolvimento (UNIVATES)

ABSTRACT: The use of antibiotics is essential for treating infections; however, their overuse and improper disposal have contributed to wastewater contamination and increased bacterial resistance, posing risks to public health and the environment. These compounds, frequently present in domestic, hospital, and industrial effluents, are not completely removed by conventional treatment systems, thereby promoting the spread of resistant bacteria. Given this scenario, the study evaluated the efficiency of a filtration system using activated carbon and silver in removing the antibiotics ciprofloxacin and amoxicillin, as well as analyzing the toxicity of the treated effluent using the aquatic plant Lemna minor as a bioindicator. The analyses showed a rapid reduction in antibiotic concentration, especially in the first minutes of filtration, indicating high system efficiency. Ecotoxicological tests demonstrated that the treated effluent did not exhibit toxic effects, allowing for normal plant growth, unlike the untreated solutions. Thus, the filtration system proved to be an effective and environmentally safe alternative for the removal of antibiotics from contaminated water.

KEYWORDS: pharmaceuticals, bioaccumulation, toxicity, activated carbon.

RESUMO: O uso de antibióticos é essencial no tratamento de infecções, porém seu uso excessivo e descarte inadequado têm contribuído para a contaminação de águas residuais e para o aumento da resistência bacteriana, gerando riscos à saúde pública e ao meio ambiente. Esses compostos, frequentemente presentes em efluentes domésticos, hospitalares e industriais, não são completamente removidos pelos sistemas convencionais de tratamento, favorecendo a disseminação de bactérias resistentes. Diante desse cenário, o estudo avaliou a eficiência de um sistema de filtração com carvão ativado e prata na remoção dos antibióticos ciprofloxacina e amoxicilina, além de analisar a toxicidade do efluente tratado utilizando a planta aquática Lemna minor como bioindicadora. As análises mostraram uma rápida redução na concentração dos antibióticos, especialmente nos primeiros minutos de filtração, indicando alta eficiência do sistema. Os testes ecotoxicológicos demonstraram que o efluente tratado não apresentou efeitos tóxicos, permitindo o desenvolvimento normal das plantas, ao contrário das soluções não tratadas. Assim, o sistema de filtração se mostrou uma alternativa eficaz e ambientalmente segura para a remoção de antibióticos em águas contaminadas.

PALAVRAS-CHAVE: fármacos, bioacumulação, toxicidade, carvão ativado.

1. INTRODUCTION

Antibiotics are a class of drugs designed to kill or inhibit the growth of microorganisms, such as bacteria, fungi, and protozoa. They are widely used in the treatment of bacterial infections, including pneumonia, urinary tract infections, and skin infections. These drugs work by interfering with essential cellular processes in microorganisms, such as cell wall synthesis, protein production, and DNA replication. However, the excessive and inappropriate use of antibiotics has significantly contributed to the emergence of resistant bacteria, leading to serious consequences such as increased morbidity and mortality, prolonged illness duration, and rising public health costs (MUTEEB et al., 2023).

The presence of antibiotics in wastewater has become a growing global concern, posing a significant threat to both human health and the environment. These compounds, derived from prescription and over-the-counter medications, are frequently detected in domestic, hospital, and industrial effluents, as well as in surface waters. The main sources of contamination include the improper disposal of unused or expired medications, the excretion of antibiotics by humans and animals, and runoff from agricultural areas and veterinary facilities (GEVAO et al., 2022).

The persistence of antibiotics in the aquatic environment favors the selection of resistant bacteria and the spread of resistance genes, potentially causing damage to aquatic ecosystems and indirect risks to human health through exposure to contaminated water. This scenario highlights the limitations of conventional wastewater treatment systems, which often fail to completely remove these emerging contaminants (RAGAB et al., 2024; HEMDAN et al., 2024; ELFIKY et al., 2024).

Antibiotic resistance is characterized by the ability of bacteria to resist the effects of these drugs, rendering conventional treatments less effective or even ineffective (KHAN et al., 2024). This resistance can arise through various mechanisms, such as the production of enzymes capable of degrading antibiotics, the modification of target sites, and the development of efflux pumps that remove the drug from inside the bacterial cell, or through removal by adsorbents (REYGAERT, 2018).

Thus, it becomes necessary to seek more efficient and sustainable treatment alternatives. In this context, filtration systems stand out as a promising strategy for removing antibiotics from wastewater, especially when applied on an industrial scale. Industrial filters offer advantages such as operational simplicity, economic viability, and potential for large-scale application, and are considered a relevant alternative to conventional treatment methods (ELFIKY et al., 2024).

However, although antibiotic removal efficiency is a widely evaluated parameter, there remains a significant gap in the literature regarding the analysis of residual toxic effects following treatment processes. The mere removal of the contaminant does not necessarily guarantee the environmental safety of the treated effluent, since byproducts or residues may remain biologically active (RAGAB et al., 2024).

In this regard, conducting toxicity tests after treatment is essential for a more comprehensive assessment of the environmental efficacy of filtration systems. Bioindicator organisms, such as *Lemna minor*, have been widely used in ecotoxicological assays due to their high sensitivity to contaminants, rapid growth, ease of cultivation, and ecological relevance. Thus, the use of *Lemna minor* allows for an integrated assessment of the potential toxic effects of the treated effluent, contributing to the understanding of environmental impacts and the development of safer and more efficient strategies for treating wastewater contaminated with antibiotics (GEVAO et al., 2022; HEMDAN et al., 2024).In this context, the present study was conducted with the objective of evaluating the efficiency of a filtration system in removing the antibiotics ciprofloxacin and amoxicillin from an aqueous solution, as well as analyzing the toxicity of the treated effluent through an ecotoxicological assay using the aquatic plant *Lemna minor*.

As part of the methodology, an aqueous solution of the antibiotic ciprofloxacin was initially prepared at a concentration of 10 mg/L, along with a solution of the antibiotic amoxicillin at a concentration of 40 mg/L, both purchased from Sigma-Aldrich. A total volume of two liters of each of these solutions was passed through a filtration system consisting of an activated carbon filter combined with silver, operating in recirculation mode (Figure 1a). The filter was provided by Dynamis World Service. The flow-through reactor filtration processes took place over a total period of one hour at a flow rate of 20 L/h (Figure 1b), with samples of the two antibiotic solutions collected every ten minutes to monitor their removal.

Figure 1a. Photo of the carbon filter with silver particles and 1b Photo of the assembled flow-through system.

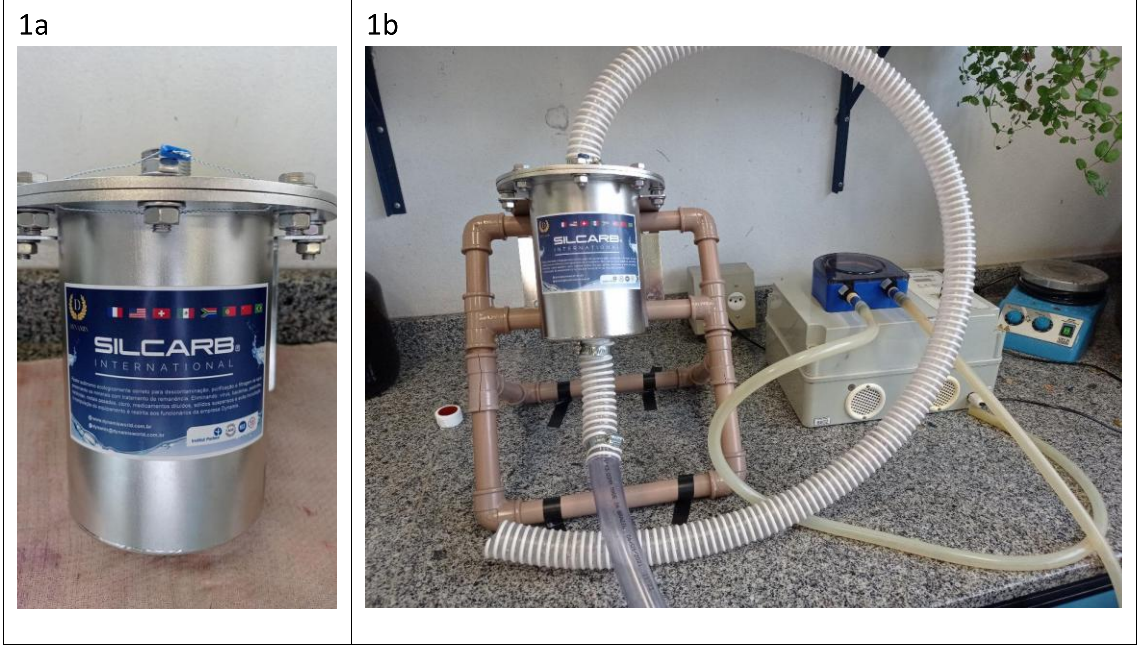
1a
1b

Source: Authors

The concentrations of ciprofloxacin and amoxicillin in the collected samples were determined by ultraviolet-visible (UV-Vis) absorption spectrophotometry, using quartz cuvettes and wavelengths of 275 nm and 278 nm, respectively. Spectrophotometric readings were taken immediately after each collection, allowing for the assessment of changes in antibiotic concentration over the filtration period.

To assess the toxicity of the treated effluent, ecotoxicological tests were conducted using the aquatic macrophyte *Lemna minor*. The assays were conducted using different dilutions of the filtered ciprofloxacin and amoxicillin solutions, collected thirty minutes after the start of the filtration process. The concentrations tested ranged from 100% to 0.78125% of the filtered solutions. In parallel, a comparative test was conducted using a solution of each of the two antibiotics at the same initial concentration (10 mg/L of ciprofloxacin and 40 mg/L of amoxicillin) for those not subjected to the treatment process, employing the same dilutions.

As experimental controls, the plants were also exposed to ultrapure water, considered a non-toxic medium, and to a potassium dichromate solution at a concentration of 1 mol/L, used as a positive toxicity control. The ecotoxicological assay lasted a total of seven days, during which the response of *Lemna minor* was observed, considering aspects such as development, growth, and coloration of the specimens.

The results obtained from spectrophotometric analyses and toxicity tests were used to evaluate the efficiency of the filtration system in removing ciprofloxacin and amoxicillin, as well as the environmental safety of the treated effluent. Figures 2 and 3 show the degradation curves of ciprofloxacin and amoxicillin over time, respectively.

Figure 2. Decay of the ciprofloxacin wavelength over time during the filtration process using Silcarb.

Source: Authors

Figure 3. Decay of the wavelength of amoxicillin over time during the filtration process using Silcarb.

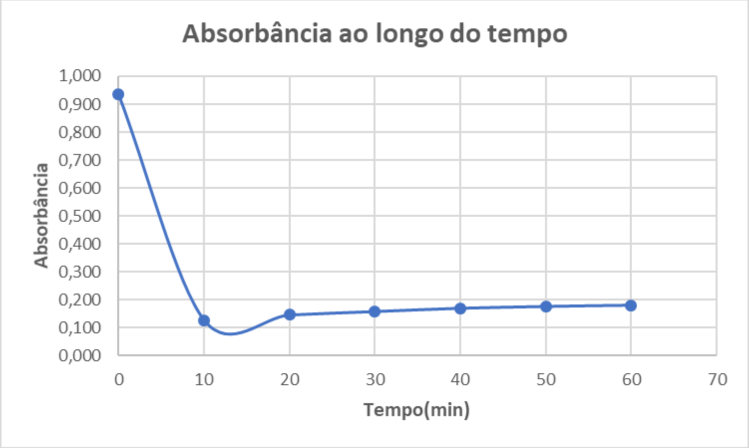

Source: Authors

As can be observed, spectrophotometric analyses indicated a rapid reduction in both the concentration of ciprofloxacin and amoxicillin in the filtered solutions, with a significant decrease already observed in the first samples, especially during the first 10 minutes of operation. These results demonstrate the high initial efficiency of the activated carbon filter combined with silver in removing the two antibiotics.

Furthermore, the ecotoxicological assessment conducted using the aquatic plant *Lemna minor* showed that the filtered solutions did not exhibit toxic effects on the tested plant organisms. The plants exposed to the treated effluent maintained healthy coloration and continued their development throughout the experimental period, in contrast to the specimens subjected to the unfiltered ciprofloxacin solution and the unfiltered amoxicillin solution, which exhibited virtually stagnant growth. These results confirm that the filtration process was capable not only of reducing the concentration of antibiotics but also of eliminating adverse effects associated with their presence in the aquatic environment.

Thus, the study demonstrates that the filtration system employed constitutes an efficient alternative for the removal of antibiotics, such as ciprofloxacin and amoxicillin, from contaminated water, combining high adsorption efficiency with the environmental safety of the treated effluent. The filtrates proved suitable for discharge into water bodies without exacerbating environmental impacts related to the bioaccumulation of antibiotics and the impairment of aquatic plant development

REFERENCES

GUO, Kexin; HAN, Lei; LUO, Jingyang; LU, Guanghua; LI, Yiping; LIU, Jianchao. Occurrence and accumulation characteristics of antibiotics in soil and effects on the carbon and nitrogen cycles. **Current Opinion in Environmental Science & Health**, pp. 1–16, 2025. Available at: https://doi.org/10.1016/j.coesh.2025.100619. Accessed on: Apr. 15, 2025.

XU, Yongtao; LI, Dan; YUAN, Ying; FANG, Fei; XI, Beidou; TAN, Wenbing. Antibiotic Resistance Occurrence and Ecological Impact in Landfill Leachate: A Review on the Compound Effect of Antibiotics and Non-antibiotics. **Emerging Contaminants**, pp. 1–42, 2025. Available at: https://doi.org/10.1016/j.encon.2025.100508. Accessed on: Apr. 15, 2025.

ELFIKY, A. A. et al. Environmental occurrence, fate, and removal of antibiotics from wastewater: a critical review. *Journal of Environmental Chemical Engineering*, vol. 12, no. 1, pp. 109–125, 2024.

GEVAO, B. et al. Sources, occurrence, and ecological risks of antibiotics in wastewater and surface water. *Environmental Research*, vol. 214, pp. 113–127, 2022.

HEMDAN, B. A. et al. Antibiotics in aquatic environments: impacts on ecosystems and human health. *Science of the Total Environment*, vol. 906, pp. 167–182, 2024.

KHAN, J. et al. Antibiotic resistance: global health threat and mitigation strategies. *Frontiers in Microbiology*, vol. 15, pp. 1–15, 2024.

MUTEEB, G. et al. Antibiotics and antimicrobial resistance: mechanisms and environmental implications. *Environmental Pollution*, vol. 325, pp. 121–135, 2023.

RAGAB, S. et al. Advanced wastewater treatment technologies for antibiotic removal. *Journal of Water Process Engineering*, vol. 55, pp. 104–118, 2024.

REYGAERT, W. C. An overview of the antimicrobial resistance mechanisms of bacteria. *AIMS Microbiology*, vol. 4, no. 3, pp. 482–501, 2018.

CHAPTER 10

PROPOSAL OF A NUMERICAL METHOD FOR APPROXIMATING THE SUM OF DERIVATIVES OF SINGLE-VARIABLE FUNCTION

Filipe Cardoso de Oliveira
Industrial Engineering Specialist
Universidade Tecnológica Federal do Paraná (UTFPR)
E-mail: eng.oliveirafilipe93@gmail.com

Julio Cesar Lombaldo Fernandes
Postdoctoral Fellow in Applied Mathematics
Universidade Federal do Rio Grande do Sul (UFRGS)
E-mail: julio.lombaldo@ufrgs.br

Edson Leite Araujo
Doctor of Computer Science
Universidade Federal do Vale do São Francsico (UNIVASF)
E-mail: edson.araujo@univasf.edu.br

Lino Marcos Silva
Doctor in Applied Mathematics
Universidade Federal do Vale do São Francsico (UNIVASF)
E-mail: lino.silva@univasf.edu.br

ABSTRACT: The paper proposes a numerical method for calculating the sum of derivatives at a point of a generic function y(x). The advantage of this method is that it does not require knowing the analytical derivative of the function to be approximated, only the original function y(x). The paper begins by discussing the importance of numerical methods in modern science, providing a brief history and overview of classical and advanced methods. The detailed approach of classical methods is then presented, including the bisection method, Newton-Raphson method, false position method, regula falsi method, and Horner's method. The paper then considers additional considerations and recent advances in numerical methods, including the selection of the appropriate method, the development of methods for large-scale problems, improving accuracy and reliability, and integrating methods with other areas of science and engineering. The paper concludes by emphasizing the importance of numerical methods in scientific and technological research, acknowledging their limitations, and highlighting the need for further research to improve their accuracy, efficiency, and reliability.

KEYWORDS: numerical methods, numerical approximation, algorithm development, error analysis.

RESUMO: O artigo propõe um método numérico para calcular a soma das derivadas em um ponto de uma função genérica y(x). A vantagem desse método é que ele não requer o conhecimento da derivada analítica da função a ser aproximada, apenas da função original y(x). O artigo começa discutindo a importância dos métodos numéricos na ciência moderna, fornecendo um breve histórico e uma visão geral dos métodos clássicos e avançados. Em seguida, é apresentada a abordagem detalhada dos métodos clássicos, incluindo o método da bissecção, o método de Newton-Raphson, o método da falsa posição, o método da regula falsi e o método de Horner. O artigo, então, considera considerações adicionais e avanços recentes em métodos numéricos, incluindo a seleção do método apropriado, o desenvolvimento de métodos para problemas de larga escala, a melhoria da precisão e confiabilidade e a integração de métodos com outras áreas da ciência e engenharia. O artigo conclui enfatizando a importância dos métodos numéricos na pesquisa científica e tecnológica, reconhecendo suas limitações e destacando a necessidade de mais pesquisas para melhorar sua precisão, eficiência e confiabilidade.

PALAVRAS-CHAVE: métodos numéricos, aproximação numérica, desenvolvimento de algoritmos, análise de erros.

1. INTRODUCTION

Numerical methods play a fundamental role in modern science and engineering, providing robust tools to solve complex mathematical problems that do not admit exact analytical solutions or whose complexity makes a purely theoretical approach unfeasible. These methods are widely used in various fields, such as engineering, physics, chemistry, mathematics, and economics, enabling the modeling and simulation of real-world phenomena with precision and efficiency [1, 2]. The history of numerical methods dates back to Ancient Greece, with Euclid using the bisection method to solve quadratic equations [1]. Over the centuries, mathematicians such as Niccolò Fontana Tartaglia made significant contributions to the development of these techniques, with notable advancements like the Newton-Raphson method, proposed in the 16th century [1]. With the advent of modern computing, numerical methods evolved rapidly, becoming indispensable for solving large-scale and highly complex problems. Currently, numerical methods are classified into two main categories: classical methods and advanced methods. Classical methods, such as bisection, Newton-Raphson, false position, and regula falsi, are characterized by their simplicity and robustness, although they may have limitations in large-scale or highly complex problems [2, 3]. On the other hand, advanced methods, such as finite elements, finite differences, and hierarchical methods, offer greater precision and efficiency but require more sophisticated implementations and a deep understanding of their theoretical foundations [6, 8]. In this context, this work proposes a new numerical method for calculating the summation of derivatives at a specific point of a generic function y(x). The main innovation of this method lies in its ability to approximate the summation of derivatives without requiring prior knowledge of the analytical expression of the function's derivative, using only the original function y(x). This approach offers significant flexibility, especially in situations where the analytical derivative is unknown, difficult to obtain, or computationally expensive to calculate. Furthermore, the proposed method has the potential to be applied to problems where the function is defined discretely or empirically, broadening its scope of applicability. The relevance of this work aligns with current trends in the field of numerical methods, which aim to develop more efficient, precise, and adaptable techniques for complex and large-scale problems. Recent advances include the development of parallel and distributed algorithms, hierarchical methods, and data compression techniques, which enable the solution of problems with millions or billions of variables [6, 8]. Additionally, the integration of numerical methods with other areas, such as artificial intelligence and machine learning, opens new perspectives for the optimization and automation of computational processes [7].

2. METHODOLOGY AND DERIVATION

2.1 METHODOLOGY

The construction of the mathematical model proposed in this work followed several steps, as detailed in this chapter. Methodologically, the research can be categorized as applied, with a quantitative approach, descriptive objectives, and the use of technical procedures such as modeling and simulation [4]. The applied nature of the work stems from its ability to generate knowledge. Regarding the research approach, it is classified as quantitative because it allows for the numerical quantification of variables, confirmation of cause-and-effect relationships, and the statistical acceptance or rejection of hypotheses [4]. The objectives are descriptive, as they seek to describe the characteristics of a phenomenon or the relationships between specific variables. In terms of technical procedures, we use modeling and simulation, representing the phenomenon of interest through a model that approximates the value of a function [4]. Concerning the objectives, the adopted methodology is based on the Normative Axiomatic research method. In this type of research, the researcher can propose new models or variations of existing models, employing known methods to solve problems and, eventually, developing new, more efficient methods [5]. The construction of the mathematical model follows the abstraction of the real system into an idealized system. Initially, the model is verbally described by the researcher as a conceptual model. Next, the conceptual model is transformed into a mathematical or analytical model, involving mathematical abstraction. It is important to note that simplifications can be applied to the mathematical model in relation to the real system, as long as they do not compromise its validity [5]. During the construction of the model, the researcher defines the variables to be considered and 3 the relationships between them. The deduction of the problem involves the use of mathematical techniques and, in more complex cases, algorithms. Subsequently, it is discussed whether the model found is consistent with the observed reality, preparing for the solution of the proposed model [5]. In the model solution phase, the researcher employs computational algorithms to solve the problem based on the previously developed model. These algorithms, generally known in the literature, can be implemented in specific software. Additionally, sensitivity tests are conducted to identify potential modeling errors or poor performance of the chosen algorithm [5].

2.2 DERIVATION

Let $y(x)$ be any function. We aim to calculate $\sum y'(x)$. Starting from the homogeneous ODE in (1), we have:

$$y'(x) - P(x)y(x) = 0 \tag{1}$$

$$y'(x) = P(x)y(x) \tag{2}$$

Integrating both sides, we obtain:

$$\int_a^b y'(x) = \int_a^b P(x)y(x) \tag{3}$$

By the fundamental theorem of calculus, it is possible to rewrite the equality in (3) as follows:

$$y(a) - y(b) = \int_a^b P(x)y(x) \tag{4}$$

A numerical approximation for the integral on the right-hand side of equation (4) can be obtained using the Monte Carlo method. Thus, we can rewrite equation (4) as follows:

$$y(a) - y(b) \approx \frac{b-a}{k} \sum_{i=1}^{k} P(x_i) y(x_i) \tag{5}$$

Returning to equation (3) and substituting the Monte Carlo approximation on both sides of the equation, we obtain the following approximation:

$$\frac{b-a}{k} \sum_{i=1}^{k} y'(x_i) \approx \frac{b-a}{k} \sum_{i=1}^{k} P(x_i) y(x_i) \tag{6}$$

Since $\frac{b-a}{k} \neq 0$ for all k, we can state that:

$$\sum_{i=1}^{k} y'(x_i) \approx \sum_{i=1}^{k} P(x_i) y(x_i) \tag{7}$$

Substituting (7) into (5) and manipulating algebraically, we arrive at the following equation:

$$\sum_{i=1}^{k} y'(x_i) \approx \frac{k[y(b) - y(a)]}{b-a} \tag{8}$$

A second derivation follows through the Mean Value Theorem, as shown below: Let $f : [a, b] \to R$ be a function continuous on the interval $[a, b]$ and differentiable on (a, b). Consider $P : a = x_0 < x_1 < x_2 < \cdots < x_n = b$ an equally spaced partition of $[a, b]$, that is:

$$\Delta x = x_1 - x_0 = x_2 - x_1 = \cdots = x_n - x_{n-1} = \frac{b-a}{n} \tag{9}$$

Applying the Mean Value Theorem to the interval $[x_{i-1}, x_i]$, it follows that there exists $c_i \in (x_{i-1}, x_i)$ such that:

$$f(x_i) - f(x_{i-1}) = f'(c)(x_i - x_{i-1}) \tag{10}$$

Therefore,

$$f'(c_i) = \frac{f(x_i) - f(x_{i-1})}{\Delta x} \tag{11}$$

Thus, by applying the summation operator to both sides of the equation, we obtain:

$$\sum_{i=1}^{n} f'(c_i) = \sum_{i=1}^{n} \frac{f(x_i) - f(x_{i-1})}{\Delta x} \tag{12}$$

$$\sum_{i=1}^{n} f'(c_i) = \frac{1}{\Delta x} \sum_{i=1}^{n} [f(x_i) - f(x_{i-1})] \tag{13}$$

$$\sum_{i=1}^{n} f'(c_i) = \frac{1}{\Delta x} [f(x_n) - f(x_0)] \tag{14}$$

Since $\Delta x = \frac{b-a}{n}$, we substitute into the final equation:

$$\sum_{i=1}^{n} f'(c_i) \approx \frac{n[f(x_n) - f(x_0)]}{b-a} \tag{15}$$

From this analysis, we derived two key equations that form the foundation of our proposed numerical method for approximating the summation of derivatives of a function. These equations, (8) and (15), provide a direct relationship between the summation of derivatives and the function values at the endpoints of the interval $[a, b]$. Specifically:

$$\sum_{i=1}^{k} y'(x_i) \approx \frac{k[y(b) - y(a)]}{b-a} \tag{16}$$

This equation expresses the summation of the derivatives $y'(x_i)$ at k points within the interval $[a, b]$ in terms of the function values at the endpoints $y(b)$ and $y(a)$. The parameter k represents the number of subdivisions or points used in the approximation, allowing for flexibility in balancing accuracy and computational effort.

$$\sum_{i=1}^{n} f'(c_i) \approx \frac{n[f(x_n) - f(x_0)]}{b-a} \tag{17}$$

Derived from the Mean Value Theorem, this equation similarly relates the summation of derivatives $f'(c_i)$ to the function values at the endpoints $f(x_n)$ and $f(x_0)$. Here, n represents the number of partitions in the interval, and c_i are points guaranteed by the Mean Value Theorem where the derivative equals the average rate of change over each subinterval.

These equations are innovative because they eliminate the need for explicit knowledge of the derivative $y'(x)$ or $f'(x)$. Instead, they rely solely on the function values at the endpoints of the interval, making the method highly practical for applications where the analytical form of the derivative is unknown or difficult to compute. Furthermore, the method is robust and applicable to any continuous and differentiable function on the interval $[a, b]$, ensuring its versatility across a wide range of problems.

The parameter k (or n) plays a crucial role in controlling the accuracy of the approximation. As k increases, the summation more closely approximates the true value of the integral of the derivative, providing a trade-off between computational effort and precision. This flexibility makes the method particularly suitable for large-scale problems or situations where computational resources are limited.

In summary, the proposed method offers a novel and efficient approach to approximating the summation of derivatives, leveraging fundamental principles of calculus and numerical analysis. By relying on function values at the endpoints and avoiding the need for explicit derivative calculations, this method represents a significant advancement in numerical techniques for solving problems involving derivatives. Future work could explore its application to higher-dimensional problems, optimization, and integration with machine learning algorithms, further expanding its utility in scientific and engineering domains.

3. RESULTS AND DISCUSSION

This work proposed and evaluated a novel numerical method for approximating the summation of the derivative of a function. The method was applied to the functions $y(x) = e^{2x}$ and $y(x) = ln(2x + 1)$ on the closed interval $[0, 2]$ using varying values of the parameter k. The results, presented in Tables 1 and 2, demonstrate that the proposed method provides accurate approximations of the summation of the derivative, even without prior knowledge of the analytical derivative. As k increases, the accuracy of the approximation improves significantly, indicating that the method effectively captures the behavior of the function. The simplicity and robustness of the method make it a valuable tool for approximating the summation of derivatives, particularly in situations where the exact form of the derivative is unknown or computationally expensive to obtain.

The performance of the method was evaluated through extensive tests, as summarized in Tables 1 and 2. For the exponential function $y(x) = e^{2x}$, the percentage error decreased from 46.77% for $k = 5$ to an impressive 0.00032% for $k = 655360$ (see Table 1). Similarly, for the logarithmic function $y(x) = ln(2x + 1)$ the error decreased from 32.84% for $k = 5$ to 0.00023% for $k = 655360$ (see Table 2). These results highlight the method's ability to achieve high precision with increasing computational refinement.

Table 1. Comparison of Real Value VS Approximation for the Function $y(x) = e^{2x}$

k	Real Value	Approximation	Error (%)
5	196,665	133,995	**46,76989%**
10	327,153	267,991	**22,07606%**
20	593,365	535,982	**10,70627%**
40	1128,454	1071,963	**5,26989%**
80	2199,971	2143,926	**2,61412%**
160	4343,674	4287,852	**1,30185%**
320	8631,414	8575,704	**0,64962%**
640	17207,062	17151,408	**0,32449%**
1280	34358,442	34302,816	**0,16216%**
2560	68661,244	68605,632	**0,08106%**
5120	137266,869	137211,264	**0,04053%**

10240	274478,130	274422,528	**0,02026%**
20480	548900,656	548845,056	**0,01013%**
40960	1097745,712	1097690,113	**0,00507%**
81920	2195435,824	2195380,225	**0,00253%**
163840	4390816,049	4390760,451	**0,00127%**
327680	8781576,500	8781520,901	**0,00063%**
655360	17563097,401	17563041,803	**0,00032%**

Source: Author (2025)

Table 2. Comparison of Real Value VS Approximation for the Function $y(x) = ln(2x + 1)$

k	Real Value	Approximation	Error (%)
5	5,345	4,024	**32,83627%**
10	9,310	8,047	**15,69490%**
20	17,326	16,094	**7,65359%**
40	33,405	32,189	**3,77740%**
80	65,586	64,378	**1,87643%**
160	129,959	128,755	**0,93511%**
320	258,712	257,510	**0,46678%**
640	516,221	515,020	**0,23319%**
1280	1031,241	1030,040	**0,11655%**
2560	2061,281	2060,081	**0,05826%**
5120	4121,361	4120,161	**0,02913%**
10240	8241,522	8240,322	**0,01456%**
20480	16481,844	16480,644	**0,00728%**
40960	32962,489	32961,288	**0,00364%**
81920	65923,777	65922,577	**0,00182%**
163840	131846,354	131845,154	**0,00091%**
327680	263691,508	263690,308	**0,00046%**
655360	527381,815	527380,615	**0,00023%**

Source: Author (2025)

The proposed method stands out for its simplicity, efficiency, and broad applicability. By relying solely on function values at the endpoints of the interval, it eliminates the need for explicit derivative calculations, making it particularly useful in practical scenarios where analytical derivatives are unavailable or difficult to compute. Furthermore, the method's convergence behavior, as demonstrated by the decreasing errors with increasing k (see Tables 1 and 2), underscores its reliability and effectiveness for a wide range of functions.

In conclusion, the proposed numerical method represents a significant advancement in the approximation of derivative summations. Its simplicity, combined with its demonstrated accuracy and robustness, makes it a powerful tool for both theoretical and applied mathematics. Future research could explore its extension to higher-dimensional problems, optimization tasks, and integration with machine learning algorithms, further expanding its utility in scientific and engineering domains. We believe this method has the potential to become a standard tool in numerical analysis, offering a practical and efficient alternative for derivative-related computations in diverse applications.

REFERENCES

[1] BOYCE, W. E.; DIPRIMA, R. C. **Métodos numéricos**. 9. ed. Rio de Janeiro: LTC, 2013.

[2] BURDEN, R. L.; FAIRES, D. J. **Análise numérica**. 11. ed. Rio de Janeiro: LTC, 2014.

[3] CHAPRA, S. C.; CANALE, R. P. **Métodos numéricos para engenharia**. 6. ed. Rio de Janeiro: LTC, 2010.

[4] GANGA, Gilberto Miller Devós. **Trabalho de conclusão de curso (TCC) na engenharia de produção: um guia prático de conteúdo e forma**. São Paulo: Atlas, 2012.

[5] MORABITO, Reinado; PUREZA, Vitória. **Metodologia de pesquisa em engenharia de produção e gestão de operações**. Rio de Janeiro: Elsevier, 2012.

[6] QUARTERONI, Alfio; SALERI, Fausto; GERVASIO, Paola. **Scientific computing with MATLAB and Octave**. 2. ed. Cham: Springer, 2001.

[7] QUARTERONI, Alfio; VALLI, Alberto. **Numerical approximation of partial differential equations**. Cham: Springer, 2016.

[8] SMITH, Barry T.; BJORSTAD, Petter E.; GROPP, William D. **Domain decomposition: parallel multilevel methods for elliptic partial differential equations**. Cambridge: Cambridge University Press, 2014.

CHAPTER 11

ACOUSTIC SYNTHESIS OF RANDOM WALL-PRESSURE FIELDS FROM TURBULENT BOUNDARY LAYERS USING MONOPOLE ARRAYS AND ACOUSTIC RADIATION MODES

Clinton André Merlo
Doctor in Mechanical Engineering
Universidade Federal de Itajubá (UNIFEI)
E-mail: clintonmerlo@unifei.edu.br

Otávio Lage Dias
Graduate in Computer Engineering
Universidade Federal de Itajubá (UNIFEI)
E-mail: d2023011241@unifei.edu.br

Rogério Fernandes Brito
Doctor in Mechanical Engineering
Universidade Federal de Itajubá (UNIFEI)
E-mail: rogbrito@unifei.edu.br

ABSTRACT: This work investigates the acoustic synthesis of wall-pressure fields characteristic of turbulent boundary layers (TBL) by means of planar arrays of monopole sources with image symmetry. The empirical–statistical model proposed by Corcos was adopted to describe the spatial and spectral coherence of the target field, while the acoustic radiation was represented through the monopole array, thus avoiding the use of high-cost numerical methods. To stabilize the inverse problem and reduce the source effort, regularization based on Acoustic Radiation Modes (ARMs) was employed. The quality of the synthesis was assessed through metrics that quantify spectral fidelity, spatial coherence, and excitation effort. The results showed that the Least Squares (LS) method provides higher statistical fidelity to the target field but leads to amplitudes that are impractical for experimental implementations. In contrast, ARMs regularization significantly reduced the source effort—by several orders of magnitude—although with a partial loss of fidelity at higher frequencies. It is concluded that acoustic synthesis using monopole arrays constitutes a promising alternative for the reproduction of wall-pressure fields generated by TBL, providing a solid conceptual basis for future experimental implementations.

KEYWORDS: turbulent boundary layer. acoustic synthesis. wall-pressure fields. monopoles. acoustic radiation modes.

RESUMO: Este trabalho investiga a síntese acústica de campos de pressão parietal, ca-racterísticos de camadas limite turbulentas (TBL), por meio de arranjos planos de fontes monopolares com simetria por imagem. O modelo empírico-estatístico proposto por Corcos foi adotado para descrever a coerência espacial e espec-tral do campo alvo, enquanto a radiação foi representada pelo arranjo de mo-nopolos, evitando o uso de métodos numéricos de alto custo. Para estabilizar o problema inverso e reduzir o esforço das fontes, empregou-se a regularização via Modos de Radiação Acústica (ARMs). A qualidade da síntese foi avaliada por métricas que quantificam a fidelidade espectral, a coerência espacial e o esforço de excitação. Os resultados mostraram que o método de Mínimos Qua-drados (MQ) proporciona maior fidelidade estatística ao campo alvo, porém com amplitudes inviáveis para aplicações práticas. Em contrapartida, a regulariza-ção por ARMs reduziu o esforço das fontes em várias ordens de magnitude, embora com perda parcial de fidelidade em altas frequências. Conclui-se que a síntese acústica com arranjos de monopolos constitui uma alternativa pro-missora para a reprodução de campos de pressão parietal gerados por TBL, oferecendo uma base conceitual sólida para futuras implementações experi-mentais.

PALAVRAS-CHAVE: camada limite turbulenta, síntese acústica, campos de pressão parietal, monopolos. modos de radiação acústica.

1. INTRODUCTION

The study of the interaction between turbulent flows and rigid surfaces represents a central topic in aeroacoustics, with direct implications for aerospace, automotive, and structural vibroacoustic applications. In particular, wall-pressure fields generated by Turbulent Boundary Layers (TBL) exhibit a highly stochastic nature, characterized by broadband spectra and finite spatial coherence, acting as the primary excitation mechanism for panels and structural elements. The ability to reproduce such pressure fields in controlled environments is essential for assessing panel acoustic transparency, developing noise isolation and control strategies, and validating predictive models.

The acoustic synthesis of wall-pressure fields using controlled source arrays has emerged as an effective technique, extensively investigated in both experimental and numerical studies. Pioneering works by Elliott *et al*. (2005), Bravo & Maury (2006), and Maury & Bravo (2006) demonstrated that spatially correlated pressure fields can be generated from uncorrelated white-noise excitation signals, subsequently processed through shaping filters. These filters are designed to reproduce the cross-spectral density (CSD) matrix of the target field, thereby preserving its statistical coherence and spectral properties. More recently, Merlo (2023) extended this approach by applying Acoustic Radiation Mode concepts to the synthesis of diffuse fields, highlighting the technique's potential for reproducing complex, statistically consistent stochastic fields.

The classical description for the spatial coherence of TBL-induced wall pressure was established by Corcos (1964), whose model represents coherence as exponentials decaying in the streamwise and spanwise directions, modulated by a convective phase associated with a characteristic turbulence velocity. In the present work, the power spectral density (PSD) of the wall-pressure field is provided by the semi-empirical Efimtsov (1982) model, developed for high Reynolds numbers. The Efimtsov spectrum complements the Corcos coherence—capturing high-frequency decay and turbulent-scale effects—so their combination offers a robust basis for synthesizing TBL-induced pressure fields.

In this work, wall-pressure field synthesis means reproducing, in the observation plane, the second-order statistics (PSD and CSD) of the target field modeled by Corcos–Efimtsov. The approach does not attempt to reconstruct the full hydrodynamic physics of the flow; instead, it aims to statistically match the pressure field in the plane of interest.

To synthesize the acoustic field representing the modeled target field, a planar monopole array with image symmetry is employed. This configuration inherently satisfies the rigid-panel (Neumann) boundary condition, thereby avoiding full-field numerical methods such as FEM or BEM. Monopoles offer several modeling advantages, including conceptual simplicity, analytical field representations, and straightforward integration with synthesis techniques based on second-order statistical properties.

However, the synthesis formulation involves solving an inverse problem, in which the optimal source signals must be determined so that the radiated field statistically reproduces the target field. When addressed using the direct Least Squares (LS) method, this problem tends to be ill-conditioned, resulting in solutions with excessively high and physically unfeasible source amplitudes. To overcome this issue, the present work incorporates regularization via Acoustic Radiation Modes (ARMs), as proposed by Pasqual *et al*. (2010) and later applied by Merlo (2019) in the acoustic synthesis of diffuse random pressure fields. ARMs are the eigenvectors of the matrix relating source volume velocities to radiated power, forming an orthogonal basis of maximum radiation efficiency. By restricting the synthesis space to the most efficient modes, source effort can be drastically reduced and numerical stability improved, albeit with a partial loss of fidelity at high frequencies.

The proposed methodology is evaluated using well-established metrics in statistical synthesis of wall-pressure fields, each addressing a specific aspect of target-field reproduction. The normalized mean-square error $\hat{J}_e$ quantifies overall energy deviation; the residual error $\varepsilon_{\mathbf{y}}$ measures the preservation of spatial coherence; and the root-mean-square source-velocity norm $\| \overline{\mathbf{q}^{*2}} \|$ reflects the effort required to generate the field. Joint analysis of these metrics enables an optimal balance between statistical fidelity and practical feasibility, supporting future implementations with real sources.

2. THEORETICAL BACKGROUND

The proposed methodology combines statistical modeling, acoustic synthesis of wall-pressure fields, and modal regularization to reproduce, using a reduced array of monopole sources, the random pressure field generated by a TBL over a rigid panel. The objective is for the synthesized field to preserve the statistical properties of the target field, particularly its cross-spectral density matrix.

2.1 TBL CROSS-SPECTRAL DENSITY

The target field is modeled using the classical Corcos formulation for spatial coherence, combined with a spectral law for the wall-pressure PSD. The cross-spectral density between two points is

$$S_{ww}(\omega) = S_0(\omega)\, e^{-|r_x|/L_x(\omega)}\, e^{-|r_y|/L_y(\omega)}\, e^{-j\omega r_y/U_c} \qquad (1)$$

where:

> $S_0(\omega)$ is the wall-pressure power spectral density, r_x and r_y denote the spanwise and streamwise separations, respectively, and the Corcos correlation lengths follow the chosen convention $L_x = \alpha_x U_c/\omega$, $L_y = \alpha_y U_c/\omega$, $\alpha_x = 1.2$ (spanwise) and $\alpha_y = 8$ (streamwise).

The convection velocity is set to $U_c = 0.7U_\infty$ (about 70% of the free-stream velocity U_∞). For the spectral term $S_0(\omega)$, the semi-empirical Efimtsov model is adopted, which depends on the height-based Reynolds number Re_y, the Strouhal number St, the friction velocity U_τ and the wall shear stress τ_w

$$S_0(\omega) = \frac{0.01\tau_w^2\delta}{U_\tau[1+0.02\,St^{2/3}]}, \qquad St = \frac{\omega\delta}{U_\tau} \qquad (2)$$

The aerodynamic parameters are defined as $U_\tau = U_\infty\sqrt{C_f/2}$ and $\tau_w = (1/2)\rho U_\infty^2 C_f$, where ρ is the air density and δ is the boundary-layer thickness. The TBL friction coefficient is obtained from the empirical correlation

$$C_f = 0.37\left(\log_{10} Re_y\right)^{-2.584} \tag{3}$$

In this work, all spectral quantities are expressed in terms of frequency f (Hz). Following Miller *et al*. (2012), the Efimtsov spectrum, originally given per rad/s, is converted to PSD per hertz via $S_0(f) = 2\pi\, S_0(2\pi f)$, which yields

$$S_0(f) = \frac{2\pi(0.01\tau_w^2\delta)}{U_\tau\left[1+0.02\left(\frac{2\pi f\delta}{U_\tau}\right)^{2/3}\right]} \tag{4}$$

This form is used together with the Corcos model to construct the cross-spectral density matrix of the wall-pressure field induced by a turbulent boundary layer over the rigid panel.

2.2 STATISTICAL SHAPING FILTER

The target pressure field is generated from uncorrelated white-noise signals $\mathbf{x}$, filtered through a shaping matrix $\mathbf{D}$

$$\mathbf{w} = \mathbf{D}\mathbf{x} \tag{5}$$

This matrix is designed so that the synthesized field exhibits the same cross-spectral density matrix as the target field

$$\mathbf{S}_{ww} = \mathbf{D}\mathbf{D}^{\mathrm{H}} \tag{6}$$

The matrix is obtained via the spectral decomposition of $\mathbf{S}_{ww}$

$$\mathbf{D} = \mathbf{Q}\mathbf{\Lambda}^{1/2} \tag{7}$$

where:

$\mathbf{Q}$ contains the eigenvectors and $\mathbf{\Lambda}$ the eigenvalues. In this way, $\mathbf{D}$ acts as a statistical shaping filter, responsible for transforming the white-noise signals so that the target field exhibits coherence and spectral properties consistent with the Corcos–Efimtsov model.

2.3 ACOUSTIC CONTROL FILTER

The synthesis is performed using a monopole array with image symmetry. The coupling matrix $\mathbf{A}_\mathrm{d}$ relates the signals emitted by the sources to the pressures measured at the observation points. The elements of $\mathbf{A}_\mathrm{d}$ are obtained from the acoustic pressure field expression:

$$p(x_j, y_j, z_j, k) = -j\omega\rho_0 \sum_{i=1}^{n} Q_i \left[\frac{e^{jkr_{ij}^-}}{4\pi r_{ij}^-} + \frac{e^{jkr_{ij}^+}}{4\pi r_{ij}^+}\right] \quad (8)$$

where:

Q_i is the volume velocity of the *i*-th monopole source, and r_{ij}^- and r_{ij}^+ are the distances from the real monopole and its image to the observation point (x_j, y_j, z_j), respectively. The spectrum of the generated field is expressed as

$$\mathbf{y} = \mathbf{A}_\mathrm{d}\mathbf{M}\mathbf{x} \quad (9)$$

where:

$\mathbf{M}$ is the control filter matrix, responsible for adjusting the source signals so that the synthesized field reproduces the statistical properties of the target field. The spectral density of the generated field is

$$\mathbf{S}_{yy} = \mathbf{A}_\mathrm{d}\mathbf{M}\mathbf{M}^\mathrm{H}\mathbf{A}_\mathrm{d}^\mathrm{H} \quad (10)$$

2.4 UNREGULARIZED ACOUSTIC SYNTHESIS

The error spectral density is defined as

$$\mathbf{S}_{ee} = \mathbf{A}_{\mathrm{d}}\mathbf{M}\mathbf{M}^{\mathrm{H}}\mathbf{A}_{\mathrm{d}}^{\mathrm{H}} - \mathbf{A}_{\mathrm{d}}\mathbf{M}\mathbf{D}^{\mathrm{H}} - \mathbf{D}\mathbf{M}^{\mathrm{H}}\mathbf{A}_{\mathrm{d}}^{\mathrm{H}} + \mathbf{D}\mathbf{D}^{\mathrm{H}} \tag{11}$$

Thus, minimizing the mean-square error in the Least Squares sense, $J_e = \mathrm{Tr}[\mathbf{S}_{ee}]$, leads to the optimal control matrix

$$\mathbf{M}_{\mathrm{ot}} = (\mathbf{A}_{\mathrm{d}}^{\mathrm{H}}\mathbf{A}_{\mathrm{d}})^{-1}\mathbf{A}_{\mathrm{d}}^{\mathrm{H}}\mathbf{D} \tag{12}$$

and to the optimal source velocity vector

$$\mathbf{q}_{\mathrm{ot}}^{*} = \mathbf{M}_{\mathrm{ot}}\mathbf{x} \tag{13}$$

and, consequently, to the optimal generated pressure field

$$\mathbf{y}_{\mathrm{ot}} = \mathbf{A}_{\mathrm{d}}\, \mathbf{q}_{\mathrm{ot}}^{*} \tag{14}$$

2.5 REGULARIZED ACOUSTIC SYNTHESIS

To ensure efficiency and stability, the synthesis is regularized by considering only the most efficient ARMs. The modal matrix contains the normalized eigenvectors associated with the dominant eigenvalues of the radiation problem, derived from the model's power-coupling matrix $\mathbf{W}$. The source velocity vector is decomposed in a reduced modal subspace

$$\tilde{\mathbf{q}}^{*} = \widetilde{\mathbf{\Psi}}_{\tilde{\mathrm{d}}}\, \tilde{\boldsymbol{\alpha}}^{*} \tag{15}$$

where:

$\widetilde{\mathbf{\Psi}}_{\tilde{\mathrm{d}}}$ is the reduced modal matrix formed by the $\tilde{n}$ most efficient ARMs, and $\tilde{\boldsymbol{\alpha}}^{*}$ is the vector of modal contributions. The generated pressure field is then

$$\tilde{\mathbf{y}} = \mathbf{A}_{\mathrm{d}}\, \widetilde{\mathbf{\Psi}}_{\tilde{\mathrm{d}}}\; \tilde{\boldsymbol{\alpha}}^{*} \tag{16}$$

The spectral density of the error for the regularized synthesis is

$$\mathbf{S}_{\tilde{e}\tilde{e}} = \mathbf{A}_{\mathrm{d}}\widetilde{\mathbf{\Psi}}_{\tilde{\mathrm{d}}}\,\widetilde{\mathbf{M}}\widetilde{\mathbf{M}}^{\mathrm{H}}\widetilde{\mathbf{\Psi}}_{\tilde{\mathrm{d}}}^{\mathrm{H}}\mathbf{A}_{\mathrm{d}}^{\mathrm{H}} - \mathbf{A}_{\mathrm{d}}\widetilde{\mathbf{\Psi}}_{\tilde{\mathrm{d}}}\widetilde{\mathbf{M}}\mathbf{D}^{\mathrm{H}} - \mathbf{D}\widetilde{\mathbf{M}}^{\mathrm{H}}\widetilde{\mathbf{\Psi}}_{\tilde{\mathrm{d}}}^{\mathrm{H}}\mathbf{A}_{\mathrm{d}}^{\mathrm{H}} + \mathbf{D}\mathbf{D}^{\mathrm{H}} \tag{17}$$

where:

$\widetilde{\mathbf{M}}$ is the reduced control filter matrix. Minimizing the regularized mean-square error, $J_{\tilde{\mathrm{e}}} = \mathrm{Tr}[\mathbf{S}_{\tilde{e}\tilde{e}}]$, leads to the optimal control matrix

$$\widetilde{\mathbf{M}}_{\mathrm{ot}} = (\widetilde{\mathbf{\Psi}}_{\tilde{\mathrm{d}}}^{\mathrm{H}}\,\mathbf{A}_{\mathrm{d}}^{\mathrm{H}}\,\mathbf{A}_{\mathrm{d}}\,\widetilde{\mathbf{\Psi}}_{\tilde{\mathrm{d}}})^{-1}\;\widetilde{\mathbf{\Psi}}_{\tilde{\mathrm{d}}}^{\mathrm{H}}\,\mathbf{A}_{\mathrm{d}}^{\mathrm{H}}\,\mathbf{D} \tag{18}$$

which generates the optimal ARMs contributions

$$\widetilde{\boldsymbol{\alpha}}_{\mathrm{ot}}^{*} = \widetilde{\mathbf{M}}_{\mathrm{ot}}\,\mathbf{x} \tag{19}$$

and, consequently, the regularized pressure field

$$\tilde{\mathbf{y}}_{\mathrm{ot}} = \mathbf{A}_{\mathrm{d}}\,\widetilde{\mathbf{\Psi}}_{\tilde{\mathrm{d}}}\;\widetilde{\boldsymbol{\alpha}}_{\mathrm{ot}}^{*} \tag{20}$$

2.6 CONTROL METRICS

The synthesized acoustic field, which corresponds statistically to the TBL-induced wall-pressure field, was evaluated using three complementary metrics that quantify spectral fidelity, spatial coherence, and physical feasibility of the reconstruction. These metrics are defined and examined for both the unregularized case and the ARMs-regularized case.

2.6.1 Normalized mean-square error

This metric quantifies the overall spectral fidelity, representing the portion of the target field's total energy $\mathbf{S}_{ww}$ that lies outside the synthesis space.

$$\hat{J}_{e} = \frac{\mathrm{Tr}[\left(\mathbf{I} - \mathbf{A}_{\mathrm{d}}\mathbf{A}_{\mathrm{d}}^{\dagger}\right)\mathbf{S}_{ww}]}{\mathrm{Tr}[\mathbf{S}_{ww}]} \tag{21}$$

$$\hat{J}_{\tilde{\mathrm{e}}} = \frac{\mathrm{Tr}\left[\left(\mathbf{I} - \mathbf{A}_{\mathrm{d}}\widetilde{\boldsymbol{\Psi}}_{\tilde{\mathrm{d}}}\left(\mathbf{A}_{\mathrm{d}}\widetilde{\boldsymbol{\Psi}}_{\tilde{\mathrm{d}}}\right)^{\dagger}\right)\mathbf{S}_{ww}\right]}{\mathrm{Tr}[\mathbf{S}_{ww}]} \tag{22}$$

where:

$\mathbf{A}_{\mathrm{d}}{}^{\dagger}$ and $\left(\mathbf{A}_{\mathrm{d}}\widetilde{\boldsymbol{\Psi}}_{\tilde{\mathrm{d}}}\right)^{\dagger}$ are the pseudoinverses of the matrices $\mathbf{A}_{\mathrm{d}}$ and $\mathbf{A}_{\mathrm{d}}\widetilde{\boldsymbol{\Psi}}_{\tilde{\mathrm{d}}}$, respectively. Criterion: $\hat{J}_e < -10\ \mathrm{dB}$ indicates that less than 10% of the total energy of the target field lies outside the synthesis space, indicating good fidelity.

2.6.2 Residual error

This metric indicates how well the spatial structure of the target field is preserved by the synthesized field, not only in terms of total energy (as in $\hat{J}_e$) but also in how that energy is distributed spatially across the measurement points.

$$\varepsilon_{\mathbf{y}} = \frac{\|\mathbf{C}_{ww} - \mathbf{C}_{yy}\|_{\mathrm{F}}}{\|\mathbf{C}_{ww}\|_{\mathrm{F}}} \tag{23}$$

$$\varepsilon_{\tilde{\mathbf{y}}} = \frac{\left\|\mathbf{C}_{ww} - \mathbf{C}_{\tilde{y}\tilde{y}}\right\|_{\mathrm{F}}}{\|\mathbf{C}_{ww}\|_{\mathrm{F}}} \tag{24}$$

where:

$\|\cdot\|_{\mathrm{F}}$ denotes the Frobenius norm, $\mathbf{C}_{ww}$, $\mathbf{C}_{yy}$ and $\mathbf{C}_{\tilde{y}\tilde{y}}$ are the spatial correlation matrices of the target and generated pressure fields.

The construction of $\mathbf{C}_{yy}$, based on the spectral density matrix $\mathbf{S}_{yy}$, is detailed in Bravo & Maury (2006). Criterion: $\varepsilon_{\mathbf{y}} < -1\ \mathrm{dB}$ indicates acceptable spatial reproduction. This means that the residual error contains less than 20% of the energy of the original correlation matrix, reflecting good preservation of the spatial structure.

2.6.3 Root-mean-square source velocity norm

This metric quantifies the total effort of the sources (monopoles) in reproducing the desired field, i.e., it indicates how much energy the sources need to radiate to generate the target pressure field.

$$\parallel \overline{\mathbf{q}^{*2}} \parallel = \sqrt{\mathrm{Tr}\left[\mathbf{A}_{\mathrm{d}}^{\dagger}\mathbf{D}\mathbf{D}^{\mathrm{H}}\left(\mathbf{A}_{\mathrm{d}}^{\dagger}\right)^{\mathrm{H}}\right]} \tag{25}$$

$$\parallel \overline{\tilde{\mathbf{q}}^{*2}} \parallel = \sqrt{\mathrm{Tr}\left[\tilde{\mathbf{\Psi}}_{\tilde{\mathrm{d}}}\left(\mathbf{A}_{\mathrm{d}}\tilde{\mathbf{\Psi}}_{\tilde{\mathrm{d}}}\right)^{\dagger}\mathbf{D}\mathbf{D}^{\mathrm{H}}\left(\left(\mathbf{A}_{\mathrm{d}}\tilde{\mathbf{\Psi}}_{\tilde{\mathrm{d}}}\right)^{\dagger}\right)^{\mathrm{H}}\tilde{\mathbf{\Psi}}_{\tilde{\mathrm{d}}}^{\mathrm{H}}\right]} \tag{26}$$

High values suggest a risk of saturation, instability, or nonlinearity, sensitivity to noise, and poor conditioning of the transfer matrix. Low values — achieved via ARMs — indicate a more efficient and stable synthesis, with reduced physical and numerical effort.

3. NUMERICAL SYNTHESIS RESULTS

Numerical simulations targeted acoustic synthesis up to $f_{max} = 1\ \mathrm{kHz}$ over a rigid, acoustically reflecting panel of dimensions $0.328\mathrm{m}\ (\mathrm{spanwise}, x) \times 0.768\mathrm{m}\ (\mathrm{streamwise}, y)$. A planar array of monopole sources, coextensive with the panel, was used together with image sources to enforce a Neumann boundary at the panel plane. The source grid comprised $n_x \times n_y = 24 \times 10 = 240$ monopoles with spacings $s_x = 0.01426\ \mathrm{m}$ and $s_y = 0.08533\ \mathrm{m}$; these spacings satisfy the acoustic grating-lobe condition $\Delta_s \leq c/(2f_{max}) = 0.1715\ \mathrm{m}$ and also the spanwise correlation sampling rule of 2.1 sources per L_x, i.e., $s_x \lesssim L_x/2.1$. In the more restrictive case $\mathrm{Mach}\ 0.7$, $L_x = \alpha_x U_c/(2\pi f_{max}) \approx 0.0321\ \mathrm{m}$ so $L_x/2.1 \approx 0.0153\ \mathrm{m}$ and $s_x = 0.01426\ \mathrm{m}$ complies; similarly, $L_y/2.1 \approx 0.102\ \mathrm{m}$ and $s_y = 0.08533\ \mathrm{m}$ complies. The microphone array comprised $m_x \times m_y = 49 \times 23 = 1127$ equally spaced sensors located $0.002\ \mathrm{m}$ above the panel, with spacings $d_x = 0.006833\ \mathrm{m}$ and $d_y = 0.03491\ \mathrm{m}$. Aliasing limits derived from Corcos coherence and the convective Nyquist criterion provide comfortable margins up to $1\,\mathrm{kHz}$: for $\mathrm{Mach}\ 0.7$, $f_{\mathrm{lim},x} = 2349\ \mathrm{Hz}$ and $f_{\mathrm{lim},y} = 2407\ \mathrm{Hz}$ $(\mathrm{coherence\ only} = 3065\ \mathrm{Hz},\ \mathrm{Nyquist} = 2407\ \mathrm{Hz})$; for $\mathrm{Mach}\ 0.9$, $f_{\mathrm{lim},x} = 3020\ \mathrm{Hz}$ and $f_{\mathrm{lim},y} = 3095\ \mathrm{Hz}$ $(\mathrm{coherence\ only} = 3941\ \mathrm{Hz},\ \mathrm{Nyquist} = 3095\ \mathrm{Hz})$. The monopole plane was placed $0.1\mathrm{m}$ from the panel with coincident centers. Control performance was evaluated using unregularized least squares (LS) and LS regularized with Acoustic Radiation Modes (ARMs), employing a 60-mode subset (far-field and near-field ARMs) selected from the 240 available by radiation efficiency.

Table 1. Approximate aerodynamic parameters.

Parameter	Mach 0.7	Mach 0.9
Free-stream velocity U_∞ $(\mathrm{m/s})$	240.1	308.7
Shear stress τ_w $(\mathrm{N/m^2})$	66.5623	106.0907
Friction velocity U_τ $(\mathrm{m/s})$	7.4169	9.3637
Boundary layer thickness δ (m)	0.0336	0.0326

Source: the authors (2025)

Table 1 presents the approximate aerodynamic parameters of the flow, for two Mach numbers, over a rigid flat panel, which were used in the numerical simulations. The parameters were estimated assuming air at $20^\circ\mathrm{C}$ and 1 atm, with air density $\rho_0 = 1.21\ \mathrm{kg/m^3}$, sound speed $c = 343\ \mathrm{m/s}$, and kinematic viscosity $\nu = 1.5111 \times 10^{-5}\ \mathrm{m^2/s}$.

Figure 1. Normalized mean-square error as a function of frequency for two Mach numbers.

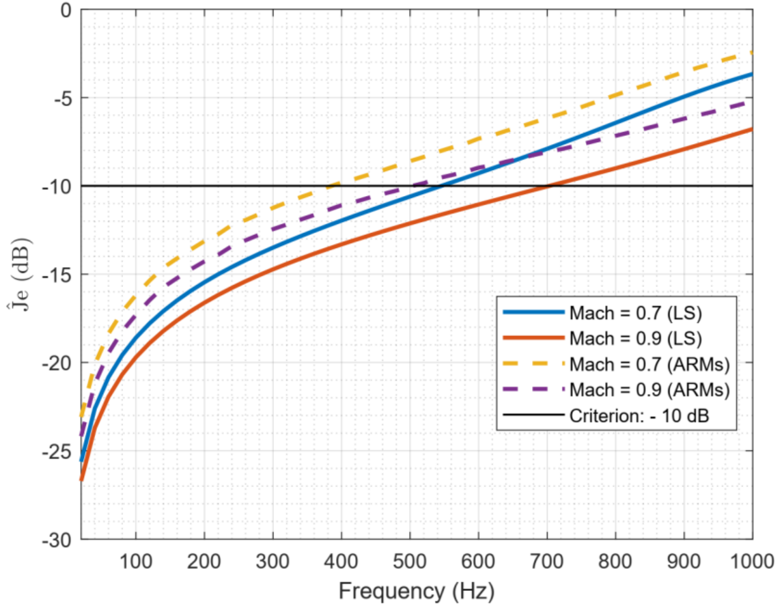

Source: the authors (2025).

Figure 1 presents the behavior of the normalized mean-square error as a function of frequency, a metric that quantifies the overall spectral fidelity between the synthesized pressure field and the target field modeled using the combined Corcos–Efimtsov formulation. The LS method exhibits lower error levels across most of the frequency range, remaining below $-10\,\mathrm{dB}$ over the band and approaching the limit near $1\,\mathrm{kHz}$. This indicates that less than 10% of the total energy of the target field lies outside the synthesis space, demonstrating excellent statistical agreement.

This performance directly results from exploiting all available degrees of freedom in the monopole array, allowing the LS method to fully project the target field onto the radiation space represented by the coupling matrix $\mathbf{A}_{\mathrm{d}}$. Consequently, the amplitudes and phases of the sources are optimally adjusted, ensuring that the radiated field accurately reproduces the spectral energy distribution of the turbulent boundary layer.

In contrast, the ARMs-regularized solution exhibits higher $\hat{J}_e$ values, particularly at high frequencies. This difference stems from the modal reduction applied — only the 60 most efficient radiation modes were retained out of the 240 available. Modal truncation constrains the system's ability to reproduce higher-order spatial components, which are associated with short-scale fluctuations and become increasingly relevant in the high-frequency region. As a result, part of the target-field energy is not captured, increasing the synthesis error.

Overall, Figure 1 highlights the trade-off between fidelity and stability: while the LS approach provides maximum spectral accuracy at the expense of higher source effort and numerical sensitivity, the ARMs regularization sacrifices some fidelity in favor of robustness and practical feasibility.

Figure 2 shows the residual error versus frequency, a metric that emphasizes preservation of the spatial coherence of the wall-pressure field. Unlike $\hat{J}_e$, which gauges global energy deviation, $\varepsilon_{\mathbf{y}}$ compares the correlation structures of the target field ($\mathbf{C}_{ww}$) and the synthesized field ($\mathbf{C}_{yy}$), thus indicating how well phase–amplitude relationships across the surface are reproduced. The curves include Mach 0.7 and 0.9 for both LS and ARMs, with the $-1\,\mathrm{dB}$ acceptability line shown for reference.

Figure 2. Residual error as a function of frequency for two Mach numbers.

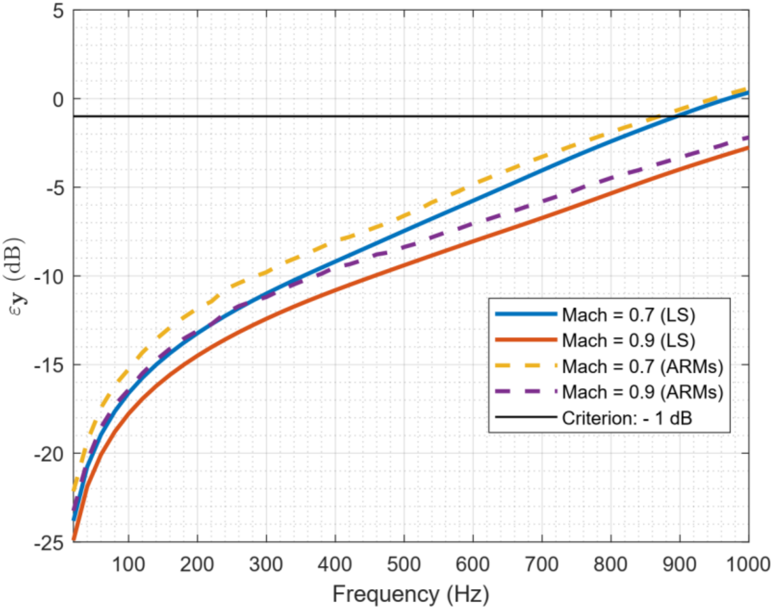

Source: the authors (2025).

Consistent with Figure 1, the LS solution yields the lowest $\varepsilon_{\mathbf{y}}$ across the band, typically remaining at or below $-1\,\mathrm{dB}$, with Mach 0.7 marginally outperforming Mach 0.9 near the upper frequencies. This indicates that LS preserves the convective coherence pattern while matching mean energy, benefiting from access to the full radiation space.

ARMs regularization leads to higher $\varepsilon_{\mathbf{y}}$, especially toward $900 - 1000\ \mathrm{Hz}$, where some curves approach or slightly exceed the $-1\,\mathrm{dB}$ threshold. The increase reflects modal truncation: limiting the subspace attenuates short-scale components and underestimates transverse coherence. Overall, Figure 2 illustrates the expected trade-off: LS maximizes coherence fidelity at the cost of higher source effort, whereas ARMs provide a more robust, physically stable solution with some loss of fine spatial detail—appropriate for practical implementations.

Figure 3. Spatial correlation structures for the theoretical reproduction of a TBL field at Mach 0.9 (top), for the synthesized field without regularization using the LS method (middle), and with ARMs regularization (bottom).

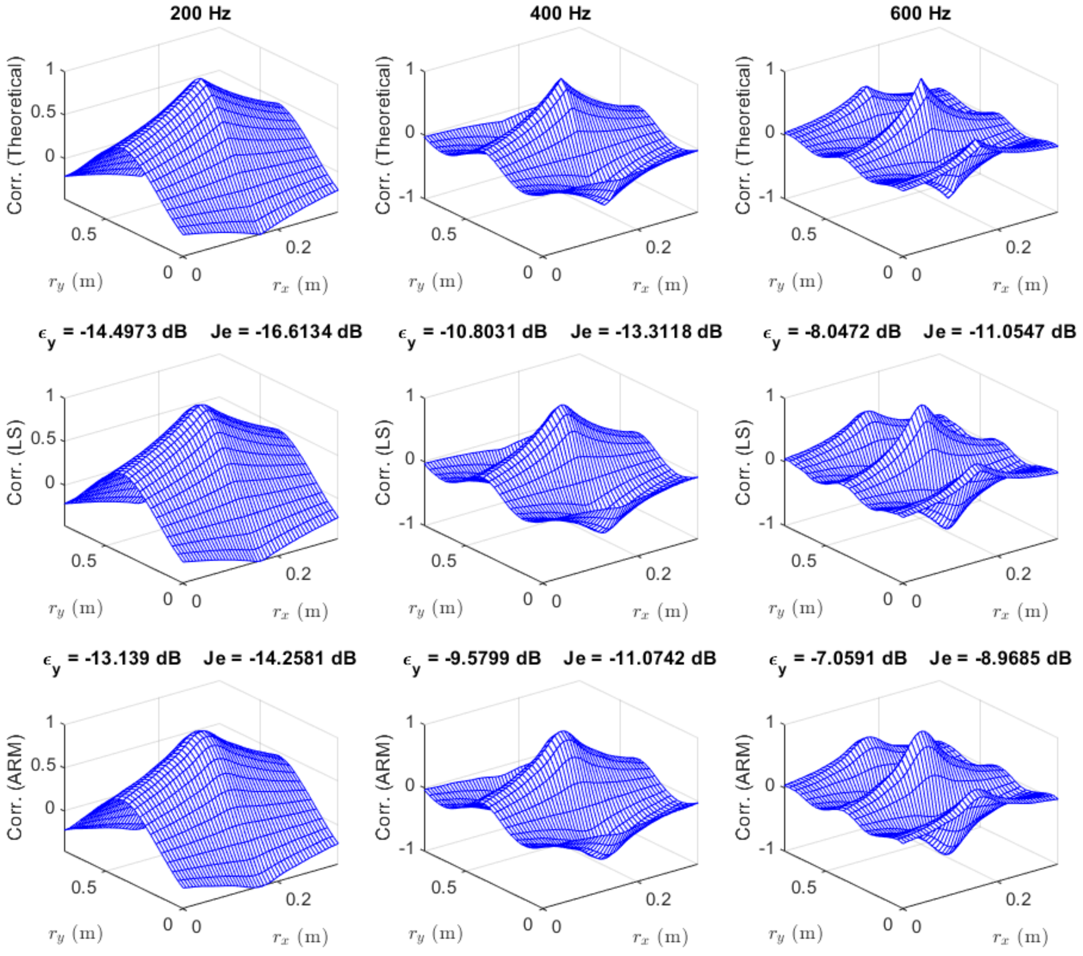

Source: the authors (2025).

Figure 3 compares the spatial correlation structures of wall-pressure fluctuations generated by the turbulent boundary layer (TBL), highlighting how the theoretical coherence patterns are reproduced by the synthesis methods. The top row shows the theoretical field predicted by the Corcos model. At $200\ \mathrm{Hz}$, the correlation pattern extends over a wide, coherent region associated with large eddies convecting along the surface. As frequency increases to $400\ \mathrm{Hz}$ and $600\ \mathrm{Hz}$, the contours become more oscillatory and fragmented, reflecting shorter correlation lengths and phase reversals linked to smaller turbulent structures.

The middle row shows the LS-synthesized fields. The agreement with the theoretical model is excellent across the band. At $200\ \mathrm{Hz}$, the synthesized and theoretical fields are nearly identical ($\hat{J}_e = -16.6\ \mathrm{dB}$, $\varepsilon_{\mathrm{y}} = -14.5\ \mathrm{dB}$), and even at $400\ \mathrm{Hz}$ and $600\ \mathrm{Hz}$ the amplitude and phase structures remain well preserved

($\hat{J}_e = -13.3\ \mathrm{dB}, -11.1\ \mathrm{dB}$; $\varepsilon_{\mathbf{y}} = -10.8\ \mathrm{dB}, -8.0\ \mathrm{dB}$). These results confirm that LS effectively captures the convective topology of the TBL pressure field, preserving spatial coherence and the anisotropy imposed by the mean flow.

The ARMs-based synthesis (bottom row) reproduces the general correlation pattern but exhibits gradual smoothing at higher frequencies. Retaining only the 60 most efficient radiation modes limits the reconstruction of short-wavelength components, especially in the spanwise direction. Fine-scale coherence features are partially filtered out, slightly increasing the errors ($\hat{J}_e = -14.3\ \mathrm{dB}$ to $-9\ \mathrm{dB}$; $\varepsilon_{\mathbf{y}} = -13.1\ \mathrm{dB}$ to $-7\ \mathrm{dB}$) but improving numerical stability and reducing source effort. This truncation acts as a physically meaningful regularization, suppressing near-singular modes that add little to the radiated energy yet amplify instability.

Figure 4. Root-mean-square velocity norm as a function of frequency for two Mach numbers.

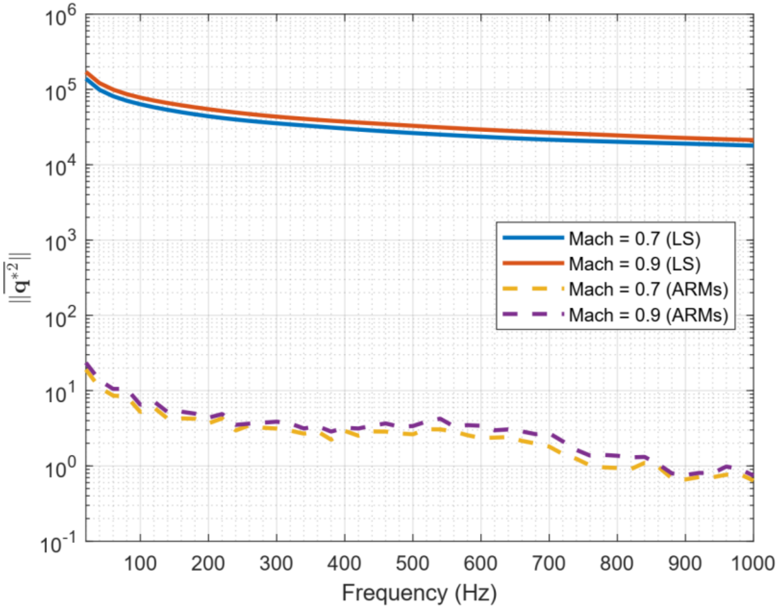

Source: the authors (2025).

Figure 4 presents the root-mean-square velocity norm of the sources, which quantifies the physical and energetic effort required to synthesize the target field. This parameter represents the total power radiated by the array and is directly linked to the conditioning of the inverse problem and the experimental feasibility.

The LS method exhibits very high $\|\overline{\mathbf{q}^{*2}}\|$ values—ranging roughly from 10^4 up to 10^5 over the band—indicating source amplitudes that are impractical for experimental implementation. This behavior results from the ill-conditioned nature of the coupling matrix $(\mathbf{A}_\mathrm{d})$: by minimizing the synthesis error without regularization, the LS solution amplifies components associated with small singular values, yielding unstable and energetically unbalanced source distributions. Consequently, although LS ensures the highest statistical fidelity (i.e., the lowest $\hat{J}_e$ and $\varepsilon_\mathbf{y}$), its energetic cost renders physical implementation unfeasible.

In contrast, the ARMs method reduces source effort by several orders of magnitude, with typical values between 10^0 and 10^1. This efficiency stems from modal regularization, which confines the synthesis to the most efficient radiation modes—those converting source energy into sound most effectively. By excluding ill-conditioned and inefficient modes, ARMs stabilizes the inverse problem and yields a more uniform, physically coherent distribution of source amplitudes.

Therefore, the LS method provides maximum fidelity, but at the cost of high energetic effort and numerical instability. In contrast, the ARMs method yields a more stable, efficient, and experimentally feasible solution, with only a slight loss of fidelity. This balance between statistical accuracy and practical feasibility represents the core objective of the proposed methodology.

To establish the frequency range over which the ARMs-regularized synthesis remains statistically valid, a cut-off frequency was defined based on the residual-error criterion $(\varepsilon_\mathbf{y} < -1\ \mathrm{dB})$. This threshold ensures that at least $\sim 80\%$ of the spatial-correlation energy of the target field is preserved, corresponding to good reproduction of the coherence structure characteristic of wall-pressure fluctuations induced by turbulent boundary layers. Although the normalized mean-square error criterion $(\hat{J}_e < -10\ \mathrm{dB})$ also indicates acceptable global spectral fidelity, it is less sensitive to spatial-phase deviations and thus less physically representative of the synthesized field. The residual-error-based definition of f_c therefore provides a more stringent and physically meaningful limit, identifying the highest frequency at which the ARMs approach can accurately reproduce both the amplitude and the convective coherence of the target pressure field; beyond this frequency, modal truncation progressively smooths the field and reduces coherence even if the overall energy level remains approximately correct.

Table 2. Estimated cut-off frequencies for ARMs-regularized synthesis (target f_{max} = 1 kHz)

Mach	$\tilde{n}$ (ARMs)	$f_{c,\hat{J}_e}$ [Hz]	$f_{c,\varepsilon_{\mathbf{y}}}$ [Hz]	Observation
0.7	40	310	820	Stable through mid frequencies; does not reach 1 kHz in residual.
0.9	40	400	1060	Gradual coherence loss above ~ 900 Hz; residual meets the 1 kHz target with a small margin.
0.7	60	390	860	Spatial coherence preserved up to ~ 860 Hz; still below 1 kHz for Mach $= 0.7$.
0.9	60	510	1110	Robust performance; residual comfortably exceeds 1 kHz; $\hat{J}_e$ advances to $\sim$ 500 Hz.
0.7	80	440	880	Near full-band reproduction; residual approaches but does not reach 1 kHz.
0.9	80	560	1130	Upper-band extension with a comfortable margin $>$ 1 kHz in residual; $\hat{J}_e$ improved without instability.
0.7	240 (LS)	550	890	Unregularized LS raises $f_{c,\hat{J}_e}$, but residual gains are modest; higher conditioning/effort risk.
0.9	240 (LS)	700	1150	Residual well above 1 kHz; $\hat{J}_e$ remains <1 kHz; watch conditioning and control effort.

Source: the authors (2025)

Table 2 summarizes the estimated cut-off frequencies for two Mach numbers (0.7 and 0.9) and three ARMs truncations ($\tilde{n} = 40, 60, 80$), including the unregularized LS reference ($\tilde{n} = 240$). The values were obtained from the frequency-domain curves of $\hat{J}_e\,(f)$ and $\varepsilon_{\mathbf{y}}\,(f)$. For each case, $f_{c,\,\varepsilon_{\mathbf{y}}}$ denotes the first frequency at which the residual error exceeds -1 dB, while $f_{c,\,\hat{J}_e}$ corresponds to the -10 dB limit. As expected, retaining more ARMs extends the coherent bandwidth, enabling accurate reproduction of spatial coherence at higher frequencies. Consistent with the table, for Mach 0.9 the residual cut-off exceeds 1 kHz even with $\tilde{n} = 40$, while for Mach 0.7 it remains below 1 kHz up to $\tilde{n} = 80$. Thus, higher-speed flows—whose wall-pressure spectra contain more high-frequency energy—benefit from increased modal retention. Insufficient truncation leads to coherence degradation at high frequencies, underscoring the importance of appropriate ARMs-based regularization.

4. CONCLUSIONS

The results confirm that the proposed methodology can statistically reproduce random wall-pressure fields representative of turbulent boundary layers (TBL) by using a planar array of monopole sources together with image sources to impose a Neumann boundary at the panel plane. Although monopoles are idealizations, their analytical tractability and well-characterized radiation enable a clear physical interpretation of the synthesis process and an efficient numerical implementation.

The unregularized least-squares (LS) formulation achieved the highest statistical fidelity, accurately reproducing both the spectral energy distribution and the spatial coherence of the Corcos–Efimtsov target fields (Mach 0.7 and 0.9, up to $1\,\mathrm{kHz}$). However, the required source effort was prohibitively large, reflecting the ill-conditioning of the coupling operator and limiting experimental feasibility.

Acoustic Radiation Mode (ARM) regularization stabilized the inversion and reduced energetic demand by several orders of magnitude while preserving the dominant coherence and spectral features of the target. The moderate loss of fidelity observed at the highest frequencies is attributable to modal truncation, which confines the solution space to the most efficient radiating modes, and nevertheless, the ARM-based synthesis remained physically consistent, stable, and experimentally realizable.

Overall, the study establishes a coherent framework for controlled reproduction of TBL-induced wall-pressure fields that balances accuracy, robustness, and computational efficiency. The approach provides a solid basis for experimental validation and for future extensions to non-uniform source layouts, structural/acoustic coupling, and near-field synthesis.

REFERENCES

BRAVO, T.; MAURY, C. The experimental synthesis of random pressure fields: methodology. *The Journal of the Acoustical Society of America*, **120**(5), 2702–2711, 2006.

CORCOS, G. M. The structure of the turbulent pressure field in boundary-layer flows. *Journal of Fluid Mechanics*, **18**(3), 353–378, 1964.

EFIMTSOV, B. M. Characteristics of the field of turbulent wall pressure fluctuations at large Reynolds numbers. *Soviet Physics Acoustics*, **28**, 289–292, 1982.

ELLIOTT, S. J.; MAURY, C.; GARDONIO, P. The synthesis of spatially correlated random pressure fields. *The Journal of the Acoustical Society of America*, **117**(3), 1186–1201, 2005.

MAURY, C.; BRAVO, T. The experimental synthesis of random pressure fields: practical feasibility. *The Journal of the Acoustical Society of America*, **120**(5), 2712–2723, 2006.

MERLO, C. A. Synthesis of the diffuse random pressure field using active and reactive radiation modes. *Contemporary Journal*, **3**(11), 20849–20872, 2023.

MERLO, C. A.; PASQUAL, A. M.; MEDEIROS, E. B. Sound field synthesis on flat panels using a planar source array controlled by its active and reactive radiation modes. *Acta Acustica united with Acustica*, **105**(1), 139–151, 2019.

MILLER, T. S.; GALLMAN, J. M.; MOELLER, M. J. Review of turbulent boundary layer models for acoustic analysis. *Journal of Aircraft*, **49**(6), 1739–1754, 2012.

PASQUAL, A. M.; ARRUDA, J. R. F.; HERZOG, P. Application of acoustic radiation modes in the directivity control by a spherical loudspeaker array. *Acta Acustica united with Acustica*, **96**(1), 32–42, 2010.

Agência Brasileira ISBN
ISBN: 978-65-83309-52-5

STUDIES
PUBLICAÇÕES
2026